

1

---

2                   **A Novel Multidimensional Search for**  
3                   **Diboson Resonances in the Boosted Dijet Final State**

4                   **and**

5                   **Encoding Jet Substructure with a Deep Neural Network**

---

7                   Dissertation

8                   zur  
9                   Erlangung der naturwissenschaftlichen Doktorwürde  
10                   (Dr. sc. nat.)

11                   vorgelegt der  
12                   Mathematisch-naturwissenschaftlichen Fakultät  
13                   der  
14                   Universität Zürich

15                   von

16                   Thea Klaeboe Arrestad  
17                   aus  
18                   Norwegen

19                   Promotionskommission:

20                   Prof. Dr. Ben Kilminster (Vorsitz)  
21                   Prof. Dr. Florencia Canelli  
22                   Prof. Dr. Jesse Thaler  
23                   Dr. Andreas Hinzmann

24                   Zürich 2019



## Abstract

In this doctoral thesis I will present three different searches for new heavy resonances decaying into pairs of vector bosons in the all-hadronic final state. The analyzed data were collected by the CMS experiment at the LHC during the first three years of data-taking at a collision center-of-mass energy of 13 TeV, corresponding to an integrated luminosity of 2.7(2015), 35.9(2016) and 77.3(2016+2017)  $\text{fb}^{-1}$ , and the searches were the first of their kind to ever be performed at such a high collision energy. The diboson final states under consideration are challenging to resolve due to the bosons being highly energetic (“boosted”), resulting in the two quarks from the decay being collimated and merging into a single jet. This leads to a dijet final state topology where each jet displays some energy substructure. The first search I will present, was one of the two first CMS searches in boosted final states with 13 TeV data to become published, and the first to take advantage of jet substructure at the trigger level. It was a high profile analysis due to a previously observed  $3.4$  ( $1.3$ )  $\sigma$  excess around 2 TeV in the 8 TeV dataset, as analyzed by ATLAS (CMS), and I brought the search to a published result within six months after 13 TeV data taking began (and within ten months after embarking on my PhD). Following this, in my second analysis I optimized, validated and commissioned the novel PUPPI softdrop jet grooming algorithm for vector-boson tagging and, in addition, developed dedicated mass corrections for the softdrop jet mass. The algorithm and corresponding mass corrections are now the default for vector boson tagging in CMS and used by several analyses. It was the first published result taking advantage of PUPPI softdrop jet grooming. The third and final search I will present introduces a novel multidimensional search framework, which can be used to search for resonances peaking anywhere in the 3D spectrum of the dijet and groomed jet mass spectra. A simultaneous fit to the W and Z jet mass peaks from the Standard Model  $V(\bar{q}q)+\text{jets}$  process has been performed, allowing the first extraction of the jet mass scale and resolution (and eventually  $V(\bar{q}q)+\text{jets}$  cross section) from this region. Validated through a search with hadronically decaying vector bosons in the final state, which I will present here, the framework can be used to incorporate all resonance searches with hadronically decaying vector boson or hadronically decaying Higgs boson final states, as well as for generic searches for any boosted object peaking in jet mass. Finally, I will present a deep neural network for vector-boson tagging which, through custom layers, encodes jet clustering- and substructure-like variables into the deep layers themselves. This significantly improves the analysis sensitivity, and can also be used as a stepping stone in the development of a generic anti-QCD tagger. The latter will be of great importance when attempting to use the multidimensional framework for model-independent searches.



## Zusammenfassung

In dieser Doktorarbeit werde ich drei verschiedene Suchen nach neuen starken Resonanzen vorstellen, die im all-hadronischen Endzustand in Paare von Vektorbosonen zerfallen. Die analysierten Daten wurden durch das CMS-Experiment am Large Hadron Collider (LHC) während der ersten drei Jahre der Datenaufnahme bei einer Kollisionsschwerpunktsenergie von 13 TeV gesammelt, und die Suchen waren die ersten ihrer Art jemals bei einer so hohen Kollisionsenergie durchgeführt worden. Die Dibosonendzustände, die in Betracht gezogen werden, sind schwierig zu lösen, da die Bosonen sehr energiereich ("boosted") sind, was dazu führt, dass die beiden Quarks aus dem Zerfall sehr stark aufeinander abgestimmt sind und zu einem einzigen Jet zusammengeführt werden. Dies führt zu einer Dijet-Endzustands-Topologie, bei der jeder Jet eine Energieunterstruktur aufweist. Die erste Suche, die ich vorstellen werde, war eine der ersten CMS-Suchen in angehobenen Endzuständen mit 13 TeV Daten, die veröffentlicht wurden, und die erste, die die Jet-Substruktur auf Trigger-Ebene nutzte. Es war eine hochkarätige Analyse aufgrund eines beobachteten  $3.4 (1.3) \sigma$  Überschusses um 2 TeV im 8 TeV Datensatz, der von ATLAS (CMS) analysiert wurde, und ich brachte die Suche innerhalb von sechs Monaten zu einem veröffentlichten Ergebnis nach 13 TeV wurde mit der Datenaufnahme begonnen (und innerhalb von zehn Monaten nach Beginn meiner Promotion). Durch die zweite Analyse wurde der neuartige PUPPI Softdrop Jet Grooming Algorithmus für das Vektor Boson Tagging optimiert, validiert und in Betrieb genommen. Außerdem wurden spezielle Massenkorrekturen für die Softdrop Jet Masse entwickelt. Der Algorithmus und die entsprechenden Massenkorrekturen sind jetzt der Standard für das Vektor Boson Tagging in CMS und werden von mehreren Analysen verwendet. Es war das erste veröffentlichte Ergebnis, bei dem die PUPPI Softdrop Jet grooming genutzt wurde. Die dritte und letzte Suche, die ich darlegen werde, führt ein neues multidimensionales Such-Framework ein, mit dem nach Resonanzen gesucht werden kann, die irgendwo im Dijet- und im Jet Groomed Massenspektrum ansteigen. Validiert durch eine Suche mit hadronisch zerfallenden Vektorbosonen im Endzustand, die ich hier vorstellen möchte, kann der Rahmen verwendet werden, um alle Resonanzsuchen mit hadronisch zerfallendem Vektorboson oder Higgs-Boson-Endzustand sowie generische Suchen nach geboosteten zu integrieren Objekt in Jet Masse.



---

# Contents

93	<b>1 The Standard Model and Beyond</b>	<b>13</b>
94	1.1 The Standard Model . . . . .	14
95	1.1.1 Fundamental particles: Quarks and leptons . . . . .	14
96	1.1.2 The Standard Model Lagrangian . . . . .	16
97	1.1.3 The electroweak sector . . . . .	20
98	1.1.4 Spontaneous symmetry breaking and The Higgs Sector . . . . .	23
99	1.2 Beyond Standard Model Physics . . . . .	28
100	1.2.1 Theories of New Physics . . . . .	29
101	<b>2 Experimental setup</b>	<b>35</b>
102	2.1 The Large Hadron Collider . . . . .	36
103	2.2 The CMS detector . . . . .	39
104	2.2.1 Coordinate system . . . . .	40
105	2.2.2 Tracking detectors . . . . .	41
106	2.2.3 Electromagnetic calorimeter . . . . .	43
107	2.2.4 Hadronic calorimeter . . . . .	45
108	2.2.5 Muon chambers . . . . .	48
109	2.3 Trigger system . . . . .	49
110	<b>3 Event reconstruction</b>	<b>51</b>
111	3.1 Track and primary vertex reconstruction . . . . .	52
112	3.2 The Particle Flow Algorithm . . . . .	53
113	3.2.1 Reconstruction of the Particle Flow inputs . . . . .	53
114	3.2.2 Particle Flow identification . . . . .	55
115	3.3 Pile-up removal . . . . .	60
116	3.3.1 Charged Hadron Subtraction . . . . .	60
117	3.3.2 Pile up per particle identification (PUPPI) . . . . .	60

118	3.4	Jet reconstruction . . . . .	62
119	3.4.1	Jet clustering . . . . .	63
120	3.4.2	PF jets in CMS . . . . .	65
121	3.4.3	Jet energy corrections . . . . .	66
122	3.5	Jet substructure reconstruction . . . . .	68
123	3.5.1	Grooming . . . . .	69
124	3.5.2	N-subjettiness . . . . .	72
125	3.5.3	Vector boson tagging . . . . .	73
126	3.6	Monte Carlo Event Generators . . . . .	76
127	<b>4</b>	<b>Diboson resonance searches in CMS</b>	<b>79</b>
128	4.1	Search I: First search for diboson resonances at 13 TeV . . . . .	80
129	4.1.1	A small bump . . . . .	81
130	4.1.2	Analysis strategy . . . . .	82
131	4.1.3	Data and simulated samples . . . . .	84
132	4.1.4	Event selection . . . . .	85
133	4.1.5	Background modeling . . . . .	101
134	4.1.6	Signal modeling . . . . .	104
135	4.1.7	V-tagging scale factors . . . . .	105
136	4.1.8	Systematic uncertainties . . . . .	116
137	4.1.9	Results . . . . .	117
138	4.1.10	Limits: All-hadronic analysis . . . . .	117
139	4.1.11	Limits: Semi-leptonic and all-hadronic combination . . . . .	118
140	4.2	Search II: A new pileup resistant, perturbative safe tagger . . . . .	124
141	4.2.1	Towards robust boosted jet tagging . . . . .	125
142	4.2.2	Analysis strategy . . . . .	126
143	4.2.3	Data and simulated samples . . . . .	127
144	4.2.4	Event selection . . . . .	128
145	4.2.5	Developing a new W-tagger . . . . .	132
146	4.2.6	W-tagging mistagging rate measurement . . . . .	142
147	4.2.7	Mass and purity categorization . . . . .	145
148	4.2.8	Background modeling: F-test . . . . .	146
149	4.2.9	Signal modeling . . . . .	146
150	4.2.10	Systematic uncertainties . . . . .	147
151	4.2.11	Results . . . . .	149

152	4.3	Search III: A novel framework for multi-dimensional searches . . . . .	154
153	4.3.1	Small bumps and tri-bosons . . . . .	155
154	4.3.2	Analysis strategy . . . . .	156
155	4.3.3	Data and simulated samples . . . . .	157
156	4.3.4	Event selection . . . . .	157
157	4.3.5	Triggering . . . . .	158
158	4.3.6	A mass and $p_T$ decorrelated tagger . . . . .	163
159	4.3.7	The multidimensional fit . . . . .	172
160	4.3.8	Modeling of the signal . . . . .	172
161	4.3.9	Modeling of the non-resonant background . . . . .	174
162	4.3.10	Modeling of the resonant background . . . . .	181
163	4.3.11	Systematic uncertainties . . . . .	186
164	4.4	Background model validation . . . . .	189
165	4.4.1	Variations of QCD multijet predictions . . . . .	189
166	4.4.2	Fit to data control region . . . . .	190
167	4.4.3	Bias test in pseudodata . . . . .	192
168	4.4.4	Results . . . . .	197
169	4.5	Summary and outlook . . . . .	204
170	<b>5</b>	<b>Encoding jet substructure in a deep neural network</b>	<b>207</b>
171	5.1	Infusing deep neural networks with physics . . . . .	208
172	5.2	LoLa . . . . .	209
173	5.2.1	Architecture . . . . .	209
174	5.2.2	Input . . . . .	210
175	5.2.3	The Combination Layer . . . . .	212
176	5.2.4	The Lorentz Layer . . . . .	213
177	5.3	Performance . . . . .	215
178	5.4	$p_T$ and mass dependence . . . . .	216
179	5.4.1	$p_T$ decorrelation . . . . .	217
180	5.4.2	Mass sculpting . . . . .	219
181	5.5	Validation on an independent sample . . . . .	221
182	5.6	Summary and outlook . . . . .	224
183	<b>6</b>	<b>Conclusion and outlook</b>	<b>225</b>

184	<b>A Search I: Limits per mass category</b>	<b>229</b>
185	A.1 Limits per mass category . . . . .	229
186	<b>B Search II</b>	<b>239</b>
187	B.1 W-tagging scale factor measurement: Additional plots . . . . .	240
188	B.2 Efficiency scale factors for $2.5 \text{ fb}^{-1}$ . . . . .	241
189	B.3 Background fit checks . . . . .	241
190	B.3.1 Background fit checks in data sideband . . . . .	244
191	B.3.2 Background fit checks in QCD MC . . . . .	248
192	B.4 F-test in signal region . . . . .	249
193	<b>C Search III</b>	<b>259</b>
194	C.1 Signal fits . . . . .	260
195	C.2 2016 kernels . . . . .	260
196	C.3 Resonant background . . . . .	260

---

# Introduction

198 The Standard Model of particle physics (SM) is one of the greatest accomplishments of fundamental science. The degree to which it can accurately predict observed phenomena is unprecedented,  
199 and it has allowed us to incorporate all of particle physics into one single equation that explains  
200 what we can see in the world around us. Almost all. Its greatest shortcoming is its failure to  
201 successfully incorporate gravity, leaving large scale phenomena unexplained. This, together with  
202 a few other shortcomings, has lead scientists to search for extensions to the Standard Model,  
203 commonly referred to as *Beyond Standard Model physics (BSM)*. These models are usually  
204 accompanied by predicted observables not included in the Standard Model, where the observation  
205 of these, or the lack thereof, is a way of falsifying or supporting the model. In this thesis, I  
206 attempt to do exactly that by searching for new massive particles predicted by SM extensions.  
207 These particles have the property that they can decay into vector bosons,  $W^\pm$  and  $Z^0$ , and  
208 usually have a very small interaction probability. The vector bosons are heavy and unstable  
209 and will quickly decay into leptons or quarks, and in order to make up for the small interaction  
210 probability, I look for two vector bosons decaying hadronically, which occurs  $\sim 70\%$  of the time,  
211 significantly more frequently than leptonic decays. This final state is complicated by the presence  
212 of an overwhelming QCD multijet background, and the fact that, due to the high mass of the  
213 resonance, the vector bosons are highly energetic and their quark decay products are so collimated  
214 they get merged into a single jet. Fortunately, the latter offers an opportunity to separate  
215 vector boson jets from quark and gluon jets through the jets mass and how many prongs the jet  
216 appears to have. Methods to do this separation are referred to as *jet substructure methods* and  
217 is something I will heavily focus on in this thesis, due to my own personal contributions to the field.  
218

219 Three analyses will be described, where each has benefitted from novel findings in the pre-  
220 vious: The first search was the first analysis of its kind to ever be performed at a center-of-mass  
221 energy of  $\sqrt{s} = 13 \text{ TeV}$  and the first published result to take advantage of jet substructure at  
222 trigger level. The second led to the development of a novel pileup robust and perturbative  
223 safe vector boson tagging algorithm, which afterwards became the default tagging algorithm in

225 CMS. Finally, the third search introduces a completely new way of doing diboson searches in a  
226 multi-dimensional space, allowing for the incorporation of all VV, VH and HH searches (where  
227  $V = W, Z$  and  $H = \text{Higgs boson}$ ) into one common framework as well as any generic search for  
228 resonances peaking in jet mass and dijet invariant mass. I have performed every aspect of the  
229 three analyses, making original contributions to all, despite the latter where we were a small  
230 team of three analysts dividing the workload.

231

232 In the final chapter of this thesis, I will introduce an ongoing work on a deep neural net-  
233 work for vector boson tagging intended to improve the analysis sensitivity for future searches and  
234 which in addition could be used to develop a generic anti-QCD tagger due to its deep encoding of  
235 jet substructure. Such a tagger would, in combination with the multidimensional fit framework,  
236 lead to a completely new way of doing model independent searches.

237

238 This thesis is organized in the following way. In Chapter 1, I will go through the theoreti-  
239 cal motivations behind the searches presented here through introducing the Standard Model,  
240 its known shortcomings and possible alternatives. This is followed by a description of the  
241 experimental setup used to collect the analyzed data, in Chapter 2, as well as the different  
242 algorithms used in order to reconstruct each event in Chapter 3. The remaining part of the thesis  
243 is dedicated to my own personal contributions: The three searches are presented chronologically  
244 in Chapter 4, each with a personal introduction motivating the search in question. Following this,  
245 and ending my thesis work, is a description of the deep neural network based vector boson tagger  
246 for future analyses, in Chapter 5. Both chapters end with their own concluding summary and  
247 outlook, Section sec:searchIII:outlook and Section sec:lola:outlook. To bring everything together,  
248 Chapter 6, the final chapter of this thesis, provides a final conclusion of the work presented.

249

---

## CHAPTER 1

---

250

### The Standard Model and Beyond

<sup>251</sup> **1.1 The Standard Model**

<sup>252</sup> Everything this thesis is built on has its roots in the Standard Model (SM). The Standard Model  
<sup>253</sup> of particle physics addresses the question *What is matter made of?* on the smallest possible scale.  
<sup>254</sup> It links the fundamental constituents of the universe together along with the forces that bind  
<sup>255</sup> them, in order to describe and predict the laws of nature. The Standard Model is formulated as a  
<sup>256</sup> quantum field theory, where the fundamental particles are spin-1/2 fermions which interact with  
<sup>257</sup> one another through the exchange of spin-1 gauge bosons. These interactions come in three forms,  
<sup>258</sup> mediated by three different types of gauge bosons: The electromagnetic force, mediated through  
<sup>259</sup> photons; the weak force, mediated through W and Z bosons; and the strong force, mediated by  
<sup>260</sup> gluons. How the fundamental particles interact also defines which properties they exhibit. In  
<sup>261</sup> addition, the Standard Model includes a field very different from the others, the Higgs field. The  
<sup>262</sup> Higgs field interacts both fermions and bosons and is what gives all particles their mass.  
<sup>263</sup> One thing the Standard Model fails to incorporate is the force of gravity. This shortcoming is one  
<sup>264</sup> of the main motivations for looking for alternative models beyond the Standard Model (BSM),  
<sup>265</sup> which is the main topic of this thesis.

<sup>266</sup> **1.1.1 Fundamental particles: Quarks and leptons**

<sup>267</sup> It appears that all matter in the universe can be described by a very small collection of fundamental  
<sup>268</sup> particles, six leptons and six quarks. These are collectively called fermions and are, as far as  
<sup>269</sup> we can tell, truly elementary (not composed of any other particles). Leptons are particles with  
<sup>270</sup> integer or zero electric charge, defined in units of electron charge. They come in three flavors, or  
<sup>271</sup> generations, and their mass increases with generation. Each generation of leptons consists of two  
<sup>272</sup> particles: one charged lepton and one neutrally charged particle denoted *neutrino* ( $\nu$ ). The three  
<sup>273</sup> generations can be arranged in a doublet structure, and are as follows

$$\begin{pmatrix} \nu_e \\ e \end{pmatrix} \quad \begin{pmatrix} \nu_\mu \\ \mu \end{pmatrix} \quad \begin{pmatrix} \nu_\tau \\ \tau \end{pmatrix} \quad (1.1)$$

<sup>274</sup> The charged leptons can be positively or negatively charged, defined in units of electron charge  
<sup>275</sup>  $e$ . By convention the leptons of matter are negatively charged,  $e^-$ ,  $\mu^-$ , and  $\tau^-$ , whereas the  
<sup>276</sup> positively charged leptons,  $e^+$ ,  $\mu^+$ , and  $\tau^+$  are considered their anti-particles. A summary of  
<sup>277</sup> the lepton properties is listed in Table 1.1. Leptons interact with one another through the  
<sup>278</sup> *electromagnetic and weak force*, which will be explained in more detail in Section 1.1.3.  
<sup>279</sup> The other six fundamental particles of matter are the *quarks*. They are distinguished from the

Lepton	Mass	Charge
$e^-$	0.5 MeV	$e$
$\mu^-$	106 MeV	$e$
$\tau^-$	1777 MeV	$e$
$\nu_e$	< 3 eV	0
$\nu_\mu$	< 0.19 MeV	0
$\nu_\tau$	< 18.2 MeV	0

**Table 1.1:** Lepton Properties [1].

Quark	Mass	Charge
u	1 – 5 MeV	$\frac{2}{3}e$
d	3 – 9 MeV	$-\frac{1}{3}e$
c	1.15 – 1.35 GeV	$\frac{2}{3}e$
s	75 – 170 MeV	$-\frac{1}{3}e$
t	$172.4 \pm 0.1$ GeV	$\frac{2}{3}e$
b	4.0 – 4.4 GeV	$-\frac{1}{3}e$

**Table 1.2:** Quark Properties

leptons in that they interact with one another through the *strong force*, described in Section 1.1.2. This force binds the quarks together to form baryons (like protons and neutrons) or mesons (like pions), and in addition, keeps the quarks from being observed as free particles such that they are only visible through their baryon/meson bound states. Also organized in three generations, the six quarks are called *up*, *down*, *charm*, *strange*, *top* and *bottom*, and are organized in flavor doublets as follow

$$\begin{pmatrix} u \\ d \end{pmatrix} \quad \begin{pmatrix} c \\ s \end{pmatrix} \quad \begin{pmatrix} t \\ b \end{pmatrix} \quad (1.2)$$

Each quark comes with a fractional charge of  $\frac{2}{3}$  (u, c and t) and  $-\frac{1}{3}$  (d, s and b) of one electron charge. As with the leptons, there are also distinct particles of opposite charge, anti-quarks. As mentioned above, quarks can interact with one another through the strong force. However, they also interact through the weak and electromagnetic forces. Some of the quark properties are listed in Table 1.2. These 12 fermions, together with their corresponding anti-particles, represent the fundamental particles of the universe and constitute all matter around us. There are four fundamental forces that we know of: gravity, electromagnetism, the weak force and the strong force. Gravity is extremely weak compared to the other forces and we currently lack a quantum field theory of its interaction, therefore it is typically ignored in high energy physics

experiments. All particles that are electrically charged, the charged leptons ( $e$ ,  $\mu$  and  $\tau$ ) and all of the quarks, interact through the electromagnetic force. These interactions are governed by the laws of Quantum Electrodynamics (QED), and are mediated through the massless and electrically neutral spin-1 photons. All of the fermions, including the electrically neutral neutrinos, feel the weak force and undergo weak interactions. The weak force is mediated through vector bosons ( $PW^+$ ,  $PW^-$  and  $Z^0$ ), which are heavy charged particles with a spin of 1. Finally, there is the strong force, mediated by the massless and electrically neutral spin-1 gluon. Only quarks interact via the strong force, and it is that interaction that makes the quarks so fundamentally different from electrons and neutrinos. The strong force keeps us from observing quarks as free particles, and keeps them in bound states referred to as *hadrons*. Their interaction is governed by the laws of Quantum Chromodynamics (QCD). All of these interactions can be represented in one common gauge theory, the Standard Model.

### 1.1.2 The Standard Model Lagrangian

The Standard Model is a quantum gauge field theory in which each particle is described as a dynamical field with a value at each space-time coordinate. These fields are governed by a Lagrangian density function, the Standard Model. For instance, the Lagrangian density of a free fermion, one not interacting with any other fields, is

$$\mathcal{L} = \bar{\Psi}(x^\mu)(i\lambda^\mu\partial_\mu - m)\Psi(x^\mu) \quad (1.3)$$

where  $\Psi(x^\mu)$  represents any spin-1/2 fermion field, also called *Dirac field*, as a function of space-time;  $\bar{\Psi} = \Psi^\dagger\gamma_0$ , where  $\gamma^0$  is one of the gamma matrices  $\gamma^\mu$ , which is included in order to make  $\Psi^\dagger\Psi$  invariant under Lorentz transformation; and  $m$  is the mass of the fermion in question. Any interaction between the fundamental particles due to the fundamental forces, can be described as variations in the Lagrangian of quantum fields and are represented as additional terms in the equation above.

Being a gauge theory, the Standard Model has the property of gauge invariance, meaning that measurable quantities stay the same despite the fields themselves changing. If observables stay the same after a field transformation, there is a symmetry in the system. The symmetries of the Standard Model arise due to the fact that fermions of a given type are indistinguishable from one another. These symmetries result in the presence of *force mediators*, which arise as a representation of infinitesimal generators of some symmetry group. The fermion fields can be arranged as particle multiplets where one transforms into the other under a symmetry transformation. A symmetry transformation produce rotations between the particles of a given

326 multiplet, but never to a field outside of that group. The symmetry group of the Standard Model  
327 is the direct product

$$SU(3)_C \otimes SU(2)_L \otimes U(1)_Y. \quad (1.4)$$

$SU(3)_C$  is the color  $C$  symmetry allowing the rotation of quarks, arranged in color multiplets, into one another, corresponding to interactions produced by the strong force. The colors are denoted as red, green and blue.  $SU(2)_L \otimes U(1)_Y$  represent the electroweak force with weak left-handed isospin  $L$  and weak hypercharge  $Y$  symmetries, acting on  $L$  and  $Y$  multiplets, respectively. The particle multiplets of the Standard Model can then be written as  $\mathcal{G}_{SM} \ni x = (C, L)_{(Y)}$  (here for the 1st generation only) and are:

$$\begin{aligned} Q &= (3, 2)_{(1/3)} = \begin{pmatrix} u_r & u_g & u_b \\ d_r & d_g & d_b \end{pmatrix} && \sim \text{quark multiplet} \\ L &= (1, 2)_{(-1)} = \begin{pmatrix} \nu_e & e \end{pmatrix} && \sim \text{leptonic doublet} \\ u^c &= (\bar{3}, 1)_{(-4/3)} = \begin{pmatrix} u_r^c & u_g^c & u_b^c \end{pmatrix} && \sim \text{anti-up quarks} \\ d^c &= (\bar{3}, 1)_{(2/3)} = \begin{pmatrix} d_r^c & d_g^c & d_b^c \end{pmatrix} && \sim \text{anti-down quarks} \\ e^c &= (1, 1)_{(2)} && \sim \text{positron} \end{aligned}$$

328 The anti-neutrino is not included here because it is a SM *singlet* and does not transform under  
329 the SM group  $\mathcal{G}_{SM}$ , but it could be written as  $\nu^c = (1, 1)_{(0)}$ . The positron  $e^c$ , on the other hand,  
330 is included as its hypercharge is non-zero and it therefore undergoes  $U(1)_Y$  interactions. These  
331 five multiplets exist for each of the tree generations.

332 The numbers representing each multiplet correspond to which representation it belongs to. For  
333 instance, we see that the quark multiplet transforms as a triplet under  $SU(3)_C$ , a doublet under  
334  $SU(2)_L$  and has a non-zero hypercharge, corresponding to a non-trivial representation under  
335  $U(1)_Y$ . That corresponds to saying that quarks interact through all of the three fundamental  
336 interactions. From that notation, it is also clear that leptons do not carry color charge and will  
337 only interact via the electroweak interactions.

338 From the multiplets above, we see that  $u^c$  and  $d^c$  transform as singlets under  $SU(2)_L$ , meaning  
339 they do not interact. This, however, does not mean they do not feel the electroweak force. The  
340 electroweak gauge bosons W and Z are not directly part of  $SU(2)_L$ , rather, they are a linear  
341 combination of  $SU(2)_L$  and  $U(1)_Y$  and anything with a non-zero weak hypercharge  $Y$  will interact  
342 with them. This is also true for the photon, which also is a linear combination of  $SU(2)_L$  and

<sup>343</sup>  $U(1)_Y$ .

<sup>344</sup> These interactions; the strong, weak and electromagnetic, will be explained in more detail in the  
<sup>345</sup> following sections.

### <sup>346</sup> The Quantum Chromodynamics sector

<sup>347</sup> The group  $SU(3)_C$  describe the strong interaction mediated by gluons, and is described by  
<sup>348</sup> the quantum gauge theory Quantum Chromodynamics (QCD). The group is generated by  
<sup>349</sup> 8 linearly independent matrices  $T^a = \frac{\lambda^a}{2}$ , where  $\lambda^a$  are the Gell-Mann matrices [2]. The  
<sup>350</sup> generator matrices do not commute with one another, but rather satisfy the commutation relation  
<sup>351</sup>  $[\lambda^i/2, \lambda^j/2] = if^{ijk}\lambda_k/2$ . This property makes  $SU(3)_C$  group *non-Abelian*, which consequently  
<sup>352</sup> results in the gluons themselves being charged and display self-interactions. Gluons are charged  
<sup>353</sup> with one unit of color and one unit of anti-color. Quarks, the only fundamental particles interacting  
<sup>354</sup> with the strong force, are arranged in the simplest representation of  $SU(3)$  and come with one  
<sup>355</sup> unit of color or anti-color.

<sup>356</sup> The generators are collectively referred to as the *group representation* of  $SU(3)_C$ , because any  
<sup>357</sup> group element can be written as  $e^{-i\theta^a g_a}$ , where  $a$  runs from 1 to 8,  $\theta^a$  are real numbers  
<sup>358</sup> and  $g_a$  represent one of the eight linearly independent  $\lambda/2$  matrices. That means that, given one  
<sup>359</sup> representation, one can always find another one through any local gauge transformation that  
<sup>360</sup> leaves the commutator unchanged. In this case, the group elements are the quark fields, and a  
<sup>361</sup> local gauge transformation of fields become

$$\Psi(x^\mu) \rightarrow e^{-ig_s\theta^a(x^\mu)T^a} \Psi(x^\mu) \quad (1.5)$$

<sup>362</sup> where  $g_s$  is the strong coupling,  $\theta^a(x^\mu)$  some arbitrary function and  $a$  runs over the eight generators  
<sup>363</sup> of the group. In order to keep the QCD Lagrangian invariant under such a transformation, an  
<sup>364</sup> additional term must be added, replacing the partial derivative  $\partial_\mu$  with the *covariant derivative*

$$D_\mu = \partial_\mu + ig_s A_\mu^a T^a, \quad (1.6)$$

<sup>365</sup> where we now have introduced a tensor  $A_\mu^a$  that represents the 8 gluon fields. The QCD Lagrangian  
<sup>366</sup> then becomes

$$\mathcal{L}_{QCD} = -\frac{1}{4} F_{\mu\nu}^a F_{\mu\nu}^a + \bar{\Psi}(x^\mu)(i\lambda^\mu D_\mu - m)\Psi(x^\mu), \quad (1.7)$$

<sup>367</sup> where  $F_{\mu\nu}^a$  is the gauge field of the group, the gluon field tensor

$$F_{\mu\nu}^a = \partial_\mu A_\nu^a - \partial_\nu A_\mu^a + g_s f^{abc} A_\mu^b A_\nu^c. \quad (1.8)$$

368 The first term in Equation 1.7 represents the quark-gluon interaction, leading to vertices like the  
 369 one on the right in Figure 1.1. The second, the gluon field kinetic term, pick up the *structure*  
 370 *constant*  $f^{abc}$  due to the commutation relation of the  $\lambda$  matrices. This term creates self-interactions  
 between the gluon fields, like the two shown on the right in Figure 1.1. These self-interactions

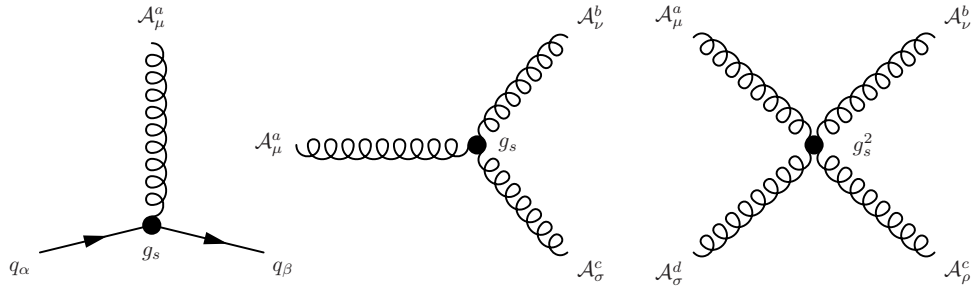


**Figure 1.1:** The QCD interaction vertices: Quark interaction with the gluon field (left), and three- (middle) and four-gluon (right) self-interaction vertices.

371  
 372 have severe consequences: any bare color charge, like a quark, will be surrounded by a sea of  
 373 virtual gluons and quarks that share the same color. When probing the quark color at higher  
 374 and higher energies, corresponding to shorter and shorter distances, the color charge decreases  
 375 until only the bare charge is visible. There, the quarks are essentially free and can be observed as  
 376 distinguishable particles. This property is referred to as *asymptotic freedom*. For the same reasons,  
 377 when going further and further away from a bare color charge, the sea of charges surrounding  
 378 it makes the observed charge increase. That results in a strong attractive force between color  
 379 charges at large distances, where the potential energy between the two grows linearly with the  
 380 distance between them as

$$V(r) = -\frac{4\alpha_s}{3r} + kr, \quad (1.9)$$

381 where  $r$  is the distance between the quarks and  $\alpha_s$  is the coupling strength of QCD, describing  
 382 how the observed charge between two quarks increases depending on the distance between them.  
 383 When the distance between the quarks grows very large, this potential energy is enough to create  
 384 real quark-antiquark pairs from the vacuum in order to reduce the potential energy, a process  
 385 called *fragmentation*. Whenever one tries to separate quarks from one another they will fragment,  
 386 which consequently means that quarks are never observed on their own. Rather, they form  
 387 colorless (uncharged under the color charge) bound states of mesons or baryons (collectively  
 388 called hadrons), a property called *color confinement*. The energy for which the confinement into  
 389 hadrons occurs, also called *hadronization*, is defined through experimental measurement and  
 390 found to be  $\Lambda_{QCD} = 100 - 500$  MeV (around the mass of the lightest hadrons). The effective

<sup>391</sup> charge between the quarks,  $\alpha_S$ , changes as a function of energy as

$$\alpha_S(Q) = -\frac{6\pi}{33 - 2n_f} \ln(Q/\Lambda_{QCD}) \quad (1.10)$$

<sup>392</sup> where  $Q$  is the energy of the probe used to measure the charge and  $n_f$  is the number of quark  
<sup>393</sup> flavors (u, d, c, s, b, t) at that energy.  $\alpha_S$  is around 0.1 for energies between 100-1000 GeV.

### <sup>394</sup> 1.1.3 The electroweak sector

<sup>395</sup> The electromagnetic and weak interactions arise from the breaking of  $SU(2)_L \otimes U(1)_Y$  symmetry.  
<sup>396</sup> While the unification of the electromagnetic and weak force is obtained under the  $SU(2)_L \otimes U(1)_Y$   
<sup>397</sup> group, the predicted gauge bosons of such a group are not observed in nature (three charged  
<sup>398</sup> massless vector bosons, and one neutral massless boson). Rather, the  $W^\pm$ ,  $Z^0$  and the photon  
<sup>399</sup> arise from the spontaneous symmetry breaking of  $SU(2)_L \otimes U(1)_Y$  to  $U(1)_{EM}$ . This happens  
<sup>400</sup> due to the *Higgs mechanism*, and exactly how this occurs will be the topic of Section 1.1.4.

<sup>401</sup> The symmetry under  $SU(2)_L$  is called weak left-handed isospin  $L$ , and the symmetry under  
<sup>402</sup>  $U(1)_Y$  is the weak hypercharge  $Y$ . The name “left-handed” arise from the fact that *parity* is  
<sup>403</sup> violated in the electroweak interactions. All the fundamental fermions have a *chirality*, defined as  
<sup>404</sup> the projection of the particles spin along its direction of motion. From observations, the weak  
<sup>405</sup> interactions is observed to only interact with fermions of left-handed chirality (vector minus axial  
<sup>406</sup> coupling, V-A). The left-handed fermion fields are therefore in the simplest doublet representation  
<sup>407</sup> of  $SU(2)$  with weak isospin  $I = 1/2$ , while the fermions of right-handed chirality are in the singlet  
<sup>408</sup> representation with weak isospin  $I = 0$ , meaning they do not interact with the gauge bosons of  
<sup>409</sup>  $SU(2)_L$ . To obtain the correct chiral components  $\Psi_L$  and  $\Psi_R$ , The chirality of any fermion  $\Psi$  can  
<sup>410</sup> be defined through the operator  $\gamma^5$ , the product of the four Dirac matrices [3]  $\gamma^5 = i\gamma^1\gamma^2\gamma^3\gamma^4$ ,  
<sup>411</sup> which has eigenvalues  $\pm 1$ . Any Dirac field can be projected into its chiral components  $\Psi_L$  or  $\Psi_R$   
<sup>412</sup> through the projection operation

$$\Psi_L = \frac{1 - \gamma^5}{2} \quad \text{and} \quad \Psi_R = \frac{1 + \gamma^5}{2}. \quad (1.11)$$

The gauge field tensor of the group of  $SU(2)_L$  symmetry is  $W_{\mu\nu}^a$ , where  $a$  runs over the 3 generators  
of the group. The conserved charge associated with the group is the *third* component of weak  
isospin  $I_3$ , and all weak interactions must preserve  $I_3$ . The generators of the group are defined as  
 $T_i = \frac{\sigma_i}{2}$ , where  $\sigma_i$  are the Pauli matrices [4]. The group is non-abelian and the generators follow  
the commutation relation  $[\sigma_i/2, \sigma_j/2] = i\epsilon_{ijk}\sigma_k/2$ , where  $\epsilon_{ijk}$  is the Levi-Civita permutation  
symbol [5]. This in turn implies self-interactions between the gauge bosons of the group, as

was the case for  $SU(3)_C$ . The left-handed fermion fields are doublets under  $SU(2)_L$ , while the right-handed components transform as singlets and hence do not interact with the gauge field tensor.

The latter group,  $U(1)_Y$  of weak hypercharge  $Y$ , is abelian and hence display no self-interaction. The gauge field tensor  $B_{\mu\nu}^a$  interacts with both left- and right-handed Dirac fields. Similar to the case for QCD, a local gauge transformation of  $SU(2)_L \otimes U(1)_Y$  requires the addition of additional terms in the derivative in order to keep the Lagrangian invariant. The partial derivative  $\partial_\mu$  is replaced by the covariant derivatives

$$D_\mu \Psi_L = (\partial_\mu + ig_2 T_a W_\mu^a + ig_1 \frac{Y}{2} B_\mu^a) \Psi_L \quad (1.12)$$

$$D_\mu \Psi_R = (\partial_\mu + ig_1 \frac{Y}{2} B_\mu^a) \Psi_R. \quad (1.13)$$

<sup>413</sup> The electroweak Lagrangian can be written as a sum of four terms

$$\mathcal{L}_{EW} = \mathcal{L}_{gauge} + \mathcal{L}_f + \mathcal{L}_{Yukawa} + \mathcal{L}_\phi. \quad (1.14)$$

<sup>414</sup> The first term,  $\mathcal{L}_{gauge}$ , represent the kinetic field tensor and is

$$\mathcal{L}_{gauge} = -\frac{1}{4} W_a^{\mu\nu} W_{\mu\nu}^a - \frac{1}{4} \mathcal{B}^{\mu\nu} \mathcal{B}_{\mu\nu} \quad (1.15)$$

where the gauge field tensors are

$$W_{\mu\nu}^a = \partial_\mu W_\nu^a - \partial_\nu W_\mu^a - g_2 \epsilon^{ijk} W_\mu^j W_\nu^k, \text{ with } i = 1 - 3 \quad (1.16)$$

$$B_{\mu\nu} = \partial_\mu B_\nu - \partial_\nu B_\mu. \quad (1.17)$$

<sup>415</sup> The non-abelian nature of  $SU(2)_L$  leads to trilinear and quadrilinear couplings between the  
<sup>416</sup> photon and vector bosons as illustrated in Figure 1.2.

The second term describe the boson fields coupling to fermions and is

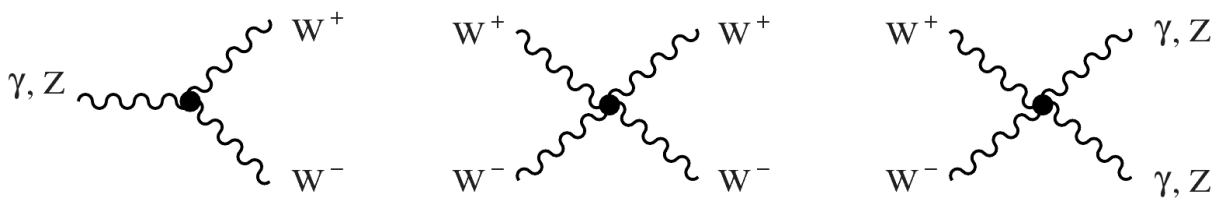


**Figure 1.2:** The electroweak self-interaction vertices: trilinear (left), and quadri-linear (middle and right) vertices.

417

$$\mathcal{L}_f = \bar{Q}_i i\lambda^\mu D_\mu Q_i + \bar{u}_i^c i\lambda^\mu D_\mu u_i^c + \bar{d}_i^c i\lambda^\mu D_\mu d_i^c + \bar{L}_i i\lambda^\mu D_\mu L_i + \bar{e}_i^c i\lambda^\mu D_\mu e_i^c, \quad (1.18)$$

418 where we have expressed each term using the particle multiplets in Equation ?? and the subscript  
 419  $i$  runs over the three fermion generations. They all interact differently under  $SU(2)_L \times U(1)_Y$   
 420 due to their different charges.

421 Up until now we have considered the Lagrangian before spontaneous symmetry breaking, where  
 422 we have three charged massless bosons and one massless neutral boson, a constellation we know  
 423 to be wrong from observations. When I have referred to interaction vertices, I have loosely  
 424 referred to  $W$ ,  $Z$  and  $\gamma$  vertices without explicitly defining them (and we have only been working  
 425 with the covariant derivatives as defined in Equation 1.12). We will show in Section 1.1.4 that,  
 426 due to spontaneous symmetry breaking, the charged gauge boson fields  $W^\pm$  in reality are linear  
 427 combinations of  $W_\mu^1$  and  $W_\mu^2$ :

$$W^\pm = \frac{1}{\sqrt{2}}(W_\mu^1 \mp iW_\mu^2). \quad (1.19)$$

428 These are responsible for *charged current interactions*, which turn up-type fermions into their  
 429 corresponding down-type fermions within the same generation, and vice-versa. The electrically  
 430 neutral  $Z$  boson and the photon fields are expressed in terms of  $W_\mu^3$  and  $B_\mu$  through the weak  
 431 mixing angle [6] as

$$\begin{pmatrix} \gamma \\ Z^0 \end{pmatrix} = \begin{pmatrix} \cos \theta_W & \sin \theta_W \\ -\sin \theta_W & \cos \theta_W \end{pmatrix} \begin{pmatrix} B \\ W^3 \end{pmatrix} \quad (1.20)$$

432 where  $\theta_W$  can be expressed through the  $SU(2)_L$  and  $U(1)_Y$  couplings  $g_1$  and  $g_2$  as

$$\cos \theta_W = \frac{g_1}{g_1^2 + g_2^2} \quad \text{and} \quad \sin \theta_W = \frac{g_2}{g_1^2 + g_2^2}. \quad (1.21)$$

433 The electric charge is therefore defined through weak isospin and hypercharge, and is

$$Q = I_3 + \frac{Y}{2}. \quad (1.22)$$

434 A few of the fermion-boson vertices are shown in Figure 1.3. The last two terms,  $\mathcal{L}_{Yukawa}$  and  $\mathcal{L}_\phi$ ,  
 435 are related to the Higgs boson and represent couplings to the Higgs field: its interactions with  
 436 itself and the gauge bosons, and the Yukawa interaction with the fermions that generate their  
 437 masses due to the non-zero Higgs vacuum expectation value. Introduced as an extension to the  
 438 original SM, the Higgs sector is one of the great accomplishments of particle physics and one of  
 439 the reasons why the LHC was built. How it arises is what we will turn to next.

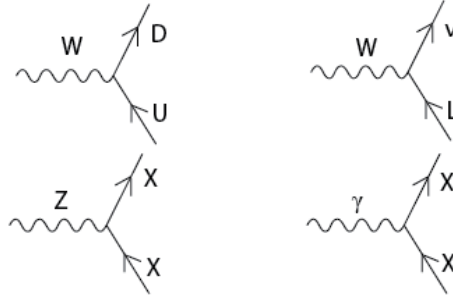


**Figure 1.3:** The electroweak fermion interaction vertices. Top: Charged current interaction vertex connecting a charged vector boson  $W^\pm$  to quarks (left) and leptons (right). Bottom: Neutral current interactions between the neutral  $Z^0$  boson and any fermion (left), and between a  $\gamma$  and electrically charged fermions.

#### 440 1.1.4 Spontaneous symmetry breaking and The Higgs Sector

441 The problem of having massless gauge bosons under  $SU(2)_L \times U(1)_Y$ , while observing massive  $W$   
 442 and  $Z$  bosons, was independently solved by three different groups and has become known as the  
 443 Englert–Brout–Higgs–Guralnik–Hagen–Kibble mechanism of spontaneous symmetry breaking [7–  
 444 9], an accomplishment for which Peter Higgs and Francois Englert shared the 2013 Nobel Prize.  
 445 It began with the realization that the breaking of a local gauge symmetry could give rise to a final  
 446 mass for the gauge boson involved. This was first discovered in association with superconductivity,  
 447 where it was found that when a normal metal becomes superconducting the photon field inside  
 448 the superconductor would acquire a finite mass [10].

#### 449 Spontaneous breaking of a global gauge symmetry

450 In order to achieve spontaneous symmetry breaking, Jeffrey Goldstone [11] suggested introducing  
 451 a massive complex scalar field  $\phi$  with quantum numbers of the vacuum and then give the field a  
 452 vacuum expectation value. The field

$$\phi = \frac{1}{\sqrt{2}}(\phi_1 + i\phi_2) \quad (1.23)$$

453 would have a Lagrangian of the form

$$\mathcal{L} = \partial^\mu \bar{\phi} \partial_\mu \phi - \mu_0^2 \bar{\phi} \phi - \frac{\lambda_0}{6} \bar{\phi} \phi^2, \quad (1.24)$$

454 where  $\lambda_0$  is the coupling constant and  $\mu_0$  is the mass. The Lagrangian is invariant under  $U(1)$ ,  
 455 though in this case under a global symmetry and not a local one. If one takes  $\mu_0^2$  to be negative,

<sup>456</sup> the potential will get a minima along a circle of radius  $v$  such that

$$\phi_1^2 + \phi_2^2 = v^2 \quad \text{and} \quad v^2 = \frac{\mu_0^2}{\lambda_0} \quad (1.25)$$

and take the form of a “Mexican Hat” as shown in Figure 1.4.  $v$  is referred to as the vacuum

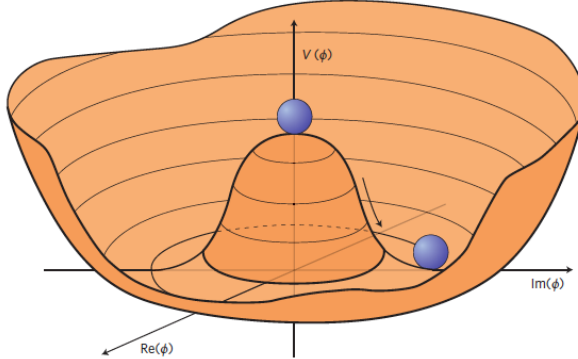


**Figure 1.4:** The potential  $V(\phi)$  for a complex scalar field with  $\mu_0^2 < 0$  [12].

<sup>457</sup>

<sup>458</sup> expectation value. The lowest value of the Hamiltonian is now at  $\phi = v$  rather than at  $\phi = 0$ .  
<sup>459</sup> Goldstone then translated the field to a minimum energy position  $\phi' = \phi + v$  and gave the field a  
<sup>460</sup> vacuum expectation value, effectively breaking the symmetry between the two field components  
<sup>461</sup> but keeping the Lagrangian invariant. This complex field can be expanded around the ground  
<sup>462</sup> state in terms of two real fields  $\eta$  and  $\epsilon$  that represent deviations from the minimum:

$$\phi(x) = \frac{1}{\sqrt{2}} * (v + \eta(x) + i\epsilon(x)) \quad (1.26)$$

<sup>463</sup> The Lagrangian then becomes

$$\mathcal{L} = \frac{1}{2}(\partial_\mu \epsilon)^2 + \frac{1}{2}(\partial_\mu \eta)^2 + \mu_0^2 \eta^2. \quad (1.27)$$

<sup>464</sup> The third term has the form of a mass term for the scalar  $\eta$  field. However, the  $\epsilon$  field has no  
<sup>465</sup> mass term meaning that the theory contains a massless scalar, referred to as a *Goldstone boson*.  
<sup>466</sup> This is expressed through *Goldstones theorem*, which states that whenever a continuous symmetry  
<sup>467</sup> of a physical system is spontaneously broken, massless scalars will occur. So rather than solving  
<sup>468</sup> the problem of massless vector bosons, the theory acquired a massless scalar not observed in  
<sup>469</sup> Nature and the gauge theory of weak interactions had to look elsewhere for solutions.

<sup>470</sup> **The Higgs mechanism**

<sup>471</sup> The solution to the problem came a few years later, in 1964, when spontaneous symmetry breaking  
<sup>472</sup> of a *local* gauge symmetry was studied rather than a global. For a  $U(1)$  symmetry, this requires  
<sup>473</sup> the Lagrangian to be invariant under  $\phi \rightarrow e^{i\theta(x)}\phi$  with the usual derivative replacement

$$D_\mu = \partial_\mu - ieA_\mu. \quad (1.28)$$

<sup>474</sup> After translating the field  $\phi$  to its true ground state and writing out the Lagrangian

$$\mathcal{L} = \frac{1}{2}(\partial_\mu\epsilon)^2 + \frac{1}{2}(\partial_\mu\eta)^2 - v^2\lambda\eta^2 + \frac{1}{2}v^2e^2A_\mu A^\mu - evA_\mu\partial^\mu\epsilon - \frac{1}{4}F_a^{\mu\nu}F_{\mu\nu}^a \quad (1.29)$$

<sup>475</sup> we see that the particle spectrum now contains a massless Goldstone boson  $\epsilon$ , a massive scalar  
<sup>476</sup>  $\eta$  and, finally, a massive vector  $A_\mu$  with  $m_A = ev$ . After having succeeded with dynamically  
<sup>477</sup> creating the mass for the gauge field, one had to tackle the problem of the massless scalar. The  
<sup>478</sup> solution was found through the realization that one of the fields were unphysical; by giving mass  
<sup>479</sup> to the vector  $A_\mu$ , the polarization degrees of freedom had increased from 2 to 3 through adding  
<sup>480</sup> a longitudinal polarization. However, this should not be possible when simply translating field  
<sup>481</sup> variables. It was found that through a simple gauge transformation with a different set of fields

$$A_\mu \rightarrow A_\mu + \frac{1}{ev}\partial_\mu\theta, \quad (1.30)$$

<sup>482</sup> the Goldstone boson would disappear and turn into the longitudinal polarization of the massive  
<sup>483</sup> gauge boson and the theory was left with one massive vector gauge boson  $A_\mu$  and another massive  
<sup>484</sup> scalar  $h$ . This is what is referred to as the *Higgs mechanism*.

<sup>485</sup> **The Weinberg-Salam Model**

The final step is to formulate the Higgs mechanism such that the vector bosons  $W^\pm$  and  $Z^0$  becomes massive, while the photon remains massless. To do so, Sheldon Glashow, Abdus Salam, and Steven Weinberg (all awarded the 1979 Nobel Prize for electroweak unification), added a gauge invariant term to the electroweak Lagrangian of the following form:

$$\mathcal{L}_{Higgs} = \left| (i\partial_\mu - g_2 T_a W_\mu^a - vg_1 \frac{Y}{2} B_\mu^a) \phi \right|^2 - V(\phi) \quad (1.31)$$

<sup>486</sup> The  $\phi_i$  has to belong to  $SU(2) \times U(1)$  multiplets, and the simplest choice is four fields in an  
<sup>487</sup> isospin doublet of weak hypercharge  $Y = 1$ :

$$\phi = \begin{pmatrix} \phi^+ \\ \phi^0 \end{pmatrix} = \begin{pmatrix} \frac{\phi_1 + i\phi_2}{\sqrt{2}} \\ \frac{\phi_3 + i\phi_4}{\sqrt{2}} \end{pmatrix}. \quad (1.32)$$

<sup>488</sup> To generate the masses, the Higgs potential from the section above is used, with a vacuum  
<sup>489</sup> expectation value of

$$\phi_0 = \frac{1}{\sqrt{2}} \begin{pmatrix} 0 \\ v \end{pmatrix}. \quad (1.33)$$

This specific choice of charges, VEV and fields insure that the  $U(1)_{em}$  symmetry with  $Q = T^3 + \frac{Y}{2}$  remains unbroken, keeping the photon massless. The three others break the symmetry and become massive gauge bosons: the  $W^+$ ,  $W^-$  and  $Z^0$ . The mass term for the gauge bosons then finally become

$$M_W = \frac{1}{2} v g_1 \quad (1.34)$$

$$M_Z = \frac{1}{2} v \sqrt{g_1^2 + g_2^2} \quad (1.35)$$

$$\frac{M_W}{M_Z} = \cos \theta_W. \quad (1.36)$$

<sup>490</sup> As mentioned in Section 1.1.3, the fermions also get their mass through interaction with the  
<sup>491</sup> Higgs field,  $\mathcal{L}_{Yukawa}$ . This is done the same way as for the boson: an additional  $SU(2) \times U(1)$   
<sup>492</sup> invariant term for each generation is added, for instance for the electron

$$-G_e \left[ \begin{pmatrix} \bar{\nu}_e & \bar{e} \end{pmatrix}_L \begin{pmatrix} \phi^+ \\ \phi^0 \end{pmatrix} e^R + \bar{e}_R \begin{pmatrix} \phi^- & \bar{\phi}^0 \end{pmatrix} \begin{pmatrix} \nu_e \\ e \end{pmatrix}_L \right], \quad (1.37)$$

<sup>493</sup> where  $G_E$  is the electron coupling. We then spontaneously break the symmetry with

$$\phi = \frac{1}{\sqrt{2}} \begin{pmatrix} 0 \\ v + h(x) \end{pmatrix}, \quad (1.38)$$

<sup>494</sup> where the neutral Higgs field  $h(x)$  is the only remnant of the Higgs doublet after spontaneous  
<sup>495</sup> symmetry breaking. After substitution, the final Lagrangian for the electron mass becomes

$$\mathcal{L}_{Yukawa}^e = -\frac{G_e}{\sqrt{2}} v (\bar{e}_L e_R + \bar{e}_R e_L) (1 + \frac{h}{v}). \quad (1.39)$$

<sup>496</sup> We can choose  $G_e$  such that

$$m_e = -\frac{G_e v}{\sqrt{2}} \quad (1.40)$$

<sup>497</sup> and generate the electron mass as

$$\mathcal{L}_{Yukawa}^e = -m_e \bar{e} e - \frac{m_e}{v} \bar{e} e h. \quad (1.41)$$

<sup>498</sup> In summary, all the fermion masses are generated through the interaction of the fermion fields  
<sup>499</sup> with the Higgs field. From the equation above, we see that the fermion masses are not predicted  
<sup>500</sup> from the theory as the coupling  $G$  is arbitrary. The Standard Model therefore cannot provide an  
<sup>501</sup> explanation the difference in hierarchy between the couplings. We also see that the Lagrangian  
<sup>502</sup> contains an interaction term coupling the Higgs scalar to the fermions and that this term depends  
<sup>503</sup> on the mass of the fermion. The Higgs boson therefore couples more strongly to heavy fermions  
<sup>504</sup> than to lighter ones.

## 505 1.2 Beyond Standard Model Physics

506 Despite being an extremely successful and predictive theory, the Standard Model has its short-  
507 comings. The most obvious one is its failure to successfully incorporate the gravitational force.  
508 Gravity is beautifully described in General Relativity as a classical theory: a force caused by  
509 the curvature of space-time in the presence of matter and energy. The theory does not utilize  
510 quantum fields and energy is not quantized. The scales between the Standard model, a quantum  
511 field theory, and General Relativity are completely different: space-time is curved on astronomical  
512 scales, where the force of gravity is measurable, while quantum field theories deal with things on  
513 the smallest possible scales, where variations in space-time are essentially invisible. Hence, to the  
514 Standard Model, space-time is approximately flat and gravity does not exist. In order to have an  
515 elegant unified theory of all the forces, attempts has been made to have a quantum field theory of  
516 the gravitational force by extending the Standard Model particle family to incorporate a particle  
517 to mediate the gravitational force called the *graviton*, a massless gauge boson of spin-2. The  
518 problem is that gravity is universally attractive, meaning nothing “cancels” it. That leads to loop  
519 divergences that cannot be reabsorbed through renormalization and every effort of integrating  
520 gravity in the SM has thus far failed. However, it has been shown that General Relativity is  
521 an inevitable consequence of the quantum mechanics of interacting gravitons, which has led to  
522 several proposals for extending the SM models to incorporate them.

523 In addition to the difficulties of incorporating gravity into a quantum field theory framework,  
524 problems occur at small distances at which quantum gravitational effects would become apparent,  
525 the Planck scale. This can be represented by the Planck mass, the mass of the smallest possible  
526 black hole. When comparing the Planck mass to the masses of the electroweak bosons W and Z,  
527 we find that the Planck mass is  $10^{16}$  times heavier than the electroweak bosons, such that there  
528 is a *hierarchy* between the mass scales of gravity and the electroweak forces. The reason why  
529 this observed hierarchy occurs has to do with the Higgs vacuum expectation value (VEV): the  
530 Higgs field has a vacuum expectation value of 246 GeV and is what gives the W and Z bosons  
531 their mass. However, when actually calculating the Higgs VEV and taking all loop corrections  
532 into account, it would receive corrections on the order of the Planck energy, yielding a Higgs  
533 boson mass  $10^{16}$  times larger than observed. This is called the *hierarchy problem*. Quantum loop  
534 corrections of this magnitude only happen for scalar particles such as the Higgs boson. Fermions  
535 are protected from such divergences through their chiral structure and gauge bosons are protected  
536 through gauge invariance. The question is then why the Higgs VEV, and consequently the Higgs,  
537 W and Z boson masses are so much smaller than the natural mass scale.

538 Of course, it is possible that the Higgs boson mass just happens to be 125 GeV due to some

539 fine-tuned, large cancellations that keep the mass from approaching the Planck mass, as is  
 540 currently held by the Standard Model. However, this is neither very elegant nor very probable  
 541 without a well-motivated reason why such a cancellation should occur. Rather, in order to resolve  
 542 the problem of scales, theories Beyond the Standard Model (BSM) have been introduced. The  
 543 theories that I will probe in this thesis are amongst those.

### 544 1.2.1 Theories of New Physics

545 Two Beyond Standard Model theories will be considered in this thesis: Compositeness and  
 546 extra dimensional theories. Compositeness attacks the hierarchy problem by assuming that the  
 547 Standard Model breaks down at an energy between the weak and Planck scales and that, around  
 548 the TeV scale, the Higgs boson no longer appears to be a single scalar particle but a composite  
 549 state of two fermions. In the following, I will present the study of composite models in the context  
 550 of the *Heavy Vector Triplet formalism*, described in Section 1.2.1. Warped extra dimensional  
 551 theories attempt to solve the hierarchy problem by concentrating gravity on another “brane” and  
 552 letting its strength fall off exponentially through an extra dimension. Both of these, compositeness  
 553 and extra dimensional theories, will be described in the following.

#### 554 Compositeness

555 In composite Higgs models, the Higgs boson is assumed to be a bound state of fundamental  
 556 constituents held together by some new strong force [13, 14]. This removes the hierarchy problem  
 557 since we no longer have an elementary scalar in the Standard Model, hence no loop corrections  
 558 going to infinity. The compositeness of the Higgs boson becomes apparent at the energy scale  $\Lambda$ ,  
 559 where  $\Lambda$  has to be at least 10 TeV, since anything below that is ruled out by electroweak precision  
 560 measurements. The Higgs boson is assumed to be a pseudo-Goldstone boson of some approximate  
 561 symmetry, where pseudo-Goldstone bosons are bosons with a tiny mass that approach zero in  
 562 the limit of the symmetry becoming exact. The approximate symmetry is broken at the scale  
 563  $f$ , where  $\Lambda = 4\pi f$ . Being a pseudo-Goldstone boson, the Higgs boson mass is protected from  
 564 divergent quantum loop corrections up to the scale of compositeness and, above that scale, is no  
 565 longer an elementary scalar. The theory is based on the breaking of two parallel, large global  
 566 symmetries  $[SU(2)_1 \times U(1)_1] \times [SU(2)_2 \times U(1)_2]$ , with Goldstone bosons becoming the longitudinal  
 567 components of the three predicted gauge bosons of the symmetry group  $W'^{\pm}$  and  $Z'$ . These have  
 568 masses of the order of the compositeness scale

$$M(W'^{\pm}) \simeq M(Z') = \frac{g}{\sin 2\theta} f, \quad (1.42)$$

569 where  $\tan \theta = g_1/g_2$ , the ratio of couplings of the  $SU(2)$  groups. The predicted decay widths are  
 570 roughly the same for  $Z'$  and  $W'$  and are as follows:

$$\begin{aligned}\Gamma(W'^{\pm} \rightarrow \ell\nu, Z' \rightarrow \ell\ell) &= \frac{g^2 \cot^2 \theta}{96\pi} M \\ \Gamma(W'^{\pm} \rightarrow q\bar{q}', Z' \rightarrow q\bar{q}) &= \frac{g^2 \cot^2 \theta}{32\pi} M \\ \Gamma(W'^{\pm} \rightarrow WZ, Z' \rightarrow WW) &= \frac{g^2 \cot^2 2\theta}{192\pi} M\end{aligned}\quad (1.43)$$

571 Decays into fermions therefore dominate at  $\cot \theta \geq 1/2$ , whereas decays into bosons are enhanced  
 572 for very low  $\cot \theta$ .

573 These generic composite models can be studied with the Heavy Vector Triplet formalism.

### 574 Heavy Vector Triplet formalism

575 There are many BSM theories that predict the presence of spin-1 particles with masses at the  
 576 TeV scale, each with their own list of model parameters. In most cases, however, when looking for  
 577 such new particles, experiments are not sensitive to the specifics of the model but only the masses  
 578 and couplings of the resonances. We can therefore start from a *simplified model* that describes  
 579 the dynamics of the new spin-1 vector through a simple phenomenological Lagrangian that only  
 580 retains couplings and mass. In the Heavy Vector Triplet formalism [15], a real vector  $V_\mu^a$ , where  
 581  $r$  runs from 1 to 3, is introduced in the adjoint representation of  $SU(2)L$  and represents one  
 582 charged and one neutral heavy spin-one particle with charge eigenstates

$$V_\mu^\pm = \frac{V_\mu^1 \mp iV_\mu^2}{\sqrt{2}} \quad \text{and} \quad V_\mu^0 = V_\mu^3. \quad (1.44)$$

583 The simplified Lagrangian governing the dynamics is given as

$$\begin{aligned}\mathcal{L}_V = -\frac{1}{4} \mathcal{D}_{[\mu} V_{\nu]}^a \mathcal{D}^{[\mu} V^{\nu]}_a + \frac{m_V^2}{2} V_\mu^a V^{\mu a} \\ + ig_V c_H V_\mu^a H^\dagger \tau^a \overleftrightarrow{\mathcal{D}}^\mu H + \frac{g^2}{g_V} c_F V_\mu^a J_F^{\mu a} \\ + \text{additional terms.}\end{aligned}\quad (1.45)$$

584 The first line describes the kinematic and mass terms of the vector  $V$ , and the second line, which  
 585 is of most interest to us, describes the coupling to the Higgs boson current and the left-handed  
 586 fermionic currents. In the coupling to the Higgs current, the coefficient  $c_H$  leads to vertices  
 587 involving the Higgs field and the Goldstone bosons, representing the longitudinally polarized SM

588 vector bosons, W and Z. This term therefore governs the decay modes of the  $V$  into electroweak  
 589 bosons, the decay mode of interest for this thesis. The second coupling term describes the  
 590 interaction with leptons and quarks and is governed by the parameter  $c_F$ . A formalism is adopted  
 591 where the interactions are weighted with a coupling  $g_V$  and  $g^2/g_V$ , where  $g$  is the gauge coupling of  
 592 the group and  $g_V$  represents the “typical strength” of the vector interactions. Another interesting  
 593 feature of the theory is that, after electroweak symmetry breaking provides the heavy vector with  
 594 its mass, the charged and neutral vectors are found to be mass degenerate and expected to have  
 595 similar production and decay rates.

596 After having defined the generic framework, explicit models with fixed values of  $c_H$  and  $c_f$  can be  
 597 studied, where only the resonance mass  $m_V$  and coupling  $g_V$  are left as free parameters. In this  
 598 thesis, we probe two benchmark models called HVT model A and HVT model B, as introduced  
 599 in [15]. The reason why these two models are interesting is that the first probes rather weakly  
 600 coupled extensions of the SM, and the latter, strongly coupled scenarios. That implies very  
 601 different sizes of  $g_V$ , where values of  $g_V = 1$  for model A and  $g_V = 3$  for model B are used in [15].  
 602 For these values of  $g_V$ , model A predicts a comparable branching fraction for decays into bosons  
 603 and fermions, the decay into fermions only enhanced by a factor of 2, while for model B, the  
 604 dominant branching fraction is to dibosons with decays into fermions severely suppressed. The  
 605 branching fraction for the different decay modes of HVT model A and B, are shown in Figure 1.5.  
 For obvious reasons, model B is of most interest for the searches presented here.

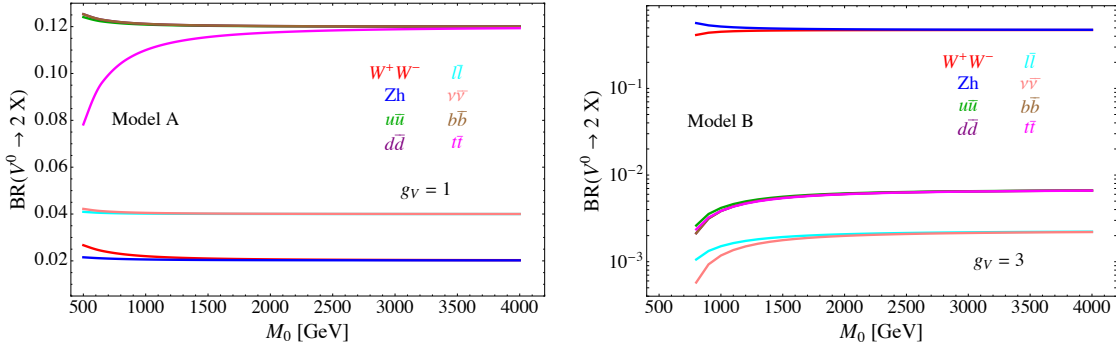


**Figure 1.5:** Predicted branching fractions of a  $Z'$  for two explicit HVT models: Model A $_{g_V=1}$  (left) and model B $_{g_V=3}$  (right) [15].

607 **Warped extra dimensions**

608 Extra dimensional theories also offer solutions to the hierarchy problem. This thesis focuses on  
609 Randall-Sundrum (RS) warped extra dimensional scenarios [16]. In RS models, a new curved  
610 spatial dimension  $y$  is proposed, leading to a 5-dimensional space-time bounded by two (3+1)-  
611 dimensional planes, or *branes*: the UV/Planck and the IR/TeV brane. The new metric now  
612 depends on the radius  $r$  and the curvature factor  $k$  of the new extra dimension

$$ds^2 = e^{-2ky} \eta_{\mu\nu} dx^\mu dx^\nu + dy^2; 0 < y < \pi R \quad (1.46)$$

613 Gravity is concentrated and relatively strong at the Planck brane at  $y = 0$ , which is separated  
614 from us by the fifth dimension. Our observed four-dimensional reality and the Standard Model  
615 particles reside at the TeV brane, at  $y = \pi R$ . Only gravity, transmitted through gravitons, is  
616 allowed to propagate through the warped 5D space-time (the “bulk”) and is not confined to  
either brane. Figure 1.6 illustrates how the branes and the bulk are connected. Due to the

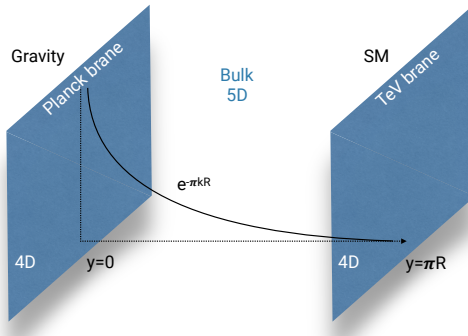


**Figure 1.6:** The RS model predicts an extra dimension where a 5D space-time stretches between two 4D branes: the Planck brane where gravity is concentrate, and the TeV brane where the SM particles are confined.

617  
618 warping, the Planck mass on the Planck brane gets reduced by a factor of  $e^{-\pi k R}$  at the TeV  
619 brane, thereby solving the hierarchy problem. The Planck mass on the TeV brane, which depends  
620 on the geometry of the extra dimension, becomes

$$\bar{M}_{Pl}^2 = V_1 M_*^3, \quad (1.47)$$

621 where  $V_1$  is the volume of the 1 dimensional added warped dimension and  $M_*^3$  is the 5D Planck  
 622 mass. One distinct prediction of the model, and a way in which we can test its validity, is the  
 623 prediction of a tower of TeV-scale excitations with spin-2, so called Kaluza-Klein states, that  
 624 could be observed in high energy experiments.

625 In this thesis, we are more interested in an alternative to the original RS model called the “bulk”  
 626 scenario [17, 18]. In this case, the Standard Model particles, besides the Higgs boson, are also  
 627 allowed to propagate in the bulk. The light 1st and 2nd generation fermions are localized near  
 628 the Planck brane, yielding small couplings to the Higgs boson that still resides at the TeV brane,  
 629 explaining their small masses. Similarly, the top quark is now located near the TeV brane,  
 630 resulting in a stronger Yukawa coupling to the Higgs boson. In addition, with the gravitons  
 631 located near the TeV brane and the fermions now residing near the Planck brane, the graviton  
 632 coupling to fermions is strongly suppressed. SM gluons have a flat distribution throughout the  
 633 bulk, making gluon-gluon production the dominant production channel of gravitons. Due to the  
 634 weak vector bosons absorbing the Higgs degree of freedom in spontaneous symmetry breaking,  
 635 their wave-functions fall off steeply near the TeV brane, resulting in a coupling to the gravitons  
 636 similar to that of the Higgs and the top. The only free parameters of the theory is the mass of  
 637 the lightest KK graviton and the ratio  $\tilde{k} = \frac{k}{M_{Pl}}$ , which controls the widths of the new resonances.  
 638 The branching ratios of the Bulk Graviton is shown in Figure 1.7.

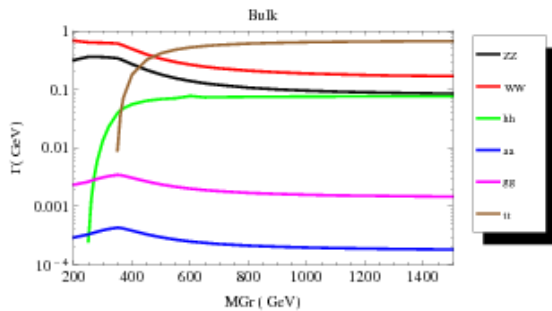


**Figure 1.7:** Predicted branching fractions for a Bulk Graviton.



---

639

## CHAPTER 2

---

640

### Experimental setup

## 641 2.1 The Large Hadron Collider

642 In March 1984, the European Organization for Nuclear Research CERN) and the European  
643 Committee for Future Accelerators (ECFA) held a workshop in Lausanne entitled “Large Hadron  
644 Collider in the LEP Tunnel”. This is history’s first written mention of the Large Hadron Collider  
645 (LHC) and the topic under discussion was exactly how to build a new type of high-energy collider,  
646 capable of bringing hadrons to collide rather than leptons. The LHC would be housed in a tunnel  
647 which, at the time, was under excavation to host the Large Electron-Positron Collider (LEP)  
648 designed to collide leptons with center-of-mass-energies up to around 200 GeV. LEP was a circular  
649 collider with a circumference of 27 km and the tunnel hosting it was located roughly 100 meters  
650 underground beneath France and Switzerland, at the outskirts of Geneva. The justification for  
651 building a machine like the LHC was that, once LEP got to its maximum center-of-mass energy,  
652 a new and more powerful collider would be needed in its place in order to probe higher energies.  
653 While collisions of electrons with positrons provide exceptionally clean and precise measurements  
654 due to their being point particles, their lightness prevent them from being accelerated to higher  
655 energies in circular colliders due to synchrotron radiation. Collisions of hadrons, however, would  
656 allow for center-of-mass energies two orders of magnitude higher than that of LEP. Therefore,  
657 after obtaining sufficient statistics when running at a center-of-mass-energy of twice the W boson  
658 mass (160 GeV) and reaching a maximum center-of-mass energy of 209 GeV, in a search for the  
659 Higgs boson, LEP was dismantled in 2000 in order to make room for the LHC.

660 The Large Hadron Collider first circulated protons in September 2008 and, while having  
661 the same 27-kilometer radius as the LEP collider, is capable of accelerating protons up to a  
662 center-of-mass energy of around 14 TeV, 70 times that of LEP. The accelerator consists of two  
663 oppositely circulating proton beams, isolated from each other and under ultrahigh vacuum. The  
664 protons are accelerated up to speeds close to the speed of light through radio frequency (RF)  
665 cavities, before being focused to collide at four different interaction points along the ring. These  
666 four collision points correspond to the location of the four LHC particle detectors; ATLAS, CMS,  
667 LHCb and ALICE. While ATLAS and CMS are general-purpose detectors, built in order to study  
668 a large range of different physics processes, LHCb and ALICE are built for dedicated purposes;  
669 LHCb for b-physics processes and ALICE for heavy ion collisions. The journey of a proton from  
670 a gas to one of the LHC collision points is as follows. First, hydrogen nuclei are extracted from a  
671 small tank of compressed hydrogen gas and stripped of their electrons. The remaining protons are  
672 then injected into the LINAC2, a linear accelerator responsible for increasing the proton energy  
673 to about 50 MeV through RF cavities that push charged particles forward by switching between  
674 positive and negative electric fields. The LINAC2 additionally divides the constant stream of

675 particles into equally spaced “bunches” by careful tuning of the frequency of the field switch. The  
 676 accelerated protons are then injected into the Proton Synchrotron Booster (PSB), where their  
 677 energy is increased by thirty fold, to an energy of roughly 1.4 GeV. The two final acceleration  
 678 stages before the protons reach the LHC ring are the Proton Synchrotron and Super Proton  
 679 Synchrotron, eventually producing protons with a total energy of 450 GeV. The protons are now  
 680 ready for the final stage of their travel and are injected into the two beam pipes of the LHC in  
 681 opposite directions. They are injected in trains of 144 bunches each (on order of  $10^{11}$  protons per  
 682 bunch), where each bunch is roughly 7.5 meters apart (or 25 ns). There are some larger beam  
 683 gaps present in each beam in order to give special magnets sufficient time to switch on in order  
 684 to inject or dump the beam. The largest beam abort gap is roughly 3 ms or 900 m long. The  
 685 ring is filled with proton bunches until these are equally distributed throughout the two rings, a  
 686 process taking roughly 4 minutes. This is called a “fill”. Here, the protons are accelerated to  
 687 their current maximum energy of 6.5 TeV, a process taking roughly 20 minutes, through eight RF  
 688 cavities. These RF cavities are also responsible for keeping the proton bunches tightly bunched.  
 689 A complete sketch of the CERN accelerator complex is shown in Figure 2.1. After the beams  
 690 have reached their maximum energy and are stably circulating in the LHC ring, the bunches are  
 691 brought to collide. The goal of such a collision, which occurs every 25 nanoseconds, is that some  
 692 of the protons in each bunch will inelastically collide, allowing the quark and gluon constituents of  
 693 each proton to interact with one another and produce new and interesting particles. The number  
 694 of times such an interaction will take place inside a detector per area and time is quantified  
 695 through the instantaneous luminosity  $\mathcal{L}$ , which is the proportionality factor between the number  
 696 of observable events per second and the cross section  $\sigma$  of the process you are interested in,

$$\frac{dN_{events}}{dt} = \mathcal{L}\sigma. \quad (2.1)$$

697 The cross section is the probability that an event (like one which would produce new and interesting  
 698 particles) will occur and is measured in barns, where 1 barn =  $10^{-28}$  m<sup>2</sup>. This luminosity should  
 699 therefore be as high as possible. It depends only on parameters of the accelerator beams and can,  
 700 in the case of the LHC, be defined through accelerator quantities as

$$\mathcal{L} = \frac{N_b^2 n_b f_{rev} \gamma_r}{4\pi\epsilon_n \beta_*} F, \quad (2.2)$$

701 where  $N_b$  is the number of particles per bunch,  $n_b$  is the number of bunches,  $f_{rev}$  is their revolution  
 702 frequency,  $\gamma_r$  is the relativistic gamma factor,  $\epsilon_n$  is the normalized transverse beam emittance  
 703 (how confined the particles are in space and momentum),  $\beta_*$  is the beta function at the collision  
 704 point (how narrow, or “squeezed”, the beam is) and  $F$  is a reduction factor to account for

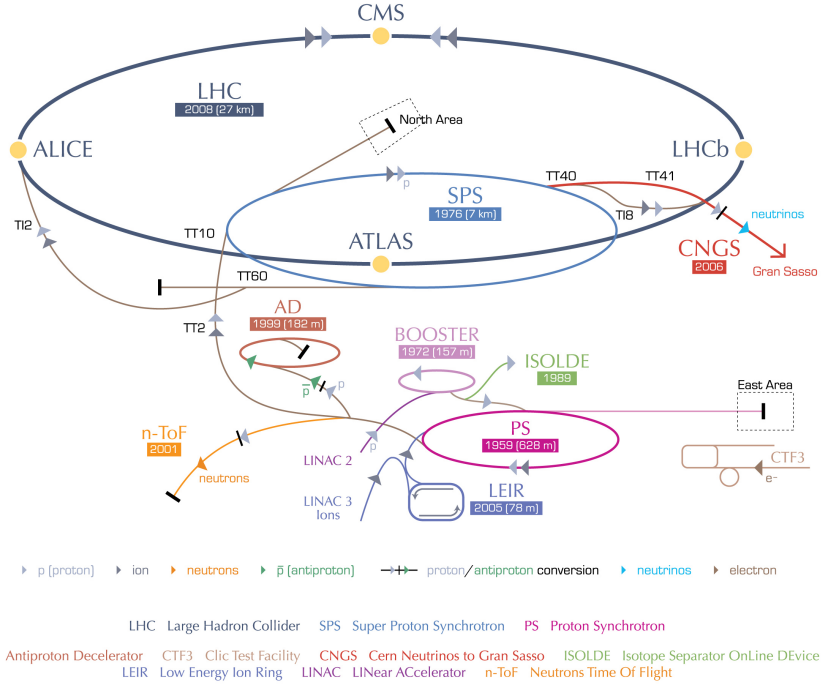


**Figure 2.1:** The Large Hadron Collider accelerator complex. The four collision points along the ring correspond to the location of the LHC particle detectors CMS, LHCb, ATLAS and ALICE [19].

the case where the beams do not collide head-on but at slight crossing angles. From this, it becomes clear that the main goal of the LHC is to maximize the number of particles ( $N_b, n_b$ ), their frequency ( $f_{rev}$ ) and their energy ( $\gamma_r$ ), while at the same time ensuring the protons are packed together as tightly as possible (lower  $\epsilon_n$  and  $\beta^*$ ). Using the nominal values for the LHC, the peak instantaneous luminosity is roughly  $\mathcal{L} \sim 10^{34} \text{ cm}^{-2} \text{ s}^{-1}$ .

The peak luminosity of the LHC by the end of Run 2 in 2018 was about  $2.0 \cdot 10^{34} \text{ cm}^{-2} \text{ s}^{-1}$ , corresponding to 2 times the nominal design instantaneous luminosity.

To quantify the size and statistical power of a given LHC dataset, the integrated luminosity is used. This is the integral of the instantaneous luminosity over time and is defined as

$$\mathcal{L}_{int} = \int \mathcal{L} dt. \quad (2.3)$$

Parameter	Units	Nominal	2015	2016	2017
Energy	[TeV]	7.0	6.5	6.5	6.5
Bunch spacing	[ns]	25	25	25	25
Bunch intensity	$\times 10^{11}$ [protons/bunch]	1.15	1.15	1.15	1.2-1.45
Bunches per train		144	144	96	144
Total number of bunches		2808	2244	2220	2556
$\beta^*$	[cm]	55	80	40	27/25
Peak luminosity	$\times 10^{34}$ [cm $^{-2}$ s $^{-1}$ ]	1.0	0.5	1.4	2.0
Integrated luminosity			4.2	39.7	50.2

**Table 2.1:** Some key LHC detector parameters achieved during the first years of data taking with a center-of-mass energy of 13 TeV.

714 It is usually defined in units of inverse cross section,  $\text{fb}^{-1}$ .

715 Despite the LHC starting up in 2008, there would be another year before data taking began  
716 due to technical difficulties with the magnets. In March 2010, the LHC saw its first collision  
717 with a center-of-mass energy of 7 TeV, and continued running at this energy, collecting around 5  
718 inverse femtobarns of data by the end of 2011. In 2012, the energy was increased to 8 TeV and  
719 the LHC continued running until a planned long shutdown scheduled to begin in February 2013,  
720 collecting a total of  $\sim 20 \text{ fb}^{-1}$ , which allowed the Higgs boson to be discovered. This marked the  
721 end of Run 1 and the beginning of a two-year maintenance project intended to prepare the LHC  
722 for running at a center-of-mass energy of 13 TeV, a period referred to as Run 2.

723 Run 2 started in June 2015, and provides the dataset used in thesis. With the accelerator  
724 now running at 90% of its nominal energy, and with a peak luminosity between 1-2 times the  
725 design luminosity, the LHC managed to collect an impressive  $\sim 160 \text{ fb}^{-1}$  with center-of-mass  
726 energy of 13 TeV up until its planned shutdown at the end of 2018. Some key LHC accelerator  
727 parameters that were in use for the datasets analyzed in this thesis are quoted in Table 2.1.

## 728 2.2 The CMS detector

729 The Compact Muon Solenoid (CMS) detector is true to its name. With a diameter of 15 meters and  
730 a weight of 14000 tons, it is 60% smaller but twice as heavy as its counterpart, the ATLAS detector.  
731 Its large weight is due to its solenoid: A superconducting niobium titanium coil circulating 18500  
732 Amps and capable of generating a magnetic field of 3.8 Tesla, making it the worlds largest and  
733 most powerful magnet. Together with its corresponding iron return yoke, responsible for returning  
734 the escaping magnetic flux, it accounts for 90% of the total detector weight. The CMS detector  
735 is cylindrically symmetric and organized such that the inner tracking system begins at a radius

of around 3 cm from the beam pipe. It consists of an inner silicon pixel detector and an outer silicon strip tracker, stretching out to a radius of roughly 1.2 meters. Following the tracker are two calorimeter layers: the electromagnetic calorimeter (ECAL) consisting of lead tungstate scintillating crystals and responsible for measuring the energy of electromagnetically interacting particles, followed by the hadronic calorimeter (HCAL) that measures the energy of hadrons. Contrary to “standard” configurations for general purpose detectors, the CMS calorimeters are located inside the superconducting solenoid. This allows the detector to be rather compact, by reducing the necessary radii of the calorimeters, and results in a strong magnetic field due to the large coil radius. The muon detectors are alternated with three layers of steel return yoke, responsible for containing and returning the magnetic field. Only muons and weakly interacting particles are expected to transverse the full detector volume without being stopped. Since the muons bend in the magnetic field of the return yoke, an additional momentum measurement can be made. A schematic overview of the CMS detector is shown in Figure 2.2. In the following, the different sub-detectors will be described in detail.

### 2.2.1 Coordinate system

To describe locations within the CMS detector, a Euclidian space coordinate system is used. Here, the positive z axis points along the beam pipe towards the west, the positive x axis points towards the center of the LHC ring, and the positive y axis up towards the surface of the earth. Due to the cylindrical symmetry of the detector, polar coordinates are more convenient and most frequently encountered. In this scheme, the azimuthal angle  $\phi$  is measured in the xy-plane, where  $\phi = 0$  correspond to the positive x axis and  $\phi = \pi/2$  correspond to the positive y axis. The polar angle  $\theta$  is measured with respect to the z axis,  $\theta = 0$  aligning with the positive and  $\theta = \pi$  with the negative z axis. To define a particles’ angle with respect to the beam line, the pseudorapidity  $\eta = -\ln \tan(\theta/2)$  is preferred over  $\theta$ . This is due to the fact that particle production is approximately constant as a function of pseudorapidity and, more importantly, because differences in pseudorapidity are Lorentz invariant under boosts along the z-axis when assuming massless particles. To measure angular difference between particles in the detector, the variable  $\Delta R = \sqrt{\Delta\eta^2 + \Delta\phi^2}$  is used, which is also Lorentz invariant under longitudinal boosts. A summary of the CMS coordinate system together with some example values are shown in Figure 2.3.

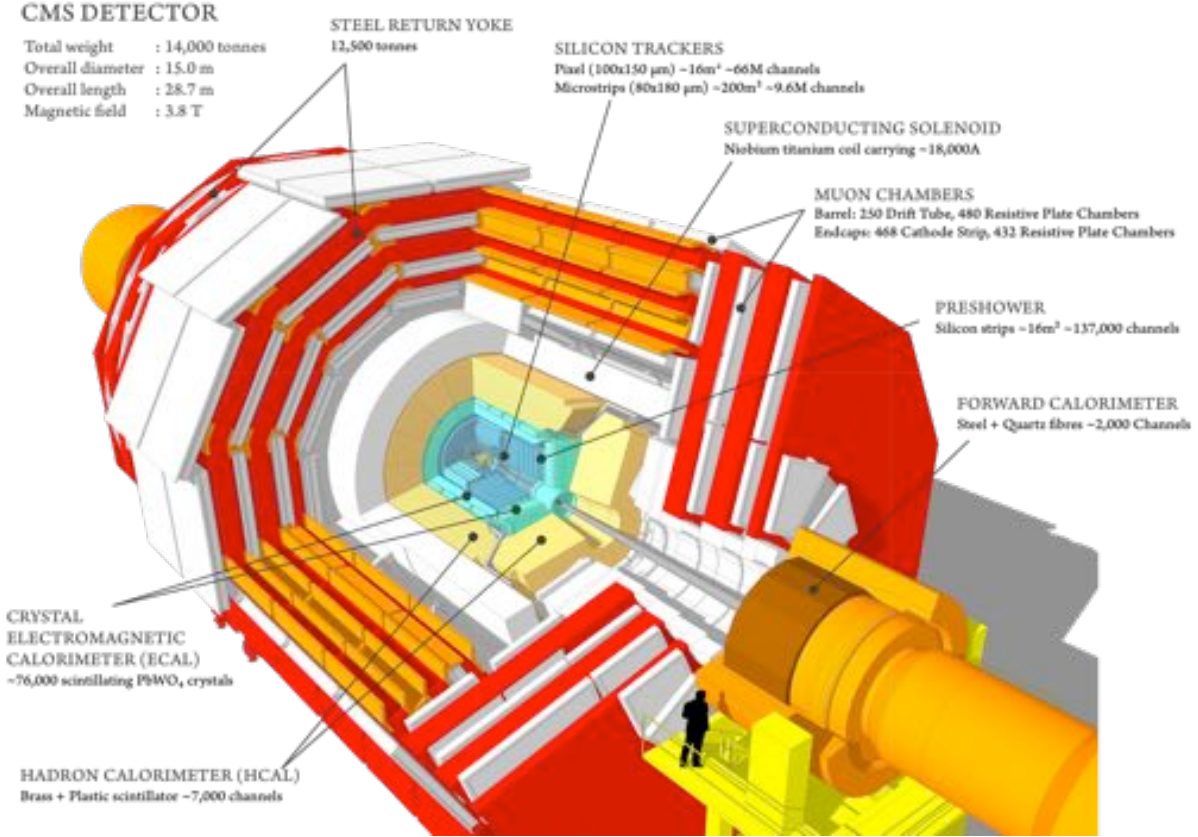


**Figure 2.2:** The CMS detector and its subsystems: the silicon tracker, electromagnetic and hadron calorimeters, superconducting solenoid and the muon chambers inter-layered with the steel return yoke [20].

### 2.2.2 Tracking detectors

The CMS tracker is responsible for accurately reconstructing the momentum of charged particles and consists of two sub-detectors. Closest to the interaction point, and where the particle intensity is the highest, the silicon pixel detector is located. Upgraded in 2017, from the so-called Phase-0 to the Phase-1 detector, it is structured with four cylindrical barrel layers at radii 2.9, 6.8, 10.9 and 16.0 cm (the barrel pixel detector) and three disks in each of the forward regions placed at a distance from the nominal interaction point of 29.1, 39.6 and 51.6 cm (the forward pixel detector). A sketch of the current Phase-1 pixel detector compared to the Phase-0 detector is shown in Figure 2.4. The sensors located closest to the beam pipe are subject to hit intensities of  $\mathcal{O}(\text{MHz}/\text{mm}^2)$  such that strict constraints on the sensor pixel size are required in order to minimize occupancy in the detector. The sensor pixels are  $100 \mu\text{m} \times 150 \mu\text{m}$  with a thickness

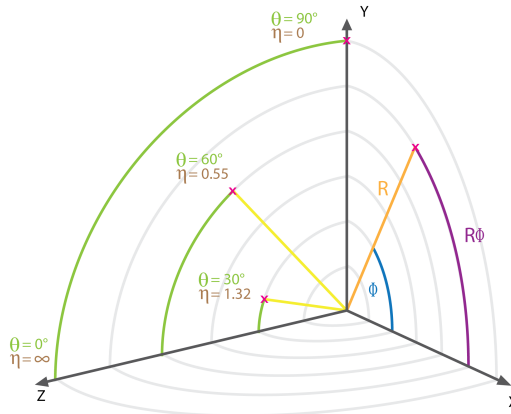


**Figure 2.3:** The CMS coordinate system [21], shown with some values of  $\theta$  and  $\eta$ .

of 285  $\mu\text{m}$ , and when counting both barrel and forward pixel detectors, sum up to a total of 124 million channels. The sensors are mounted on detector modules each with 16 read-out chips, where the type of readout chip depends on how close the module is to the beam pipe. The inner layer uses readout chips with a rate capability of 600 MHz/cm<sup>2</sup>, while for the outer layers, readout chips with a rate capability of up to 200 MHz/cm<sup>2</sup> are sufficient. Since the hit intensity

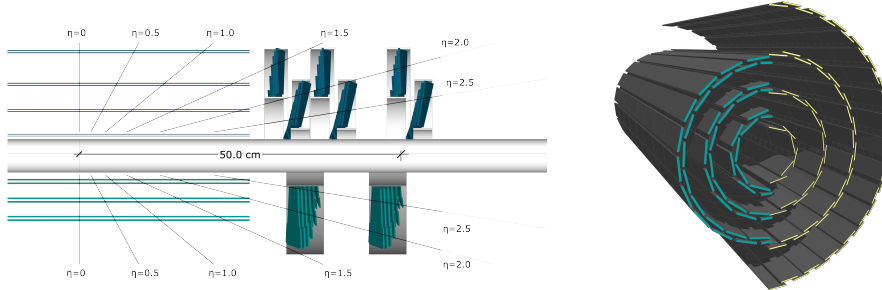


**Figure 2.4:** Left: The pixel detector layout before (bottom) and after (top) the Phase-1 upgrade. Right: The barrel pixel detector before (left) and after (right) the Phase-1 upgrade [22].

reduces as you go further away from the beam pipe, the pixel sensors are replaced by silicon strip sensors of larger size, making up the second of the two tracker sub-systems, the silicon strip tracker. There are ten strip layers in total, stretching out to a radius of roughly 130 cm. These are divided into four sections: The inner barrel (TIB) with four strip layers, the two inner endcaps (TID) consisting of three disks each, the outer barrel (TOB) consisting of 6 cylindrical layers, and the two endcaps (TEC) with 9 strip layers each. A schematic overview of the strip tracker layout is shown in Figure 2.5. The strips in the TIB and TID are 10 cm long, with a width of 80

<sup>789</sup>  $\mu\text{m}$  and a thickness of  $320 \mu\text{m}$ . The TOB and TEC sections consist of slightly larger strips of  $25$   
<sup>790</sup>  $\text{cm} \times 180 \mu\text{m}$  and a thickness of  $500 \mu\text{m}$ . The strip tracker has a total of  $10$  million detector  
<sup>791</sup> strips and covers an area of  $\sim 200 \text{ m}^2$ . To prolong the silicon detector lifetime, the entire tracker  
<sup>792</sup> (pixel and strip) is kept at a temperature of  $-20^\circ\text{C}$  with a dedicated cooling system. The tracker  
has a coverage of up to  $|\eta| < 2.6$  and a resolution of roughly  $\sigma/p_T \approx 1.5 \times 10^{-5} p_T + 0.005$ .

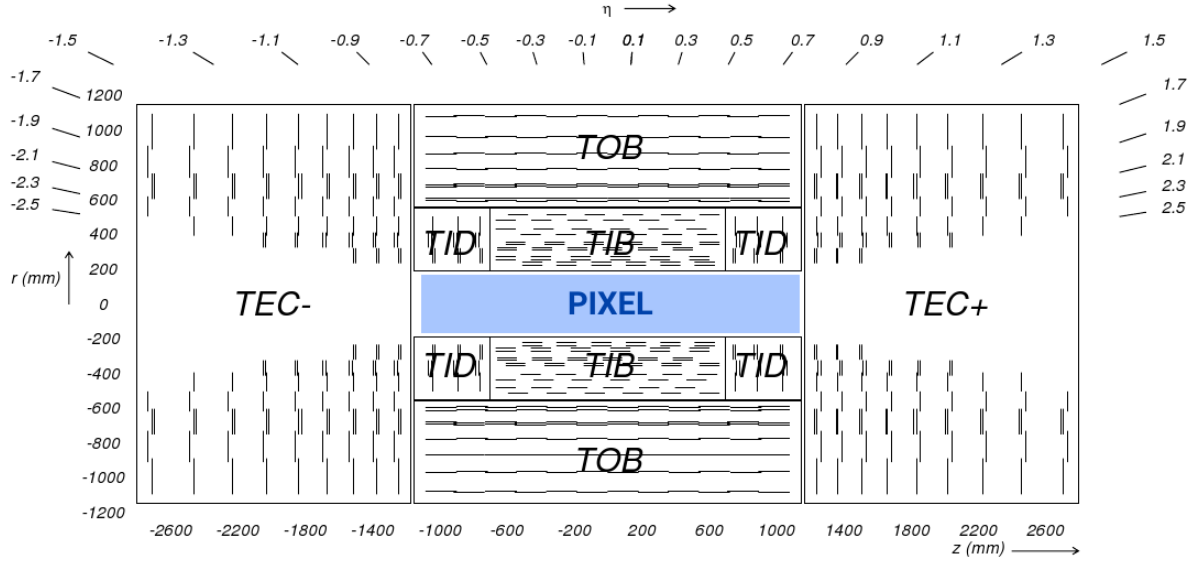


**Figure 2.5:** Schematic of the CMS silicon strip tracker and its four subsections: the inner barrel (TIB), inner endcaps (TID), the outer barrel (TOB), and the two endcaps (TEC) [23].

<sup>793</sup>

### <sup>794</sup> 2.2.3 Electromagnetic calorimeter

<sup>795</sup> Surrounding the tracking detectors is the electromagnetic crystal calorimeter (ECAL). Consisting  
<sup>796</sup> of  $75\,848$  laterally segmented scintillating lead tungstate ( $\text{PbWO}_4$ ) crystals, it was designed to  
<sup>797</sup> have the best possible photon energy and position resolution in order to resolve a Higgs boson  
<sup>798</sup> decaying into two photons, one of the cleanest discovery channels of the Higgs boson. With a  
<sup>799</sup> design energy resolution of  $0.5\%$  above  $100 \text{ GeV}$  for photons and electrons, the choice of detector  
<sup>800</sup> material for the ECAL has been its most crucial design feature. In order to withstand the high  
<sup>801</sup> doses of radiation and the high magnetic field present within the detector, while at the same time  
<sup>802</sup> generating well-defined signal responses within the  $25$  nanoseconds between particle collisions,  
<sup>803</sup> an extremely dense and transparent material capable of producing fast and clean photon bursts  
<sup>804</sup> when hit, is required. Metal-heavy lead tungstate crystals, each taking roughly two days to  
<sup>805</sup> artificially grow (and a total of about ten years to grow all of them), were chosen. With a density

of  $\delta = 8.28 \text{ g/cm}^3$  (slightly higher than for stainless steel), the crystals are compact enough to yield excellent performance without taking up too much volume, allowing the ECAL to fit within the CMS superconducting solenoid. The homogeneous medium allows for a better energy resolution as it minimizes the effects from sampling fluctuations, and it additionally contains enough oxygen in crystalline form to make it highly transparent to the entire scintillation emission spectrum. With an extremely short radiation length and small Moli  re radius ( $X_0 = 0.85 \text{ cm}$ ,  $R_M = 2.19 \text{ cm}$ ), the required homogeneity, granularity, and compactness is obtained, while at the same time emitting 80% of generated light within the 25 ns timeframe required. The largest drawbacks with a lead tungstate detector are the low light yield (100  $\gamma$  per MeV), requiring dedicated avalanche photodiodes to increase the gain, and the light yield, which strongly depends on the temperature. The detector response to an incident electron changes by  $3.8 \pm 0.4 \%$  per degree Celsius which requires the ECAL temperature to be kept stable at  $18.0 \pm 0.5$  degree Celsius, which is obtained through an intricate water cooling system. The ECAL is completely hermetic and sorted into a barrel part (EB), covering pseudorapidities up to  $|\eta| < 1.48$ , and two endcap parts (EE) extending the total coverage to  $|\eta| < 3.0$ , in order to match the tracker coverage of  $|\eta| < 2.5$ . In order to improve the separation power between the  $\gamma$  and  $\pi_0$ , a pre-shower detector (ES) using lead absorbers and silicon sensors covers the forward region between  $1.65 < |\eta| < 2.6$ . The crystals in the barrel are organized into supermodules, each consisting of about 1700 crystals, while the endcap is divided into two half disks consisting of 3662 crystals each (so-called “Dees”). Each PbWO<sub>4</sub> crystal weighs around 1.5 kg and has a slightly tapered shape with a front face of  $2.2 \times 2.2 \text{ cm}^2$  in the barrel and  $2.86 \times 2.86 \text{ cm}^2$  in the endcaps. The crystals are 23 and 22 cm long in the barrel and endcaps, respectively. The total volume of the calorimeter including barrel and endcaps is  $11 \text{ m}^2$  and it weighs a total of 92 tonnes. The ECAL detector layout is illustrated in Figure 2.6.

Having no longitudinal segmentation, the ECAL relies on an accurate reconstruction of the event primary vertex, provided by the tracker, in order to reconstruct the photon angle correctly.

The obtained energy resolution of the ECAL can be parametrized in three parts: a stochastic, a noise, and a constant term [24]. It is given as

$$\frac{\sigma E}{E} = \frac{2.8\%}{\sqrt{E}} \oplus \frac{0.128 \text{ GeV}}{E} \oplus 0.3\%,$$

in which the constant values were estimated using an electron test beam. The constant term of 0.3% is dominated by the non-uniformity in longitudinal light collection [25], and one of the main goals of the detector design was to get this term below 1%. The energy resolution as a function of electron energy is shown in Figure 2.7.

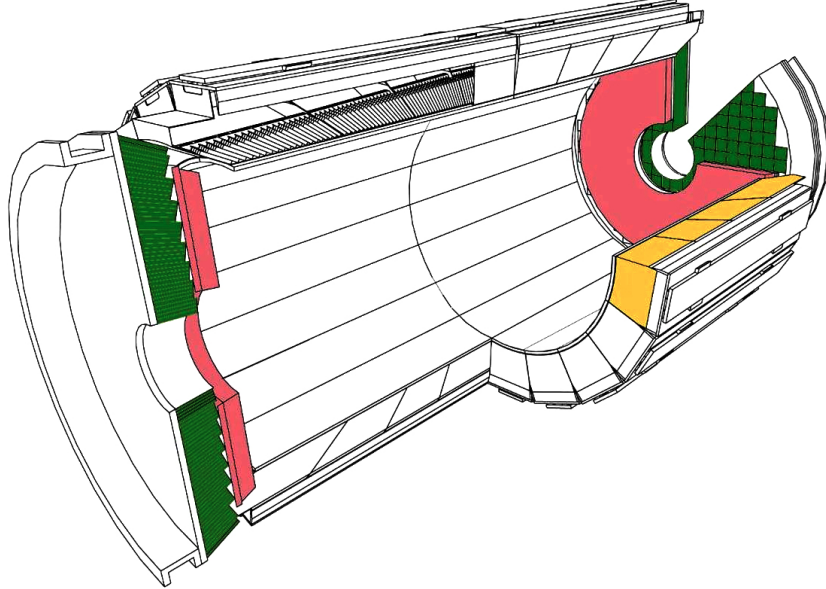


**Figure 2.6:** A schematic of the CMS electromagnetic calorimeter showing the barrel supermodules (yellow), the individual barrel crystals (black, top left), the endcap modules (green), and the pre-shower detectors (pink) [23].

#### 2.2.4 Hadronic calorimeter

Outside the electromagnetic calorimeter is the hadronic calorimeter (HCAL). The HCAL is a sampling calorimeter, meaning it consists of alternating layers of dense brass absorber material and plastic scintillators. When a particle hits an absorber plate, it interacts with the absorber material and generates a shower of secondary particles which themselves generate new particle showers. These particles then generate light in the scintillating material which is proportional to their energy, and summing up the total amount of generated light over consecutive layers within a region, called a “tower”, is representative of the initial particles energy. It is the combined response of the ECAL and the HCAL that are responsible for measuring the energy of quarks, gluons and neutrinos through the reconstruction of particle jet energy and missing transverse energy. The hadron calorimeter is split into four regions: the inner (HB) and outer (HO) barrel, the endcap (HE) and the forward region (HF). A schematic of the CMS HCAL is shown in Figure 2.8. The inner barrel lies within the superconducting solenoid volume and covers the pseudorapidity range  $|\eta| < 1.3$ . It consists of 36 identical wedges, each of which weigh 26 tonnes, split into two half barrels (HB+ and HB-). A photograph of the wedges taken during installation is shown in Figure 2.9. The wedges are made up of flat brass absorber plates oriented parallel to the beam axis. These plates consist of a 4-cm thick front steel plate followed by eight 5-cm

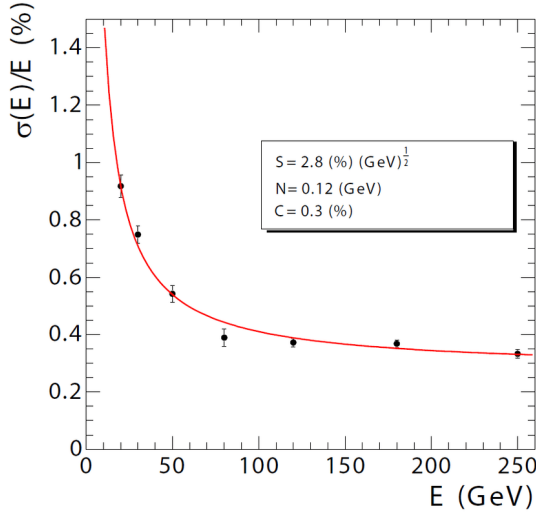


**Figure 2.7:** The ECAL energy resolution as a function of electron energy as measured in an electron test beam. [24]

thick brass plates, six 5.6- cm thick brass plates and ending with a 7.5- cm thick steel back plate. The absorber plates alternate with 4-mm thick plastic scintillator tiles, which are the active medium of the detector, and which are read out using wavelength-shifting plastic fibers. The effective thickness of the barrel hadron calorimeter in terms of interaction lengths increases with the polar angle  $\theta$ , starting out at about  $5.8 \lambda_I$  at an angle of 90 degrees, and increasing to  $10.6 \lambda_I$  at  $|\eta| < 1.3$ . As the energy resolution of the calorimeter depends on how much of the particles shower can be absorbed by the calorimeter, the quality of the energy measurement depends on its thickness. Due to the CMS design, the HB is confined to the volume between the ECAL (ending at a radius of 1.77 m) and the magnetic coil (starting at a radius of 2.95 m). In the central  $\eta$  region, the combined ECAL and HCAL interaction length is too small to sufficiently contain hadron showers. In order to ensure adequate sampling, especially of late starting showers, an additional layer of scintillator has therefore been added outside of the solenoid coil. This is the outer barrel (HO). It uses the coil itself as an absorbing material, increasing the total barrel calorimeter interaction length to  $11.8 \lambda_I$ . The hadron calorimeter endcaps (HE) are located in the forward region close to the beam pipe and cover the pseudorapidity range  $1.3 < |\eta| < 3.0$ , a region containing about 35% of the particles produced in collisions. Due to its close proximity to the beam pipe, the endcaps need to handle extremely high rates as well as have a high radiation tolerance. As the resolution in the endcap region is degraded due to pile-up and magnetic field effects, the hadron calorimeter endcaps were designed to minimize the cracks between HB and HE, rather than having the best single-particle resolution (as is the case for the barrel). The absorber



**Figure 2.8:** The four regions of the CMS hadron calorimeter: the inner (HB) and outer (HO) barrel, the endcap (HE) and the forward region (HF) [23]

plates in the endcaps are mounted in a staggered geometry rather than on top of each other as is done in the barrel, in order to contain no dead material and provide a hermetic self-supporting construction. The HCAL is read out in individual towers with a size  $\Delta\eta \times \Delta\phi = 0.087 \times 0.087$  in the barrel, and  $0.17 \times 0.17$  at larger pseudorapidities. In order to obtain a completely hermetic calorimeter, an additional hadron forward calorimeter (HF) is added in the very forward region. Stretching out to a pseudorapidity of  $|\eta| = 5.2$ , this detector is located so close to the beam pipe that the particle rate exceeds  $10^{11}$  per  $\text{cm}^2$ , receiving roughly 760 GeV per proton-proton collision compared to an average of 100 GeV for the rest of the detector. It consists of two cylindrical steel structures, each with an outer radius of 130 cm and an inner radius of 12.5 cm, located 11.2 meters on either side of the interaction point. Also a sampling calorimeter, it consists of grooved 5-mm thick steel absorber plates, where the quartz fiber active medium is inserted into these grooves. The energy resolution of the CMS ECAL and HCAL detectors for pions is measured in a test beam as a function of energy and is shown in Figure 2.10. The typical electronics noise of the HCAL is measured to be 200 MeV per tower. The inclusion of the HO improves the resolution by 10% for a pion energy of 300 GeV. The final energy resolution parametrization when using ECAL+HB+HO is given by a stochastic and a constant term, as was the case for the ECAL detector, and is

$$\frac{\sigma E}{E} = \frac{84.7\%}{\sqrt{E}} \oplus 7.4\%.$$



**Figure 2.9:** The installation of the barrel HCAL wedges, consisting of alternating layers of brass absorber plates and plastic scintillator, each weighing roughly 26 tonnes [26].

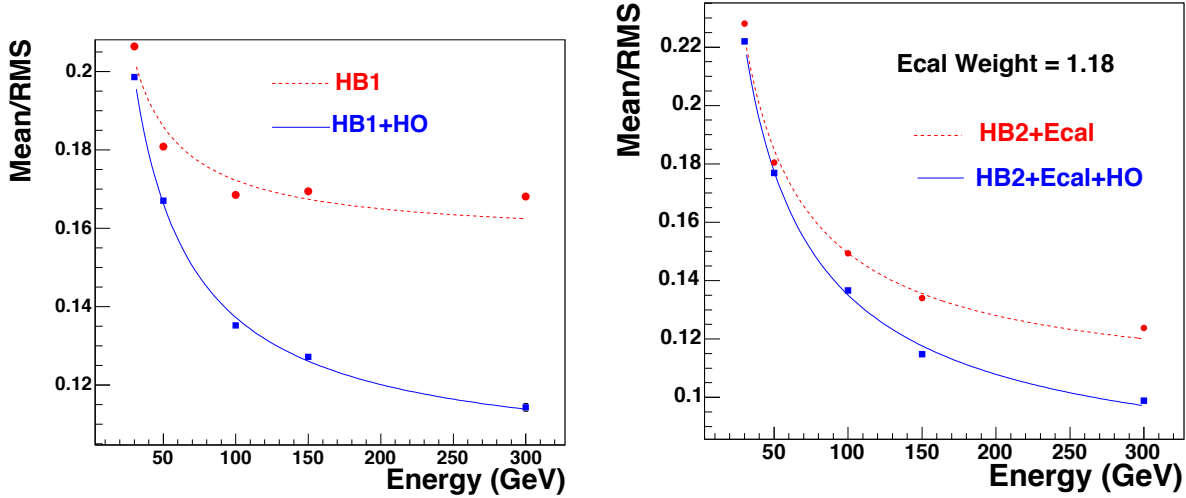


**Figure 2.10:** The calorimeter energy resolution as a function of pion energy using the HB only or HB+HO (left), and when adding ECAL and HCAL measurements (right) [27].

### 839 2.2.5 Muon chambers

840 The outer part of the CMS detector is dedicated to performing muon identification, momentum  
 841 measurements, and triggering. The muon system is made up of three types of gaseous particle  
 842 detectors: drift tube (DT) chambers, cathode strip chambers (CSCs), and resistive plate chambers

(RPCs), all integrated into the magnetic return yoke structure. In the barrel region, where particle rates are low and the magnetic field uniform, DT chambers are used and cover the pseudorapidity region  $|\eta| < 1.2$ . In the endcap regions, however, the muon rates and background levels are considerably higher and the magnetic field itself is large and non-uniform. Therefore, CSCs with finer segmentation, higher radiation resistance, and faster signal collection are used, and cover the region  $0.9 < |\eta| < 2.4$ . To ensure accurate muon triggering, RPCs are used as a complimentary dedicated muon triggering system, which has been added both in the barrel and in the endcaps. These provide an excellent time resolution and cover the region  $|\eta| < 1.6$ . These chambers also assist in resolving ambiguities if multiple hits are present within a CSC or DT chamber. A schematic overview of the muon system is shown in Figure 2.11.

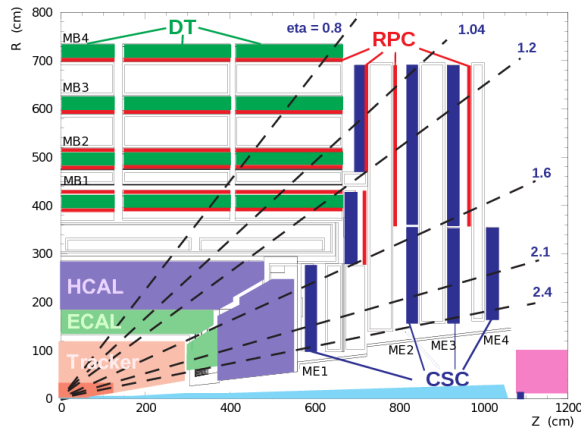


**Figure 2.11:** A schematic overview of the muon chambers: the DT chambers in the barrel, the CSCs in the endcaps, and the redundant RPC system stretching out to  $|\eta| < 1.6$ , which are used for triggering purposes [28].

852

### 853 2.3 Trigger system

854 With bunches in CMS colliding at a rate of 40 MHz, there are only 25 nanoseconds between  
 855 collisions available to process event data. For typical instantaneous luminosities, one billion  
 856 collisions take place every second, and with an event size of roughly 1 MB, it is impossible for  
 857 all of these events to be read out and stored to disk. The CMS triggering system is therefore  
 858 designed to make ultra fast high-quality decisions about which events are interesting and which  
 859 events are not. The first stage of triggering, called Level 1 (L1), is designed to reduce the event  
 860 rate to a maximum of 100 kHz through custom-designed hardware. It uses coarse data from  
 861 the muons system and calorimeters in order to make a decision on whether the event should be

recorded or not, a decision that needs to happen within  $3.2\mu s$ . During this time, the full event data from each sub-detector is stored in detector front-end electronics, awaiting the L1 decision. The information used by L1 is gathered in three steps. First, trigger primitives are created. For the muon system, these consist of track segments from each of the three types of muon detectors. For the calorimeter, trigger primitives are generated by calculating the transverse energy in a trigger tower ( $\Delta\eta - \Delta\phi$  of  $0.087 \times 0.087$ ) and assigning it to the correct bunch crossing. Trigger primitives from the calorimeter are then passed on to a regional trigger, which defines electrons, muons and jet candidates. Some of this information is passed to the regional muon trigger in order to provide information about whether the particle is minimum ionizing. The global muon trigger then combines track information with calorimeter information and selects a maximum of four muon candidates and calculates their momentum, position, charge and quality. The output from the regional calorimeter trigger is also passed to a global calorimeter trigger which provides information about the jets, total transverse energy and missing energy in the event. Combining the information from the global muon trigger and the global calorimeter trigger, the L1 trigger decides whether to keep the event or not by combining several decisions by simple logic operations (AND/OR/NOT), forming up to 128 algorithms.

If the event is accepted, the full event information is read out at a rate of 100 kHz and passed to the High Level Trigger (HLT), a farm of commercially available computers. Here, the full precision of the detector data is used in order to make decisions based on offline-quality reconstruction algorithms. The goal of the HLT is to eventually reduce the event rate to an average of 400 Hz, which will be stored on tape.

---

883

## CHAPTER 3

---

884

### Event reconstruction

### 3.1 Track and primary vertex reconstruction

The CMS tracker gets traversed by  $\mathcal{O}$  1000 charged particles at each bunch crossing, produced by an average of roughly 34 proton-proton interactions happening simultaneously. This makes track reconstructions extremely challenging, and is the reason why a high granularity of the tracker is vital. The average number of vertices per event for the whole Run 2 is shown in Figure 3.1, with a combined average of 34 number of interactions per bunch crossing. Track reconstruction describes

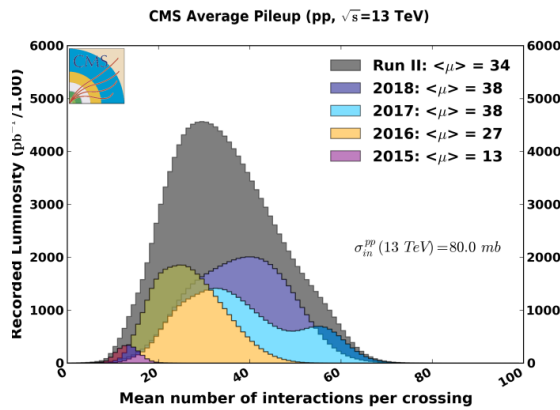


**Figure 3.1:** The average number of vertices per event in CMS during the Run 2 datataking [29].

the process of taking hits from the pixel and strip detectors, combining them and estimating the momentum and flight direction of the charged particle responsible for producing the hits. It is an extremely computationally heavy process and is based on what is called a combinatorial Kalman filter [30]. A Kalman filter is an algorithm that uses time-dependent observations in order to estimate unknown variables, by proceeding progressively from one measurement to the next, improving the knowledge of the trajectory with each new measurement. The track reconstruction software in CMS (called the Combinatorial Track Finder (CTF)) constructs its collection of tracks by iteratively looping over the hits and reconstructing tracks, then removing those which are already used as inputs for a previous track. It starts from a seed in the inner most tracker layers, usually two or three hits, and then extrapolates the seed trajectories searching for additional hits to associate to that candidate. It then disregards tracks that fail certain criteria based on a  $\chi^2$  calculation taking both hit and trajectory uncertainties into account, as well as the number of missing hits. The track reconstruction algorithm is effective over the full tracker coverage range up to  $|\eta| < 2.5$  and can reconstruct particles with momenta as low as 0.1 GeV or particles which are produced up to 60 cm from the beam line. In the central region, particles with a momentum of 100 GeV have a  $p_T$ -resolution of roughly 2.8 %, a transverse impact parameter resolution of 10

907  $\mu\text{m}$  and a longitudinal impact parameter of  $30 \mu\text{m}$ .

908 In order to define the location and uncertainty of every proton-proton interaction in an  
909 event, primary-vertex reconstruction is performed. Primary vertices lie within a radius of a few  
910 millimeters of the beam axis and are defined as the common origin of groups of tracks. The  
911 reconstruction algorithm takes as input the reconstructed tracks from the previous step which  
912 pass certain selection criteria, clusters the tracks that share a common origin and then fit for the  
913 position of each vertex. Each track must have at least 2 hits in the pixel layers and no less than 5  
914 hits in the pixel+strip as well as a  $\chi^2 < 20$  from a fit to the particle trajectory to be considered  
915 as input for the vertex finder. The primary vertex resolution is around  $12 \mu\text{m}$  in  $x$  and  $10 \mu\text{m}$  in  
916  $z$  for vertices with at least 50 tracks.

917 Offline, all events are required to have at least one primary vertex reconstructed within a 24  
918 cm window along the beam axis, with a transverse distance from the nominal interaction region  
919 of less than 2 cm. The reconstructed vertex with the largest value of summed physics object  $p_T^2$   
920 is selected as the primary interaction vertex where the hard scattering process occurred.

## 921 3.2 The Particle Flow Algorithm

922 After track reconstruction, what remains is an incoherent collection of tracks, calorimeter clusters  
923 and hits in the muon chambers. In order to connect these, CMS uses an algorithm called Particle  
924 Flow (PF) [31] to combine the information obtained from all sub-detectors in order to infer which  
925 particles were actually produced in the event. The reconstructed physics object in the order of  
926 which they are reconstructed are

- 927 • Muons, through hits in the tracker and in the muon chambers
- 928 • Charged hadrons, through hits in the tracker and energy deposits in the calorimeters
- 929 • Neutral hadrons, through energy deposits in the calorimeters but no hits in the tracker
- 930 • Photons, through energy deposits in the ECAL but not in the HCAL and no hits in the  
931 tracker
- 932 • Electrons, through hits in the tracker and energy deposits in the ECAL

933 How these different particles propagate through the CMS detector is illustrated in Figure 3.2.

934

### 935 3.2.1 Reconstruction of the Particle Flow inputs

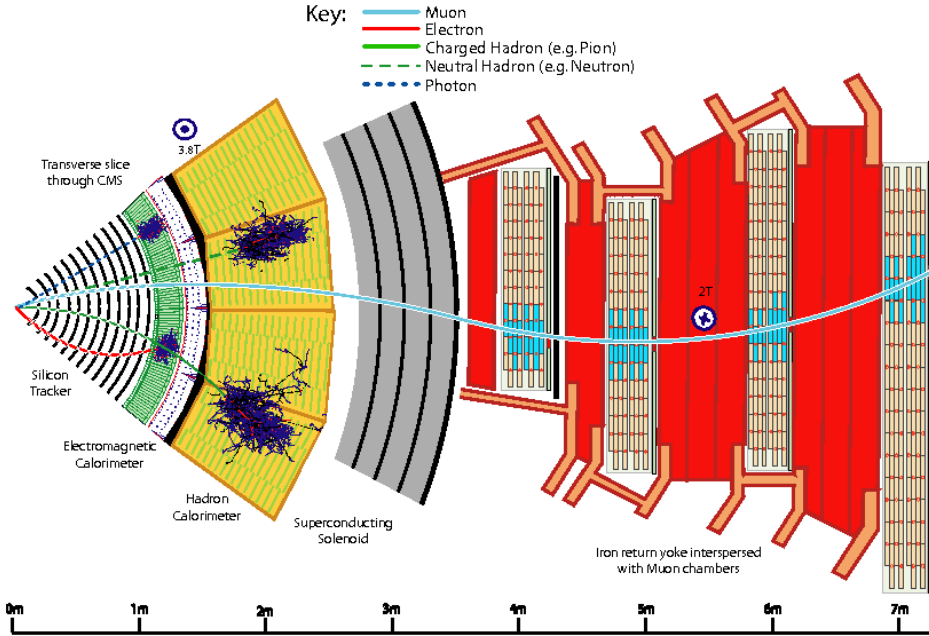


**Figure 3.2:** Particle interactions in the different subdetectors for a transverse slice through the CMS detector [31].

### 936    Electron tracking

937    Electron seeding is done in two different ways: ECAL-based or tracker-based electron seeding. In  
 938    the ECAL-based method, electrons are seeded from ECAL clusters with  $E_T > 4 \text{ GeV}$ , where the  
 939    position of the cluster is used to infer which hits in the inner tracker belongs to a given electron or  
 940    positron. As a large fraction of the electron/positron energy is emitted through bremsstrahlung  
 941    before even reaching the ECAL, ECAL superclusters covering a small window in  $\eta$  and a larger  
 942    window in  $\phi$  are defined in order to fully contain the electron as well as its bremsstrahlung  
 943    photons. As these superclusters are prone to contamination, tight isolation requirements need to  
 944    be applied, leading to reconstruction inefficiencies. Therefore, an additional tracker-based seeding  
 945    approach has been developed. All tracks with  $p_T > 2 \text{ GeV}$  are used as potential electron seeds.  
 946    These tracks are then extrapolated to the ECAL and matched to the closest ECAL cluster. The  
 947    ratio of the cluster energy to the track momentum is required to be 1. The electron candidates  
 948    are then fit with a Gaussian-sum filter (GSF) [32] and required to pass certain criteria based on  
 949    the score of a boosted-decision-tree (BDT) which combines the number of tracker hits, the  $\chi^2$  of  
 950    the GSF track, the energy loss along the track, and the distance between the extrapolated track  
 951    to the closest ECAL cluster.

**952 Muon tracking**

953 Muon tracking consists of two part: the muon spectrometer allows muons to be identified with  
954 high efficiency over the full pseudorapidity range, while maintaining a low background due to the  
955 absorbing calorimeter layers upstream. The inner tracker on the other hand, provides an accurate  
956 measurement of the muon momentum. Three muon quality flags are defined

- 957     • Standalone muon: Muon tracks based on hits in the DT or CSC only  
958     • Global muon: A standalone muon track matched to a track in the tracker if the track  
959       parameters of the two are compatible  
960     • Tracker muon: An inner track with  $p_T > 0.5$  GeV, a total momentum greater than 2.5 GeV  
961       and at least one muon segment matching the extrapolated inner track

962 Around 99% of muons produced within  $|\eta| < 2.4$  are reconstructed as a global muon or a tracker  
963 muon, and very often as both. If the global and tracker muon share the same inner tracker  
964 segment, the two are combined.

**965 Calorimeter clusters**

966 The calorimeter clustering is performed separately for each calorimeter subdetector (ECAL barrel  
967 and endcaps, HCAL barrel and endcaps and the preshower layers). The first step is to define  
968 cluster seeds from cells with an energy exceeding some predefined threshold and in addition is  
969 larger than the energy in its neighboring cells. Topological clusters are then formed by adding  
970 cells to the seed which has at least one corner in common with a cell already in the cluster, and  
971 that has an energy which is at least twice the noise level of the detector. In Figure 3.3, an example  
972 of calorimeter clustering for a five-particle jet is shown for the HCAL (left) and ECAL (right). In  
973 the HCAL (left), two seeds have been identified (gray filled areas) inside a topological cluster  
974 consisting of 9 cells. These are then defined as two HCAL clusters, with a position as indicated  
975 by the red circles. The green solid lines correspond to charged tracks reconstructed in the tracker,  
976 both pointing to the center of the HCAL cluster seeds. The observed deposits left by the same  
977 particles are shown on the right in Figure 3.3, where the  $K_L^0$ ,  $\pi^-$  and the two photons from the  
978 decay of a  $\pi^0$  leave distinct clusters in the ECAL. The  $\pi^+$  leaves no energy deposit in this case.

**979 3.2.2 Particle Flow identification**

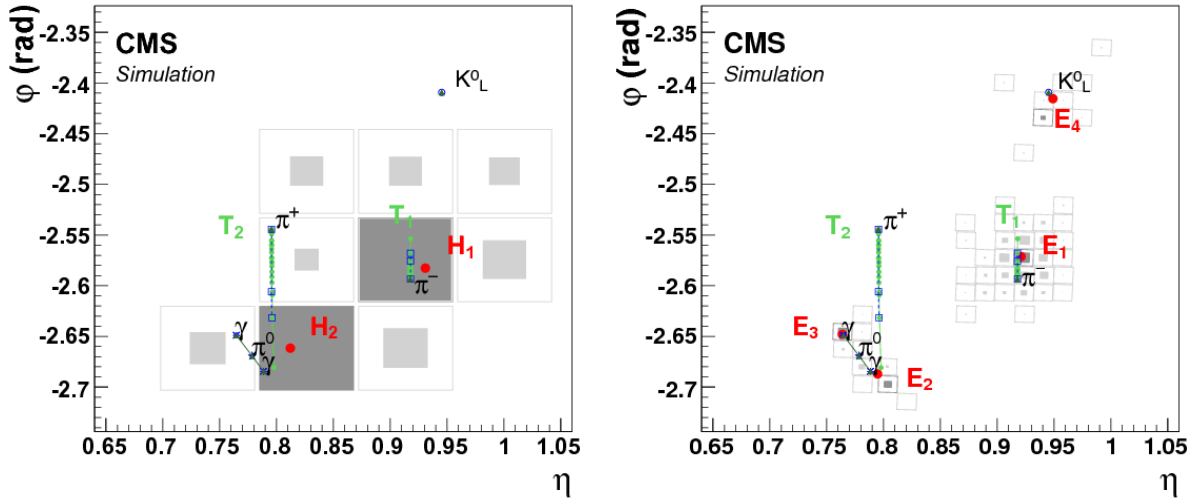


**Figure 3.3:** The  $\eta - \phi$  vies of calorimeter clusters generated by a five-particle jet in the HCAL (left) and in the ECAL (right). The squares correspond to calorimeter cells, where the inner area is proportional to the logarithm of the cell energy. Cluster seeds are depicted in dark gray. The dotted blue lines correspond to the simulated particle trajectory, while the green lines correspond to charged tracks reconstructed in the tracker [31].

### 980 The link algorithm

981 The link algorithm is the algorithm responsible for combining the particle flow elements from  
 982 different subdetectors. It can test any pair of elements in the event based on specific requirements  
 983 depending on the nature of the element, but is restricted to the nearest neighbors in the  $\eta - \phi$   
 984 plane. The outputs of the link algorithm are so-called *PF blocks* of linked elements, either directly  
 985 linked or linked through having common elements.

- 986 • **Inner track - calorimeter cluster link:** The track is interpolated from its last hit,  
 987 through the preshower layers, the ECAL and ending in the HCAL at an interaction length  
 988 depth of 1. A link is made if the track is within the cluster area, where the areas is enlarged  
 989 by up to a cell in each direction to account for detector gaps. In case several ECAL/HCAL  
 990 clusters are linked to the same track, only the one with the smallest distance in  $\eta - \phi$  is  
 991 kept.
- 992 • **Calorimeter cluster - cluster link:** A link between ECAL and HCAL clusters as well  
 993 as between ECAL and preshower clusters is made when the cluster position of the more  
 994 granular calorimeter is within the cluster envelope in the less granular calorimeter. Also  
 995 here, if there is link overlap, only the link with the smallest distance is kept

- 996     • **Inner tracker -muon chamber link:** As described in Section 3.2.1

997     For each PF block, the reconstruction proceeds in the following order. First, muons are  
 998     reconstructed and their corresponding PF elements removed from the PF block. Then the  
 999     electrons are reconstructed, with the hopes of removing their corresponding bremsstrahlung  
 1000    photons from the list of PF elements. Energetic photons are reconstructed in the same step.  
 1001    Finally, neutral and charged hadrons are reconstructed.

1002    **Muons**

1003    First, isolated global muons are selected by requiring the sum of track  $p_T$  and calorimeter energy  
 1004    deposits within a cone of  $\Delta R = 0.3$  not belonging to the muon track, to be smaller than 10  
 1005    % of the muon  $p_T$ . If the muons are non-isolated, they are required to pass the tight muon  
 1006    requirement [33] and have at least three matching track segments in the muon detector or have  
 1007    matched calorimeter deposits compatible with being a minimum ionizing particle. Muons failing  
 1008    both the requirements above are kept if the standalone muon track is of high quality and have a  
 1009    lot of hits in the muon detectors, otherwise they are discarded. The muon momentum is defined  
 1010    from the inner tracker measurement if the muon  $p_T$  is less than 200 GeV. Otherwise, its chosen  
 1011    according to the track fit with the smallest  $\chi^2$  probability.

1012  
 1013    Muons used in this thesis are required to pass an isolation requirement in order to suppress  
 1014    the background from QCD multijet events where jet constituents are identified as muons. For this,  
 1015    a cone of radius  $\Delta R = 0.3$  is constructed around the muon direction. The isolation parameter is  
 1016    defined as the scalar sum of the transverse momenta of all additional reconstructed tracks within  
 1017    the cone, divided by the muon  $p_T$ . Muon candidates with an isolation parameter less than 0.1  
 1018    are considered isolated and are used for further analysis.

1019    Further, the following selection criteria are applied:

- 1020     • The  $\chi^2$  of the global muon track fit must be less than 10  
 1021     • At least one muon-chamber hit is included in the global-muon track fit. The global muon  
 1022       track fit must include at least one muon chamber hit  
 1023     • Muon segments in at least two of the muon stations must be matched to the muon tracker  
 1024       track  
 1025     • The inner tracker track must be no more than 2 millimeters from the primary vertex in the  
 1026       xy plane and no more than 5 millimeters in the longitudinal direction  
 1027     • At least one hit in the pixel detector.

- 1028     • At least six layers of the inner tracker must contain hits.  
 1029     • At least three matching track segments must be found in the muon detectors

1030   **Electrons**

1031   The electrons are seeded from a GSF track, as described in Section 3.2.1. To differentiate electrons  
 1032   from charged hadrons, the energy deposit in the HCAL within a distance of 0.15 in the  $\eta - \phi$  plane  
 1033   of the supercluster , is required to be less than 10 % of that of the supercluster. The electron  
 1034   candidate must further pass a requirement on the output of a dedicated electron-identification  
 1035   BDT, using inputs such as track-cluster distance, track  $\chi^2$  and number of hits as input. In this  
 1036   step, isolated photons are also reconstructed, seeded from ECAL superclusters with  $|E_T > 10 \text{ GeV}$   
 1037   and no link to a GSF track. All the tracks and calorimeter deposits used to reconstruct electrons  
 1038   and isolated photons are further removed from the list of PF blocks.  
 1039   Only electrons passing certain quality requirements, corresponding to the CMS electron HEEP  
 1040   ID, are used in this thesis. These requirements are listed in Table 3.1, with the following variable  
 1041   definitions:

- 1042     •  $E_T$ : The supercluster energy  $x \sin(\theta_{track})$  where  $\theta_{track}$  is the electron track polar angle  
     measured in the inner tracker layer and extrapolated to the interaction vertex.
- 1043     •  $\eta^{sc}$ :  $\eta$  of the electron supercluster.
- 1044     • **isEcalDriven**: Electron is found through ECAL requirements rather than through Particle  
     Flow and the tracker.
- 1045     •  $\Delta\eta_{in}^{seed}$ :  $\eta$  difference between the track position measured in the inner layer, extrapolated  
     to the interaction vertex and to the calorimeter, and the  $\eta$  of the supercluster.
- 1046     •  $\Delta\phi_{in}$ :  $\phi$  difference between the track position measured in the inner layer, extrapolated to  
     the interaction vertex and to the calorimeter, and the  $\phi$  of the supercluster.
- 1047     • **H/E**: Ratio of hadronic energy in the calorimeter towers within a cone of radius 0.15 cen-  
     tered at the electrons calorimeter position, to the electromagnetic energy of the supercluster.
- 1048     •  $\sigma_{in\eta\eta}$ : Measure of the energy spread in  $\eta$  in units of crystals of electron energy in a  $5 \times 5$   
     block centered on the seed crystal.

- **ECAL Isolation:** The transverse electromagnetic energy of all reconstructed hits( with  $E > 0.08 \text{ GeV}$ ) in a cone of radius 0.3 centered at the electron calorimeter position, excluding those in an inner cone with a radius of 3 crystals and an  $\eta$  strip with a width of 3 crystals.
- **Hadronic Depth Isolation:** Defined as the transverse depth of the hadronic energy in the HCAL inside a cone of 0.3 centered on the electron calorimeter position, excluding towers in a cone of 0.15 radius.
- **Track  $p_T$  Isolation:** The sum  $p_T$  of the tracks in a  $\Delta R$  cone of 0.04 to 0.3, excluding an  $\eta$  region of 0.015.
- $d_{xy}$ : Transverse distance between the electron track and the primary vertex.

Variable	Barrel	Endcap
$E_T$	$> 35 \text{ GeV}$	$> 35 \text{ GeV}$
$\eta$ range	$ \eta_{sc}  < 1.4442$	$1.566 < \eta_{sc} < 2.5$
isEcalDriven	yes	yes
$\Delta\eta_{in}^{seed}$	$< 0.004$	$< 0.006$
$\Delta\phi_{in}$	$< 0.06$	$< 0.06$
H/E	$< 1/E + 0.05$	$< 5/E + 0.05$
full 5x5 $\sigma_{inj\eta}$	n/a	$< 0.03$
full 5x5 $E^{2x5}/E^{5x5}$	$> 0.94$ OR $E^{1x5}/E^{5x5} > 0.83$	n/a
EM+Had. Depth Iso.	$< 2 + 0.03 \times E_T + 0.28 \times \rho$	$E_T < 50 \text{ GeV}: < 2.5 + 0.28 \times \rho$ else: $< 2.5 + 0.03 \times (E_T - 50) + 0.28 \times \rho$
Track $p_T$ iso.	$E_T < 100 \text{ GeV} : < 5 + 1.5 \times \rho$ else: $< 5 + 1.5 \times \rho$	$< 5 + 0.5 \times \rho$
Inner Layer Lost Hits	$\leq 1$	$\leq 1$
$d_{xy}$	$< 0.02$	$< 0.05$

**Table 3.1:** Summary of the electron requirements allied to all electrons used in this analysis.

## Hadrons

Finally, after the removal of muons and electrons, the remaining hadrons and non-isolated photons are identified. HCAL clusters with no track link are defined as neutral hadrons, while ECAL clusters with no track link are defined as photons (photons are exclusively associated to the ECAL deposits as neutral hadrons leave only 3 % of their energy in the ECAL). The remaining HCAL clusters are then linked to one or more tracks from the inner tracker. In order to determine the particle content within a cluster, the sum of track momenta and the calorimeter energy is

1082 compared. If the calorimeter energy is compatible with the sum of track momenta, a particle for  
 1083 each track is inferred, with its corresponding energy taken from the track momentum. If the  
 1084 calorimeter energy is larger than the sum of track momenta, a photon or a neutral hadron is  
 1085 added, together with one charged hadron for each track within the cluster area.

### 1086 Missing transverse energy

1087 Neutrinos (and other predicted non-SM weakly interacting particles) do not interact in the  
 1088 detector and are instead inferred from the presence of a momentum imbalance in the detectors  
 1089 transverse plane. The missing transverse momentum is defined as the negative  $p_T$  vector sum of  
 1090 all reconstructed PF candidates in the event

$$\vec{p}_T^{\text{miss}} = - \sum_i^N \vec{p}_{T,i}. \quad (3.1)$$

1091 and its magnitude,  $|\vec{p}_T^{\text{miss}}|$ , is denoted the missing transverse energy  $E_T^{\text{miss}}$  (which is used as a  
 1092 proxy for the neutrino  $p_T$ ).

## 1093 3.3 Pile-up removal

1094 Particles originating from proton-proton interactions not associated with the hardest primary  
 1095 vertex, are denoted pileup events. These distorts observables of interest from the hard scattering  
 1096 event and must be mitigated through dedicated pileup removal techniques

### 1097 3.3.1 Charged Hadron Subtraction

1098 As mentioned previously, primary vertices are reconstructed using tracks from charged hadrons.  
 1099 If a primary vertex does not correspond to the hard scattering vertex of the event, the charged  
 1100 hadrons (as reconstructed through Particle Flow) associated to this vertex (called pileup vertex)  
 1101 are removed from the event collection of particles and will not participate in any further object  
 1102 reconstruction. This method is denoted charged hadron subtraction (CHS).

### 1103 3.3.2 Pile up per particle identification (PUPPI)

1104 CHS was the default pileup removal algorithm in CMS until very recently. In 2014, a new pileup  
 1105 removal algorithm with improved performance was proposed; the pileup per particle identification  
 1106 (PUPPI) [34] algorithm. PUPPI uses a combination of local shape information, event pileup

properties and tracking information to compute a weight describing the degree of “pileup-likeness” of a given particle. First, a variable denoted  $\alpha$  is computed based on the difference between soft radiation coming from pileup and the harder collinear QCD pattern. The shape of  $\alpha$  for charged particles is then used as a proxy for all pileup particles and is used on an event-by-event basis to calculate a weight for each particle. This weight in turn describes the degree to which particles are pileup-like and are used to rescale the particle four-momenta.

The shape variable for a given particle  $i$  is defined as

$$\alpha_i = \log \sum_{\substack{j \in \text{Ch,PV} \\ j \neq i}} \left( \frac{p_{T,j}}{\Delta R_{ij}} \right)^2 \Theta(R_0 - \Delta R_{ij}), \quad (3.2)$$

where  $\Theta$  is the step function and  $j$  refers to the neighboring charged particles from the primary vertex within a cone of radius  $R_0 = 0.4$ . Charged particles are defined as coming from the primary vertex if they are associated to the leading vertex of the event or are within a distance of  $d_z < 0.3$  cm from the leading vertex.

In order to determine the probability that a particle comes from pileup, a  $\chi^2$  calculation is performed. The probability is defined as

$$\chi_i^2 = \frac{(\alpha_i - \bar{\alpha}_{PU})^2}{RMS_{PU}^2}, \quad (3.3)$$

where  $\bar{\alpha}_{PU}$  is the median value of the  $\alpha_i$  distribution for pileup particles in the given event and  $RMS_{PU}$  is its RMS.

Each particle (neutral and charged) is then assigned a weight  $w_i = F_{\chi^2, NDF=1}(\chi_i^2)$ , where  $F_{\chi^2, NDF=1}$  is the cumulative distribution function of the  $\chi^2$  distribution with one degree of freedom. Particles with  $w_i < 0.01$  are rejected. In addition, a cut on the weighted  $p_T$  of neutral particles of  $w_i \cdot p_{T,i} > (A + B \cdot N_{PV})$  GeV is applied, where  $N_{PV}$  correspond to the number of reconstructed vertices in the event and A and B are tunable parameters.

The performance of the PUPPI algorithm compared to CHS for jet observables is shown in Figure 3.4.

The top row shows the absolute mass resolution (left) as well as the mass resolution as a function of  $N_{PV}$  for CHS jets (red) and PUPPI (pink) jets. The bottom row shows the corresponding quantities but for jet transverse momentum. A significantly better resolution on jet observables can be achieved using PUPPI compared to CHS.

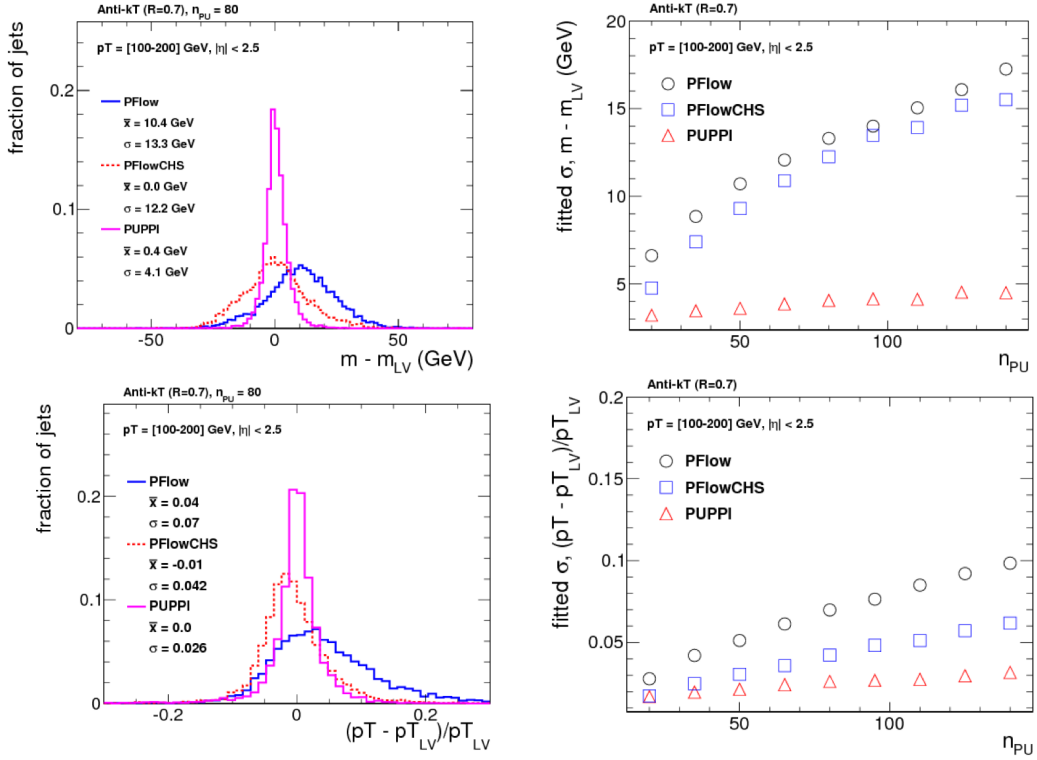


**Figure 3.4:** The mass (top) and  $p_T$  (bottom) resolution comparing PF only (blue), PF+CHS (red) and PUPPI (pink) jets. The absolute resolution (left) as well as the resolution as a function of the number of reconstructed primary vertices in the event (right) is shown [34].

## 1133 3.4 Jet reconstruction

1134 As explained in Section 1.1.2, quarks and gluons are never themselves visible in a detector. Within  
 1135  $10^{-23}$  seconds, the timescale of the strong interactions, they fragment and hadronize into a  
 1136 collimated spray of hadrons, a so-called jet. In order to infer the properties of the original parton  
 1137 generating the jet, the properties of the full particle spray needs to be evaluated. Combining  
 1138 these particles algorithmically is non-trivial, and several algorithms designed to do, called jet  
 1139 clustering algorithms, exist. These provide a set of rules for grouping particles together into jets  
 1140 and are usually based on certain distance requirements between particles as well as rules for how  
 1141 to recombine their momenta. Thanks to Particle Flow, objects like charged hadrons, neutral  
 1142 hadrons and photons together with their estimated energy and direction are already defined, and  
 1143 jet clustering in CMS therefore consists of associating these particles to one common origin.

### **3.4.1 Jet clustering**

The most common jet clustering algorithms used in hadron colliders are the Cambridge/Aachen algorithm [35], the  $k_T$  algorithm [36] and the anti- $k_T$  algorithm [37]. These are all sequential recombination algorithms, meaning they systematically go through each particle pair in the event and recombines them into one particle if the combination satisfies certain criteria. The rules, shared by all three algorithms, are as follows:

1. For each pair of particles  $i$  and  $j$ , compute the longitudinally invariant distances

$$d_{ij} = \min(p_{ti}^{2p}, p_{tj}^{2p}) \frac{\Delta R_{ij}^2}{R^2}, \text{ with } \Delta R_{ij}^2 = (\eta_i - \eta_j)^2 + (\phi_i - \phi_j)^2 \quad (3.4)$$

$$d_{iB} = p_{ti}^{2p}, \quad (3.5)$$

where  $d_{ij}$  is a measure of the relative transverse momenta between the particles,  $\Delta R_{ij}^2$  is the distance between them in the  $\eta - \phi$  plane (which can be roughly translated into a jet radius),  $\Delta R^2$  corresponds to a distance parameter which controls the extension of the jet and  $d_{iB}$  is the distance between the particle and the beam. The parameter  $p$  is what separates the three algorithms from one another and controls the relative power of energy versus geometrical scales. For the anti- $k_T$  algorithm, it is defined as  $p = -1$ , for the  $k_T$  algorithm  $p = 1$  and in the case of the C/A algorithm,  $p = 0$ . The consequences of these choices are explained in detail below.

2. Find the minimum distance of  $d_{ij}$  and  $d_{iB}$ .
3. If this is  $d_{ij}$ , recombine particles  $i$  and  $j$  and return to step 1.
4. If it is  $d_{iB}$ , the particle is defined to be a final state jet, and is removed from the list of particles. The algorithm proceeds back to step 1.
5. Repeat until no particles remain.

### **Infrared and collinear safety**

There are two requirements that are extremely important when defining jet algorithms: They must be 1) *infrared* (IR) and 2) *collinear* (C) safe. *Infrared* safety corresponds to the requirement that if the final state particles are modified by the presence of a soft emission, and there are always soft emission in QCD events (both perturbative and non-perturbative), then the set of hard jets should remain unchanged. This is illustrated by the two left figures in Figure 3.5.

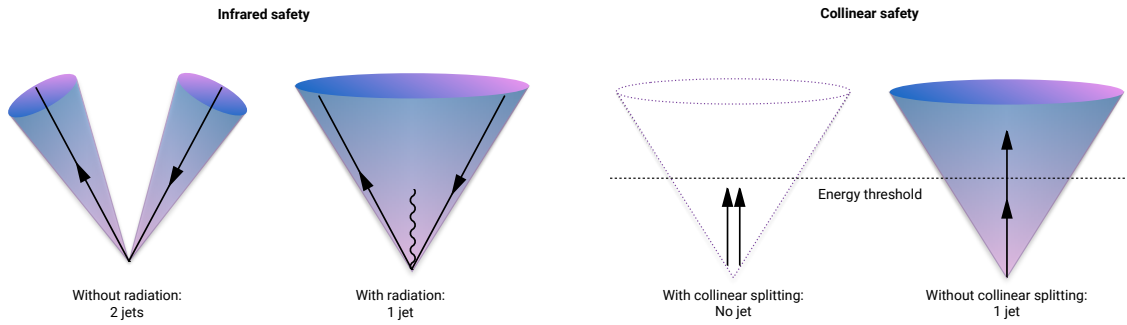


**Figure 3.5:** An illustration of what would happen for an infrared (left) and collinear (right) unsafe jet algorithm. If an algorithm is infrared unsafe, the presence of a soft emission changes the jet configuration. If an algorithm is collinear unsafe, then if a parton undergoes a collinear splitting this will change the configuration of the jet

1169 Here, the algorithm is infrared unsafe: the presence of an additional soft gluon changes the  
 1170 jet configuration from 2 to 1 jets. If an algorithm is *collinear* unsafe, it means that the jet  
 1171 configuration would change if the hard parton undergoes collinear splitting (which a hard parton  
 1172 often does as part of the fragmentation process and which are also part of non-perturbative  
 1173 dynamics, like the decay of highly energetic hadrons). This is shown in the two left figures of  
 1174 Figure 3.5, where a hard parton undergoing collinear splitting fails to be reconstructed due to its  
 1175 daughters being below the energy threshold of the algorithm.

1176 All sequential recombination algorithms are trivially infrared safe.

### 1177 The $k_T$ algorithm

1178 The  $k_T$  algorithm is the oldest of the sequential recombination algorithms and, due to its  $p = 1$   
 1179 definition in the distance measures, follows the QCD branching structure in both  $p_T$  and in angle  
 1180 (in reverse). Soft particles are clustered together first, and the final step is the clustering of  
 1181 the two hardest particles. A consequence of this definition is that there is nothing that keeps  
 1182 arbitrarily soft particles from being defined as jets, and a minimum cut on the jet  $p_T$  should be  
 1183 introduced. Despite several favorable qualities, the  $k_T$  algorithm is not the algorithm of choice in  
 1184 most hadron collider experiments due to the irregular jets it produces, a consequence of clustering  
 1185 soft particles first.

### 1186 The Cambridge/Aachen algorithm

1187 The Cambridge/Aachen algorithm, with  $p = 0$  in the distance measures, follows the QCD  
 1188 branching structure only in angle as the clustering order is based solely on spatial separation.

1189 The simplest of the algorithms, it recombines all pairs close in  $\Delta R$  until  $\Delta R_{ij} > R$ . The benefits  
1190 of this is that the clustering history contains information about the presence of any geometrical  
1191 substructure within a jet, a feature that will become important in Section 3.5.

### 1192 The anti- $k_T$ algorithm

1193 The default jet clustering algorithm in CMS is the anti- $k_T$  algorithm [37], which follows the  
1194 rules and distance measures above with  $p = -1$ . The algorithm favors the clustering of high- $p_T$ -  
1195 high- $p_T$  and high- $p_T$  – low- $p_T$  particles first, disfavoring clustering between soft particles. That  
1196 means the algorithm grows around a hard core, yielding jets with a well-defined cone shaped area.  
1197 Together with being IRC-safe and insensitive to the underlying event (any event not arising the  
1198 primary hard scattering process) and pileup, makes it the main jet algorithm in CMS.

1199 A comparison of the resulting jet area in the  $\phi - \eta$  plane after clustering with either  $k_T$ , C/A  
1200 and anti- $k_T$ , is shown in Figure 3.6. The z-axis correspond to the parton  $p_T$ . One can clearly see  
1201 that when clustering with the anti- $k_T$  algorithm, the produced jets are circular, with a radius set  
1202 by  $R$ , around the hardest parton.

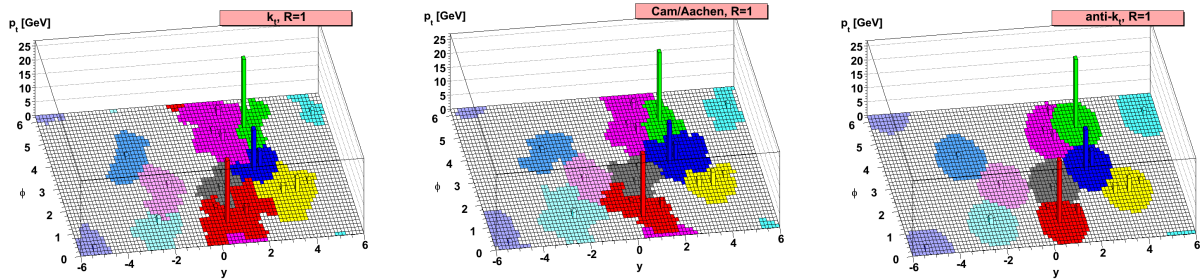


**Figure 3.6:** A comparison of the resulting jet cone area in the  $\phi - \eta - p_T$  plane after clustering the same event with three different jet algorithms:  $k_T$ , C/A and anti- $k_T$ . [37]

### 1203 3.4.2 PF jets in CMS

1204 Jet algorithms in CMS mainly use PF candidate four-vectors as input and a pileup removal  
1205 algorithm is usually applied before clustering occurs. If using CHS (Section 3.3.1), charged  
1206 hadrons not associated to the primary vertex are discarded before clustering. If PUPPI is  
1207 used (Section 3.3.2), all the PF candidates are reweighted based on how likely they are to have  
1208 originated from pileup. For the anti- $k_T$  algorithm, CMS by default uses two jet cone sizes:  $R=0.4$   
1209 and  $R=0.8$ . Jets with  $R=0.4$ , called PFAK4, are used for single-prong jets while the larger  $R=0.8$

1210 jets, PFAK8, are more often used when looking for jets containing multiple hard quarks/gluons  
1211 in order to contain all the hadronization products.

1212 These jets are further required to pass certain jet identification requirements provided by the  
1213 JetMET POG [38], in order to distinguish them from fake jets. All jets used in this analysis are  
1214 required to pass the *tight ID* requirements which are as follows:

- 1215 • The jet must contain at least two PF constituents
- 1216 • At least one of these constituents must be a charged hadron
- 1217 • The fraction of jet energy coming from neutral hadrons must be  $< 0.90$
- 1218 • The fraction of jet energy coming from neutral electromagnetic energy must be  $< 0.90$
- 1219 • The fraction of jet energy coming from charged electromagnetic energy must be  $< 0.99$

### 1220 3.4.3 Jet energy corrections

1221 All jets are further corrected for nonlinearities in  $p_T$  and rapidity using standard CMS jet energy  
1222 corrections (JEC), as described in Ref. [39]. These are intended to bring the measured jet energy  
1223 closer to the true jet energy by correcting the jet energy scale (JES) and jet energy resolution  
1224 (JER). The energy corrections are derived in three steps:

- 1225 • L1: Energy offset corrections intended to remove pileup and electronic noise, both for data  
1226 and simulation
- 1227 • L2L3: A relative (L2) and absolute (L3) correction to particle level jet response for  
1228 simulation only
- 1229 • Residual: A correction for data only meant to correct for residual differences between data  
1230 and simulation

1231 These are illustrated in Figure 3.7.

#### 1232 L1 offset correction

1233 The largest correction is the L1 pileup offset correction, which are meant to subtract the additional  
1234 energy in a jet due to pileup. This is done on an event-by-event basis through the *jet area method*  
1235 which uses the jet effective area multiplied by the average event energy density to calculate the  
1236 size of the offset energy to be subtracted from each jet. An additional  $p_T$ - and  $\eta$ -dependent term

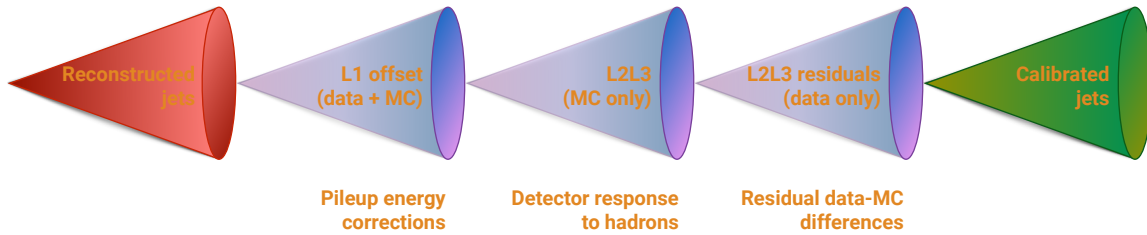


**Figure 3.7:** The CMS jet energy corrections are derived in three steps: A correction due to offset energy coming from pileup, applied to data and MC, a correction due to the particle level jet response, also applied to data and MC and finally a correction to account for residual differences between data and MC.

is added in order to account for different pileup densities in different parts of the detector and for different jet energies. For data, an additional scalefactor to account for data and simulation differences is computed. This is done by constructing a *Random Cone* (*RC*) centered at a given  $\eta, \phi$  and dividing the energy density within that cone in data, evaluated in a dataset with no hard interactions (*Zero Bias*), by that of the true energy offset in simulation

### 1242 L2 relative and L3 absolute corrections

After L1 corrections are applied, corrections to account for the detector response to hadrons are derived based on the true detector response in QCD MC. The simulated particle response is defined as the ratio

$$R_{\text{particle}} = \frac{p_{\text{T, reco}}}{p_{\text{T, particle}}} \quad (3.6)$$

These are derived in bins of particle level  $p_{\text{T}}$  and reconstructed  $\eta$ : The L2 relative corrections are intended to uniform the detector response and are derived as a function of  $\eta$ , while the L3 absolute corrections are derived as a function of jet  $p_{\text{T}}$ . These corrections are applied both to data and to MC.

### 1250 Residual data corrections

After L1 and L2L3 corrections are applied, two additional corrections are derived for data only in order to account for any residual discrepancies between data and MC. This is done by looking at the transverse momentum balance between a jet which is to be calibrated, and some reference object (either another jet, a Z boson or a photon). If the jet energy scale is not equal to one, a  $p_{\text{T}}$  imbalance will be visible. The measurements are performed in a data dijet sample, where the

statistical uncertainty is small but the energy of the reference object poorly measured, as well as in  $Z(\mu\mu) + \text{jet}$ ,  $Z(ee) + \text{jet}$  and  $\gamma + \text{jet}$  samples, where the energy of the  $Z$  and  $\gamma$  is very well known but the statistics are small.

The “L2 relative” residual correction is measured in dijet events by comparing the measured  $p_T$  of the reference jet, required to be central with  $\eta < 1.3$ , to that of the calibration jet, with an unconstrained  $\eta$ . This is done as a function of jet  $\eta$ , in bins of average jet  $p_T$ . The “L3 relative” residual correction, is instead measured in  $W/\gamma + \text{jet}$  events by comparing the measured jet  $p_T$  to the  $p_T$  of the precisely measured  $Z/\gamma$ , as a function of jet  $p_T$ . The response,

$$R_{\text{jet}, p_T} = \frac{p_{T,\text{jet}}}{p_{T,\text{ref}}}$$

is then evaluated in data and in simulation. The ratio of the two,  $R_{\text{data}}/R_{\text{MC}}$ , defines the residual corrections.

1253

1254

1255 The above description of jet energy corrections in CMS is meant as a rough, instructive  
1256 summary only. A full description of the measurement techniques used in CMS, can be found  
1257 in [39].

### 1258 3.5 Jet substructure reconstruction

1259 In analyses looking for highly energetic (“boosted”) vector bosons like, a main theme of this  
1260 thesis, the opening angle between the vector boson quark decay products become so small that  
1261 the highly boosted boson appears as a single large jet instead of two well-separated smaller jets.  
1262 The distance between the two quarks, in the case of an hadronic decay, depends on the mass of  
1263 the vector boson and its  $p_T$  and goes as

$$\Delta R = \frac{2M_V}{p_{T,V}}. \quad (3.7)$$

1264 Above a  $W$  boson  $p_T$  of 200 GeV, the two quarks are therefore merged into a single large cone jet  
1265 of size  $R = 0.8$ . A sketch of the two different situation is shown in Figure 3.8. If the  $W$   $p_T$  is well  
1266 below 200 GeV, its decay products are well-defined jets in their own right (left). However, once  
1267 the  $W$  transverse momenta starts exceeding 200 GeV, both the quarks are completely contained  
1268 within a single jet (right). In order to distinguish hadronically decaying vector boson from QCD  
1269 quark/gluon jets, the jet mass would in principle be a good discriminant as we know the  $W$  has a

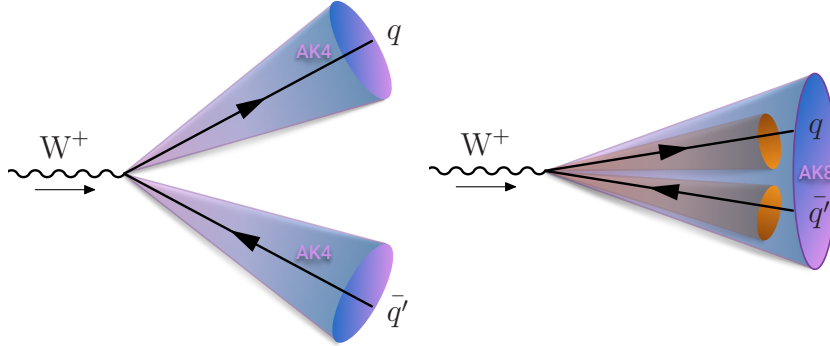


**Figure 3.8:** If the mass of the resonance is low enough, the quark decay products of each vector boson are well separated and clustered into distinguishable AK4 jets (left). If the transverse momentum of the vector boson is greater than 200 GeV, the vector boson decay products are merged into one single large cone AK8 jet.

mass of around 80 GeV while the quark/gluon mass is close to zero. At very high transverse momenta, however, the width (and therefore the mass) of QCD jets may become equally large. In addition, diffuse radiation caused by the Underlying Event and pileup give rise to a significant number of additional particles in the event contributing to the total jet mass. Therefore, being able to accurately and efficiently separate highly boosted QCD jets from highly boosted vector bosons, requires other methods. In order to get rid of UE and pileup, algorithms like PUPPI and CHS can be used. Then, to improve the mass resolution further, dedicated grooming algorithms must be applied.

### 3.5.1 Grooming

Grooming was introduced as a tool to improve the signal, most often  $W/Z/\gamma$ , mass resolution without significantly changing the background and signal event numbers. It consists of removing the softest parts of a jet in order to resolve its “true” mass, by means of reclustering and identifying soft particles within the jet which then are removed.

### Trimming

The trimming algorithm [40] is a grooming algorithm mostly used at trigger level in CMS (also where it is used in this thesis) due to it being less aggressive than other grooming algorithms. It works in the following way: Starting from a large jet clustered with either anti- $k_T$  or C/A (in the case of CMS), it reclusters the jet using the  $k_T$  algorithm in order to create subjets of some size  $R_{sub}$ . It then proceeds to check whether each subjet has a momentum fraction above a certain

threshold,

$$p_{T,i}/p_{T,jet} > p_{T,frac}.$$

- If the subjet fails this requirement, it is removed. The remaining subjets are then assembled into a new “trimmed” jet. The effect of trimming on real W jets and QCD quark/gluon jets for different values of  $r_{sub}$  and  $p_{T,frac}$  is shown in Figure 3.9. The best signal mass resolution is obtained with  $r_{sub} = 0.2$  and  $p_{T,frac} = 0.03$ , which is also the parameter setting that provides the best signal and background discrimination by pushing the QCD jet mass closer to zero. These are the default values of the tuned parameters of the trimming algorithm in CMS ( $r_{sub} = 0.2$  and  $p_{T,frac} = 0.03$ ).

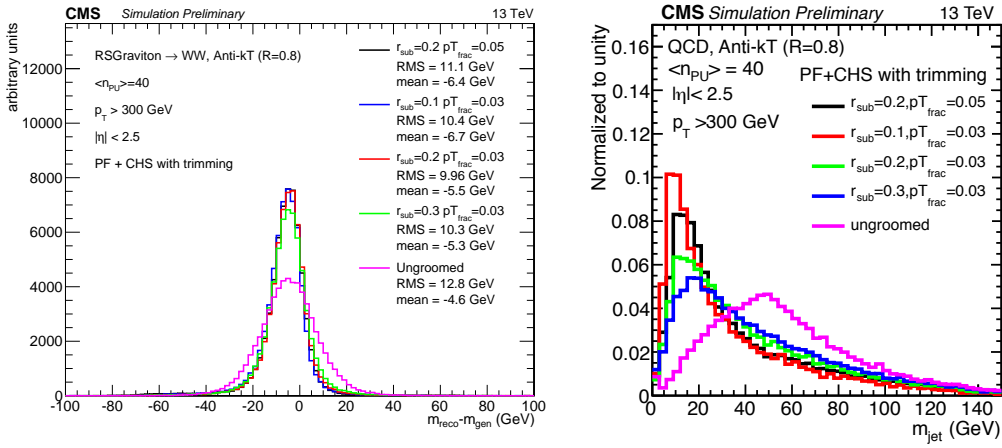


**Figure 3.9:** The effect of trimming on a signal jet (left) and a background jet (right) for different values of the tuned parameters  $r_{sub}$  and  $p_{T,frac}$  [41].

1290

## 1291 Pruning

The pruning algorithm, in addition to removing soft particles, has an additional requirement on the distance between any recombination that are at wide angle. It proceeds by reclustering the jet with the C/A algorithm, requiring at each step that

$$\frac{\min(p_{T,i}, p_{T,j})}{p_{T,P}} > z_{cut} \quad \text{and} \quad \Delta R_{i,j} < D_{cut} = \frac{2r_{cut}m_{jet}}{p_T}.$$

- The first requirement is a requirement on the hardness of the combination.  $p_{T,i}$  and  $p_{T,j}$  correspond to the transverse momenta of each protojet (single particle or group of particles already combined in a previous step) and  $p_{T,P}$  is the combined  $p_T$  of the two. The protojet with the lowest transverse momenta is removed if its hardness is below  $z_{cut}$ , or if it forms an angle

wider than  $D_{cut}$  relative to the axis of the recombination of the two protojets. In CMS, the tuned parameters are set to  $r_{cut} = 0.5$  and where  $z_{cut} = 0.1$ . Figure 3.10 shows the ungroomed as well as the pruned jet mass distribution for signal (left) and background jets. The highest amount of signal and background separation in CMS, is achieved with  $r_{cut} = 0.5$  and  $z_{cut} = 0.1$ .

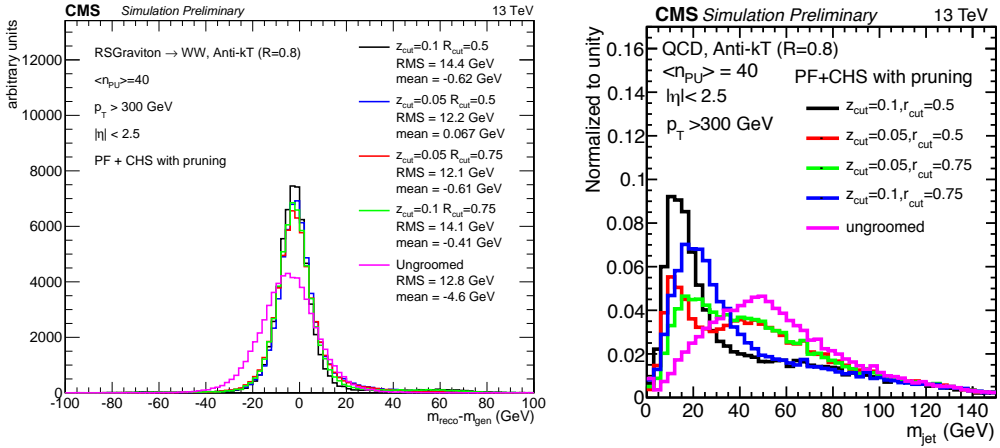


**Figure 3.10:** The effect of pruning on a signal jet (left) and a background jet (right) for different values of the tuned parameters  $z_{cut}$  and  $r_{cut}$  [41].

1299

### 1300 Modified Mass Drop Tagger and Soft Drop

The modified mass drop tagger (mMDT) [42] (a modified version of the originally suggested mass drop tagger [43]) is based on the idea that a W/Z jet is formed by two quark subjets and that, therefore, the mass of each subjet is much smaller than their combined mass (and much smaller than the mass of the boson itself). A QCD jet is, on the other hand, formed by continuous soft radiation, meaning that its heaviest subjet should be close to the mass of the jet itself. The mMDT tagger therefore starts from an already clustered jet, reclusters it with the C/A algorithm and then declusters it again defining subjets  $s_1$  and  $s_2$ . It then looks for a significant mass drop going from total jet mass to the mass of each subjet, and checks that the splitting is not too asymmetric. The modified mass drop condition is generalized through the soft drop declustering method [44], simply called Soft Drop, which allows for different types of angular requirements to enter the condition. The Soft Drop condition is the following

$$\frac{\min(p_{T,1}, p_{T,2})}{p_{T,1} + p_{T,2}} > z_{cut} \frac{\Delta R_{12}^\beta}{R_0}.$$

If no significant mass drop occurred and the splitting is not to asymmetric, the condition is met and the full jet is deemed the softdrop jet. Otherwise only the highest- $p_T$  subjet is kept and the declustering continues. If the jet can not be declustered any further, it can either be removed from consideration, so-called “tagging”-mode, or deemed the final soft-dropped jet, “grooming”-mode. A  $\beta = 0$  corresponds to the modified mass drop tagger and removes all soft emission from the jet. For  $\beta > 0$ , soft radiation is removed, but some fraction of soft-collinear radiation is kept. Lastly, with  $\beta < 0$ , Soft Drop can remove soft as well as collinear radiation. The performance of Soft Drop on W jets and QCD quark/gluon jets for different values of  $\beta$  is shown in Figure 3.11. The modified mass drop tagger (Softdrop with  $\beta=0$ ) with  $z_{cut} = 0.1$  is the default Soft Drop settings in CMS, due to it providing the best signal/background discrimination while maintaining an excellent signal mass resolution.

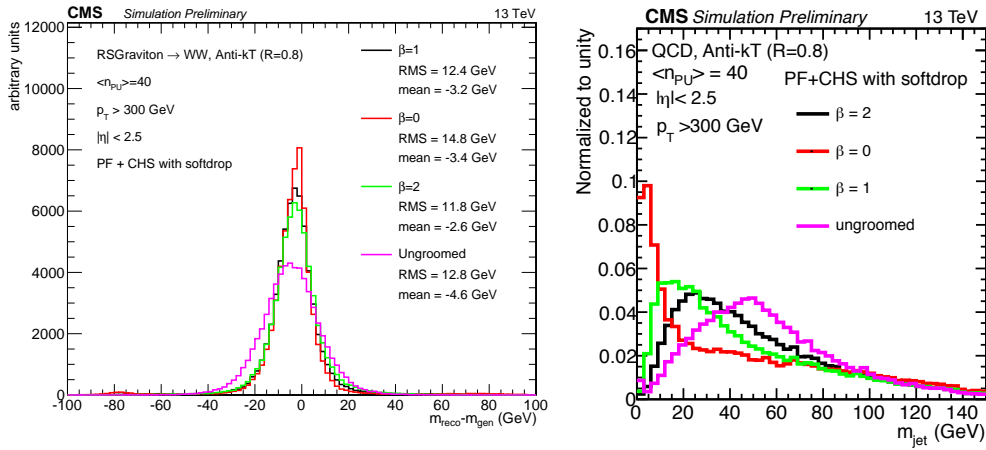


**Figure 3.11:** The effect of softdrop on a signal jet (left) and a background jet (right) for different values of the tuned parameters  $\beta$ .  $\beta = 0$  corresponds to the Modified Mass Drop Tagger, which is the default Softdrop setting in CMS [41].

### 3.5.2 N-subjettiness

After hopefully having resolved the particle mass with one of the grooming algorithms above, there is still discriminating information to be gathered from the jet structure itself. A W or Z jet consists of two well-defined high- $p_T$  subjets. A quark/gluon jet on the other hand, made from a single parton, consists of several large angle, asymmetric splittings, as illustrated in Figure 3.12. The N-subjettiness algorithm [45] takes advantage of this fact by attempting to count the number of hard subelements within a jet. This is quantified through the n-subjettiness variable,  $\tau_N$ ,

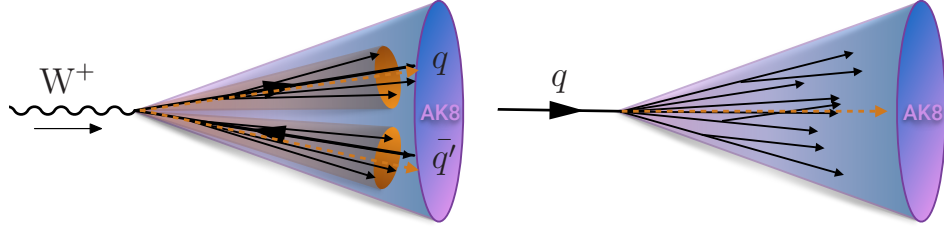


**Figure 3.12:** A jet stemming from the decay of a  $W$  will usually have two well-separated high- $p_T$  subjets, while a jet with a single-prong origin consists of several large angle splittings.

1319 defined as

$$\tau_N = \frac{1}{d_0} \sum_k p_{T,k} \min(\Delta R_{1,k}, \Delta R_{2,k}, \dots, \Delta R_{N,k}) \quad (3.8)$$

1320 where  $k$  runs over all the jet constituents,  $p_{T,k}$  is the constituent transverse momentum and  
1321  $\Delta R_{i,k}$  is the distance between the constituent and candidate subjet axes. These subjet axes are  
1322 obtained through a one-pass optimization procedure which minimizes N-subjettiness [46]. The  
1323 normalization factor in front is given as

$$d_0 = \sum_k p_{T,k} R_0 \quad (3.9)$$

1324 where  $R_0$  corresponds to the cone size of the initial jet. With this definition, jets with  $\tau_N = 0$   
1325 have most of its constituents aligned along the subjet axes. However, if  $\tau_N \gg 0$ , a large fraction  
1326 of the energy is radiated away from the subjet directions and are more likely to have more  
1327 than  $N$  subjets. In CMS, and as recommended by the authors in [45], the ratio  $\tau_2/\tau_1$  is used to  
1328 discriminate  $W$  jets from QCD jets. The reason for this is that, while signal jets are expected  
1329 to have a large  $\tau_1$ , quark/gluon can similarly have large  $\tau_1$  due to the diffuse radiation present.  
1330 However, QCD jets with a large  $\tau_1$  tend to have an equally large  $\tau_2$ , while signal jets do not, hence  
1331 the ratio of the two provides greater separation power. In CMS, the n-subjettiness algorithm is  
1332 by default applied to ungroomed jets. The distribution of  $\tau_{21}$  for signal and background jets with  
1333 different pileup subtraction algorithms applied are shown in Figure 3.13, where  $\tau_{21}$  in combination  
1334 with PF+PUPPI (green) yields a distribution most similar to the generated one (black).

### 1335 3.5.3 Vector boson tagging

1336 In order to discriminate  $W$  and  $Z$  bosons from quark/gluon jets a combination of a groomer and  
1337 shape-tagger (like n-subjettiness) is usually used. Typical values for a  $W$ -tagger are jet groomed

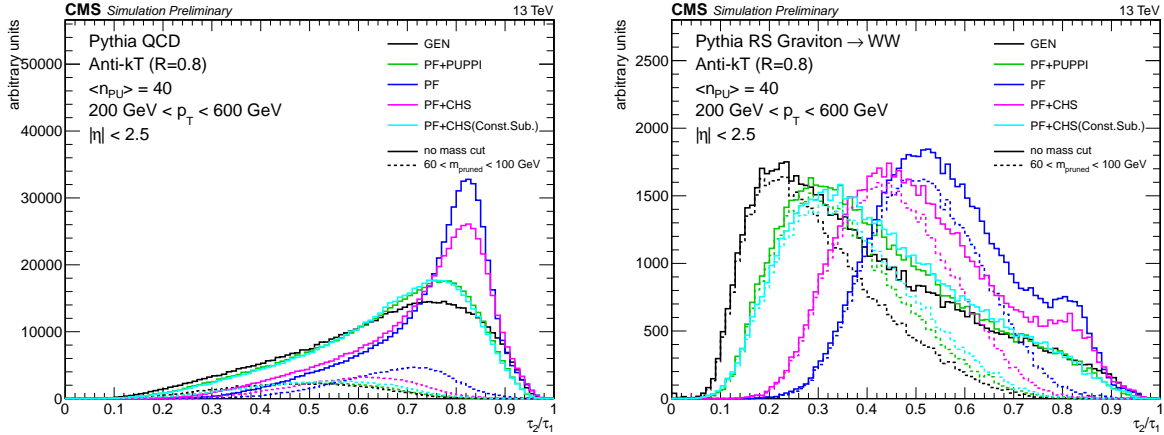


**Figure 3.13:** The distribution of the n-subjettiness ratio  $\tau_{21}$  for signal jets (left) and background jets (right) with different combinations of pileup subtraction algorithms applied. The solid lines corresponds to the  $\tau_{21}$  distribution with no mass cut applied, while the dotted lines are within a mass window of 60–100 GeV [41].

mass between 60 and 100 GeV and  $\tau_{21} < 0.5$ . Which combination and which cuts to use is analysis dependent, and have been optimized for each search presented in this thesis. The details are thoroughly explained in each section.

### 1341 Polarization effects

The vector boson polarization has a significant effect on the W-tagging efficiency. The helicity angle  $\theta$ , defined as the angle between the outgoing quark daughters of the W in the W bosons rest frame relative to its direction of motion [47], is very different for longitudinally polarized vector bosons,  $W_L$ , and transversally polarized vector bosons  $W_T$  [48]. Figure 3.14 shows the  $\cos \theta^*$  distribution for the outgoing quarks from a  $W_L \rightarrow q\bar{q}$  (black) and  $W_T \rightarrow q\bar{q}$  (red) decay, and it can be observed that transversely polarized W bosons decay with the quarks emitted closer to the vector boson direction of motion. The consequence of this, is that there is a higher asymmetry in the transverse momenta of the two quarks from a  $W_T$  decay. This in turn makes grooming algorithms, designed to remove soft constituents of a jet, tend to reject particles coming from the softer quark, resulting in a lower jet mass and a drop in tagging efficiency. Figure 3.15 shows the W-jet tagging efficiency versus q/g jet mistagging rate for a selection on the jet pruned mass of  $60 \text{ GeV} < m_{\text{pruned}} < 100 \text{ GeV}$ , scanning  $\tau_{21}$  cuts (here for CA R=0.8 jets).

The tagging efficiency for transversely polarized W bosons (green) is significantly lower than the tagging efficiency for longitudinally polarized bosons (red). This can be explained by looking

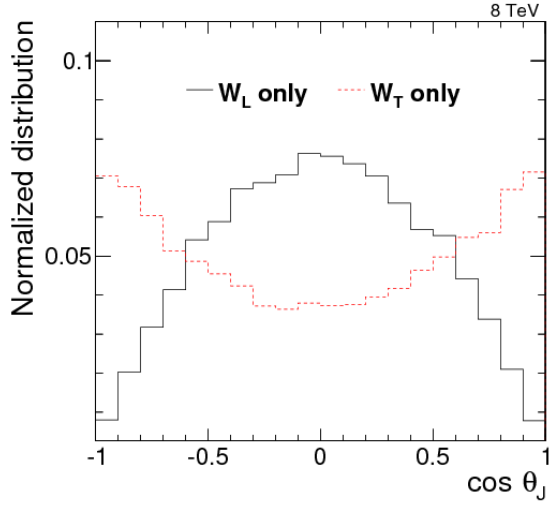


**Figure 3.14:** The helicity angle for generated quarks from  $W_L \rightarrow q\bar{q}$  (black) and  $W_T \rightarrow q\bar{q}$  (red) decays [48].

at the  $\cos \theta^*$  distribution on reconstructed level, using the C/A subjets, with a cut on the jet pruned mass of  $60 \text{ GeV} < m_{\text{pruned}} < 100 \text{ GeV}$ , shown in Figure 3.16. When comparing to the distribution at generator level with no groomed mass window applied, Figure 3.14, one can see that the  $W_T$  jets with  $\cos \theta^* \approx 1$  are completely removed.

This is due to two effects: the  $p_T$ -asymmetry explained above and the fact that the  $\Delta R$  distribution between the two quarks is much smaller in the case of  $W_L$ , making them more likely to be fully contained within a jet cone of  $R=0.8$ .

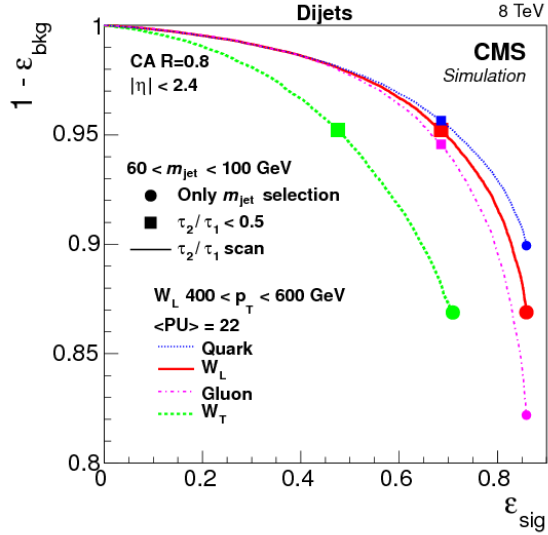


**Figure 3.15:** The helicity angle for generated quarks from  $W_L \rightarrow q\bar{q}$  (black) and  $W_T \rightarrow q\bar{q}$  (red) decays [48].

## 1363 3.6 Monte Carlo Event Generators

1364 Monte Carlo event generators offer a realistic estimate of high-energy collisions on an event-  
 1365 by-event basis, allowing us to estimate signal and background processes accurately. Simulated  
 1366 events are usually produced in three steps, describing a process from very short timescales up  
 1367 until hadronization and decay. First, a matrix element generator simulates the hard scattering  
 1368 process and subsequent decays. Secondly, the showering and hadronization of unstable particles  
 1369 is performed and, lastly, the final state particles are passed through a full detector simulation in  
 1370 order to reproduce a range of experimental effects.

1371 General-purpose Monte Carlo (GPMC) generators, like HERWIG ++ [49] and PYTHIA 8 [50],  
 1372 deal with both perturbative as well as hadronization phenomena, simulating an event all the  
 1373 way up until detector simulation. In HERWIG ++ and PYTHIA 8, the hardest processes are only  
 1374 simulated at the lowest order of perturbative expansion, meaning  $2 \rightarrow 2$  or  $2 \rightarrow 3$  scatterings. In  
 1375 order to have tree-level matrix elements with an arbitrary final-state multiplicity, they can be  
 1376 combined with programs used to generate parton-level events at higher accuracy, which are then  
 1377 processed through showering and hadronization with the GPMC generators. One popular program  
 1378 for generating matrix elements is MADGRAPH [51]. This, however, still correspond to a tree-level  
 1379 (leading order) approach. To go to next-to-leading-order (NLO), meaning the inclusion of virtual  
 1380 corrections, two methods exist: MC@NLO [52, 53] and POWHEG [54]. These combine the full

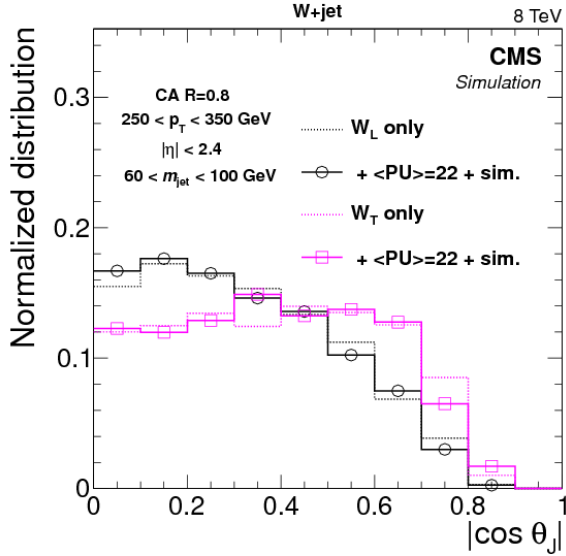


**Figure 3.16:** The helicity angle for subjets from  $W_L \rightarrow q\bar{q}$  (black) and  $W_T \rightarrow q\bar{q}$  (pink) decays. [48].

1381 next-to-leading-order prediction for inclusive processes with the subsequent parton showers, either  
 1382 by a subtraction method regularizing the real contributions, or by a matrix-element correction  
 1383 of the parton shower branching probability. After hadronization, all final state particles are  
 1384 passed through a full simulation of the CMS detector. This is done with GEANT4 [55], where  
 1385 experimental effects like object reconstruction and detector resolution are accounted for.

1386 For the work presented in this thesis, simulated samples of the Standard Model background  
 1387 processes are used to optimize the analysis and in some cases provide flexible background templates.  
 1388 QCD multijet production is simulated with four generator configurations: 1. PYTHIA standalone,  
 1389 2. the LO mode of MADGRAPH matched with PYTHIA, 3. POWHEG matched with PYTHIA and 4.  
 1390 HERWIG++ 2.7.1 with tune CUETHS1 [56]. Top quark pair production is modeled with POWHEG  
 1391 and showered with PYTHIA unless otherwise stated.  $W+jets$  and  $Z+jets$  production are simulated  
 1392 with the leading-order (LO) mode of MADGRAPH matched with PYTHIA. Signal samples are  
 1393 generated with standalone PYTHIA.

1394 All samples are processed through a GEANT4-based simulation of the CMS detector. To  
 1395 simulate the effect of additional proton-proton collisions within the same or adjacent bunch  
 1396 crossings (pileup), additional inelastic events are generated using PYTHIA and superimposed  
 1397 on the hard-scattering events. The MC simulated events are finally weighted to reproduce the  
 1398 distribution of the number of pileup interactions observed in data.



---

1399

## CHAPTER 4

---

1400

### Diboson resonance searches in CMS

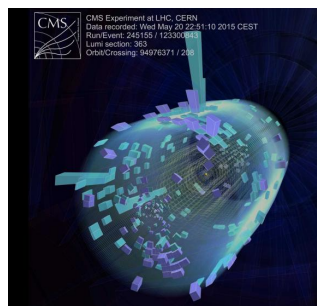
## 1401 4.1 Search I: First search for diboson resonances at 13 TeV

1402 When the LHC started its Run II data taking period in summer 2015, it would be the first time  
 1403 ever for a particle collider to produce collisions with center-of-mass energies of 13 TeV. The Higgs  
 1404 boson for which the LHC was designed to find had been discovered at the end of the previous data  
 1405 taking era, leaving us with a Standard Model that we know is, in the best case, in need of extensions  
 1406 and, in the worst case, an effective theory valid only in a certain energy domain. The Run II  
 1407 search program would therefore be oriented around two main efforts: Precision measurements of  
 1408 the newly discovered Higgs boson and searches for Beyond Standard Model physics.

1409  
 1410 I started my PhD four months before the first 13 TeV collisions took place and had to consider the following: What was the most interesting search that could be done on a short time scale  
 1411 (to be presented 6 months after first collisions, at the CERN end-of-year “Jamboree”), would be  
 1412 manageable for a student with no previous analysis experience and would be robust enough incase  
 1413 there were issues with the never-before-validated 13 TeV Monte Carlo?

1415  
 1416 The attention of the high-energy physics community has in the past years been focused on certain  
 1417 “hot topics”: In 2018, this was most certainly leptoquarks (driven by a dimuon excess around 30  
 1418 GeV), in 2016 and 2017 it was diphoton resonances (with  $> 3\sigma$  excesses observed both in ATLAS  
 1419 and in CMS). And in 2015 during the 13 TeV LHC start-up, attention was centered on diboson  
 1420 resonances in the all-hadronic final state. The choice was therefore clear: My first analysis would  
 1421 be a search for diboson resonances in the boosted dijet final state. With a background model  
 1422 based on a smooth fit to data in the signal region, eliminating the need for accurate QCD MC  
 1423 predictions, this was a simple one-background only (QCD) analysis, feasible for a first-year PhD  
 1424 student to finalize within a year. Despite its straightforwardness, due to observed 8 TeV excesses,  
 1425 it was in addition considered a high-profile analysis.

1426  
 1427 This search became one of the first “boosted” searches published with 13 TeV data as well  
 1428 as the first search to take advantage of dedicated “grooming” triggers. Published with  $2.7 \text{ fb}^{-1}$  of  
 1429 2015 data.



<sup>1430</sup> **4.1.1 A small bump**

<sup>1431</sup> On June 2nd 2015, the day before CMS recorded its first ever 13 TeV event, a pre-print appeared  
<sup>1432</sup> on the arXiv “Search for high-mass diboson resonances with boson-tagged jets in proton-proton  
<sup>1433</sup> collisions at  $\sqrt{s} = 8$  TeV with the ATLAS detector” [51]. It was an analysis of the full ATLAS  
<sup>1434</sup> Run 1 dataset, corresponding to  $20.3 \text{ fb}^{-1}$ , searching for heavy resonances decaying to vector  
<sup>1435</sup> bosons in the all-hadronic state. The analysis documented a  $3.4 \sigma$  excess for a heavy resonance  
<sup>1436</sup> decaying to W Z around 2 TeV. The corresponding CMS analysis, published the previous year,  
<sup>1437</sup> had a  $1.3 \sigma$  excess at roughly the same resonance mass, but mostly compatible with a W W  
<sup>1438</sup> final state hypothesis [57]. Figure 4.1 shows the corresponding dijet invariant mass spectrum as  
<sup>1439</sup> seen by ATLAS (left) and the upper limit on the production times the cross section for a  $G_{\text{Bulk}}$   
<sup>1440</sup> decaying to W W (right) as documented by CMS.

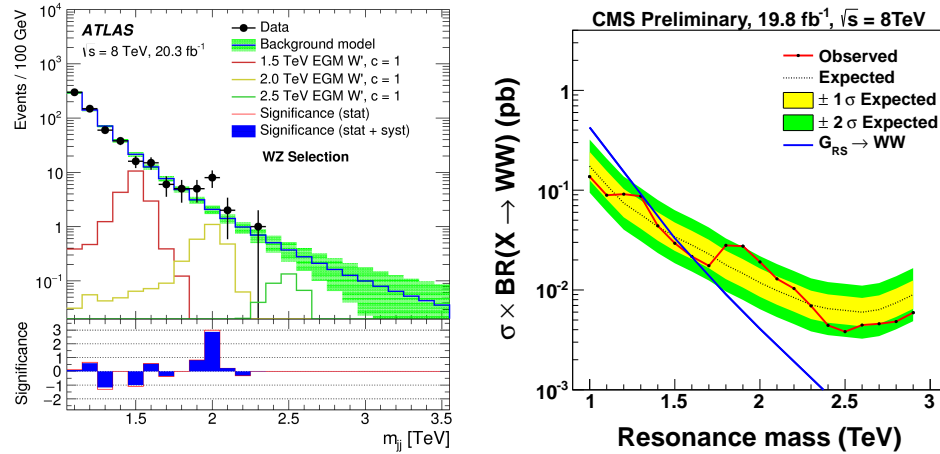


**Figure 4.1:** A “bump” corresponding to  $3.4 \sigma$  in the dijet invariant mass spectrum around 2 TeV (left) observed by ATLAS when analyzing the full 8 TeV dataset [51], together with a similar excess ( $1.3 \sigma$ ) observed in the corresponding CMS analysis [57].

<sup>1441</sup> The two measurements were found to be compatible, favoring a heavy resonance with a  
<sup>1442</sup> production cross section of around  $5 \text{ fb}^{-1}$  and a mass between 1.9 and 2.0 TeV decaying to either  
<sup>1443</sup> W W, W Z or Z Z [58]. Figure 4.2 show the obtained p-value of the ATLAS (red) and CMS  
<sup>1444</sup> (blue) search as well as their combination (black).

<sup>1445</sup> The combination of the two excesses and the timing of the ATLAS paper, naturally lead to  
<sup>1446</sup> some excitement and in the coming weeks, the arXiv was flooded with theory papers seeking an  
<sup>1447</sup> explanation for the measurements.

<sup>1448</sup> In addition, one of the main benefits of increasing the LHC center-of-mass energy from 8 to 13  
<sup>1449</sup> TeV, was that the partonic luminosity would increase. That meant that you could expect them

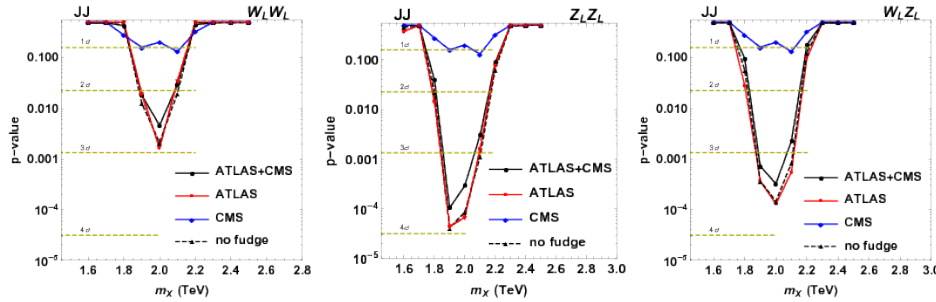


**Figure 4.2:** p-values as a function of resonance mass obtained with an emulation of the ATLAS (red) and CMS (blue) searches as well as the combination of the two (black). Here for a  $W W$  (left),  $W Z$  (middle) and  $Z Z$  (right) hypothesis [58].

same number of signal events as you would expect for the full 8 TeV dataset ( $\sim 20 \text{ fb}^{-1}$ ), for a considerably smaller 13 TeV dataset. Figure 4.3 shows the system mass that can be probed with  $3 \text{ fb}^{-1}$  of 13 TeV data (y-axis), the expected 2015 integrated luminosity, as a function of the probe-able system mass with  $20 \text{ fb}^{-1}$  of 8 TeV data (x-axis) for different partonic channels. The probable 13 TeV mass is defined by finding the system mass which results in the same number of expected events at 8 TeV, if assuming cross sections scale with partonic luminosity and  $1/m^2$ . Three different partonic scattering channels are considered: qq, qg and gg. We see that, for instance for a resonance with a mass of 2000 GeV, the reach at 13 TeV is 2241(gg), 2091(qg), 1851(qq, one type) and 2046(qq, all types) GeV.

What this meant was that, if we saw hints of a 2 TeV  $G_{\text{bulk}}$  (mainly produced through gluon fusion, gg) with the 8 TeV dataset, we should be able to confirm it with nothing but the expected  $3 \text{ fb}^{-1}$  of data expected in 2015. The pressure on seeing early results with 13 TeV data in the VV all-hadronic final state was therefore extremely high, and it was agreed with CMS Physics Coordination that a preliminary analysis would be ready in December that same year, only 6 months after the first 13 TeV collision.

### 4.1.2 Analysis strategy

When a resonance X with a mass above 1 TeV decays into a vector boson pair, the bosons have a very high energy ( $\tilde{p}_T = M_X/2 = 500 \text{ GeV}$ , assuming X is produced at rest). The boson is co-called “boosted”. The decay products of a hadronically decaying boosted vector boson, will therefore not appear as back-to-back in the lab frame but rather be very collimated, as described in Section 3.5. This results in a final state with two large high- $p_T$  jets, where an AK R=0.8 jet is expected to fully contain the two quarks coming from the vector boson decay. This is illustrated in Figure 4.4.

The two jets are both expected to have a mass around the W or Z mass, and some intrinsic

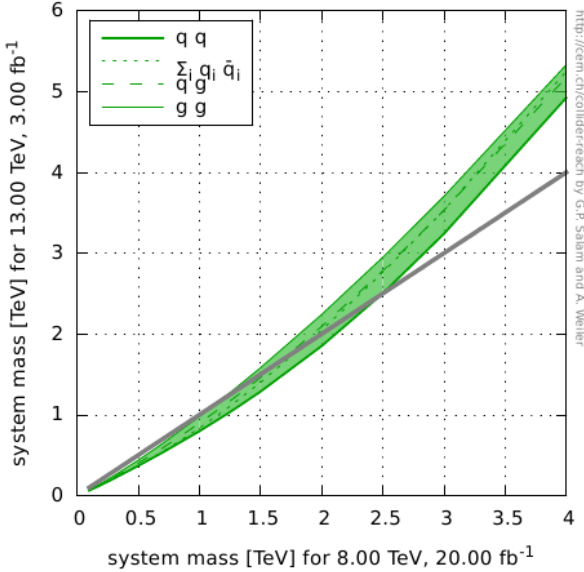


**Figure 4.3:** The system mass that can be probed with  $3 \text{ fb}^{-1}$  of 13 TeV data (y-axis) as a function of the probe-able system mass with  $20 \text{ fb}^{-1}$  of 8 TeV data (x-axis) for different partonic channels (Generated with [59]).

1473 substructure stemming from their two-prong origin. The invariant mass of the dijet system,  $m_{jj}$ ,  
 1474 should be roughly equal to the resonance mass  $M_X$ . This dijet system is the final state under  
 1475 scrutiny and the dijet invariant mass is the parameter of interest. Both WW and ZZ, as well as  
 1476 WZ final states are of interest.

1477 The main background for such an analysis, is QCD multijet events. As mentioned in Section 3.5,  
 1478 quark/gluon jets can obtain a high mass due to diffuse radiation and QCD processes have such a  
 1479 large cross section that the number of QCD jets with a mass compatible with the W mass can be  
 1480 large. In order to discriminate between the two, we take advantage of three properties: 1. The  
 1481 groomed mass of signal and background jets should be very different, 2. signal jets should appear  
 1482 two-prong like, quark/gluon jets not, and 3. the dijet invariant mass for a signal process should  
 1483 peak around the resonance mass while the QCD spectrum is predicted to be smoothly falling  
 1484 (we will get back to why this assumption is justified in Section 4.1.5). The strategy therefore  
 1485 consists of performing a smoothness test on  $m_{jj}$  of the observed data, a so-called “bump-hunt”,  
 1486 by assuming that the signal will appear as a bump on top of a smooth distribution. This is  
 1487 illustrated in Figure 4.5.

1488 The benefit of such a method is that there is no need for any background simulation and  
 1489 the strategy is simple and robust. The disadvantage is that the analysis is intrinsically limited

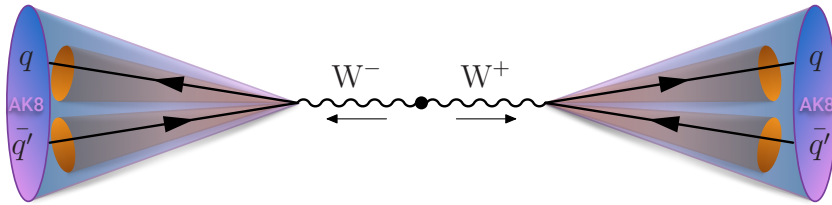


**Figure 4.4:** If a heavy ( $> 1 \text{ TeV}$ ) resonance decays into vector bosons, the transverse momentum of each boson will be large and its decay products are merged into one single large cone AK8 jet.

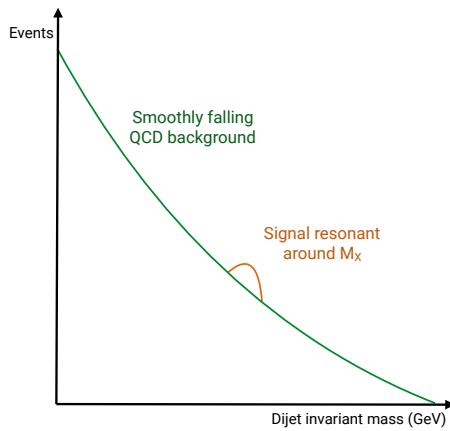


**Figure 4.5:** The search strategy consists of looking for signal “bumps” in the dijet invariant mass on top of a smoothly falling QCD multijet background.

1490 to regions where the dijet invariant mass spectrum is smooth, hence must avoid regions with  
1491 continuities due to trigger turn-ons or kinematic selections.

### 1492 4.1.3 Data and simulated samples

1493 The data analyzed in this search correspond to a total integrated luminosity of  $2.7 \text{ fb}^{-1}$  collected at  
1494 a center-of mass energy of  $13 \text{ TeV}$  between June and December 2015. The instantaneous luminosity  
1495 of the LHC during this run was around half of the design luminosity ( $0.5 \times 10^{34} \text{ cm}^{-2} \text{ s}^{-1}$ ), with  
1496 an average number of primary vertices per event of  $\langle \mu \rangle = 13$ .

1497 The bulk graviton model (see Section 1.2.1) and the HVT model ( $W'$  and  $Z'$ , see Section 1.2.1)  
1498 are used as benchmark signal processes. In these models, the vector gauge bosons are produced  
1499 with a longitudinal polarization in more than 99% of the cases, which leads to a 24% higher  
1500 acceptance per boson for reasons explained in Section 3.5.3. For the HVT model, a scenario  
1501 (model B) with  $g_V = 3$ ,  $c_H = -0.976243$ , and  $c_F = 1.02433$  is chosen, where the heavy resonance

1502 predominantly couple to bosons and the coupling to fermions is suppressed. The bulk graviton  
 1503 samples were generated with  $\tilde{k} = 0.5$ . The resonance masses considered lie in the range 1.2 to  
 1504 4 TeV and has a width of 0.1% of the resonance mass. The narrow width allows us to neglect  
 1505 detector effect as the natural width of the resonance is smaller than the detector resolution,  
 1506 making the modeling of detector effects on the signal shape independent of the model. All signal  
 1507 samples are generated at leading order with MADGRAPH5\_AMC@NLO v2.2.2 [60]

1508 Simulated samples of the production of QCD multijet events are generated to leading order  
 1509 using PYTHIA version 8.205 [61] with the CUETP8M1 tune [56].

#### 1510 4.1.4 Event selection

##### 1511 Triggering

1512 The first selection to be confronted in any analysis, is the trigger selection. Due to an overwhelming  
 1513 QCD background in all-hadronic final states, the threshold for fully-hadronic triggers is very  
 1514 large in order to keep the trigger rate low (preferably around 10-30 Hertz). In this analysis, we  
 1515 therefore decided to take advantage of triggers that place requirements on the jet groomed mass  
 1516 in addition to the “standard” triggers based on the scalar sum of jet transverse energy  $H_T$ . These  
 1517 “boosted” triggers were never before tested in data, and this analysis was the first published  
 1518 result taking advantage of grooming at the trigger level in CMS. The following  $H_T$ -based triggers  
 1519 (called inclusive triggers in the following) are used

- 1520     • HLT\_PFHT650\_WideJetMJJ900DEtaJJ1p5
- 1521     • HLT\_PFHT650\_WideJetMJJ950DEtaJJ1p5,
- 1522     • HLT\_PFHT800

1523 where the two first triggers apply an additional cut on the  $|\Delta\eta|$  between the two jets for reasons  
 1524 that will be explained below. In addition, two grooming triggers cutting on the jet trimmed mass  
 1525 (see Section 3.5.1) of 30 and 50 GeV are used

- 1526     • HLT\_AK8PFJet360\_TrimMass30
- 1527     • HLT\_AK8PFHT700\_TrimR0p1PT0p03Mass50.

1528 The tuneable parameters for the trimming algorithm at HLT are  $r_{sub} = 0.2$  and  $p_{T,frac} = 0.03$ .  
 1529 The HLT\_AK8PFJet360\_TrimMass30 trigger is seeded by single-object Level 1 triggers with jet  
 1530  $p_T$  thresholds of 176 or 200 GeV (L1\_SingleJet176 or L1\_SingleJet200), and the remaining  
 1531 triggers requires an online  $H_T > 150$  or 175 GeV (L1\_HTT150 or L1\_HTT175).

1532 In order to avoid any kinks in the dijet invariant mass spectrum due to the presence of a  
 1533 trigger turn-on, we need to define for which dijet invariant mass the analysis triggers are fully  
 1534 efficient (> 99%), then cut away everything below that point.

In order to estimate the trigger efficiency, we use a lower threshold prescaled  $H_T$  trigger HLT\_PFT650 as reference trigger. This trigger has a prescale of 40, meaning it only stores information for every 40 events that trigger it, and is seeded by L1 triggers L1\_HTT150 or L1\_HTT175. We then define the efficiency as

$$\text{Efficiency} = \frac{N_{trigger+ref}}{N_{ref}}$$

1535 where  $N_{trigger+ref}$  corresponds to events passing the trigger under study as well as the reference  
 1536 trigger and  $N_{ref}$  corresponds to all events passing the reference trigger. Figure 4.6 shows the  
 1537 trigger turn-on curves as a function of dijet invariant mass for jets where one of the jets is required  
 1538 to have a pruned mass larger than 65 GeV (in other words, compatible with a W jet). A sharp  
 1539 turn-on for the inclusive triggers (top left) is observed, reaching the 100% efficiency plateau for  
 1540 dijet masses of around 1.0–1.1 TeV. The grooming triggers, however, turn on more slowly and  
 1541 are not fully efficient before dijet invariant masses of around 1.2 TeV (top right). The real power  
 1542 of the grooming triggers become clear when adding them in OR with the  $H_T$ -based triggers. The  
 1543 bottom plot in Figure 4.6 compares the trigger turn-on curves as a function of dijet invariant  
 1544 mass for jets passing one of the three inclusive triggers only, one of the grooming triggers only  
 1545 and when combining all of them. Here, one can see that the 99% efficiency threshold is lowered  
 1546 by 75 GeV when including the substructure triggers, once substructure is required at analysis  
 1547 level. This allowed for the analysis to start at a dijet invariant mass of 1 TeV.

1548 As a measure of the performance of the grooming triggers, we have in addition looked at  
 1549 the trigger efficiencies as a function of the offline groomed mass (pruned and softdrop, see  
 1550 Sections 3.5.1 and 3.5.1), for the grooming trigger with the lowest mass threshold (30 GeV).  
 1551 This is shown in Figure 4.7, where an additional cut on the jet transverse momentum of one of  
 1552 the jets of 600 GeV is required and no other mass cut is applied. The trigger plateau is reached  
 1553 for offline groomed-jet masses around 50 GeV, an impressively sharp turn-on for a trigger paths  
 1554 first test i data (as reference trigger for this study, the prescaled trigger HLT\_PFT650 was used).

## 1555 Preselection

1556 After trigger selections and the corresponding requirement of a dijet invariant mass above 1 TeV  
 1557 to ensure a smooth falling background, the process of maximizing the signal significance while  
 1558 keeping the background low can begin. This is done through a set of jet requirements. The jets

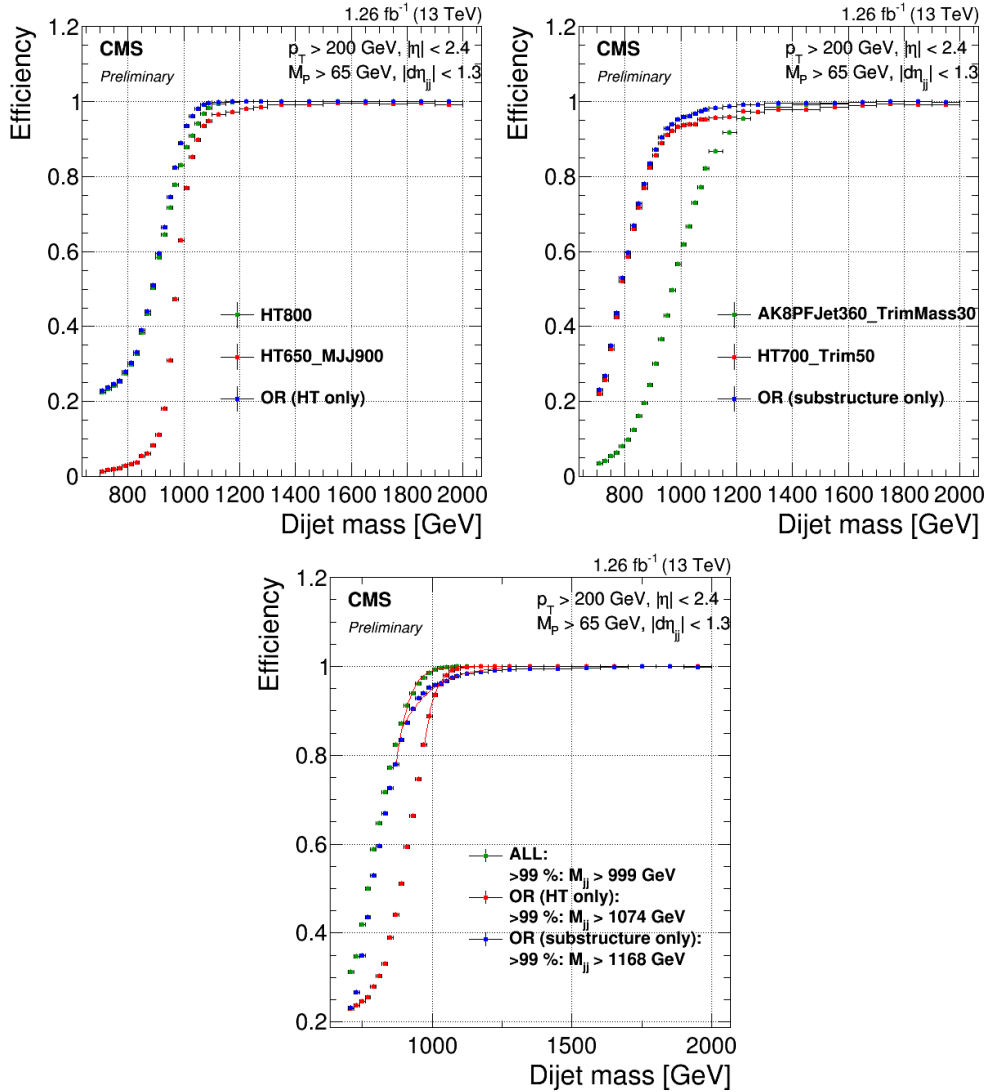


**Figure 4.6:** Top: Efficiency for the inclusive triggers (top left) and the grooming triggers (top right) as a function of dijet invariant mass for jet pairs where one jet has a pruned mass larger than 65 GeV. Bottom: Comparison of trigger efficiencies for jets passing one of the HT-triggers only (red), for jets passing one of the grooming-triggers only (blue) and for jets passing one of the HT-triggers or one of the grooming triggers (green). Here as a function of dijet invariant mass for all jet pairs passing loose selections and where one jet has a pruned mass larger than 65 GeV. The 99% efficiency threshold is lowered by 75 GeV when including substructure taggers.

used in this analysis are clustered with the anti- $k_T$  jet clustering algorithm with a clustering parameter of  $R = 0.8$  (see Section 3.4) to allow containment of the full vector boson decay products. As we know that a minimum transverse of 200 GeV is required for the decay products

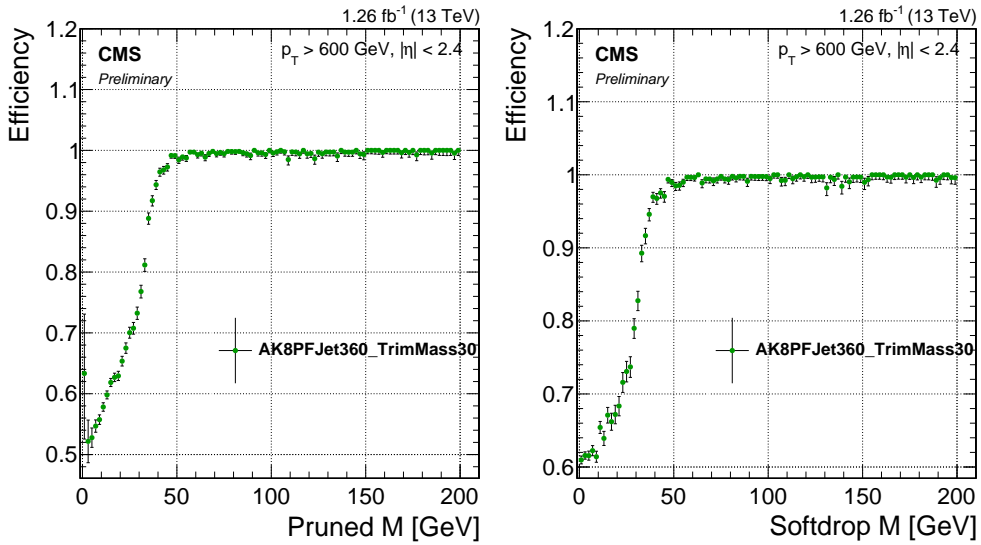


**Figure 4.7:** Efficiency for the lowest threshold grooming trigger as a function of pruned-jet (left) and softdrop-jet (right) mass for jets with  $p_T > 600 \text{ GeV}$ .

of a W/Z to be fully contained within an  $R=0.8$  jet, events are further selected by requiring at least two jets with  $p_T > 200 \text{ GeV}$ . These are in addition required to be central, with an  $|\eta| < 2.4$ .

The two highest  $p_T$  jets in the event passing these criteria are selected as potential vector boson candidates. As our main background is QCD multijet events, we further take advantage of the fact that the angular distribution between these, mainly t-channel, processes are very different from the s-channel signal processes under study. The crosssection for QCD t-channel processes as a function of the opening angle with respect to the beam axis ( $\theta^*$ ), exhibit a pole around  $\cos \theta^* = 1$ , meaning QCD t-channel jets are mostly forwardly produced, with an opening angle with respect to the beam axis close to zero. The signal jets on the other hand, produced through an s-channel process, are concentrated in the barrel region. We therefore require the jets to have a separation of  $|\Delta\eta| < 1.3$  in order to reduce the QCD multijets background. The distribution of  $|\Delta\eta|$  between the two highest- $p_T$  jets for QCD as well as for different signal scenarios, is shown in Figure 4.8

A cut of  $|\Delta\eta|_{jj} < 1.3$  makes sure to remove the t-channel pole at  $\cos \theta^* = 1$  and is in addition found to yield the best separation between signal and the QCD background.

In addition to these requirements on the jets themselves, an overlap veto with leptons in the event is applied. Here the overlap  $\Delta R(\text{jet}, \text{lepton})$  between the jet candidate and a lepton is required to be larger than 0.8. Leptons used for this veto are required to pass the identification requirements described in Section 3.2.2 and 3.2.2, have a transverse momentum larger than 35

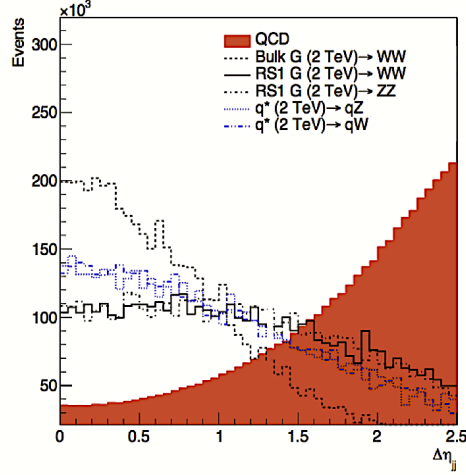


**Figure 4.8:**  $|\Delta\eta|$  between the two highest- $p_T$  jets for QCD jets and jets stemming from different signal scenarios.

1581 (30) GeV and a pseudorapidity smaller than 2.5 (2.4) in case of electrons (muons).

1582 The  $p_T$ ,  $\eta$ , dijet invariant mass and  $|\Delta\eta|_{jj}$  distribution for the two leading jets in the event  
1583 after the above preselections have been applied is shown in Figure 4.67.

#### 1584 Vector boson tagging

1585 After preselections, we take advantage of the jet substructure algorithms described in Section 3.5 to  
1586 further separate boosted W/Z jets from the QCD multijets background. In the 8 TeV analysis [57]  
1587 published the previous year, the pruning algorithm was the groomer of choice. However, recent  
1588 progress had been made in the development of alternative groomers which had favorable properties  
1589 from a theoretical point of view (see Sections 3.5.1 and 4.2.5). We therefore studied two different  
1590 grooming algorithms: pruning and softdrop (with  $\beta = 0$  and  $z_{cut} = 0.1$ ). A comparison of  
1591 the softdrop (dotted lines) and pruned (solid lines) jet mass for W, Z and H jets is shown in  
1592 Figure 4.10.

1593 One of the first observations we made comparing the two groomers, was that there appeared  
1594 to be a strong dependence of softdrop mass on the jet  $p_T$ . Figure 4.11 shows the pruned (left)  
1595 and softdrop (right) mass distributions for W jets coming from the decay of a  $G_{bulk}$  with a  
1596 resonance mass of  $0.8 \text{ TeV} < M_X < 4 \text{ TeV}$ . While the pruned jet mass mean appeared stable as  
1597 the jet transverse momenta of the jet increased ( $p_T \sim M_X/2$ ), the softdrop jet mass mean shifted  
1598 towards lower values as jet  $p_T$  increased.

1599 In order to investigate whether this was a reconstruction effect or an algorithmic effect, we

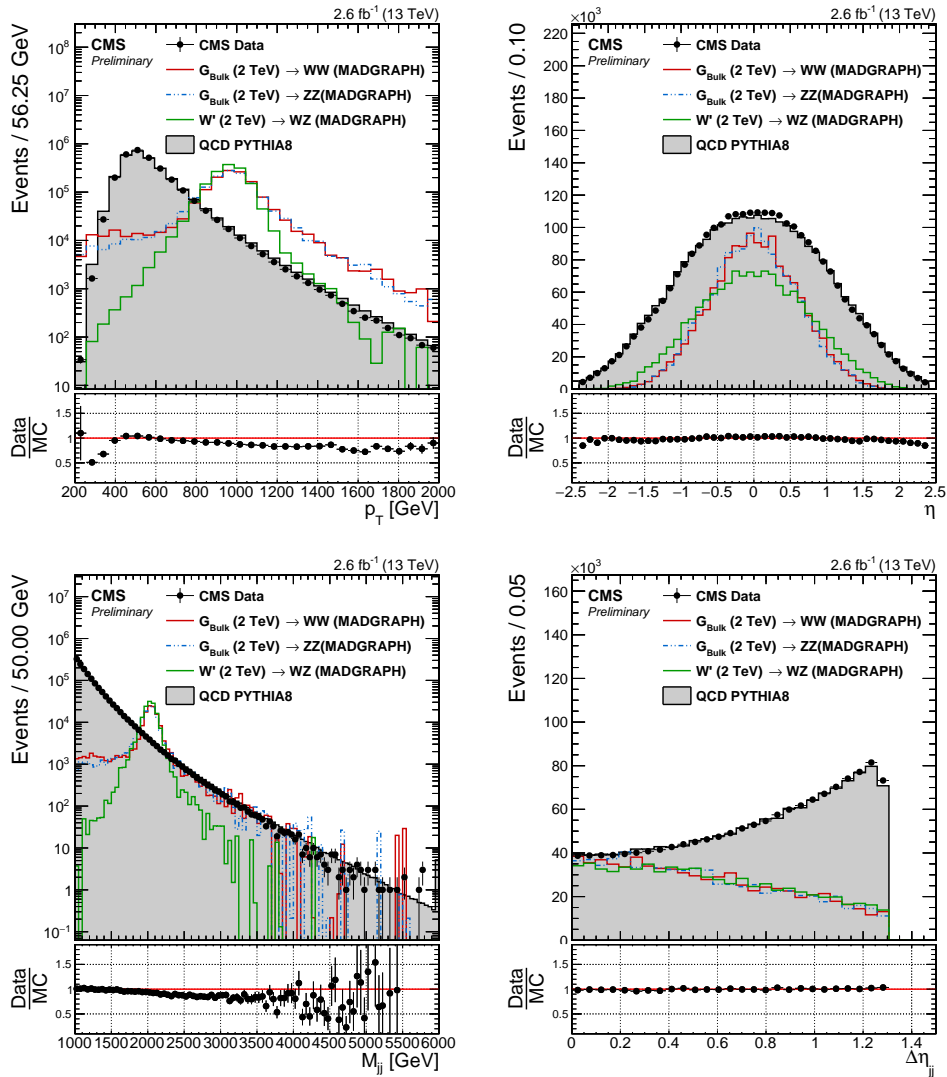


**Figure 4.9:** Jet  $p_T$  (top left),  $\eta$  (top right), dijet invariant mass (bottom left) and  $|\Delta\eta|_{jj}$  (bottom right) distribution for the two leading jets in the event after loose preselections are applied. The signal is scaled by an arbitrary number.

1600 additionally looked at the pruned and softdrop mass for generator level jets (jets clustered with  
 1601 generator level particles before they are passed through the detector simulation). Figure 4.12  
 1602 shows the reconstructed (solid line) and generator level (dotted line) jet mass distributions after  
 1603 pruning (left) or softdrop (right) have been applied. Again, the distributions are compared for jets  
 1604 with very different  $p_T$  profiles, here for W jets coming from a  $G_{\text{bulk}} \rightarrow WW$  of mass  $M_X = 0.8 \text{ TeV}$   
 1605 (red), roughly  $p_T \sim 400 \text{ GeV}$ , and  $M_X = 2.0 \text{ TeV}$  (blue),  $p_T \sim 1 \text{ TeV}$ . Interestingly, we observe a

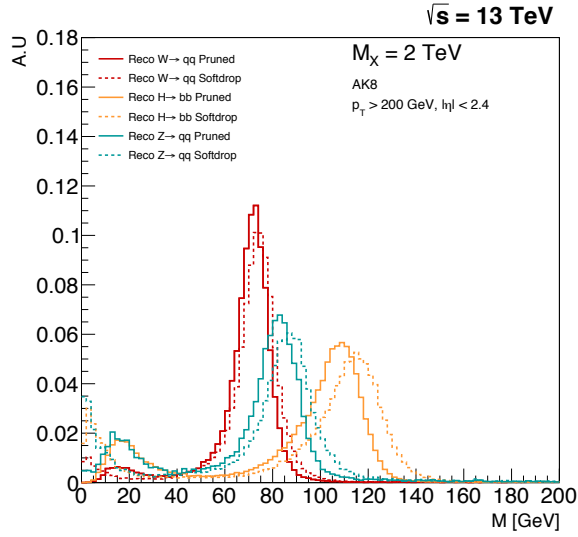


**Figure 4.10:** The softdrop (dotted lines) and the pruned (solid lines) jet mass for W, Z and H jets.

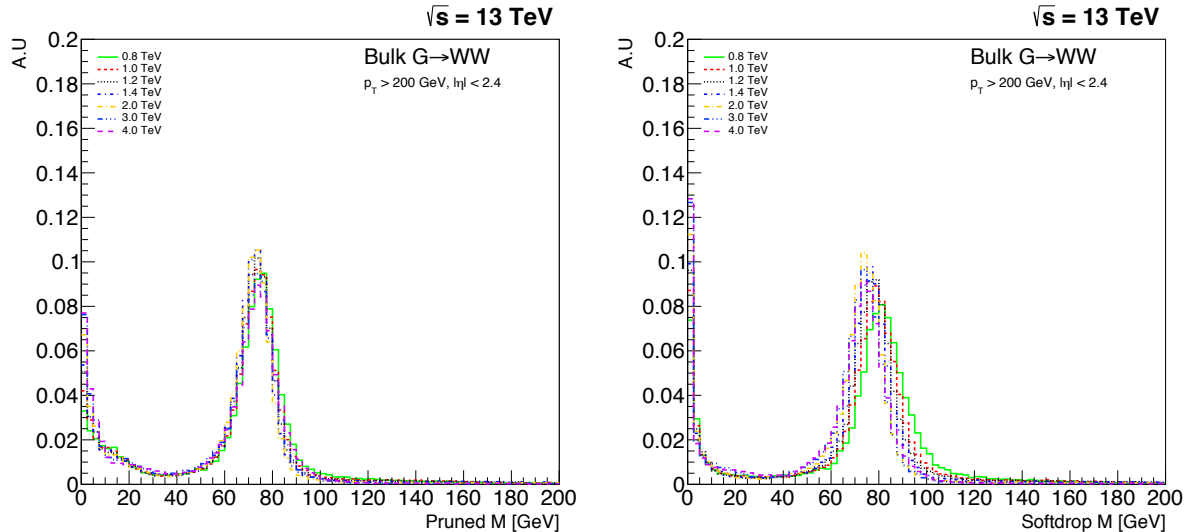


**Figure 4.11:** The jet mass distribution for W jets coming from a  $G_{\text{bulk}}$  of masses in the range  $0.8 \text{ TeV} < M_X < 4 \text{ TeV}$  decaying to WW, here with pruning applied (left) and softdrop (right). A strong shift in the jet mass mean as a function of  $p_T$  ( $\sim M_X/2$ ), is observed for jets groomed with the softdrop algorithm. Charge hadron subtraction is applied to all jets before clustering.

<sup>1606</sup>  $p_T$ -dependent mass shift already for generator level softdrop jets (comparing the dotted lines in

the right plot); an effect further enhanced at reconstruction level. This effect is not present for pruned jets, neither at generator level nor reconstruction level.

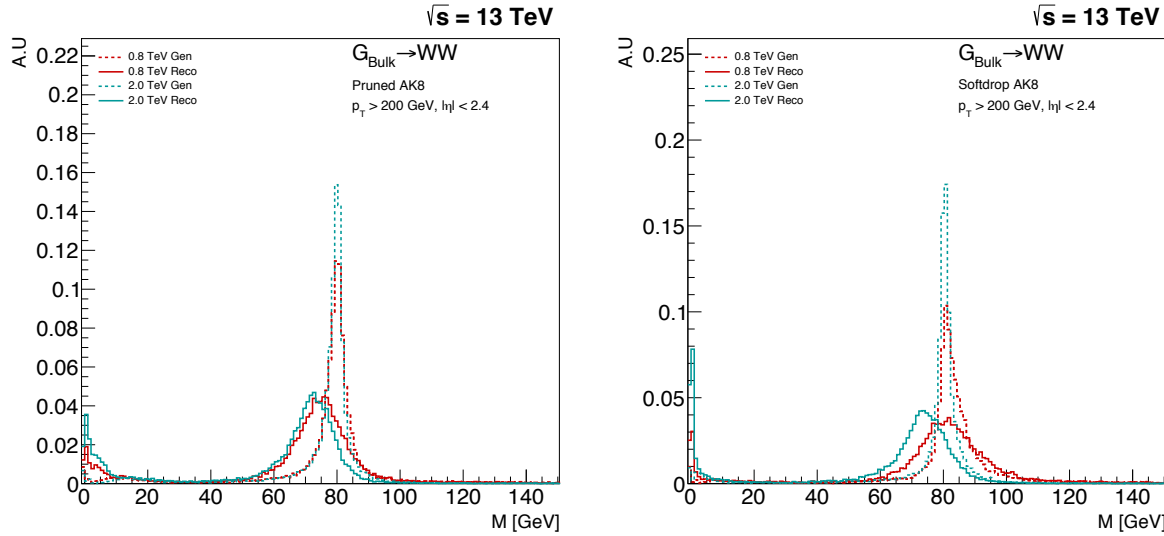


**Figure 4.12:** The reconstructed (solid line) and generator level (dotted line) jet mass distribution for W jets coming from a  $G_{\text{Bulk}} \rightarrow WW$  of mass  $M_X = 0.8 \text{ TeV}$  (red), roughly  $p_T \sim 400 \text{ GeV}$ , and  $M_X = 2.0 \text{ TeV}$  (blue),  $p_T \sim 1 \text{ TeV}$ . Here for the pruned (left) and softdrop (right) jet mass.

The observed softdrop mass  $p_T$ -dependence was problematic, due to the fact that it would require a  $p_T$  dependent mass window. This would again require several different measurements of data to simulation tagging efficiency scale factors, for the respective mass windows, or a significantly higher uncertainty on the signal yield. Due to these observations, the grooming algorithm of choice for this analysis is pruning, with  $65 \text{ GeV} < m_{\text{pruned}} < 105 \text{ GeV}$ . However, this would be a study we would return to in Search II (Section 4.2).

The shape tagger we chose for this analysis was the n-subjettiness ratio  $\tau_{21}$ .  $\tau_{21}$  is strongly correlated to the pruned jet mass, and the discriminating power of the variable is reduced when applying a pruned mass cut. The  $\tau_{21}$  distribution for the QCD background and W jets from a signal decay before (left) and after (right) a pruned mass cut of  $65 \text{ GeV} < m_{\text{pruned}} < 105 \text{ GeV}$  have been applied, is shown in Figure 4.13.

We therefore perform a cut optimization on  $\tau_{21}$  after all analysis selections, including a pruned mass window of  $65 \text{ GeV} < m_{\text{pruned}} < 105 \text{ GeV}$ , have been applied. This is done by scanning the

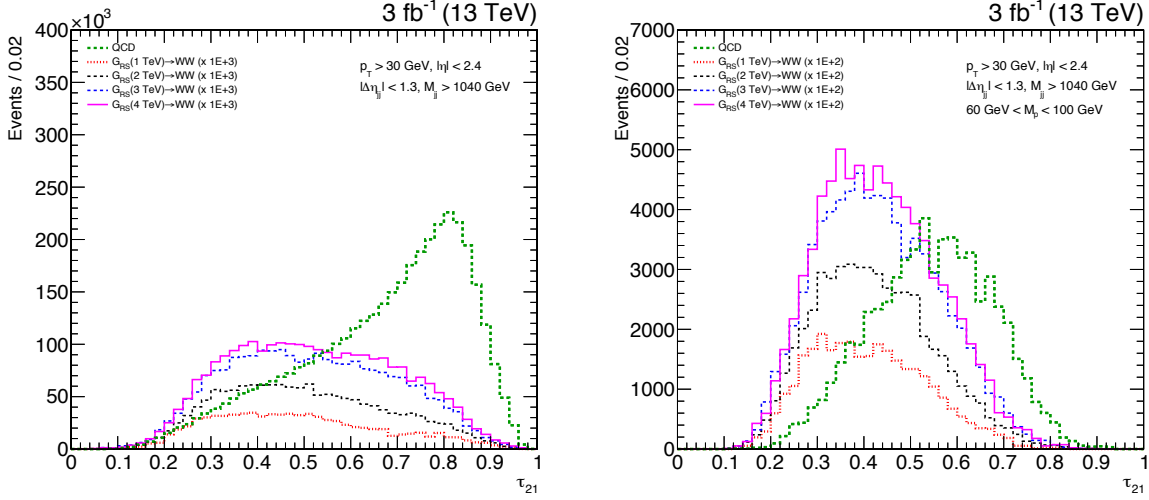


**Figure 4.13:** The  $\tau_{21}$  distribution for QCD background and signal jets before (left) and after (right) a pruned mass window is applied. The discriminating power of  $\tau_{21}$  is strongly reduced after grooming.

$\tau_{21}$  cut, and for each cut computing the Punzi significance [62] defined as

$$S = \frac{\epsilon_S}{1 + \sqrt{B}}$$

where  $\epsilon_S$  is the signal efficiency and  $B$  is the total background. The cut with the highest significance is defined as the optimal cut value. The signals under consideration are W jets coming from the decay of a  $G_{\text{bulk}}$  with  $M_X = 1 - 4 \text{ TeV}$ , against a background of light flavored QCD jets. Only jets with a dijet invariant mass in a 20% window around the resonance mass are considered. The Punzi significance as a function of the upper cut value on  $\tau_{21}$  is shown on the left in Figure 4.14.

The optimal cut gets looser as the dijet invariant mass increases, something which can be understood when looking at the QCD dijet invariant mass spectrum in Figure 4.67. The number of QCD jets falls off exponentially with  $m_{jj}$ , meaning that the background at 4 TeV is considerably lower than at 1 TeV. This allows for a looser cut on  $\tau_{21}$  as  $m_{jj}$  increases. In order to choose a single cut which works reasonably well for all mass points, we look at the ratio of a given  $\tau_{21}$  cut over the significance of the best cut at that mass points. This is shown in the right plot of Figure 4.14. The cut  $\tau_{21} < 0.45$  has the most stable performance out of the investigated cut values and is due to that, and due to the desire of keeping the background as low as possible at low  $m_{jj}$ , chosen as the nominal cut. In order to account for the fact that background is lower at

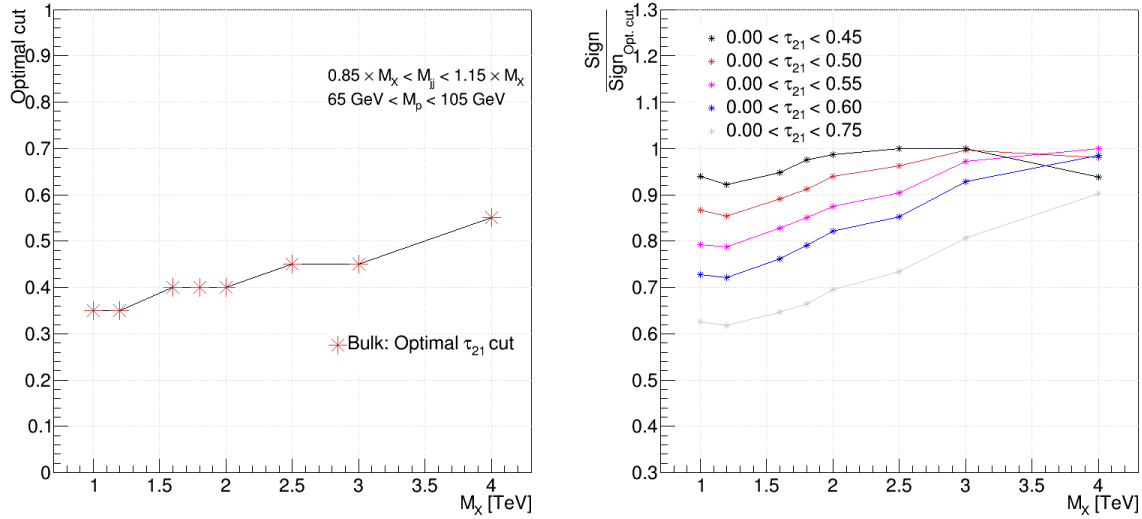


**Figure 4.14:** Optimal upper cut on  $\tau_{21}$  as a function of  $G_{\text{bulk}}$  mass (left). The optimal  $\tau_{21}$  selection for  $W'$  (HTV model) resembles the Bulk graviton selection.

1636 high- $m_{jj}$ , we add an additional analysis category,  $0.45 < \tau_{21} < 0.75$ , which contains  $> 95\%$  of the  
 1637 signal and enhances the analysis sensitivity where the background is low. These categories are  
 1638 hereafter referred to as the ‘‘high purity’’ (HP) category, for jets with  $0 < \tau_{21} \leq 0.45$ , and the low  
 1639 purity (LP) category, for jets with  $0.45 < \tau_{21} \leq 0.75$ .

1640  
 1641 The  $W$ -tagging efficiency and QCD light-flavored jet mistagging rate for a  $W$ -tagger consisting of  
 1642  $0 < \tau_{21} \leq 0.45$  and  $65 \text{ GeV} < m_{\text{pruned}} < 105 \text{ GeV}$  is shown in Figure 4.15, both as a function of  
 1643 jet  $p_T$  and as a function of number of primary vertices in the event.

1644 The signal efficiency for a pruned jet mass cut only, is around 80 % with a mistag rate of  
 1645  $\sim 15\%$ . After adding a  $\tau_{21}$  cut, the signal efficiency drops to around 55% and the mistagging  
 1646 rate to  $\sim 2\%$ . Another interesting feature is the dependence of  $\tau_{21}$  on  $p_T$  on pileup, compared  
 1647 to the resilience of the groomed mass as a function of the same variables. This will be another  
 1648 feature we explore in Search II (Section 4.2). Figure 4.1.7 shows the pruned-jet mass (left) and  
 1649 the n-subjettiness  $\tau_{21}$  distribution (right) for signal and background Monte Carlo, as well as the  
 1650 distributions measured in data.

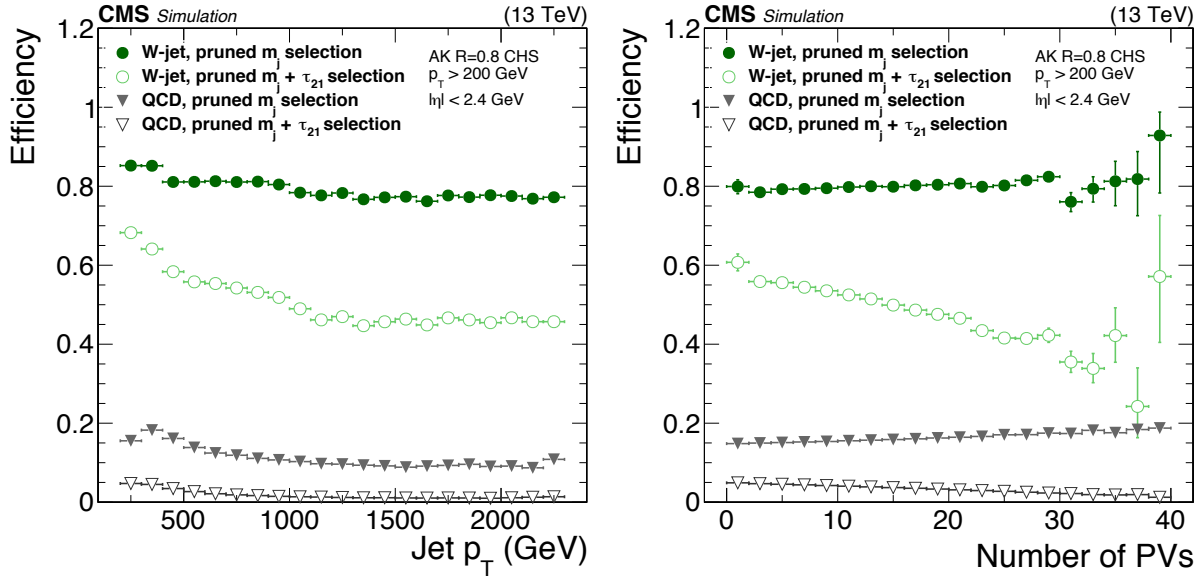


**Figure 4.15:** The W-tagging efficiency (green) and light jet mistag rate (grey) for a pruned jet mass cut only and pruned jet mass +  $\tau_{21}$  cut as a function of  $p_T$  (left) and number of primary vertices (right).

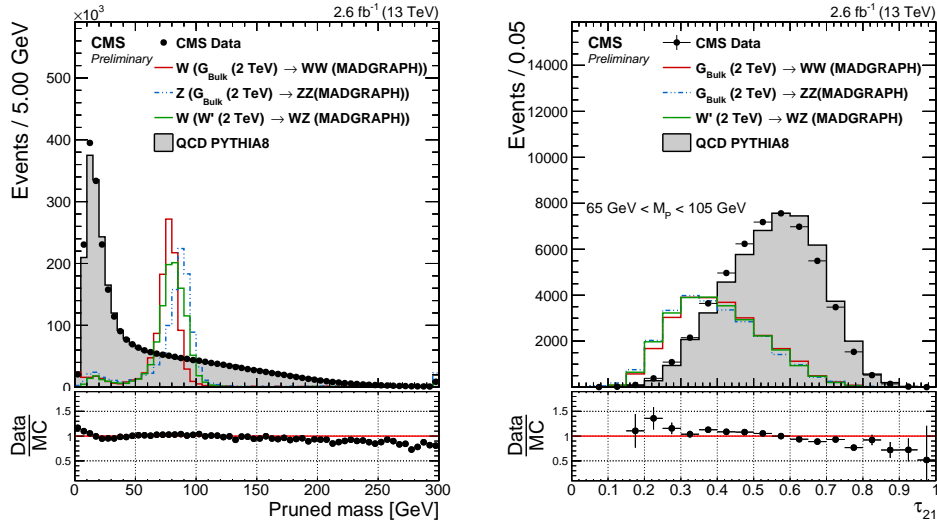


**Figure 4.16:** Pruned jet mass distribution (left) and n-subjettiness  $\tau_{21}$  (right) distribution for data and simulated samples. Simulated samples are scaled to match the distribution in data. The  $\tau_{21}$  distribution is shown for jets after a cut of  $65 \text{ GeV} < M_p < 105 \text{ GeV}$  has been applied.

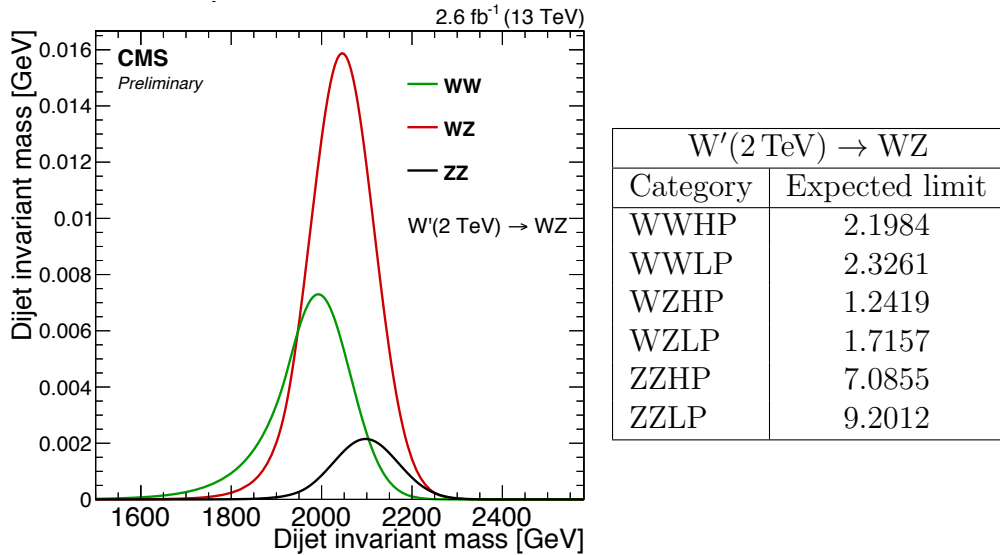


**Figure 4.17:** The expected signal yield per mass category for  $W'$  (2 TeV) decaying to a W and Z (left) together with the expected limit per mass category for the same signal (right).

### 1651 Analysis categorization

1652 As the analysis requires two W/Z-tags, we always require one HP tagged jet and then divide into  
 1653 LP and HP categories depending on whether the other jet is of high or low purity. In addition, in  
 1654 order to further enhance the analysis sensitivity, we further split the pruned jet mass window  
 1655 into a W and a Z boson window where the W window is defined as  $65 \text{ GeV} < m_{\text{pruned}} < 85 \text{ GeV}$   
 1656 and the Z boson window as  $85 \text{ GeV} < m_{\text{pruned}} < 105 \text{ GeV}$ . This has the added benefit of allowing  
 1657 us to make a discrimination between a  $G_{\text{bulk}}$  decaying to WW or ZZ, and a  $W'$  decaying into  
 1658 WZ through counting events in each category. We, for instance, expect a higher signal yield  
 1659 in WZ category for a  $W'$  decaying to a W and Z boson than for a  $G_{\text{bulk}}$  decaying to WW or  
 1660 ZZ. Figure 4.17 shows the relative expected signal yield (left) and expected limits (left) in the  
 1661 different mass categories for a 2 TeV  $W'$ .

1662 All categories are combined in the end, leading to the same or better sensitivity than when  
 1663 using the whole pruned mass window. Figure 4.18 shows the expected 95% CL upper limits on  
 1664 the production cross section of a  $W'$  decaying to WZ (left) and a  $G_{\text{bulk}}$  decaying to WW (right)  
 1665 as function of the resonance mass in the HP category. The blue line corresponds to the expected  
 1666 limits obtained when not splitting into mass categories and the red line corresponds to the limit  
 1667 using the combination of two categories. The dotted and solid black lines are the limits in the W  
 1668 and Z categories, respectively. The combination of two mass categories leads to a slightly better  
 1669 (10%) or to the same sensitivity as when using one large mass window.

1670 The real benefit of splitting into mass categories becomes obvious when defining a test  
1671 statistics based on the likelihood ratios of each signal hypothesis,  $q = -2 \ln(L_{G_{\text{bulk}}}/L_{W'})$ , shown  
1672 in Figure 4.19. For a signal with a signal strength corresponding to a  $3\text{-}4 \sigma$  excess, the test  
1673 statistics for each signal hypothesis are well separated ( $\sim 3.5\sigma$ ), allowing us to make a statement  
1674 of how  $G_{\text{bulk}}$  or  $W'$  like a possible signal is. With the high-purity and low-purity categories as  
1675 defined above for each mass window combination, this leaves us with six different signal categories.  
1676 They are as follows:

- 1677 • High-purity, 3 mass categories: WW, ZZ and WZ  
1678 • Low-purity , 3 mass categories: WW, ZZ and WZ

1679 In parallel to the mass-category based analysis, we perform an analysis without categorization  
1680 in mass (similar to the 8 TeV analysis) as a cross-check, and found the sensitivity with mass  
1681 categories to be better. The final tagging efficiency for different signal hypothesis (top) together  
1682 with the QCD mistag rate (bottom) in the different signal categories is shown in Figure 4.20.  
1683 The solid lines represent the tagging efficiency in the full mass window ( $65 \text{ GeV} < M_p < 105 \text{ GeV}$ )  
1684 before splitting into mass categories. A lower signal efficiency the ZZ mass category is observed in  
1685 all cases. This can be explained from the pruned jet mass distribution on the left in Figure 4.1.7,  
1686 where a cut at 85 GeV leaves a large fraction of the Z peak in the W mass window. As the main  
1687 benchmark models under consideration preferably decays to W bosons (in the Bulk Graviton  
1688 model the branching ratio  $\text{BR}(G_{\text{Bulk}} \rightarrow W W) = 2 * \text{BR}(G_{\text{Bulk}} \rightarrow ZZ)$ , and in the HVT model  
1689  $W'/Z' \rightarrow WZ/WW$  (but not ZZ) ), a high tagging efficiency for the W boson is preferred. In  
1690 the limit-setting procedure all the categories are combined and the overall signal efficiency is  
1691 conserved. For the combined mass-categories (solid line) the signal efficiency is between 16 and  
1692 23 % in the double-tag categories, and between 20 and 34 % in the single-V tag categories. The  
1693 mistagging rate in the double-V tag categories is below 1 % in the high-purity category. The full  
1694 analysis selections and final categories are listen in Table 4.1.

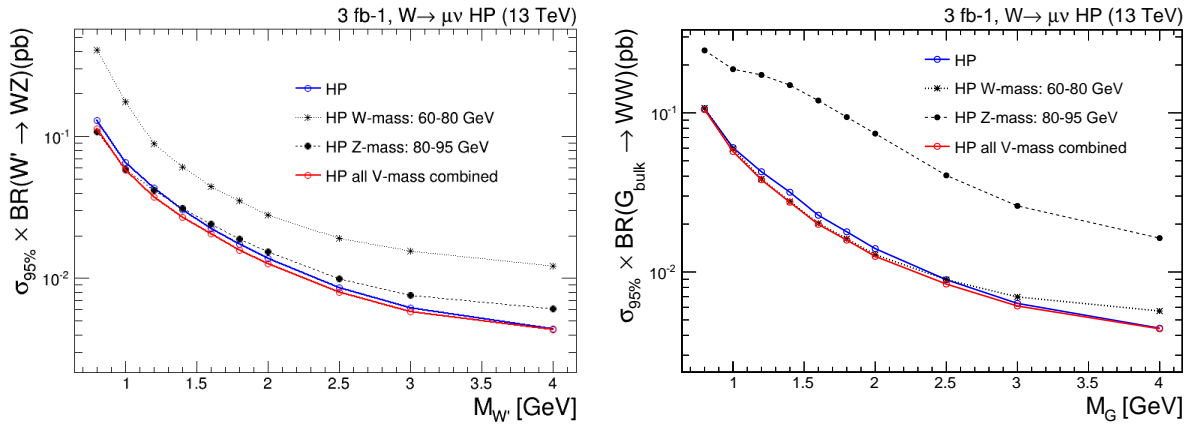


**Figure 4.18:** Expected 95% CL upper limits on the production cross section of a  $W'$  (left) and  $G_{\text{bulk}}$  (right) signal as function of the resonance mass for the different mass categories for events passing the high-purity  $\tau_{21}$  selections.

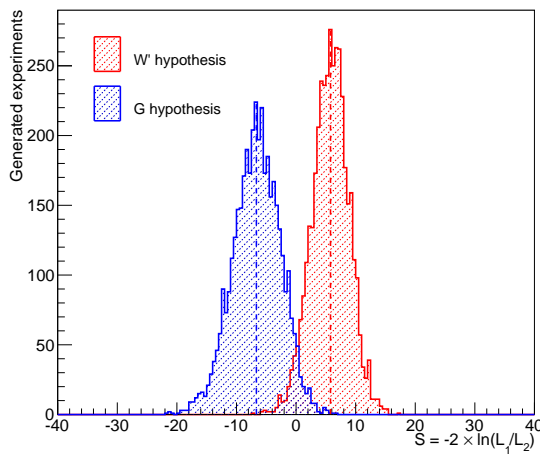


**Figure 4.19:** Distribution of the test statistic  $q = -2 \ln(L_{G_{\text{bulk}}} / L_{W'})$  for a  $G_{\text{bulk}}$  (blue) and  $W'$  signal hypothesis.

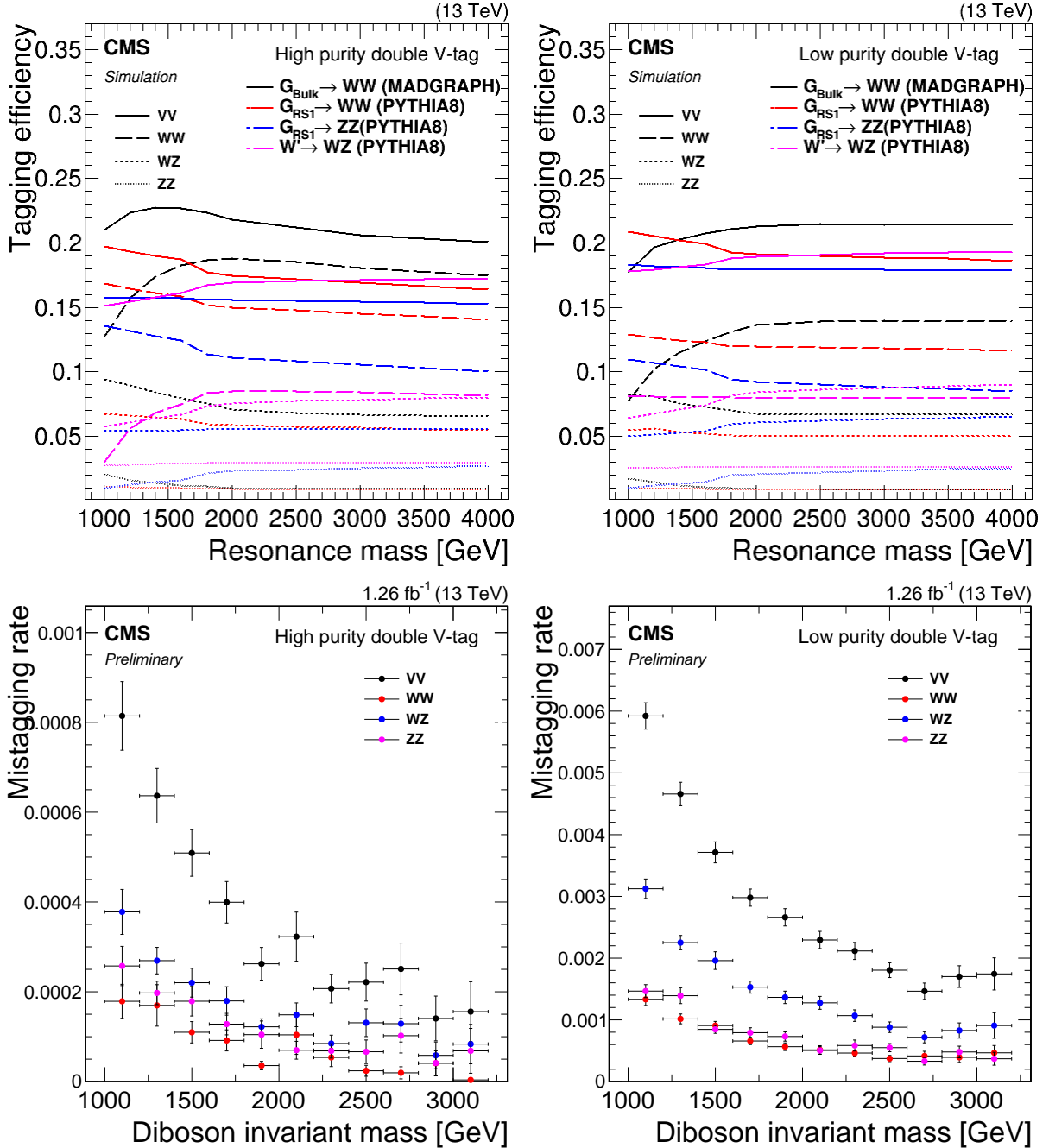


**Figure 4.20:** Tagging efficiency (top) and mistagging rate (bottom) in the different pruned mass categories in the high-purity category (left) and in the low-purity category (right)

Selection	Value
<hr/>	
Boson selections	
$V \rightarrow q\bar{q}$ (2 AK8 jets)	$p_T > 200 \text{ GeV}$ $ \eta  < 2.4$
Pruned jet mass	$65 < m_{\text{jet}_1}, m_{\text{jet}_2} < 105 \text{ GeV}$
Topology	$ \Delta\eta_{jj}  < 1.3$
Dijet invariant mass	$m_{jj} > 1 \text{ TeV}$
2- to 1-subjettiness ratio	$\tau_{21} < 0.75$
<hr/>	
$m_{\text{jet}}$ categories	
WW	$65 < m_{\text{jet}_1} < 85 \text{ GeV}, 65 < m_{\text{jet}_2} < 85 \text{ GeV}$
WZ	$65 < m_{\text{jet}_1} < 85 \text{ GeV}, 85 < m_{\text{jet}_2} < 105 \text{ GeV}$
ZZ	$85 < m_{\text{jet}_1} < 105 \text{ GeV}, 85 < m_{\text{jet}_2} < 105 \text{ GeV}$
<hr/>	
$\tau_{21}$ categories	
High-purity	$\tau_{21,\text{jet}1} < 0.45, \tau_{21,\text{jet}2} < 0.45$
Low-purity	$\tau_{21,\text{jet}1} < 0.45, 0.45 < \tau_{21,\text{jet}2} < 0.75$

**Table 4.1:** The full analysis selections, mass and  $\tau_{21}$  categories.

### 1695 4.1.5 Background modeling

1696 The background modeling in this analysis is based on a smoothness test performed directly on  
1697 unblinded data, similar to what is done in previous CMS analyses looking for bumps in the dijet  
1698 invariant mass spectrum [63, 64]. We assume that the QCD multijet background in the different  
1699 analysis categories can be described by smooth, monotonically decreasing functions of 2 or 3  
1700 parameters

$$\frac{dN}{dm_{jj}} = \frac{P_0}{(m_{jj}/\sqrt{s})^{P_2}} \quad \text{and} \quad \frac{dN}{dm_{jj}} = \frac{P_0(1 - m_{jj}/\sqrt{s})^{P_1}}{(m_{jj}/\sqrt{s})^{P_2}}, \quad (4.1)$$

where  $m$  is the dijet invariant mass,  $\sqrt{s}$  the centre of mass energy and  $P_0$  is a normalization parameter for the probability density function and  $P_1$  and  $P_2$  describe the shape. The number of fit parameters is decided through a Fishers F-test [65]. In this test, we start from the 2 parameter function and compare the goodness of fit ( $\chi^2$  divided by degrees of freedom) when fitting the data signal region with a 2, 3, 4 and 5 parameter function. We then check at 10% confidence level (CL) if additional parameters are needed to model the background distribution. The 4 and 5 parameter functions are

$$\frac{dN}{dm_{jj}} = \frac{P_0(1 - m_{jj}/\sqrt{s})^{P_1}}{(m_{jj}/\sqrt{s})^{P_2+P_3 \times \log(m_{jj}/\sqrt{s})}} \quad (4.2)$$

$$\frac{dN}{dm_{jj}} = \frac{P_0(1 - m_{jj}/\sqrt{s})^{P_1}}{(m_{jj}/\sqrt{s})^{P_2+P_3 \times \log(m_{jj}/\sqrt{s})+P_4 \times \log(m_{jj}/\sqrt{s})^2}} \quad (4.3)$$

1701 where  $P_3$  and  $P_4$  are additional free parameters. As an additional cross check, an alternative fit  
1702 function is also tested:

$$\frac{dN}{dm_{jj}} = \frac{P_0(1 - m_{jj}/\sqrt{s} + P_3(m_{jj}/\sqrt{s})^2)^{P_1}}{(m_{jj}/\sqrt{s})^{P_2}}. \quad (4.4)$$

1703 The fit range is chosen such that it start where the trigger efficiency has reached its plateau  
1704 to avoid bias from trigger inefficiency, and extends to the bin after the highest  $m_{VV}$  mass point.  
1705 The binning chosen for the fit follows the detector resolution as in [63, 64]. Before unblinding the  
1706 signal region, we check that the QCD dijet invariant mass spectrum is expected to be smooth from  
1707 the distribution in QCD MC as well as exercise the F-test in QCD MC and in a data sideband.

1708 The fits to data in the signal region using the different fit functions, are shown in Figure 4.21,  
1709 and the corresponding F-test output are given in Table 4.2 through Table 4.4. The findings can  
1710 be summarized as follows: for the WW enriched category a 2 parameter fit is sufficient to describe  
1711 the data in both the high- and low-purity categories. In the WZ category, a two parameter fit

is sufficient in the high-purity category, while three parameters are needed for the low-purity category. For the ZZ category, a 3 parameter fit is needed for both purity categories. The 2 and 3 parameters fit functions as defined in Equation B.2 will therefore be used to model the background component in the simultaneous signal and background fit.

WW enriched, HP				WW enriched, LP			
Function	Residuals	$\chi^2$	ndof	Function	Residuals	$\chi^2$	ndof
2 par	0.034	9.279	11	2 par	0.270	13.462	17
3 par	0.034	9.160	10	3 par	0.300	13.819	16
4 par	0.040	8.030	9	4 par	0.324	13.680	15
Fishers23	-0.053	CL	1.0	Fishers23	-1.723	CL	1.0
Fishers34	-1.456	CL	1.0	Fishers34	-1.191	CL	1.0

**Table 4.2:** Residuals,  $\chi^2$ , and degrees of freedom for the WW enriched HP and LP categories. A 2 parameter fit is needed to describe the data in both categories.

WZ enriched, HP				WZ enriched, LP			
Function	Residuals	$\chi^2$	ndof	Function	Residuals	$\chi^2$	ndof
2 par	0.039	9.105	16	2 par	1.016	17.602	20
3 par	0.047	7.915	15	3 par	0.270	11.424	19
4 par	0.048	8.370	14	4 par	0.269	11.421	18
Fishers23	-2.598	CL	1.0	Fishers23	55.258	CL	0.0
Fishers34	-0.491	CL	1.0	Fishers34	0.078	CL	0.783

**Table 4.3:** Residuals,  $\chi^2$ , and degrees of freedom for the WZ enriched HP (left) and LP (right) categories. A 2 parameter fit is sufficient to describe the data in the high-purity category, while three parameters are needed for the low-purity category.

ZZ enriched, HP				ZZ enriched, LP			
Function	Residuals	$\chi^2$	ndof	Function	Residuals	$\chi^2$	ndof
2 par	0.220	9.901	11	2 par	0.448	18.832	15
3 par	0.140	9.511	10	3 par	0.121	17.463	14
4 par	0.124	9.781	9	4 par	0.118	17.394	13
Fishers23	6.302	CL	0.029	Fishers23	40.438	CL	0.0
Fishers34	1.246	CL	0.290	Fishers34	0.356	CL	0.56

**Table 4.4:** Residuals,  $\chi^2$ , and degrees of freedom for the ZZ enriched LP and HP categories. A 3 parameter fit is sufficient to describe the data in both categories.

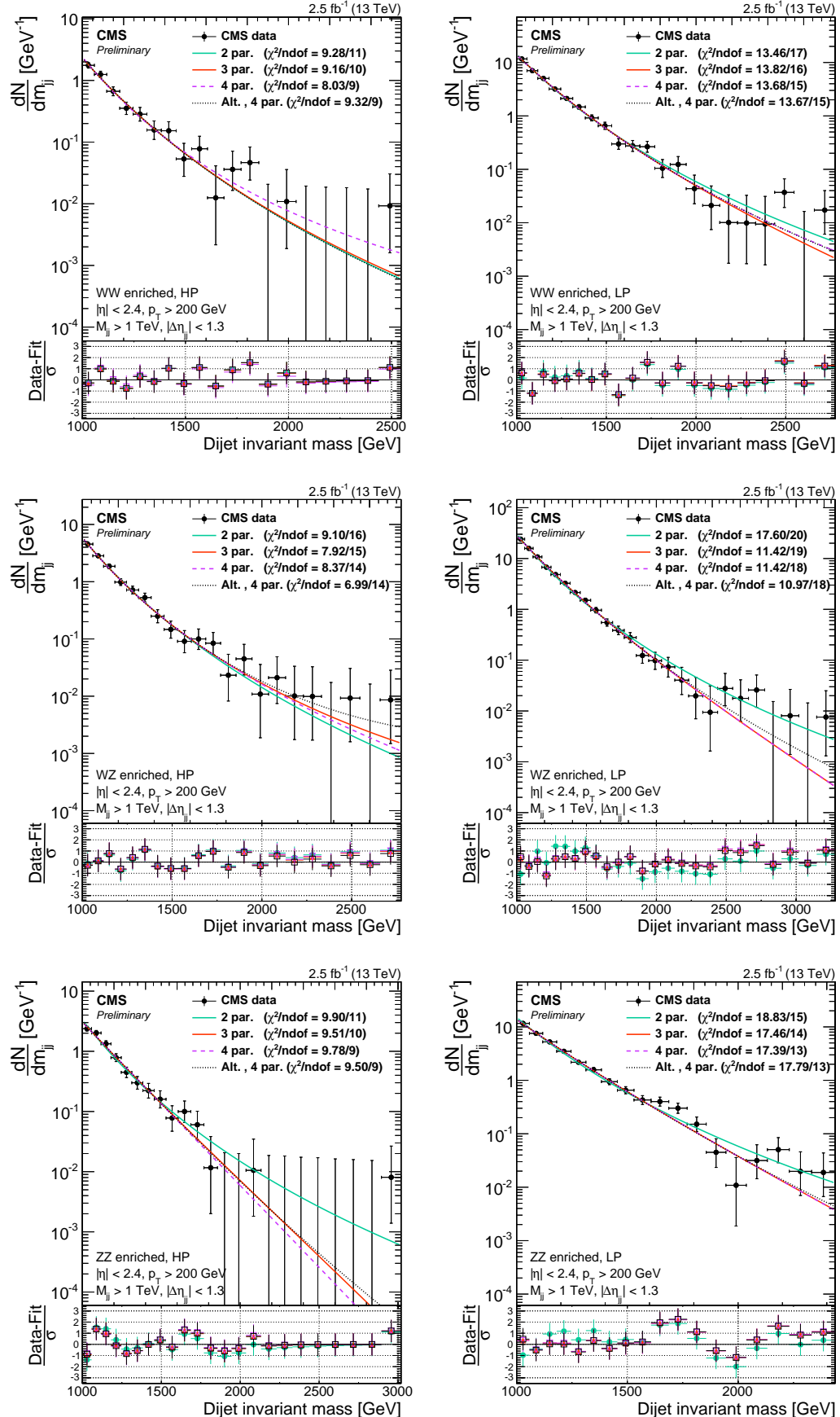
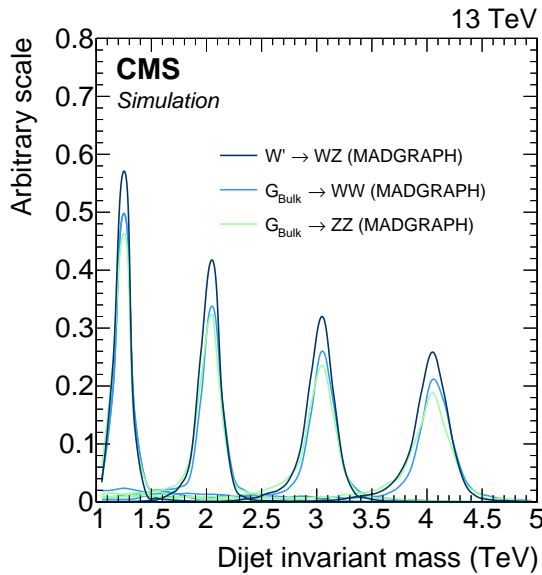


Figure 4.21: Fitted dijet mass spectrum in the different mass and purity categories in data for

### 1716 4.1.6 Signal modeling

1717 The signal shape is extracted from signal MC with masses in the range from 1 to 4 TeV. A  
1718 linear interpolation provides shapes for the mass points in between in steps of 100 GeV. From  
1719 these shapes, pdf models are constructed as composite models with a Gaussian core due to  
1720 detector resolution and an exponential tail to account for parton distribution function effects.  
1721 Parametric shape uncertainties due to jet energy scale and resolution uncertainties are inserted by  
1722 variations of the Gaussian peak position and width. The dijet invariant mass shape for different  
1723 benchmark model signals are shown in Figure 4.22. The signal and background components are  
then simultaneously fitted to the data points.



**Figure 4.22:** Dijet invariant mass from signal MC used to extract the signal shape. Here for 1.2, 2, 3 and 4 TeV resonances.

### <sup>1725</sup> 4.1.7 V-tagging scale factors

<sup>1726</sup> As seen in Figure , some discrepancy is observed in the  $\tau_{21}$  distribution between data and MC.  
<sup>1727</sup> This can lead to a bias in the signal efficiency estimation and we therefore measure the real data  
<sup>1728</sup> signal efficiency in an orthogonal data sample. The W-tagging efficiency is measured using real  
<sup>1729</sup> boosted W-jets in a semi-leptonic  $t\bar{t}$  enriched data sample. This region is mainly quark-enriched,  
<sup>1730</sup> as opposed to the QCD gluon-enriched region we saw previously, and substructure variables are  
<sup>1731</sup> better described here. The sample is obtained through requiring a final state compatible with  
<sup>1732</sup> two b-jets and two W bosons, where one of the bosons decay leptonically and the other one  
<sup>1733</sup> hadronically. There are several good reasons to use this channel: Top quark pair production  
<sup>1734</sup> events are plentifully produced at the LHC, we can ensure a high purity of the sample through  
<sup>1735</sup> high-energy lepton, b-tag and missing energy requirements and lastly we can ensure that the  
<sup>1736</sup> W jets are boosted by requiring the leptonic leg, together with the hadronic W candidate, to  
<sup>1737</sup> have high transverse momentum. The final state is illustrated in Figure 4.23, with the object of  
<sup>1738</sup> interest being the AK R=0.8 jet containing the two quark daughters of the hadronically decaying  
W.

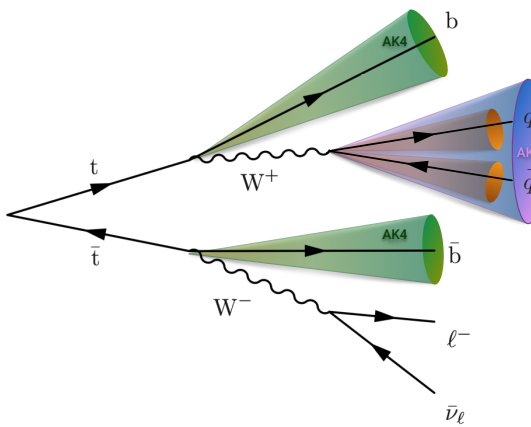


**Figure 4.23:** A top quark pair decaying into two b quarks and two W bosons, one of which decays leptonically and one on which decays hadronically

<sup>1739</sup>

### <sup>1740</sup> Event selection

The W can decay either to an electron or a muon, both final states (“channels”) are used in the analysis. We select events through triggering and selections on the leptonic leg. First, we require a high-energy lepton at trigger level, with an online  $p_T$  above 45 GeV for the muon and

135 GeV for the electron. This requires an offline muon(electron)  $p_T$  threshold of 53(120) GeV. The leptons are further required to pass the lepton requirements defined in Section 3.2.2 and Section 3.2.2, and events containing additional leptons (passing the same ID requirements, but looser cuts as defined in Table 4.5) are vetoed. Offline, we further require a high missing energy of 40(80) GeV in the muon(electron) channel. To insure a high signal (boosted hadronic W) purity, the leptonic W four-vector is reconstructed such that we can put tight momentum requirements on the leptonic leg (ensuring that both tops, and therefore vector bosons, have a high momentum). The leptonic W is reconstructed in two steps: First, the unknown z component of the neutrino momentum must be solved for through a second order equation assuming the real W mass

$$M_W^2 = m_\ell^2 + 2(E_\ell E_\nu - p_{x_\ell} p_{x_\nu} - p_{y_\ell} p_{y_\nu} - p_{z_\ell} p_{z_\nu}) = (80.4)^2.$$

1741 This results in a completely defined neutrino four-vector, which is then added to the lepton  
 1742 four-vector. The sum of the two defines the leptonic W and its momentum is required to be  
 1743 greater than 200 GeV.

1744 Further, we require at least one AK R=0.4 jet to be b-tagged with the Combined Secondary  
 1745 Vertex (CSV) algorithm [66, 67]. This algorithm exploits the relatively long lifetime of b quarks  
 1746 leading to the presence of a displaced vertex, in order to distinguish between jets originating from  
 1747 b quarks to those originating from light flavor quarks. More information on the CSV algorithm  
 1748 can be found in [66, 67]. The reason for requiring only one b-tagged jet is to ensure a high  
 1749 selection efficiency.

1750 Finally, we require at least one AK R=0.8 jet in the event with a momentum greater than 200  
 1751 GeV which will be the hadronic W candidate. It's pruned jet mass is required to be between 40  
 1752 GeV and 150 GeV. After reconstructing and selecting all our objects, a set of angular selections  
 1753 are applied to ensure a diboson like topology. These are the following:

- 1754     •  $\Delta R(l, W_{AK8}) > \pi/2$
- 1755     •  $\Delta\phi(W_{AK8}, E_T^{\text{miss}}) > 2$
- 1756     •  $\Delta\phi(W_{AK8}, W_{lep}) > 2$

1757 With these requirements, we have a nearly pure sample of  $t\bar{t}$  events, with a small contamination  
 1758 from single top, W+jets and VV events. A summary of the final selection criteria is presented in  
 1759 Table 4.5. The pruned jet mass and  $\tau_{21}$  variables in data and in MC are shown in Figure 4.24.

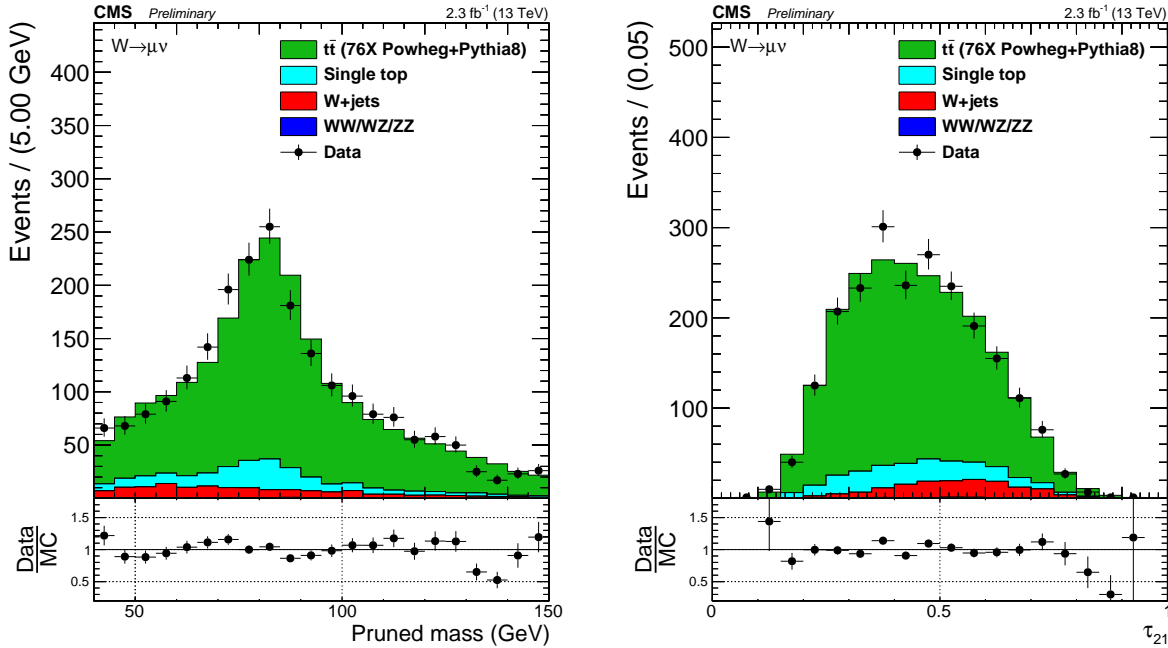
Selection	Value	Comments
<b>Tight Lepton selection</b>		
Electron $p_T$	$p_T > 120 \text{ GeV}$	
Muon $p_T$	$p_T > 53 \text{ GeV}$	
Electron $\eta$	$ \eta _{\text{SC}} < 2.5$ except $[1.4442, 1.566]$	Veto ECAL barrel-endcap transition.
Muon $\eta$	$ \eta  < 2.1$	
<b>Loose Lepton selection</b>		
Electron $p_T$	$p_T > 35 \text{ GeV}$	
Muon $p_T$	$p_T > 20 \text{ GeV}$	
Electron $\eta$	$ \eta _{\text{SC}} < 2.5$ except $[1.4442, 1.566]$	Veto ECAL barrel-endcap transition.
Muon $\eta$	$ \eta  < 2.4$	
<b>AK8 jet selections</b>		
Jet $p_T$	$p_T > 200 \text{ GeV}$	For hadronic
Jet $\eta$	$ \eta  < 2.4$	W reconstruction
<b>AK4 jet selections</b>		
Jet $p_T$	$p_T > 30 \text{ GeV}$	Used for b-tag
Jet $\eta$	$ \eta  < 2.4$	jet selection
<b><math>E_T^{\text{miss}}</math> selections</b>		
$E_T^{\text{miss}}$ (electron channel)	$E_T^{\text{miss}} > 80 \text{ GeV}$	
$E_T^{\text{miss}}$ (muon channel)	$E_T^{\text{miss}} > 40 \text{ GeV}$	
<b>Boson selections</b>		
Pruned jet mass	$40 < m_p < 150 \text{ GeV}$	
Leptonic W $p_T$	$p_T > 200 \text{ GeV}$	
Hadronic W $p_T$	$p_T > 200 \text{ GeV}$	
<b>Veto</b>		
Number of loose electrons	0	
Number of loose muons	0	
Number of b-tagged jets	$> 0$	CSV medium working point
<b>Angular selections</b>		
$\Delta R(l, W_{\text{AK8}})$	$> \pi/2$	
$\Delta\phi(W_{\text{AK8}}, E_T^{\text{miss}})$	$> 2$	
$\Delta\phi(W_{\text{AK8}}, W_{\text{lep}})$	$> 2$	

Table 4.5: Summary of the final semi-leptonic  $t\bar{t}$  selections.

## 1760 Fitting procedure

1761 For this measurement, what we are interested in is to extract and compare the W-tagging efficiency  
 1762 of the combined jet mass and  $\tau_{21}$  selection in data and in MC. We are additionally interested in  
 1763 the difference in jet mass scale (mean of the W jet mass peak) and jet mass resolution (width of  
 1764 W jet mass peak), as this also affects the signal jet mass shape and therefore efficiency. In order  
 1765 to study these variables, we look at the pruned jet mass spectrum between 40 and 150 GeV in  
 1766 two regions:

- 1767 • Pass region:  $0 < \tau_{21} \leq 0.45 \sim \text{high purity}$
- 1768 • Fail region:  $0.45 < \tau_{21} \leq 0.75 \sim \text{low purity}$



**Figure 4.24:** Distribution of pruned jet mass (left) and n-subjettiness (right) in the  $t\bar{t}$  control sample.

Our goal is to understand what the real fraction of merged W jets is in the pass category and in the fail category, assuming that the sum of the two correspond to a 100% selection efficiency (the amount of W jets falling outside of this region is negligible). The strategy is the following: We first derive probability density functions (PDFs) which describe the distribution of fully merged W jets and non-W jets in  $t\bar{t}$ , both in the pass and in the fail region. The PDFs describing real W jets and non-W jets are added with a fraction which is left floating: the fit decides what the fraction of real W to non-W jets is in the pass and in the fail region. As simultaneous fit of pass and fail is then performed (using the two composite W +non-W PDFs), where the fraction of real W jets in both pass and fail is constrained such that, if the signal efficiency in pass is  $\epsilon_S$ , the signal efficiency in fail is  $(1 - \epsilon_S)$ . This is done by letting the normalization of the PDF describing real W jets in the pass category, be defined as the *total* real W yield in pass and fail combined multiplied by some fraction,  $\epsilon_S$ . The normalization of the PDF describing real W jets in the fail category is then the total real W yield multiplied by  $(1 - \epsilon_S)$ .

To understand which part of the  $t\bar{t}$  jet mass distribution contains “real” merged Ws and which are only pure combinatorial background, non-PWs, we start from  $t\bar{t}$  MC. By matching the AK8 jet with quarks coming from the hadronic W at generator level, in a cone of  $\Delta R < 0.8$ , we can

access the real merged W and non-merged W shapes. The real W and non-W PDFs for jets that pass and fail the N-subjettiness selection  $\tau_{21} < 0.45$ , are found to be well described by the following functions:

$$f_{\text{bkg}}(m_j) = F_{\text{ExpErf}} = e^{c_0 m_j} \cdot \frac{1 + \text{Erf}((m_j - a)/b)}{2} \quad \sim \text{ for non-W jets in both pass and fail}$$

$$f^{\text{sig}}(m_j) = F_{\text{Gaus}}(m_j) + F_{\text{ExpErf}}(m_j) \quad \sim \text{ for real W jets in both pass and fail}$$

1769 Figure 4.25 shows the fitted PUPPI softdrop mass spectrum for  $t\bar{t}$  real W (top) and non-W  
1770 (bottom) distributions for jets that passed (left) and failed (right column) the N-subjettiness  
1771 selection PUPPI  $\tau_{21} < 0.4$ . The corresponding plots for the jet pruned mass can be found in  
1772 Figure B.1.

These shapes constitute the fit functions used for the simultaneous fit. As can be seen from the fit to real W jets in the pass region, the distribution is not purely Gaussian and have a tail at higher groomed masses. This tail depends on the matching requirements used to define real merged W jets and is unphysical. We therefore assume that the distribution of real W-jets can be described by a Gaussian only, allowing the exponential error function used to describe non W-jets to cover the contribution from the tails, hereby taking the number of real W-jets as the integral of the Gaussian shape only. This eliminates two additional fit functions, corresponding to six free parameters from the fit. In older estimations of the W-tagging scale factor based on the same procedure [68]), the functions used to describe the tail of the real W-jet distributions were also taken into account as contributing to the real W-jet tagging efficiency. These two calculations tests two extremes: The new method assumes a Gaussian peak, absorbing the tails into the background function making the fit more robust, while the old method assumes a Gaussian peak with tails estimated from matched MC. The latter uses a more precise definition of real W jets, but a less robust fit. Both methods were investigated and we found that the absorption of tails into the background function resulted in a decrease in the relative uncertainty on the final scale factor of 50 % and an overall improvement on the fit quality, reducing the fit  $\chi^2$  by 15 %. The fit parameters of the functions used to describe non W-jets in both the pass and in the fail region, are further constrained using the values obtained from matched  $t\bar{t}$  MC. The W-tagging scale factors ( $SF_{HP}$ ), for the high purity selection ( $\tau_{21} < 0.45$ ), are then extracted estimating the cut

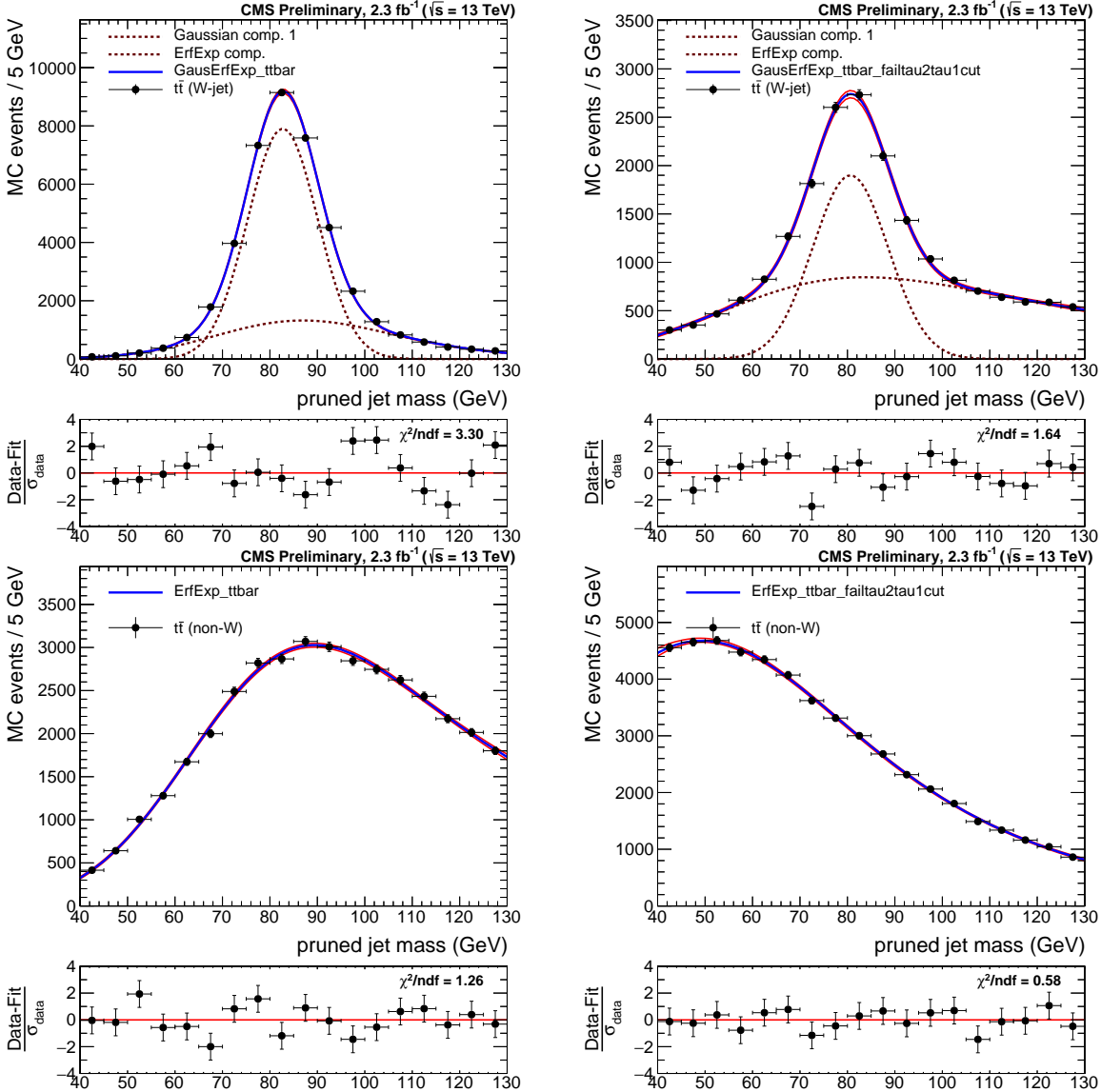


**Figure 4.25:** Fit to the real W (top) and non-W (bottom) pruned jet mass distribution for jets that pass (left) and fail (right) the cut on  $\tau_{21} < 0.45$ .

efficiency ( $\epsilon_{HP}$ ) on both data and simulated samples fitting, simultaneously, pass and fail samples:

$$L_{\text{pass}} = \prod_i^{N_{\text{evt}}^{\text{pass}}} \left[ N_W \cdot \epsilon_{HP} \cdot f_{\text{pass}}^{\text{sig}}(m_j) + N_2 \cdot f_{\text{pass}}^{\text{bkg}}(m_j) + \sum_{j=\text{ST,VV,WJet}} N_{\text{pass}}^j \cdot f_{\text{pass}}^j \right]$$

$$L_{\text{fail}} = \prod_i^{N_{\text{evt}}^{\text{fail}}} \left[ N_W \cdot (1 - \epsilon_{HP}) \cdot f_{\text{fail}}^{\text{sig}}(m_j) + N_3 \cdot f_{\text{fail}}^{\text{bkg}}(m_j) + \sum_{j=\text{ST,VV,WJet}} N_{\text{fail}}^j \cdot f_{\text{fail}}^j \right]$$

where  $N_W$  is the number of real W jets,  $N_2$  and  $N_3$  are the number of combinatorial background events passing and failing the  $\tau_{21}$  cut respectively.  $N_j$  and  $f_j$ , with  $j = \text{ST, VV, WJet}$ , are the normalizations and shapes of the minor backgrounds (single top, VV, W+jets) which are fixed from simulation. The fit functions used are

$$f_{\text{pass}}^{\text{Top}} = F_{\text{ErfExpGaus}}(x) = \frac{1 + \text{Erf}((x - a)/b)}{2} \cdot e^{-(x-x_0)^2/2\sigma^2}$$

$$f_{\text{fail}}^{\text{Top}} = F_{\text{ExpGaus}}(x) = e^{ax} \cdot e^{-(x-b)^2/2s^2}$$

$$f_{\text{pass}}^{\text{VV}} = F_{\text{ExpGaus}}(x) = e^{ax} \cdot e^{-(x-b)^2/2s^2}$$

$$f_{\text{fail}}^{\text{VV}} = F_{\text{ExpGaus}}(x) = e^{ax} \cdot e^{-(x-b)^2/2s^2}$$

$$f_{\text{pass}}^{\text{wjet}} = F_{\text{ErfExp}}(x) = e^{c_0x} \cdot \frac{1 + \text{Erf}((x - a)/b)}{2}$$

$$f_{\text{fail}}^{\text{wjet}} = F_{\text{ErfExp}}(x) = e^{c_0x} \cdot \frac{1 + \text{Erf}((x - a)/b)}{2}$$

<sup>1773</sup> with the corresponding distributions shown in Figure 4.26. The floating parameters of the fit  
<sup>1774</sup> (besides the PDF shape parameters themselves) are the rates  $N_W$ ,  $N_2$  and  $N_3$ , and the mean and  
<sup>1775</sup> sigma of the W-mass distribution defined in  $f_{\text{pass}}^{\text{sig}}(m_j)$  and  $f_{\text{fail}}^{\text{sig}}(m_j)$ . The ratio between data and  
<sup>1776</sup> simulation efficiencies are then taken as the W-tagging scale factor:

$$SF_{HP} = \frac{\epsilon_{HP}(\text{data})}{\epsilon_{HP}(\text{sim})} \quad (4.5)$$

Considering that, both for data and simulation,  $\epsilon_{HP} + \epsilon_{LP} + \epsilon_{fail} = 1$ , the scale factor for low purity category can be defined as:

$$SF_{LP} = \frac{1 - \epsilon_{HP}(\text{data}) - \epsilon_{fail}(\text{data})}{1 - \epsilon_{HP}(\text{sim}) - \epsilon_{fail}(\text{sim})}$$

<sup>1777</sup> where  $\epsilon_{fail}$  is the ratio between the number of events with  $\tau_2/\tau_1 > 0.75$  and the total number of  
<sup>1778</sup> events. As mentioned previously, the number of real W jets with  $\tau_2/\tau_1 > 0.75$  is negligible and

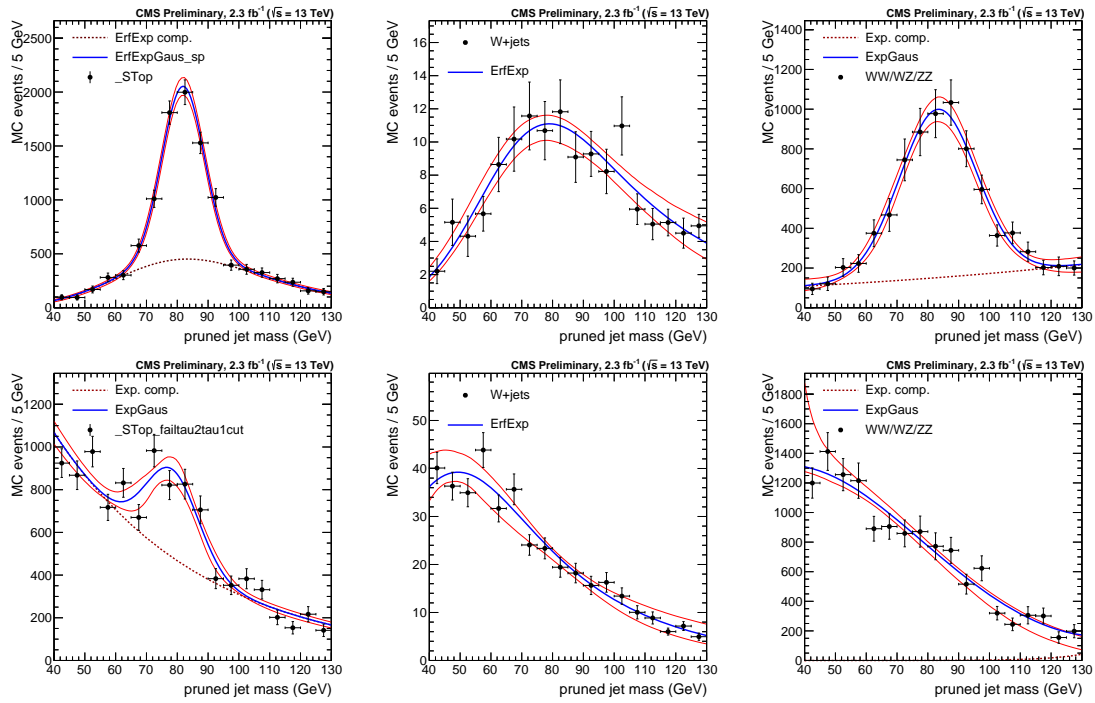


**Figure 4.26:** Fits to the pruned jet mass spectrum for the non-dominant backgrounds (Single top, W+jets and VV respectively) in the pass (top) and fail (bottom) regions.

1779 the definition of the low purity scale factor simplifies to

$$SF_{LP} = \frac{1 - \epsilon_{HP}(\text{data})}{1 - \epsilon_{HP}(\text{sim})} \quad (4.6)$$

## 1780 Systematic uncertainties

1781 As systematic uncertainties, we consider effects due to differences in  $t\bar{t}$  simulation as well as effects  
 1782 due to choice of fit method. The former is evaluated by comparing the extracted scale factor  
 1783 when using  $t\bar{t}$  MC samples produced with different matrix element (ME) and shower generators:  
 1784 POWHEG (NLO) interfaced with PYTHIA8, MADGRAPH (LO) QCD interfaced with HERWIG++  
 1785 and POWHEG interfaced with HERWIG++. The uncertainty due to different ME generators  
 1786 (POWHEG versus MADGRAPH) correspond to 3(13)% and are listed in Table 4.6 as the first quoted  
 1787 systematic uncertainty. The uncertainty due to parton showering (PYTHIA8 versus HERWIG++)  
 1788 is 8.6%, but are not relevant for analyses where no HERWIG++ based simulation is used, as is  
 1789 the case for the search presented in this chapter. For the systematic uncertainty accounting for  
 1790 effects due to choice of fit method, we compare the estimated extracted efficiency in  $t\bar{t}$  MC using

the two different fit models described above: The new model, where the signal is modeled by a Gaussian peak and the tails of the distribution are absorbed in the background fit model, and the old model, including the tails when calculating the fraction of real W jets. Figure 4.27 shows the fits obtained in the pass and fail regions using the two different models. With the new model only the Gaussian component of the fit contributes to the W-tagging efficiency while, with the old model, a Chebyshev component is additionally contributing to the total W-tagging efficiency. The estimated efficiencies obtained using both methods, after being corrected for the fraction of W jets in the tails, agree within 0.3(0.8)% and are listed as systematic uncertainty in Table 4.6. One additional uncertainty is added. As the W-tagging scale factor is evaluated in a  $t\bar{t}$  sample, the transverse momentum range is rather limited. When the W  $p_T$  reaches  $\sim 400$  GeV, the AK8 jet becomes a fully merged top jet with a mass of 170 GeV and a scale factor measurement becomes impossible. However, the jets used in the analyses presented in this thesis have very high transverse momenta, up to 2-3 TeV, and we therefore need an estimate of how the uncertainty on the W-tagging scalefactor changes as a function of  $p_T$ . This is estimated by comparing the difference in tagging between  $G_{\text{bulk}} \rightarrow WW$  signal MC showered by PYTHIA8 and HERWIG++ as a function of  $p_T$ , relative to the difference in tagging efficiency between the two at a  $p_T \sim 200$  GeV. This measurement was performed by a separate analysis team, and found to be  $5.90\% \times \ln(p_T/200 \text{ GeV})$ .

Systematic uncertainties from other sources (lepton identification, b tagging etc.) are less than 0.5% and therefore negligible.

## Results

The simultaneous fit as described above is then performed both for data and for simulation, where we take the ratio of data and MC efficiencies as efficiency scale factors. The corresponding fits are shown in Figure B.4, with the corresponding extracted efficiencies and scale factors summarized in Table 4.6.

Category	Working point	Eff. data	Eff. simulation	Scale factor
HP	$\tau_2/\tau_1 < 0.45$	$0.775 \pm 0.041$	$0.822 \pm 0.033$	$0.94 \pm 0.05 \text{ (stat)} \pm 0.03 \text{ (sys)} \pm 0.003 \text{ (sys)}$
LP	$0.45 < \tau_2/\tau_1 < 0.75$	$0.225 \pm 0.041$	$0.178 \pm 0.033$	$1.27 \pm 0.25 \text{ (stat)} \pm 0.13 \text{ (sys)} \pm 0.008 \text{ (sys)}$

**Table 4.6:** Efficiencies in data and in MC together with the corresponding W-tagging scale factors for the high purity and low purity categories.

We additionally extract the jet mass scale and jet mass resolution, used to scale and smear the jet mass signal shape in the limit setting procedure. These values are taken from the mean  $\langle m \rangle$  and width  $\sigma$  of the Gaussian component of the simultaneous fit in the pass region and are summarized in Table 4.7. Both the jet mass scale as well as the jet mass resolution is larger in

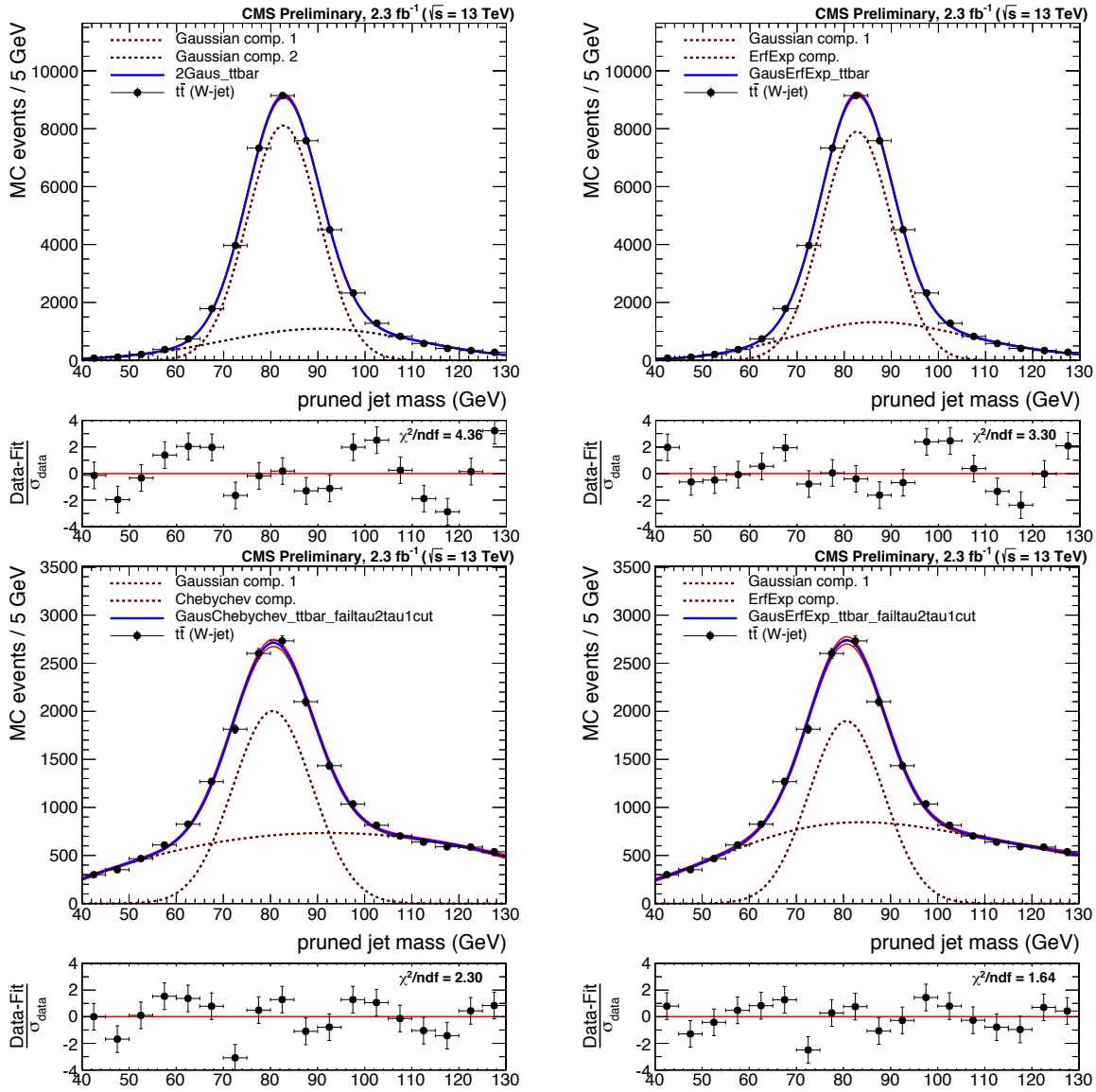


**Figure 4.27:** Fits obtained in the pass (top) and fail (bottom) regions using two different models: An alternative model with tails (top and bottom, left) where the tail component is contributing to the total W-tagging efficiency. When using the default model (top and bottom, right), only the Gaussian component of the fit contributes to the W-tagging efficiency.

simulation than in data with a relative difference of 2 and 10%, respectively. However, the jet mass resolution scale factor has a large uncertainty attached to it and is statistically insignificant (in agreement with unity within uncertainty).

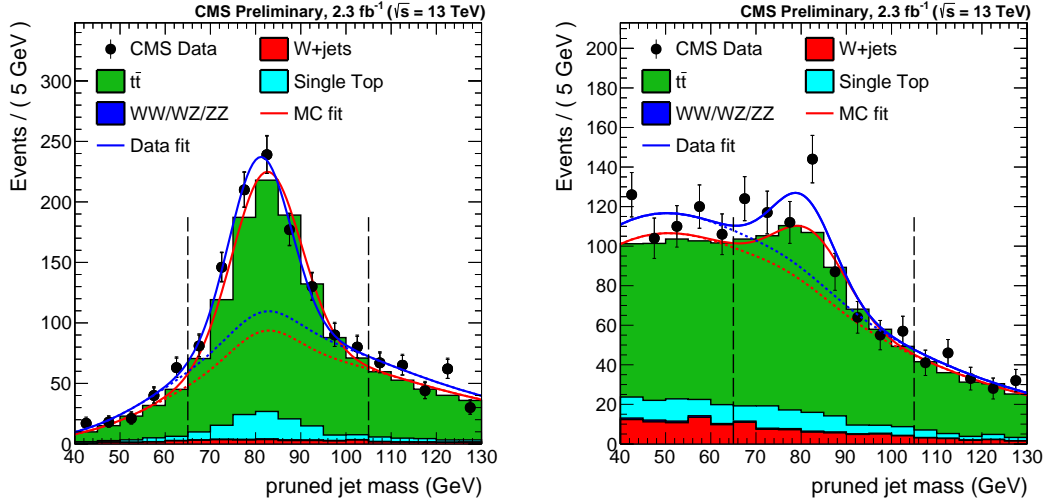


**Figure 4.28:** Pruned jet mass distribution that pass (left) and fail (right) the  $\tau_2/\tau_1 < 0.45$  selection. Results of both the fit to data (blue) and simulation (red) are shown. The background components of the fit are shown as short-dashed lines.

Parameter	Data	Simulation	Data/Simulation
Pruning $\langle m \rangle$	$80.9 \pm 0.6$ GeV	$82.5 \pm 0.1$ GeV	$0.980 \pm 0.007$
Pruning $\sigma$	$6.7 \pm 0.7$ GeV	$7.5 \pm 0.3$ GeV	$0.89 \pm 0.10$

**Table 4.7:** Jet mass scale and resolution in data and in simulation together with the relevant data-simulation scale factors.

### 1822 Impact on search variables

The obtained W-tagging scale factors are used as a scale of the signal yield. As we require two W-tagged jets, either HPHP or HPLP, the actual scale factors for the high-purity signal yield is  $SF_{HP} \times SF_{HP}$  and for the low-purity category  $SF_{HP} \times SF_{LP}$ . The signal yields are then

$$N_S^{HP} = N_{\text{HP tot. yield}} \times SF_{HP} \times SF_{HP}$$

$$N_S^{LP} = N_{\text{LP tot. yield}} \times SF_{HP} \times SF_{LP}$$

1823 The uncertainties on the scale factors are considered as anti-correlated between the HP and  
 1824 the LP categories. The jet mass scale and resolution are used to scale and smear the signal  
 1825 Monte Carlo. An uncertainty on the signal yield based on the uncertainty on jet mass scale and  
 1826 resolution is also considered by scaling and smearing the jet mass up and down within the quoted

1827 uncertainties and then recomputing the signal efficiency. The results are listed in Table 4.8.

### 1828 4.1.8 Systematic uncertainties

1829 The uncertainty on the background parametrization is statistical only and is taken as the  
1830 covariance matrix of the dijet fit function. As demonstrated in the F-test, we study different  
1831 background parameterizations and we have found these to be within the fit uncertainty of the  
1832 nominal fit. The remaining uncertainties concern the signal shape and yield and are listed in  
1833 Table 4.8. Jet reconstruction uncertainties affect both the signal yield and the signal shape.  
1834 These are evaluated by rescaling the jet four-momenta according to uncertainties on the jet  
1835 energy scale and resolution and recomputing the signal efficiency. The difference in efficiency  
1836 with and without smearing/scaling is taken as systematic uncertainties, as described above. The  
1837 jet mass/energy scale and resolution also affect the signal shape, and are added as uncertainties  
1838 in the peak position and width of the Gaussian component of the signal PDFs.

Source	Relevant quantity	HP uncertainty (%)	LP uncertainty (%)
Jet energy scale	Resonance shape	2	2
Jet energy resolution	Resonance shape	10	10
Jet energy and $m_{\text{jet}}$ scale	Signal yield	0.1–4	
Jet energy and $m_{\text{jet}}$ resolution	Signal yield	0.1–1.4	
Pileup	Signal yield	2	
Integrated luminosity	Signal yield	2	
PDFs ( $W'$ )	Signal yield	4–19	
PDFs ( $Z'$ )	Signal yield	4–13	
PDFs ( $G_{\text{bulk}}$ )	Signal yield	9–77	
Scales ( $W'$ )	Signal yield	1–14	
Scales ( $Z'$ )	Signal yield	1–13	
Scales ( $G_{\text{bulk}}$ )	Signal yield	8–22	
Jet energy and $m_{\text{jet}}$ scale	Migration	1–50	
V tagging $\tau_{21}$	Migration	14	21
V tagging $p_T$ -dependence	Migration	7–14	5–11

**Table 4.8:** Summary of systematic uncertainties and the quantities they affect. Migration uncertainties result in events switching between the purity/mass categories and changes the efficiency in each category, but do not affect the total signal efficiency.

### <sup>1839</sup> 4.1.9 Results

<sup>1840</sup> The background fits for each analysis category in the data signal region are shown in Figure  
<sup>1841</sup> 4.29. Here a background only fit is performed while, as described above, a simultaneous fit is  
<sup>1842</sup> used for the limit setting procedure. The filled area correspond to the 1 sigma error band of the  
<sup>1843</sup> background fit, obtained using linear error propagation.

<sup>1844</sup> We proceed by setting limits on the cross section of the process  $X \rightarrow VV$ , using the asymptotic  
<sup>1845</sup> CL<sub>S</sub> method as described in Section ???. The binned likelihood is defined as

$$L = \prod_i \frac{\mu_i^{n_i} e^{-\mu_i}}{n_i!} \quad (4.7)$$

<sup>1846</sup> with

$$\mu_i = \sigma \cdot N_i(S) + N_i(B) \quad (4.8)$$

<sup>1847</sup> Here  $\sigma$  is the signal strength scaling the expected number of signal events in the  $i$ -th dijet invariant  
<sup>1848</sup> mass bin  $N_i(S)$ ,  $N_i(B)$  is the expected number of background events in dijet invariant mass bin  $i$   
<sup>1849</sup> and  $n_i$  is the observed number of events in the  $i$ th dijet invariant mass bin. The background per  
<sup>1850</sup> bin  $N_i(B)$  is estimated from the background component of the best signal+background fit to  
<sup>1851</sup> the data points with the signal cross section set to zero. The number of signal events in the  $i$ -th  
<sup>1852</sup> dijet invariant mass bin,  $N_i(S)$ , is then estimated from the signal templates, where only a dijet  
<sup>1853</sup> invariant mass in a 20% window around the resonance mass is considered, containing most of the  
<sup>1854</sup> signal contribution while making sure to keep a good description of the core.

### <sup>1855</sup> 4.1.10 Limits: All-hadronic analysis

<sup>1856</sup> As mentioned in Section 4.1.3, we set limits on three different signal scenarios:  $G_{\text{bulk}} \rightarrow WW$ ,  
<sup>1857</sup>  $G_{\text{bulk}} \rightarrow ZZ$  and  $W' \rightarrow WZ$ , with a  $\tilde{k} = 0.5$  for the  $G_{\text{bulk}}$ . Figure 4.30 shows the asymptotic  
<sup>1858</sup> limits at 95 % confidence level on signal cross section as a function of the resonance mass obtained  
<sup>1859</sup> with  $2.7 \text{ fb}^{-1}$  of 13 TeV CMS data after combining all mass and purity categories (top). The  
<sup>1860</sup> corresponding p-values are shown in the bottom panel.

<sup>1861</sup> The statistics are too low to exclude the excess around 2 TeV observed in the corresponding  
<sup>1862</sup> Run 1 analysis and in addition an under-fluctuation in data is present in this region. The largest  
<sup>1863</sup> excess is observed for a  $G_{\text{bulk}} \rightarrow ZZ$  hypothesis at a resonance mass of 2.8-3 TeV, around  $2.3 \sigma$ .  
<sup>1864</sup> This is driven by the ZZ high-purity category, the category with the lowest statistics, where one  
<sup>1865</sup> event at 3 TeV yields a local significance of  $2.8 \sigma$ . A 3 parameter fit is the default background fit  
<sup>1866</sup> function for this category, however, a 2 parameter fit could also be used to describe these data. In

1867 Figure 4.31 we compare the limits and p-values obtained using a 2 parameter and a 3 parameter  
 1868 fit to describe the background in this category. The significance at 3 TeV is reduced from 2.8  
 1869 to  $1.5\sigma$  with a 2 parameter fit, reflecting the fact that the fit is poorly constrained in the high  
 1870 mass tail due to low statistics. The fit to data using both a 2 and 3 parameter fit in the ZZHP  
 1871 category is shown in Figure 4.32 and we in addition see that the 2 parameter fit lies within the  
 1872 fit uncertainties of the nominal fit.

1873

1874

1875 The lack of constraint on the fit in the dijet invariant mass tail when statistics are very low,  
 1876 is a drawback of a method relying fully on a parametric fit and reduces the analysis sensitivity  
 1877 in the high- $m_{jj}$ region. In Search II (Section 4.2) we will keep taking advantage of the dijet fit,  
 1878 however, the integrated luminosity is  $\sim 15$  times higher, resulting in more datapoints in the  
 1879  $m_{jj}$ tail which further constrains the fit. In Search III (Section 4.3), we will explore alternate  
 1880 methods which allow more control over the background shape across the full mass spectrum.

### 1881 4.1.11 Limits: Semi-leptonic and all-hadronic combination

1882 To maximize the search sensitivity, we combine the results obtained above with those of the  
 1883 corresponding semi-leptonic analysis. We assume the uncertainties on luminosity, V-tagging  
 1884 efficiency, jet mass scale and resolution to be fully correlated.

1885 The obtained exclusion limits are shown in Figure 4.33 shows the resulting expected and  
 1886 observed exclusion limits. As before, we consider a scenario where only either a  $W'$  or  $Z'$  resonance  
 1887 is expected, called the singlet hypothesis (upper two plots). In addition, we set limits on the  
 1888 triplet hypothesis, assuming the  $W'$  and  $Z'$  bosons to be degenerate in mass (bottom left plot).  
 1889 Due to larger branching fraction, the all-hadronic analysis sets stronger upper limits than the  
 1890 semi-leptonic analysis above 1.7 TeV for  $Z'$  and  $> 1.3$  TeV for  $W'$  ( $\mathcal{B}(WW \rightarrow q\bar{q}q\bar{q}) = 44\%$ ,  
 1891  $\mathcal{B}(WW \rightarrow \ell\nu q\bar{q}) = 31\%$ ,  $\mathcal{B}(WZ \rightarrow q\bar{q}q\bar{q}) = 46\%$ , and  $\mathcal{B}(WZ \rightarrow \ell\nu q\bar{q}) = 16\%$ ). The analysis  
 1892 sensitivity for  $G_{bulk}$  is too weak to set limits, but cross sections between 3–1200 fb are excluded.  
 1893 For the HVT model A and B,  $W'$  is excluded below  $< 2.0$  and 2.2 TeV, respectively.  $Z'$  resonances  
 1894 are excluded below  $< 1.6$  (1.7) TeV for HVT model B(A). If assuming a HVT Model A(B) triplet  
 1895 hypothesis, resonances below  $< 2.3 (< 2.4)$  TeV are excluded.

1896 The combined results would therefore just exclude a  $W'$  with a mass around 2 TeV, the  
 1897 favored candidate to explain the 8 TeV diboson excess. However, Bulk Graviton signals were  
 1898 still far from excluded and, with the expected ten times increase in luminosity in 2016, we were  
 1899 excited to keep on searching.

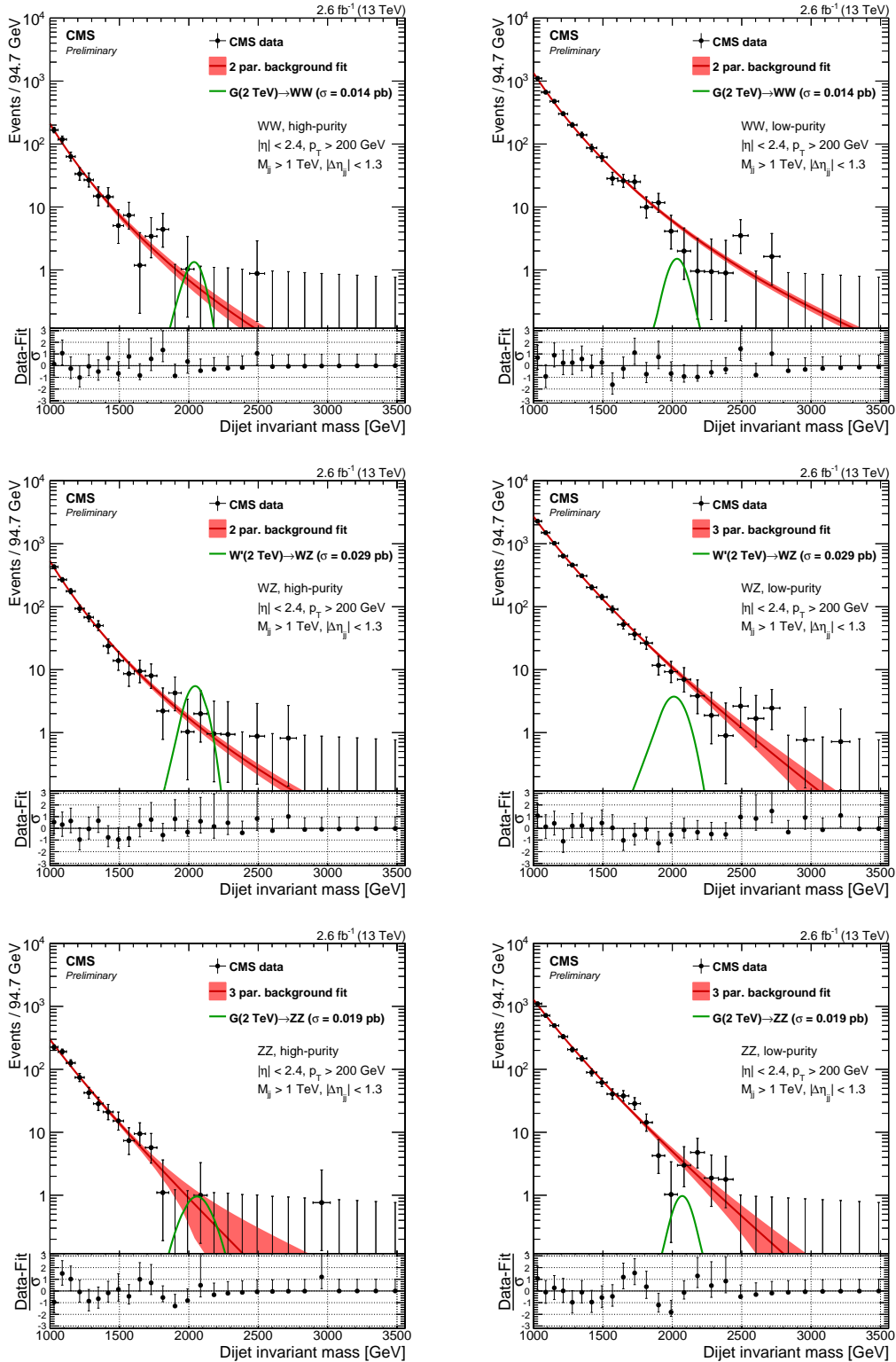


**Figure 4.29:** Fit to data in the signal region using the background fit only for the different mass and purity categories. The filled red area correspond to the 1 sigma statistical error of the fit.

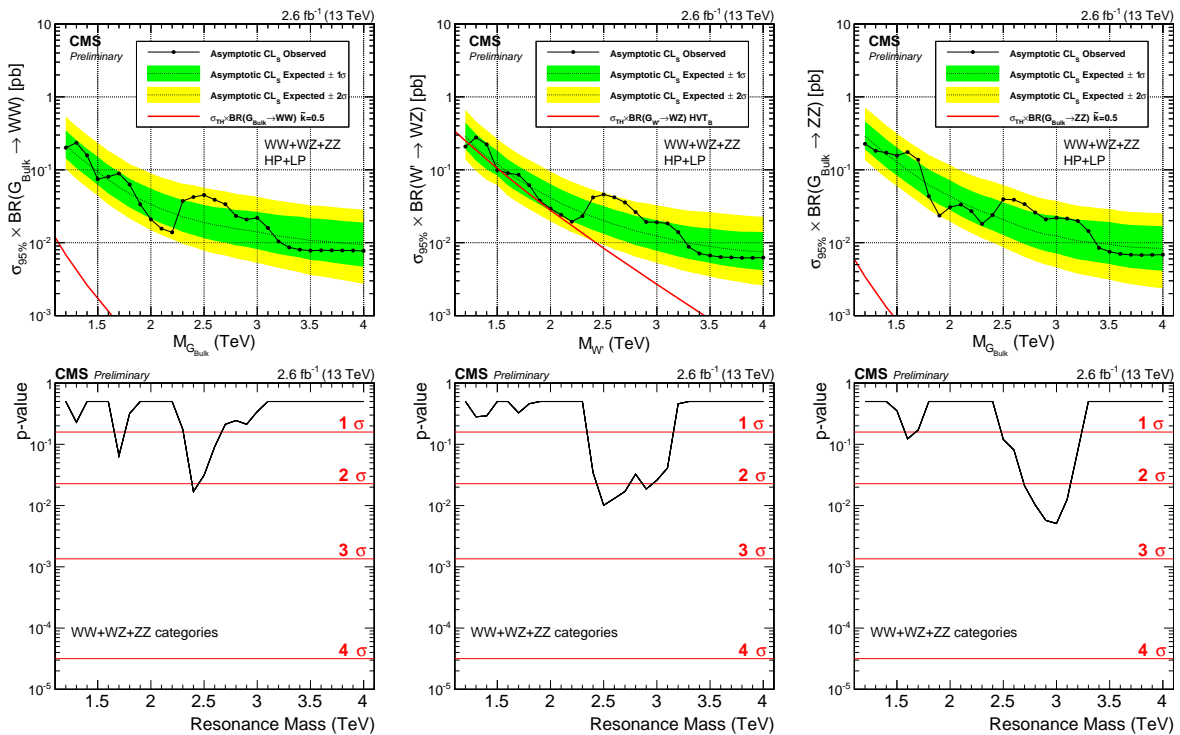


**Figure 4.30:** Expected and observed limits with corresponding p-values obtained using  $2.6 \text{ fb}^{-1}$  of CMS data after combining all mass and purity categories. Here for a Bulk  $G \rightarrow WW$  (left),  $W' \rightarrow WZ$  (middle) and  $G \rightarrow ZZ$  (right) signal.

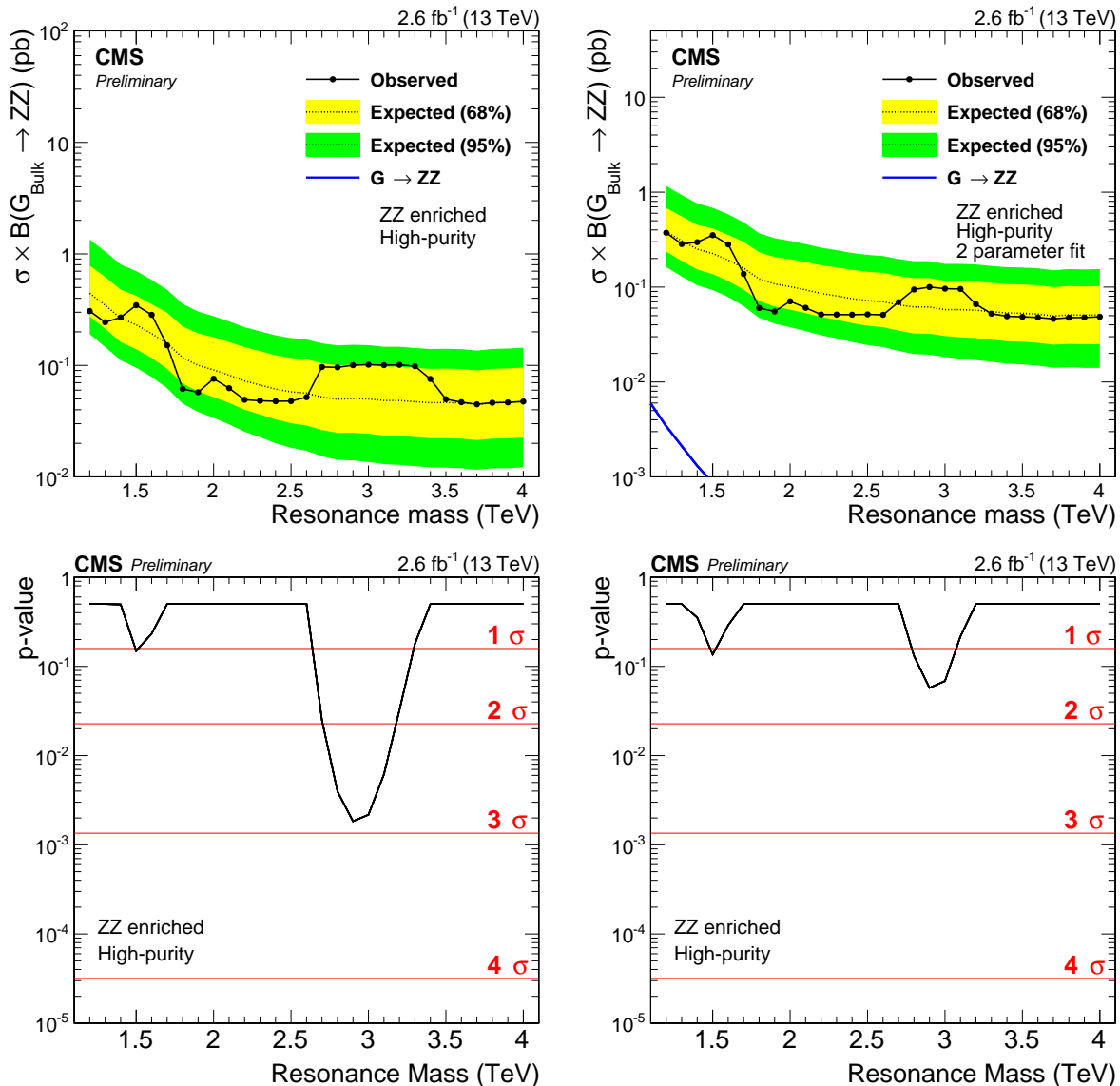


**Figure 4.31:** Expected/observed limits and corresponding p-values obtained in the ZZHP category using a 3 (left) and two (right) parameter fit to describe the background. The significance at 3 TeV is reduced from  $2.8\sigma$  to  $1.5\sigma$ .

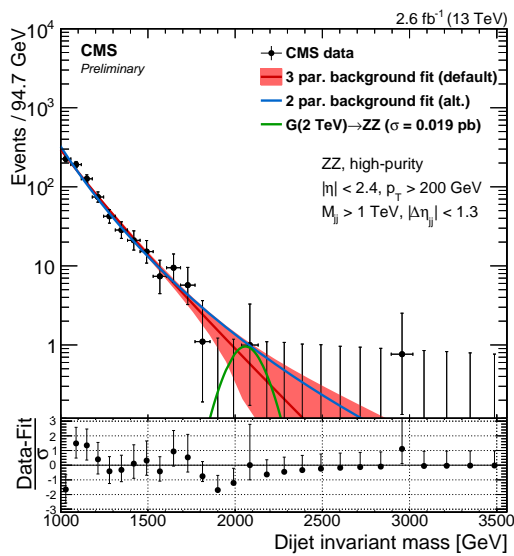


**Figure 4.32:** Background fit to data in the ZZHP category using the default 3 (red) and an alternate 2 (blue) parameter fit to describe the background.

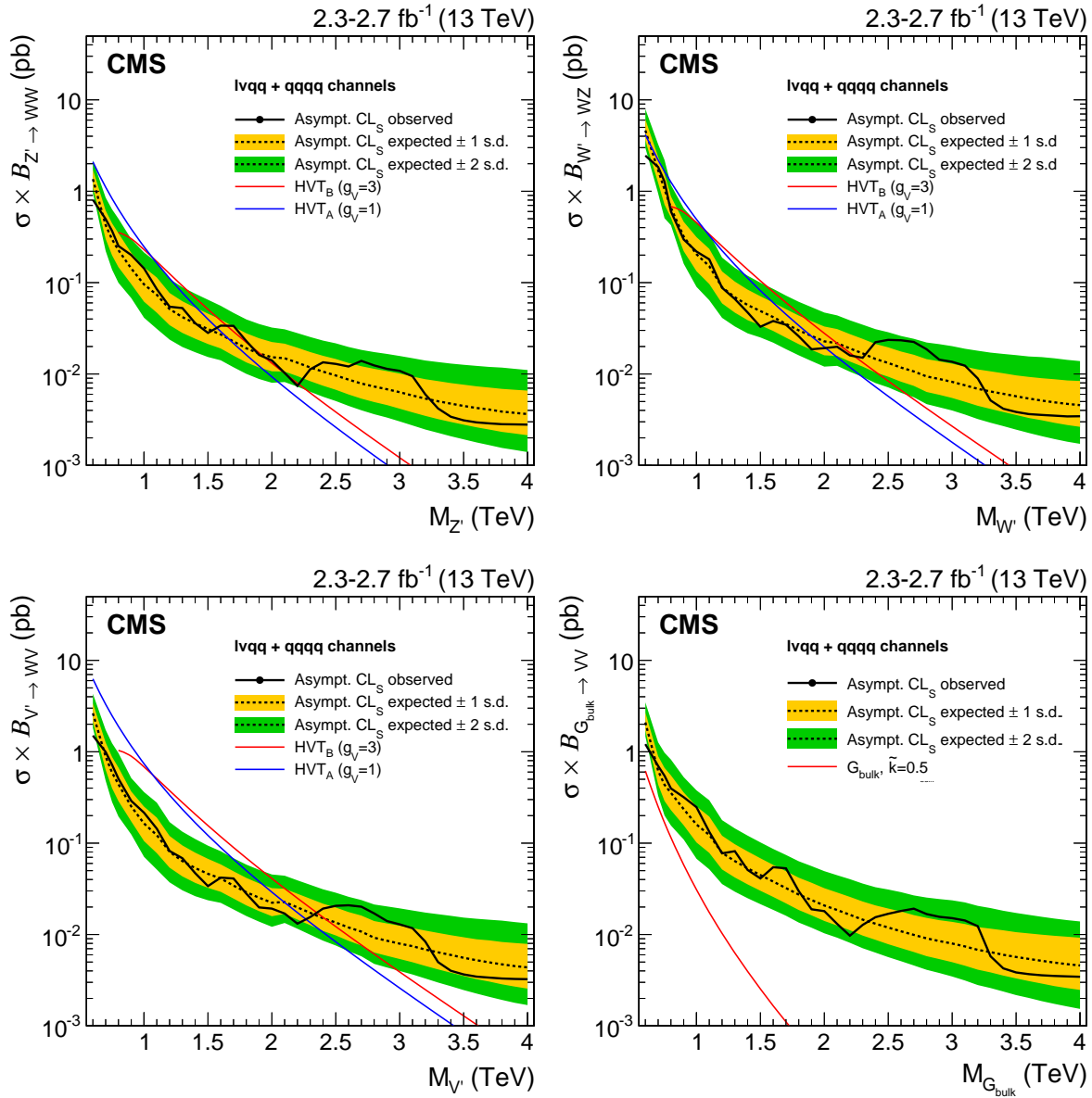


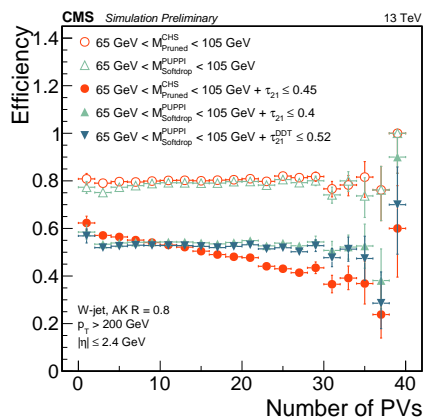
**Figure 4.33:** Observed (black solid) and expected (black dashed) 95% CL upper limits on the production of a narrow-width resonance decaying to a pair of vector bosons for different signal hypotheses. In the upper plots, limits are set in the context of a spin-1 neutral  $Z'$  (left) and charged  $W'$  (right) resonances, and compared with the prediction of the HVT Models A and B. In the lower left plot, limits are set in the same model under the triplet hypothesis ( $W'$  and  $Z'$ ). In the lower right plot, limits are set in the context of a bulk graviton with  $\tilde{k} = 0.5$  and compared with the prediction.

## 1900 4.2 Search II: A new pileup resistant, perturbative safe tagger

1901 With the first 13 TeV diboson resonance search published, we could conclude that more data  
 1902 would be needed in order to fully exclude the observed Run 1 excess. Luckily, 2016 was right  
 1903 around the corner and, with the LHC planning to reduce  $\beta^*$  from 80 cm to 40, the machine  
 1904 was expected to deliver an instantaneous luminosity three times that of the 2015 peak luminosity.  
 1905 Higher instantaneous luminosity, however, meant double the pileup.

1906  
 1907 We knew that a novel pileup subtraction algorithm had been developed, which provided far better  
 1908 pileup and underlying event rejection than the current default (CHS). We also knew that there  
 1909 had been made progress on the theory side in the development of a groomer which was insensitive  
 1910 to the soft divergences of QCD and allowed to accomplish jet grooming in a theoretically calculable  
 1911 way, SoftDrop (mMDT). With more time at hand than in 2015, I therefore decided to pursue  
 1912 a novel W-tagger for this second search. This included work like optimization, development of  
 1913 dedicated jet mass corrections (in use today and recommended by the jet physics object group) as  
 1914 well as validation of the new tagger. The tagger, together with the mass corrections, afterwards  
 1915 became the default W-tagging algorithm in CMS.

1916  
 1917 Search II became the first published analysis to use the novel PUPPI+softdrop algorithm, now  
 1918 default for W-tagging in CMS. Through this search, the tagger was optimized, commissioned and  
 1919 validated, making it available for several analysis to come. In addition, the search was extended  
 1920 to setting limits on three additional signal hypothesis. Two of these were in a final state never  
 1921 before explored at 13 TeV, the  $q^* \rightarrow qV$  single V-tag analyses. Published with  $35.9(12.9)$   $\text{fb}^{-1}$  of  
 1922 2016 data.



### 1923 4.2.1 Towards robust boosted jet tagging

1924 When we first studied W-tagging at 13 TeV in context with the analysis of the 2015 dataset,  
1925 Section 4.2.5, two interesting correlations were observed:

- 1926 1) A strong dependence of the AK8 CHS softdrop ( $\beta = 0$ ) jet mass on jet  $p_T$  and
- 1927 2) a strong dependence of the AK8 CHS  $\tau_{21}$  cut efficiency on pileup.

1928 The reason we studied the softdrop algorithm as an alternative to pruning in 2015 was, besides  
1929 the possibility it would result in a higher signal efficiency, that we knew it had certain favorable  
1930 qualities compared to other groomers: Softdrop removes all sensitivity to the soft divergences of  
1931 QCD, by removing all soft emission, more specifically the non-global logarithmic terms (NGLs)  
1932 in the jet mass [42]. These arise from constellations where, for instance, a soft gluon is radiated  
1933 into the jet cone, as illustrated in Figure 4.34. The consequence of this is that you can calculate

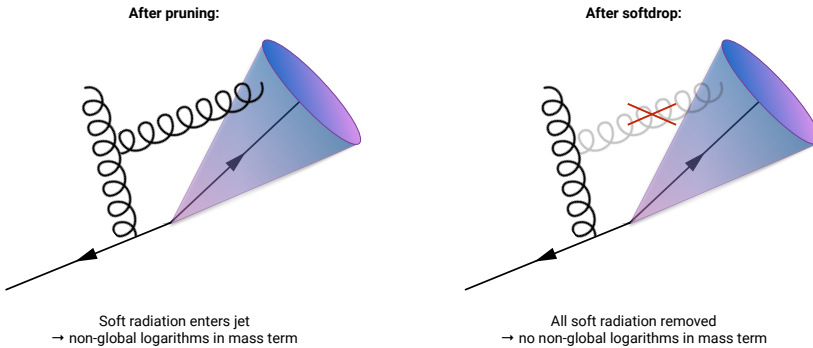


**Figure 4.34:** The pruning algorithm does not remove all soft emission and therefore has non-global logarithmic terms in the jet mass. Softdrop ( $\beta = 0$ ) completely removes soft emissions and is therefore free of non-global logarithms.

1933

- 1934 the softdrop jet mass to way higher precision than what is possible for other grooming algorithms
- 1935 or for the plain jet mass (NGLs are the main reason a full resummation of the plain jet mass
- 1936 beyond NLL (considering e.g multiple-emission effects) accuracy does not exist). Despite this not
- 1937 being a precision measurement analysis, we had theoretically well-motivated reasons for wanting
- 1938 the baseline CMS V-tagger to be softdrop-based. However, despite being less sensitive to soft
- 1939 radiation for QCD jets, signal jets groomed with softdrop were found to be far more sensitive to
- 1940 the underlying event than pruned jets [69]. Figure 4.35 shows the signal efficiency for pruning
- 1941 (left) and softdrop (right) as a function of jet transverse momenta when including FSR only,
- 1942 FSR+ISR, hadronization and hadronization + underlying event. On parton level, as well as after
- 1943 hadronization, the two algorithms perform very similar as a function of  $p_T$ . However, once UE

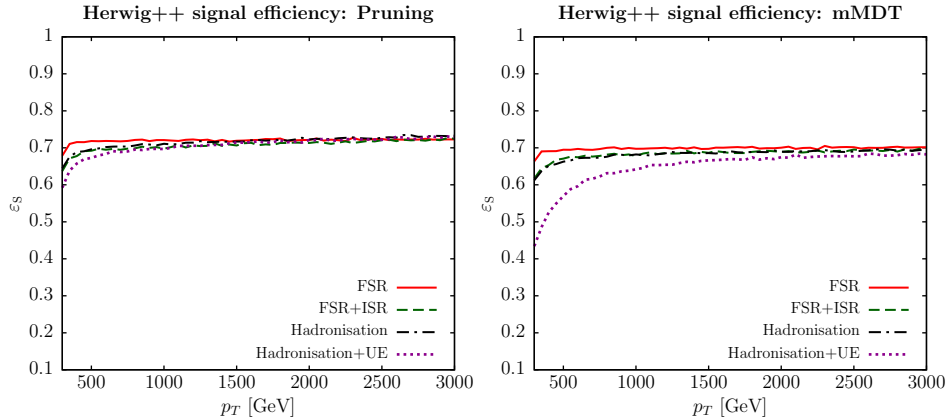


**Figure 4.35:** The signal efficiency for pruning (left) and softdrop (right) as a function of jet  $p_T$  when adding FSR, ISR, hadronization and UE. The UE has a severe impact on the softdrop efficiency for signal jets [69].

contamination is added, the softdrop tagging efficiency is severely affected. This can be explained by the larger effective radius considered by the softdrop algorithm ( $\propto m_V/p_T \sqrt{z_{cut}(1 - z_{cut})}$ ) in comparison to pruning ( $\propto m_V/p_T$ ). This observation corresponds very well with the shift in jet mass we observed for softdrop as a function of  $p_T$  in Section 4.2.5: As the jet  $p_T$  decreases the softdrop effective radius increases and the jet mass mean shifts to higher values, due to absorbing more background radiation. If softdrop would be our new default tagger, a better rejection of pileup and UE contamination would be needed. In parallel to the ongoing theoretical work on groomers, a novel pileup removal algorithm had been proposed: Pileup per particle identification (PUPPI) [34]. Described in detail in Section 3.3.2, PUPPI considers not only charged pileup but rather reweights each particle in the jet with its probability of arising from pileup. PUPPI had proven it self far superior to the current CHS algorithm in terms of jet observables for large radius jets, and therefore seemed like the obvious choice to address both issues listed above: The sensitivity of softdrop regarding UE contamination and the strong pileup dependence of  $\tau_{21}$ . The focus of Search II would therefore be on the commissioning of a novel W-tagger. There are interesting changes and inclusions in the analysis strategy as well: The inclusion of a  $Z' \rightarrow WW$  signal hypothesis and the addition of a completely new analysis, the single V-tag analysis.

## 4.2.2 Analysis strategy

The analysis strategy for this search is conceptually the same as for Search I. In addition, we'll take advantage of the n-subjettiness categorization and do an additional analysis in parallel: A

1963 search for excited quark resonances  $q^*$  [70, 71] decaying to  $qW$  or  $qZ$ . We call this the single V-tag  
 1964 analysis, and the analysis selection only differs in that one jet is not required to pass the V-tag  
 1965 selection (groomed mass and n-subjettiness). The VV analysis is hereby referred to as the double  
 V-tag analysis. The difference between the two analyses is illustrated in Figure 4.36. In addition,

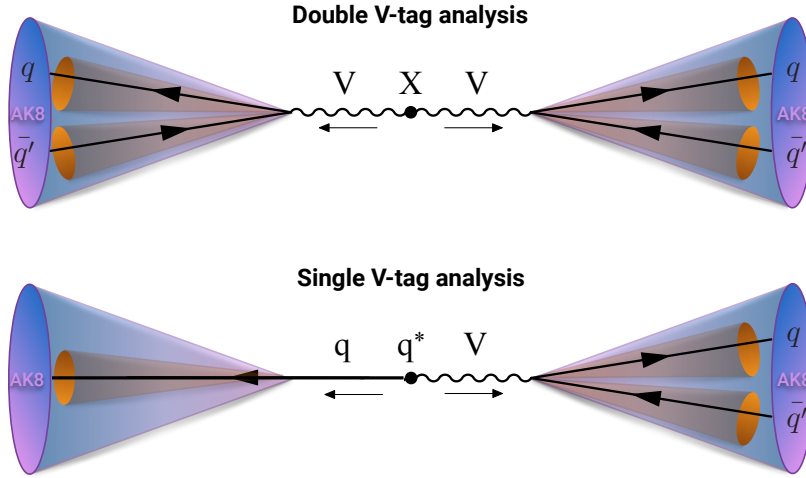


**Figure 4.36:** The double (top) and single (bottom) W/Z-tag analysis.

1966 limits are set on a  $Z' \rightarrow WW$  signal hypothesis in the double V-tag analysis, another 13 TeV first.  
 1967 This analysis was published in two steps: An early Physics Analysis Summary (PAS) based  
 1968 on  $12.9 \text{ fb}^{-1}$  of 2016 data [68], describing the new PUPPI+softdrop based V-tagger as well as  
 1969 the single V-tag analysis, and a second analysis topping up with the full 2016 data [72]. The  
 1970 commissioning of the new W Z-tagger has also been documented in a jet performance Physics  
 1971 Analysis Summary [73]. As the new V-tagger was developed and commissioned in the context  
 1972 of the early analysis, which was also where the single V-tag analysis was first published with 13  
 1973 TeV data, the main emphasis will be on the work presented in CMS-PAS-B2G-16-021 [68]. The  
 1974 second part of the results chapter, Section 4.2.11, includes the results obtained using the full 2016  
 1975 dataset of  $35.9 \text{ fb}^{-1}$ .

### 1977 **4.2.3 Data and simulated samples**

1978 As mentioned above, the analysis of the 2016 dataset was done in two steps: One analysis based  
 1979 on  $12.9 \text{ fb}^{-1}$  of early 2016 data, describing the new W-tagger and single V-tag category, and a  
 1980 second paper topping up with the full 2016 dataset, corresponding to  $35.9 \text{ fb}^{-1}$ .

1981 The G<sub>bulk</sub> and HVT signal samples are modeled in precisely the same way as in 2015. For the  
 1982 single V-tag  $q^*$  samples, we simulate unpolarized boson with a compositeness scale  $\Lambda$  set equal to

1983 the resonance mass. These are generated to leading order using PYTHIA version 8.212 [61].

1984 The background Standard Model processes; QCD, W+jets and Z+jets are all simulated to  
 1985 leading order. V+jets is simulated with MADGRAPH5\_AMC@NLO [60, 74], while three different  
 1986 combinations of matrix element and shower generators is used for QCD as these predictions are  
 1987 known to differ: PYTHIA only, the leading order mode of MADGRAPH5\_AMC@NLO matched with  
 1988 PYTHIA, and HERWIG++ 2.7.1 [49] with tune CUETHS1 [56].

#### 1989 4.2.4 Event selection

##### 1990 Triggering

1991 The triggers used in this analysis are the same ones as in 2015 (see Section 4.1.4), however, due  
 1992 to the new single V-tag analysis, the trigger turn-ons have this time been re-evaluated separately  
 1993 requiring either one or two jets to have an offline softdrop jet mass above 65 GeV.

1994 Figure 4.37 shows the trigger turn-on curves as a function of dijet invariant mass for jets  
 1995 passing one of the three inclusive triggers only, one of the grooming triggers only and when  
 1996 combining all of them. The turn-on curves are shown for all jet pairs passing loose selections as  
 1997 described in Section 4.1.4. Zero, one or two of the two jets is further required to have a softdrop  
 1998 mass larger than 65 GeV.

1999 Including grooming triggers lowers the 99% trigger efficiency threshold by around 50(80) GeV  
 2000 in the single (double) tag category once substructure is requested on the analysis level. Using the  
 2001 or of all triggers, we are safely on the trigger plateau for dijet invariant masses above 955(986)  
 2002 GeV in the double (single) tag category, setting the analysis threshold at a dijet invariant mass  
 2003 of 955 GeV for the double tag analysis and 990 GeV for the single tag analysis. For controlplots,  
 2004 where no groomed mass window is applied, a trigger threshold of 1020 GeV is used.

2005 Trigger efficiencies as a function of the offline softdrop-jet mass for the  
 2006 HLT\_AK8PFJet360\_TrimMass30 trigger are shown in Figure 4.38. Here the jet transverse momen-  
 2007 tum of one of the jets is required to be at least 600 GeV and no other mass cut is applied. This  
 2008 trigger requires one jet to have a trimmed mass above 30 GeV at HLT level and reaches the  
 2009 trigger plateau for groomed-jet masses around 50 GeV. As reference trigger, the prescaled trigger  
 2010 HLT\_PFJet320 is used.

##### 2011 Preselection

2012 The same preselections as in Search I, described in , have been applied: We require two AK R=0.8  
 2013 jets with CHS applied pre-clustering, required to pass the tight jet ID requirement,  $p_T > 200$  GeV

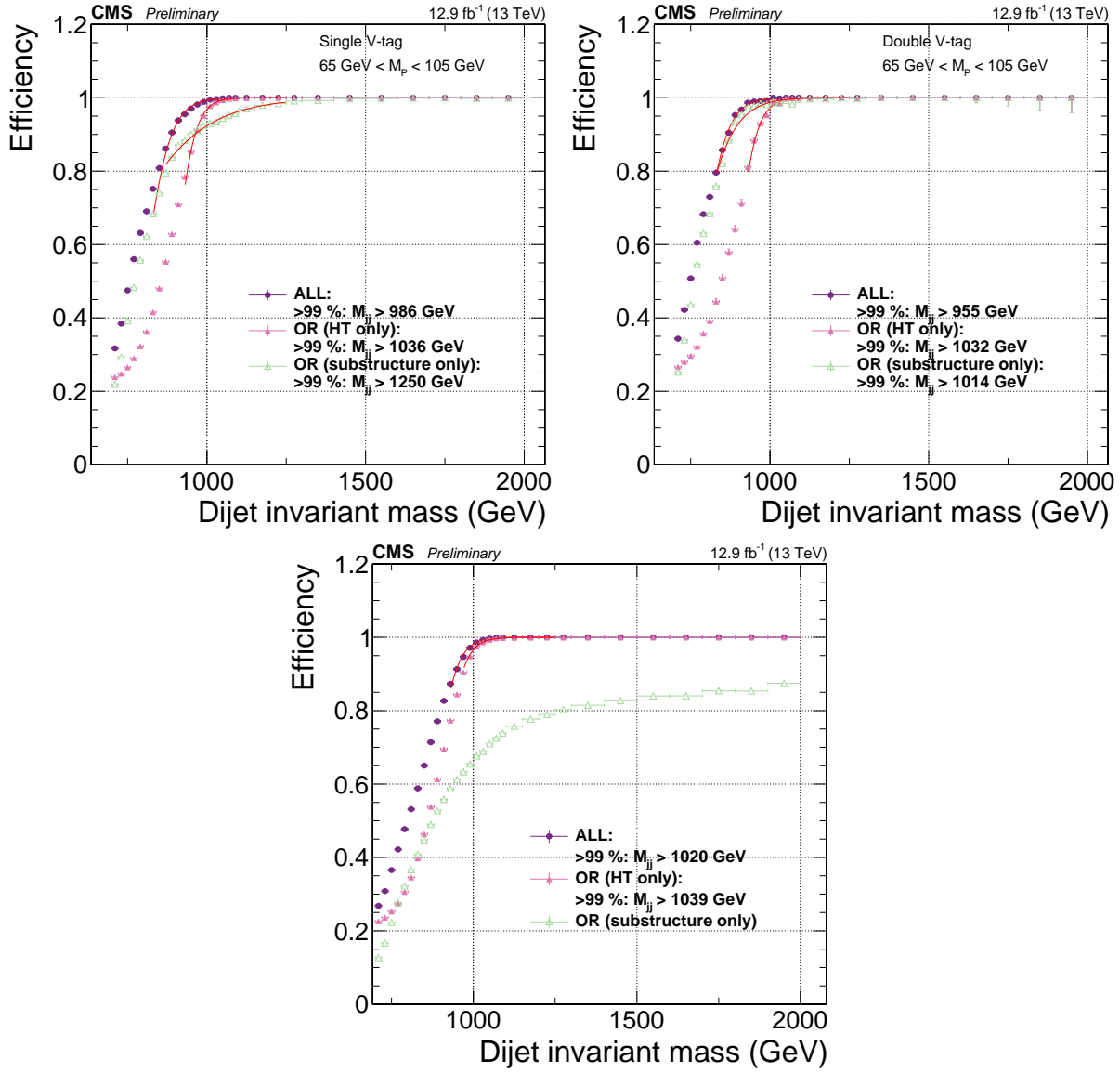


**Figure 4.37:** Comparison of trigger efficiencies for jets passing one of the HT-triggers only (pink), for jets passing one of the grooming-triggers only (green) and for jets passing one of the HT-triggers or one of the grooming triggers (purple). Here as a function of dijet invariant mass for all jet pairs passing loose selections and where one jet has a softdrop mass larger than 65 GeV (top left), both jets have a softdrop mass larger than 65 GeV (top right) and where no mass cut is applied (bottom).

<sup>2014</sup> and  $|\eta| < 2.5$ . The same QCD t-channel suppressing cut of  $|\Delta\eta| < 1.3$  is required together with  
<sup>2015</sup> the following trigger thresholds on the dijet invariant mass:  $m_{jj} > 955 \text{ GeV}$  for the double V-tag  
<sup>2016</sup> and  $990 \text{ GeV}$  for the single V-tag analysis. The jet  $p_T$  (top left),  $\eta$  (top right),  $\Delta\eta_{jj}$  and dijet

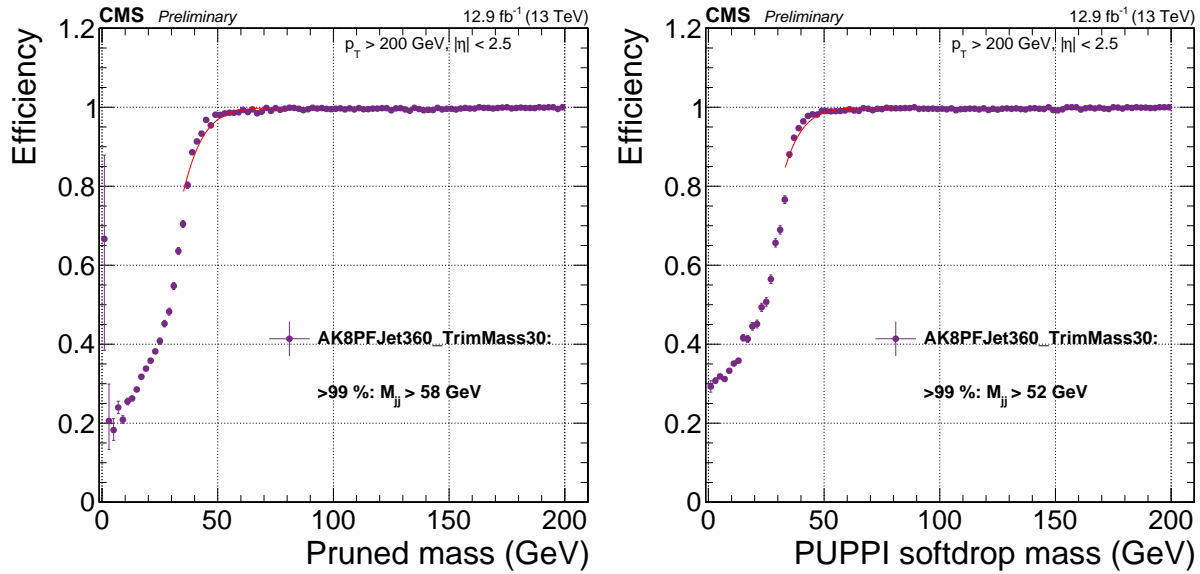


**Figure 4.38:** Efficiency for the HLT\_AK8PFJet360\_TrimMass30 trigger as a function of pruned-jet (left) and softdrop-jet (right) mass for jets with  $p_T > 600 \text{ GeV}$ .

2017 invariant mass (bottom left) for the two leading jets in the event after loose preselections are  
2018 applied is shown in Figure 4.39. A large difference in slope in the jet  $p_T$  and dijet invariant mass  
2019 spectrum depending on the QCD matrix element or shower generator is observed. Pure PYTHIA  
2020 QCD MC describes the data best, while HERWIG++ and MADGRAPH5\_AMC@NLO+PYTHIA tend  
2021 to under- or over-estimate the number of high  $p_T/m_{jj}$  jets, respectively. Pure PYTHIA QCD MC  
2022 is therefore used for all background checks in this analysis.

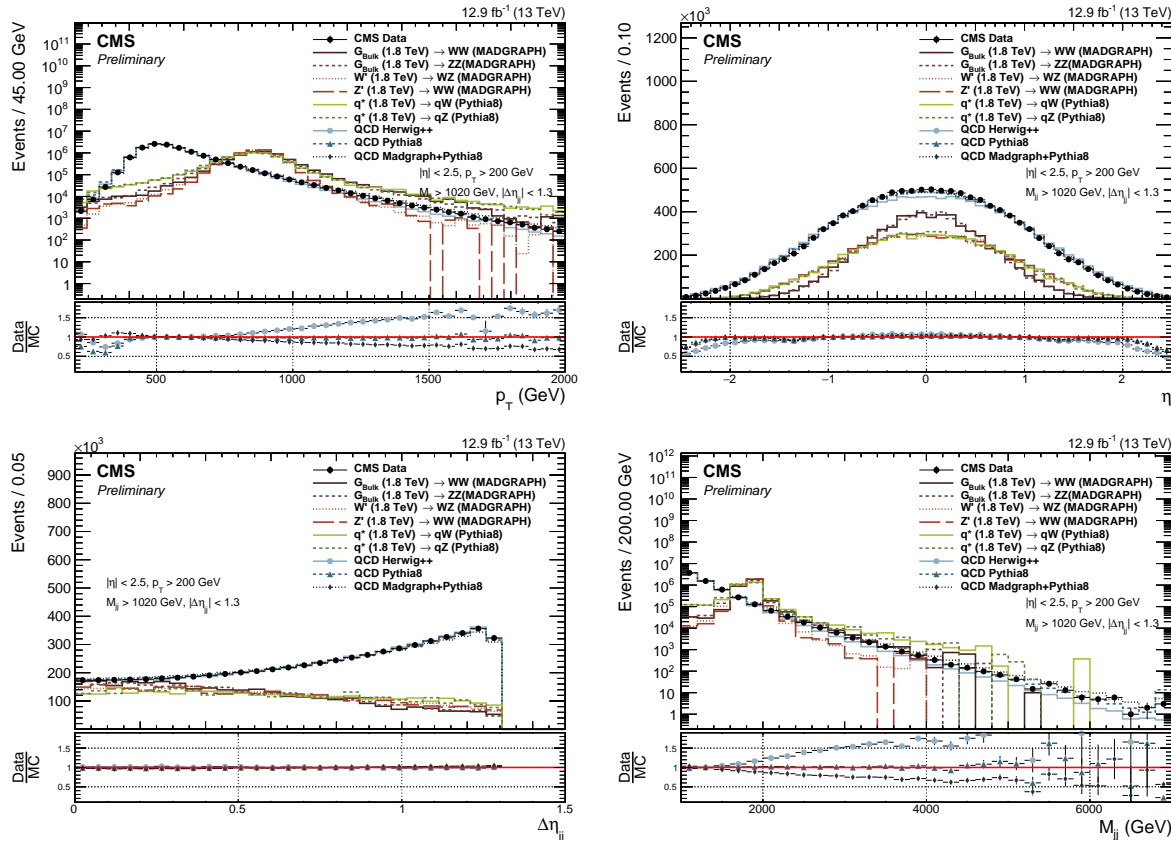


**Figure 4.39:** Jet  $p_T$  (top left),  $\eta$  (top right),  $\Delta\eta_{jj}$  and dijet invariant mass (bottom left) for the two leading jets in the event after loose preselections are applied. The signal is scaled by an arbitrary number.

### 2023 4.2.5 Developing a new W-tagger

2024 As mentioned in the introduction to this chapter, early studies had shown that the PUPPI pileup  
 2025 subtraction algorithm yielded superior resolution on large-cone jet observables like the jet mass.  
 2026 We therefore wanted to check whether the softdrop jet mass, and its observed sensitivity to the  
 2027 Underlying Event and pileup, would be improved if a better pileup subtraction algorithm was  
 2028 applied pre-clustering.

2029 Two interesting observations were made. Softdrop used together with PUPPI pileup subtraction  
 2030 displayed a much smaller  $p_T$ -dependent shift than CHS+Softdrop, as hoped. Figure 4.40  
 2031 shows the PUPPI softdrop mass for W-jets from a 1 TeV ( $p_T \sim 500$  GeV) and 4 TeV ( $p_T \sim 2$  TeV)  
 resonance, exhibiting the desired reduced  $p_T$  dependence in jet mass scale. However, when apply-

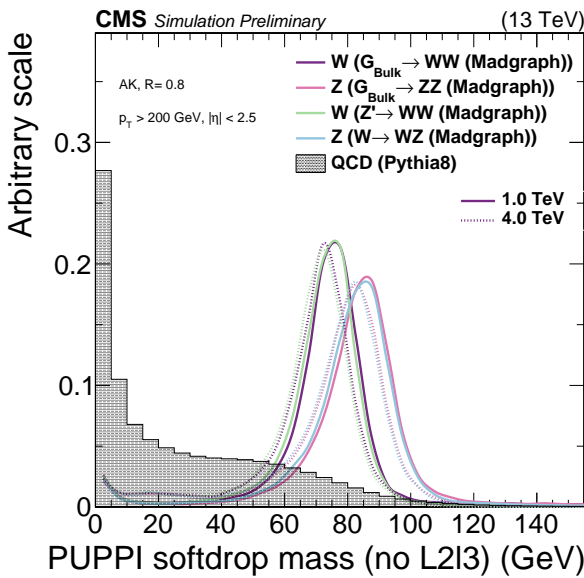


**Figure 4.40:** The PUPPI softdrop jet mass distribution with no jet energy corrections applied

2032  
 2033 ing centrally provided L2 and L3 jet energy corrections (see Section 3.4.3) to the jet groomed  
 2034 mass, as is recommended, a strong  $p_T$  dependence is re-introduced. This effect is not present  
 2035 for the pruned jet mass. Figure 4.41 show the softdrop (top left) and pruned (top right) jet  
 2036 mass distribution with recommended L2L3 corrections applied. Here, the PUPPI+softdrop jet  
 2037 mass shift is significantly increased with respect to what was observed for the uncorrected mass,  
 2038 while CHS+pruned jet mass is stable. This points to the PUPPI jet energy corrections not being  
 2039 optimal for scalar jet mass variables, while they may be good for correcting jet 4-vectors. The jet  
 2040 energy corrections derived for CHS and PUPPI jets as a function of jet  $p_T$  is shown in the bottom  
 2041 plot in Figure 4.41 . A significant slope in JEC as a function of  $p_T$  is measured for PUPPI, while

not present for CHS.

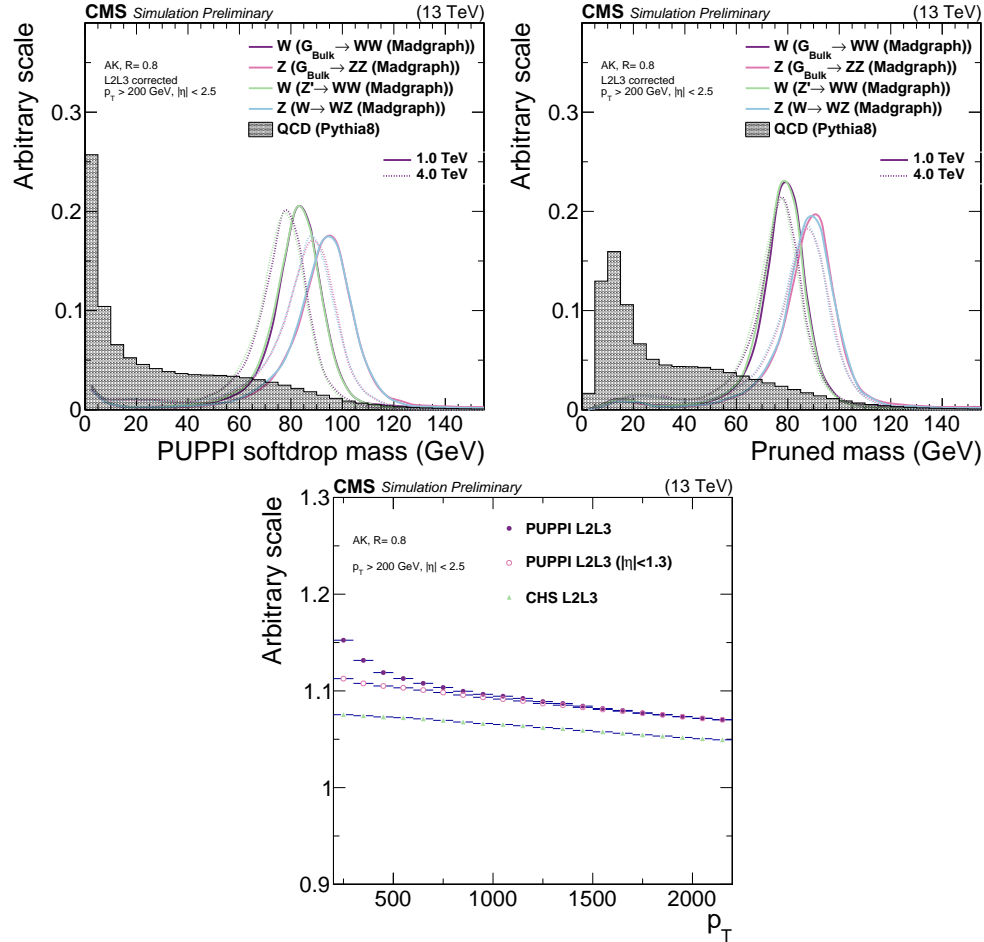


**Figure 4.41:** Top: PUPPI softdrop mass distribution (top left) and pruned jet mass distribution (top right) with L2 and L3 corrections applied. Bottom: The projection of CHS and PUPPI jet energy corrections versus jet  $p_T$ .

2042

### 2043 Dedicated PUPPI softdrop mass corrections

In order to minimize  $p_T$  dependence in the PUPPI softdrop jet mass, all jet energy corrections to the softdrop jet mass are removed. However, this still leaves a residual  $p_T$  dependence and, in addition, the uncorrected mass does not peak at the correct W-mass of 80.4 GeV. Figure 4.42 shows the mean of a Gaussian fit to the uncorrected PUPPI softdrop mass as a function of jet  $p_T$  in two different  $\eta$  bins (smaller or greater than  $|\eta| = 1.3$ ) for W-jets coming from a Bulk Graviton signal sample. A mass shift both as a function of  $\eta$  and  $p_T$  is observed, together with an average

mean significantly lower than the W-mass. In order to use PUPPI+softdrop for W-tagging, we

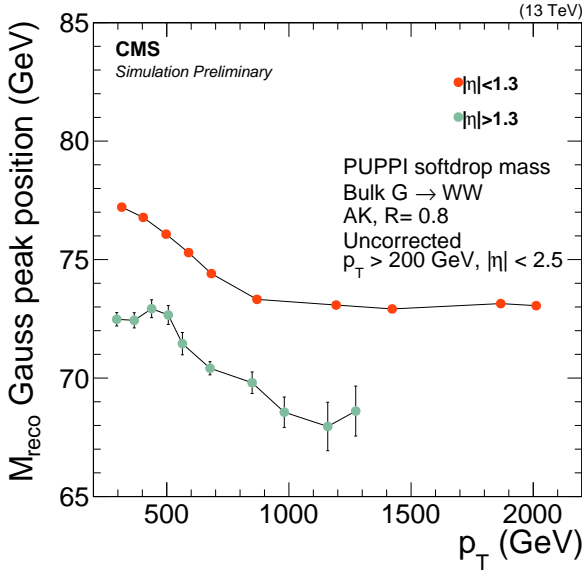


**Figure 4.42:** The mean of a Gaussian fit to the W-jet PUPPI softdrop mass peak as a function of jet  $p_T$  in two different  $\eta$  bins (smaller or greater than  $|\eta| = 1.3$ ). No corrections have been applied to the softdrop mass.

therefore derive dedicated jet mass corrections to compensate for two factors: A generator level  $p_T$ -dependence, as first observed in , and a reconstruction level  $p_T$ - and  $\eta$ -dependence, most likely caused by UE effects and the growing effective softdrop radius at low jet  $p_T$ . Figure 4.43 shows the mean of the generated softdrop mass (left) and the normalized difference in reconstructed and generated softdrop mass (right) as a function of jet  $p_T$ . The shift in generated softdrop mass at lower  $p_T$  is of the order of 2-3% while the difference between reconstructed and generated softdrop mass is a 5-10% effect. The mass shift introduced at generator level is corrected by a fit to  $M_{\text{PDG}}/M_{\text{GEN}}$  as a function of jet  $p_T$ , where  $M_{\text{PDG}} = 80.4$  GeV and  $M_{\text{GEN}}$  is the fitted mean of the generator level mass as shown in the left plot in Figure 4.43. To correct for the residual shift between generated and reconstructed softdrop mass, a fit to  $(M_{\text{RECO}} - M_{\text{GEN}})/M_{\text{RECO}}$ , where  $M_{\text{RECO}}$  is the reconstructed mass shown in the right plot in Figure 4.43 and  $M_{\text{GEN}}$  is as defined above, as a function of jet  $p_T$  in two  $\eta$  bins (smaller or greater than  $|\eta| = 1.3$ ) is performed. Polynomial fit functions of the following forms are used

$$\begin{aligned} w(p_T) &= A + B(x^2)^{-C} && \sim \text{"gen correction"} \\ w(p_T) &= A + Bx + Cx^2 + Dx^3 + Ex^4 + Fx^5 && \sim \text{"reco correction"} \end{aligned}$$

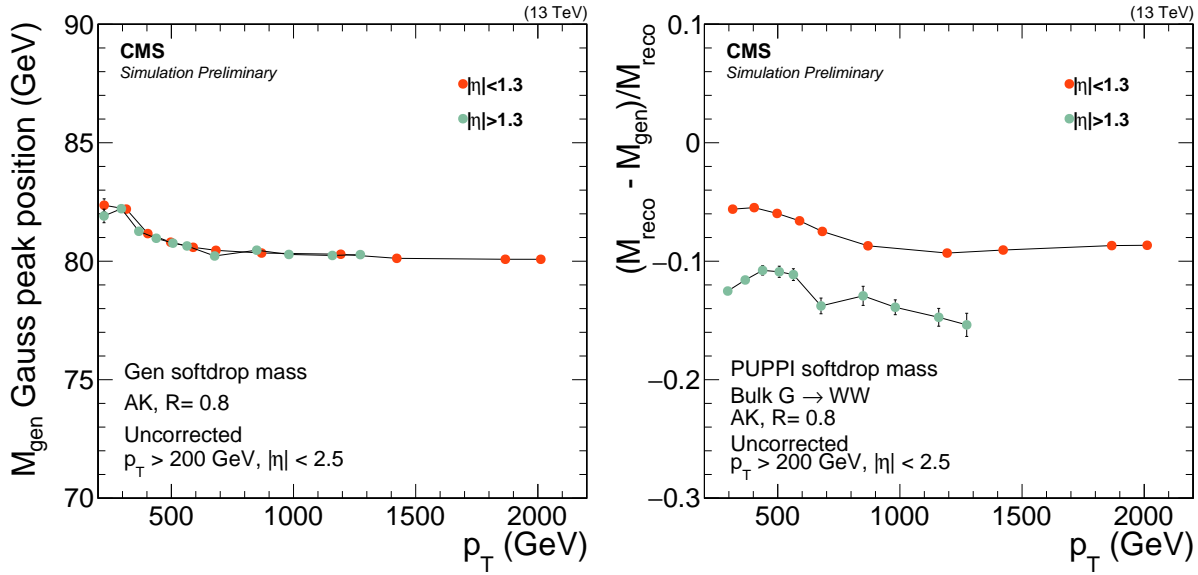


**Figure 4.43:** The mean of the fitted generator level W-jet softdrop mass distribution as a function of jet  $p_T$  (left) and the normalized difference in reconstructed and generated softdrop mass (right).

2044 The distribution and corresponding fits for the two weights is shown in Figure 4.44 for the “gen correction” (left) and “reco correction” (right). The two corrections are then applied to the

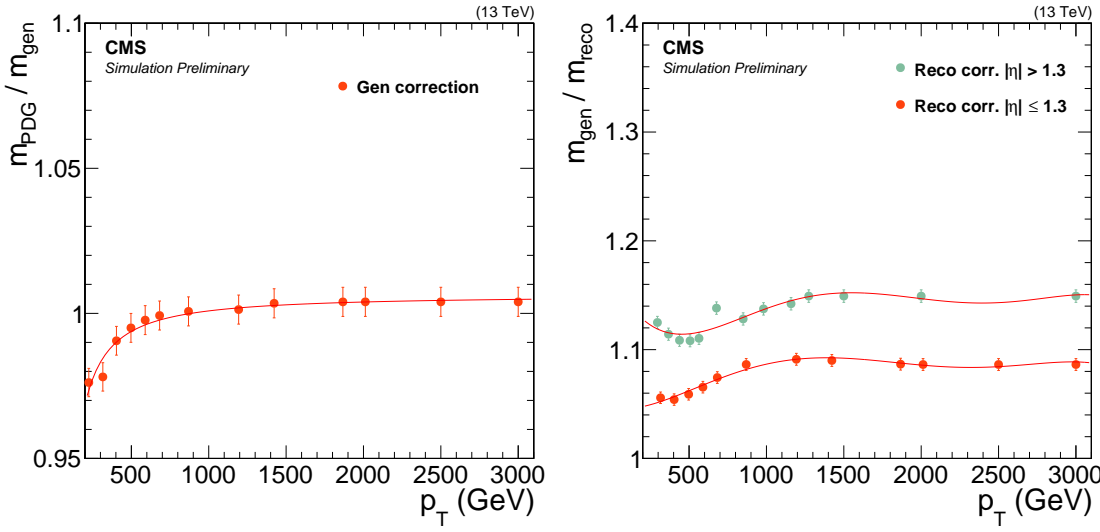


**Figure 4.44:** Fit to  $m_{\text{PDG}}/m_{\text{GEN}}$  as a function of jet  $p_T$  (left), where  $m_{\text{PDG}} = 80.4 \text{ GeV}$  and  $m_{\text{GEN}}$  is the fitted mean of the generator level mass and a fit to  $(M_{\text{RECO}} - M_{\text{GEN}})/M_{\text{RECO}}$  (right), where  $M_{\text{RECO}}$  is the reconstructed softdrop mass, as a function of jet  $p_T$  in two  $\eta$  bins.

2046 uncorrected PUPPI softdrop mass both in data and in MC as

$$M_{SD} = M_{SD, \text{uncorr}} \times w_{\text{GEN}} \times w_{\text{RECO}} \quad (4.9)$$

2047 where  $w_{\text{GEN}}$  and  $w_{\text{RECO}}$  correspond to the gen and reco corrections respectively and  $M_{SD, \text{uncorr}}$   
2048 is the uncorrected PUPPI softdrop mass.

2049 Finally, a closure test is performed in order to check that the corrected PUPPI+softdrop  
2050 W-jet mass peaks at 80.4 GeV and is stable with  $p_T$  and  $\eta$ . The fitted mean of the corrected  
2051 PUPPI softdrop mass peak as a function of jet  $p_T$  in two different  $\eta$  bins is shown in Figure 4.45.  
2052 Good closure is observed, with the corrected mass peaking around 80 GeV independent of the jet  
2053  $p_T$  and  $\eta$ . The PUPPI softdrop jet mass peak for W/Z-jets from different signal samples after jet  
2054 mass corrections have been applied is shown in Figure 4.46, for resonances with a mass of 1 and 4  
TeV. The corrections applied to Z-jets yield a mass stable with  $p_T$ , peaking around the Z mass.

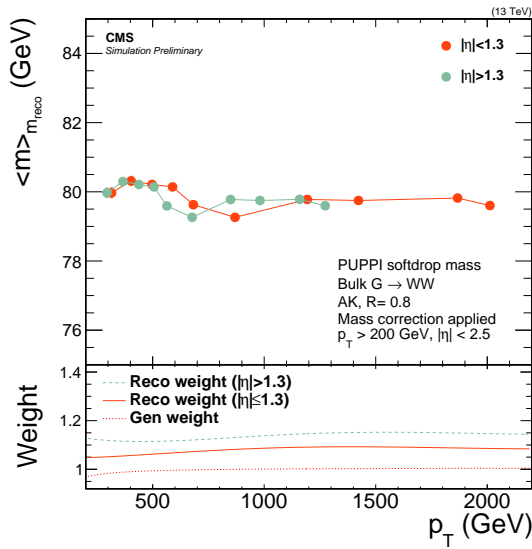


**Figure 4.45:** The mean of the fitted W-jet corrected PUPPI softdrop mass peak as a function of jet  $p_T$  in two different  $\eta$  bins.

2055

## 2056 W-tagging performance

2057 The new PUPPI+softdrop based W/Z-tagger uses a mass window of  $65 \text{ GeV} < m_{SD} < 105 \text{ GeV}$   
2058 in combination with a cut of PUPPI  $\tau_{21} < 0.4$ . We compare its performance to that of the  
2059 CHS+pruning based tagger used in Search I as well as to that of a “DDT-transformed”  $\tau_{21}$  based

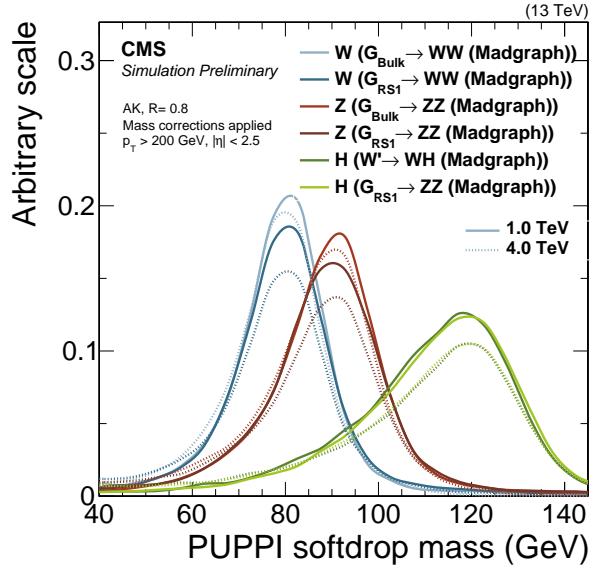


**Figure 4.46:** The W/Z/H-jet corrected PUPPI softdrop mass peak for jets from different signal samples with masses of 1 and 4 TeV.

2060 tagger [75]. The  $\tau_{21}^{DDT}$  variable is a linear transformation of  $\tau_{21}$  given as

$$\tau_{21}^{DDT} = \tau_{21} + M \times \log \left( \frac{m^2}{p_T \times 1 \text{ GeV}} \right) \quad (4.10)$$

2061 where  $M = -0.063$  is obtained from a fit of  $\tau_{21}$  against the variable  $\rho' = \log(m^2/p_T/\mu)$ , where  
 2062  $\mu = 1 \text{ GeV}$ . The purpose of this is to de-correlate  $\tau_{21}$  from the softdrop mass and  $p_T$ , yielding  
 2063 a mass and dijet invariant mass spectrum minimally sculpted by a cut on the  $\tau_{21}^{DDT}$  tagging  
 2064 variable. This is tagger that will be further explored and explained in detail in the context of  
 2065 Search III, Section 4.3.6.

2066 The background rejection efficiency for QCD light flavor jets as a function of W-jet signal  
 2067 efficiency is shown in Figure 4.47. The efficiency is measured requiring a fixed jet mass window of  
 2068 65-105 GeV, while scanning the cut on  $\tau_2/\tau_1$ . The general performance of each tagger is very  
 2069 similar, with the PUPPI+softdrop based taggers displaying a slightly higher signal efficiency for a  
 2070 given mistag rate at high  $p_T$  and CHS+pruning slightly better at low  $p_T$ . To better understand  
 2071 the difference between each tagger, we look at the tagging performance as a function of jet  $p_T$  as  
 2072 well as pileup, shown in Figure 4.48 and 4.49.

2073 Starting with the tagger  $p_T$ -dependence in Figure 4.48, we observe that the signal efficiency of a  
 2074 PUPPI+softdrop of CHS+pruned jet mass cut is flat as a function of  $p_T$ , at around 80%. The QCD  
 2075 mistagging rate drops for both groomers, with a 1-3% lower mistag rate using PUPPI+softdrop

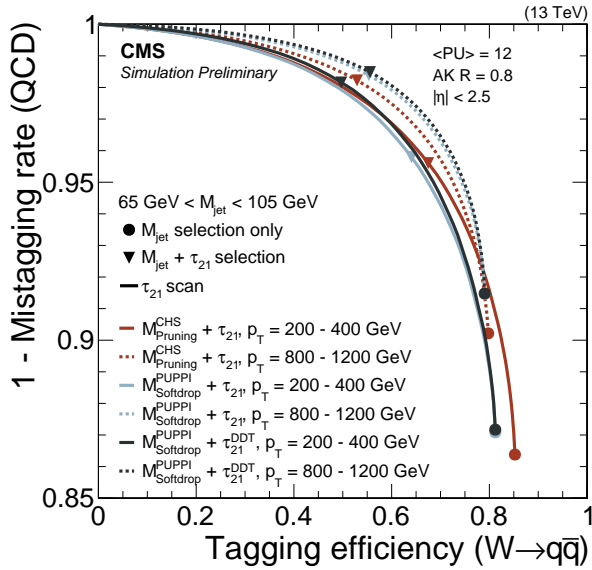


**Figure 4.47:** The background rejection efficiency for QCD light flavor jets as a function of W-jet signal efficiency. A cut on CHS pruned or PUPPI softdrop jet mass of  $65 < m_{\text{jet}} < 105$  GeV is applied while scanning the cut on  $\tau_{21}$ . The cuts corresponding to  $\tau_2/\tau_1 < 0.45$  for CHS+pruning, PUPPI  $\tau_2/\tau_1 < 0.4$  for PUPPI+softdrop or  $\tau_{21}^{\text{DDT}} < 0.52$  are indicated with triangles, while the solid circles represent the efficiency and mistag rate for a mass cut only.

2076 that CHS+pruning. Once applying an n-subjettiness cut, the signal efficiency as well as the  
 2077 mistag rate for the PUPPI  $\tau_{21}$  and CHS  $\tau_{21}$  taggers drops as a function of  $p_T$ , with an average  
 2078 signal efficiency of around 50% for a  $\sim 2\%$  mistag rate. An interesting behavior is observed for the  
 2079  $\tau_{21}^{\text{DDT}}$  tagger: While the mistag rate is flat as a function of  $p_T$ , as is the purpose of decorrelated  
 2080 taggers, the signal efficiency improves as the  $p_T$  increases, outperforming the other taggers above  
 2081 1 TeV.

2082 Turning to the tagger pileup dependence, shown in Figure 4.49, the expected benefit from  
 2083 using the PUPPI algorithm is observed: The tagging efficiency for the CHS+pruning (red solid  
 2084 circles) based tagger falls off steeply versus the number of primary vertices in the event, while the  
 2085 PUPPI+softdrop based taggers (light and dark blue solid circles) are more or less insensitive  
 2086 to pileup. Based on general performance, tagging stability versus pileup and due to theoretical  
 2087 considerations, PUPPI softdrop mass with dedicated mass corrections applied together with  
 2088 PUPPI  $\tau_{21}$  is chosen as this analysis W-tagger. The per-jet efficiency is around 50-55% for a  
 2089 1-2% mistag rate.

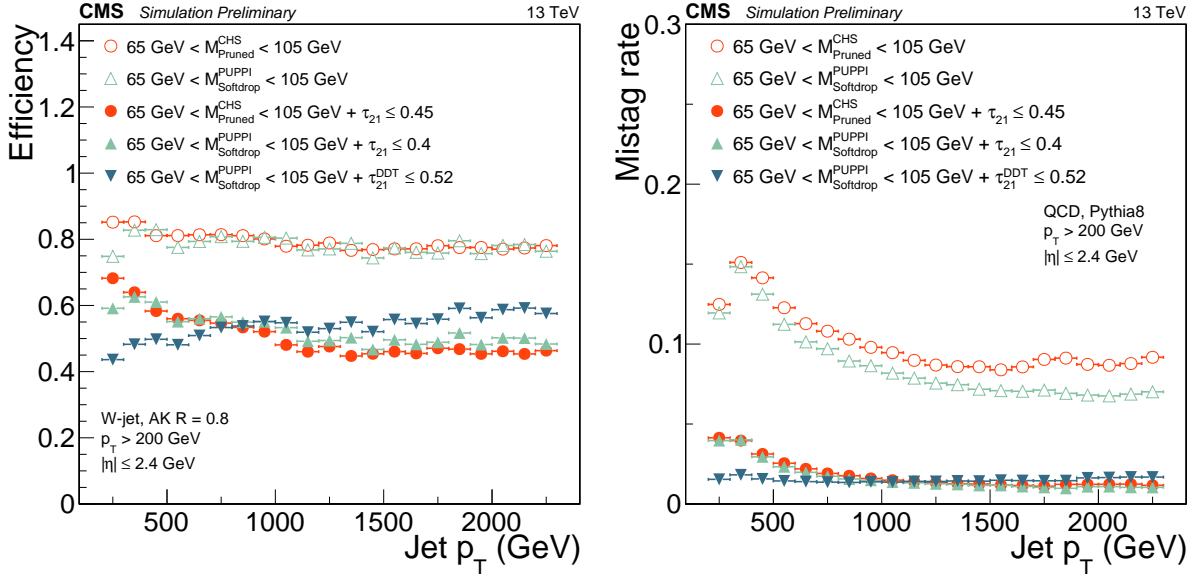


**Figure 4.48:** W-jet efficiency (left) and QCD light jet mistag rate (right) for a PUPPI+softdrop or CHS+pruned jet mass selection only (hollow circles) and the combined  $m_{\text{jet}} + (\text{PUPPI}) \tau_2/\tau_1$  (DDT) selection (solid circles) as a function of jet  $p_T$ .

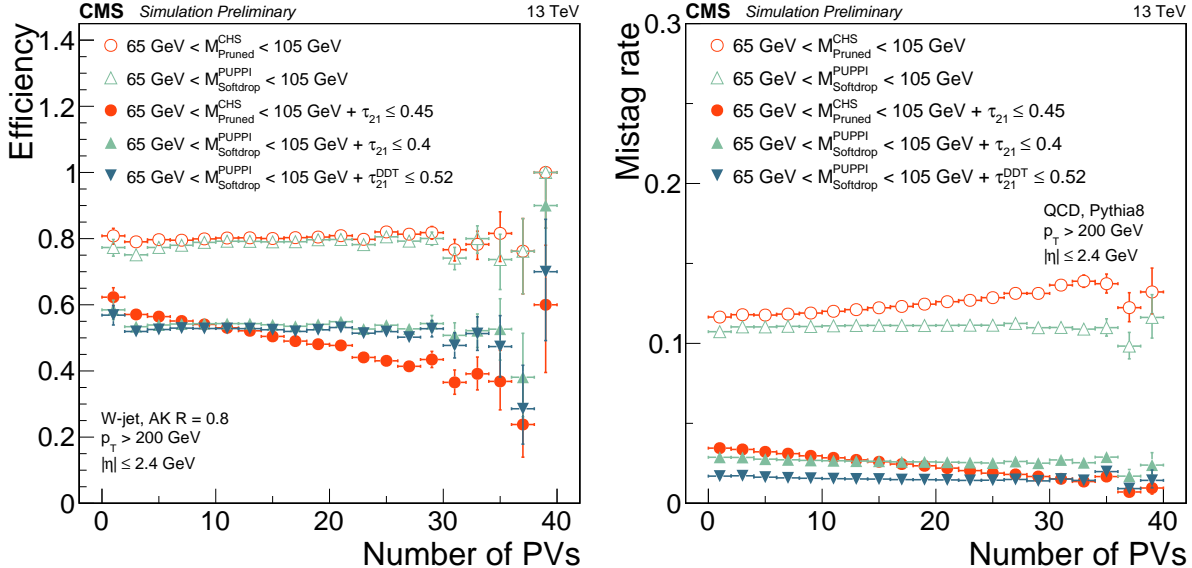


**Figure 4.49:** W-jet efficiency (left) and QCD light jet mistag rate (right) for a PUPPI+softdrop or CHS+pruned jet mass selection only (hollow circles) and the combined  $m_{\text{jet}} + (\text{PUPPI}) \tau_2/\tau_1$  (DDT) selection (solid circles) as a function of jet pileup.

#### 2090 Efficiency scale factors and mass scale/resolution measurement

2091 subsubsectionEfficiency scale factors and mass scale/resolution measurement In order to measure  
2092 the W-tagging efficiency, jet mass scale and resolution for the new PUPPI softdrop based tagger,

we use the same procedure as outlined in Section 4.1.7. We first did an early measurement of  
 the efficiency using  $2.3 \text{ fb}^{-1}$  of data collected in 2015, which was published in a jet algorithms  
 performance note [73] and served as the first commissioning of the new tagger. We then redid the  
 measurement with  $12.9$  and  $35.9 \text{ fb}^{-1}$  of 2016 data, respectively, for the two analyses presented in  
 this chapter (the latter measurement performed by a separate analysis team). The results shown  
 in the following will be those obtained when the tagger was first presented in analysis context,  
 corresponding to the  $12.9 \text{ fb}^{-1}$  of early 2016 data. In order to better understand the differences  
 between the CHS+pruning and PUPPI+softdrop based taggers, the first efficiency measurement  
 was done in parallel for both algorithms, requiring either a softdrop or a pruned jet mass between  
 $40 \text{ GeV}$  and  $150 \text{ GeV}$ . The softdrop mass is computed after PUPPI and the jet mass corrections  
 as described in Section 4.2.5 are applied, while the pruned mass is corrected with L2L3 jet energy  
 corrections. The method is the same as the one outlined in detail in Section 4.1.7 and fits to  
 matched  $t\bar{t}$  MC and minor backgrounds for the PUPPI softdrop based tagger are skipped here  
 and can be found in Appendix B.1.  
 The PUPPI softdrop jet mass and PUPPI  $\tau_{21}$  variables in data and in MC are shown in Figure B.3  
 and can be compared to the corresponding plots for the CHS pruned jet mass and CHS  $\tau_{21}$   
 distributions in Figure B.3. The data to MC agreement as well as the observed spectra, is very  
 similar between CHS pruning and PUPPI softdrop in this region.

Following what was done in Section 4.1.7, we extract and compare the W-tagging efficiency,  
 jet mass scale and resolution of the combined jet mass and  $\tau_{21}$  selection in data and in MC. This  
 is done through a simultaneous fit of the the softdrop jet mass spectrum between 40 and 150  
 GeV in two regions:

- Pass region:  $0 < \tau_{21} \leq 0.40 \sim \text{high purity}$
- Fail region:  $0.40 < \tau_{21} \leq 0.75 \sim \text{low purity}$

The corresponding fits are shown in Figure B.4, with the corresponding extracted efficiencies  
 from the Gaussian component of the total fit and scale factors summarized in Table B.1. The  
 quoted systematic uncertainties are evaluated the same was as described in Section 4.1.7 and  
 correspond to the uncertainty due to ME generator and due to choice of fit method.

	Working point	Eff. data	Eff. simulation	Scale factor
HP	$\tau_{21} < 0.4$	$0.839 \pm 0.020$	$0.817 \pm 0.012$	$1.03 \pm 0.03 \text{ (stat)} \pm 0.04 \text{ (sys)} \pm 0.06 \text{ (sys)}$
LP	$0.4 < \tau_{21} < 0.75$	$0.154 \pm 0.020$	$0.176 \pm 0.012$	$0.88 \pm 0.12 \text{ (stat)} \pm 0.17 \text{ (sys)} \pm 0.12 \text{ (sys)}$

**Table 4.9:** W-tagging scale factors for both categories the high purity and low purity categories for two taggers: Pruned jet mass +  $\tau_{21}$  and PUPPI softdrop jet mass + PUPPI  $\tau_{21}$ .

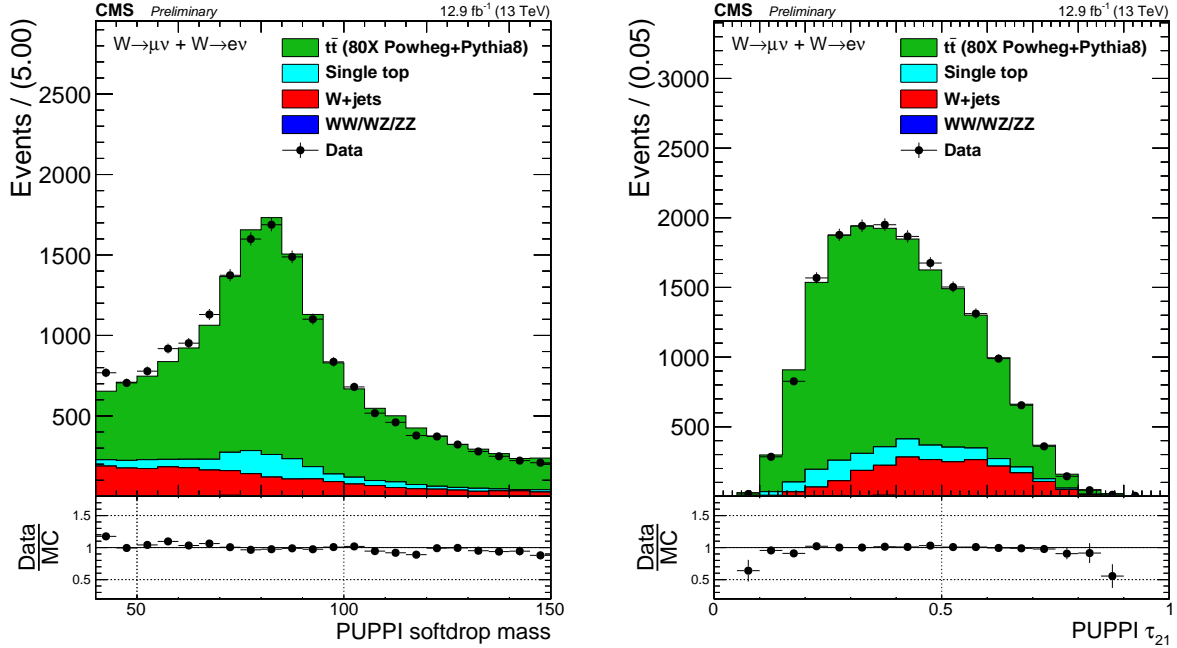


**Figure 4.50:** Distribution of the PUPPI softdrop mass (left) and PUPPI n-subjettiness (right) distribution in the  $t\bar{t}$  control sample.

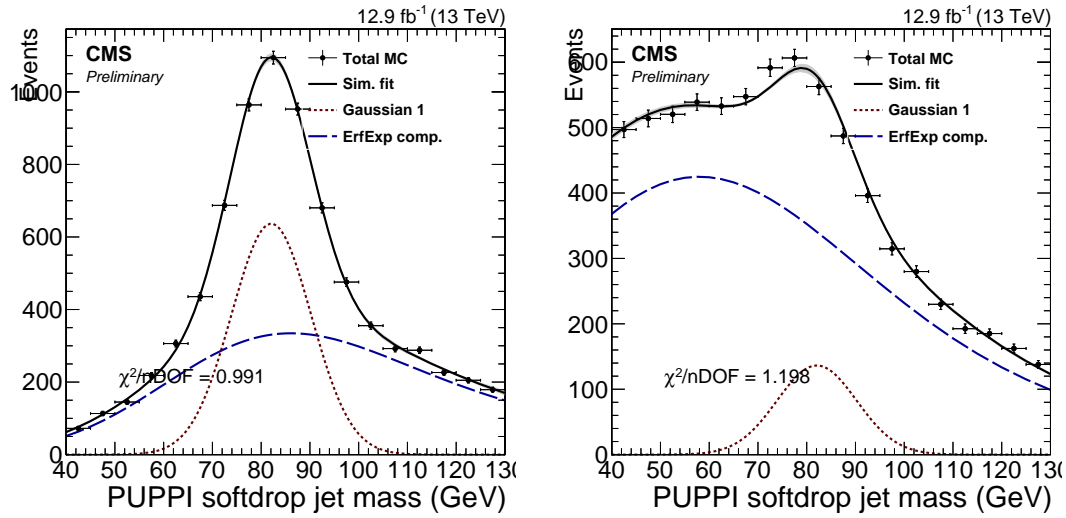


**Figure 4.51:** PUPPI softdrop jet mass distribution that pass (left) and fail (right) the PUPPI  $\tau_2/\tau_1 < 0.40$  selection. Results of both the fit to data (blue) and simulation (red) are shown and the background components of the fit are shown as short-dashed lines.

Both scale factors are comparable to unity, within uncertainties. We additionally extract the jet mass scale and jet mass resolution from the mean and width, respectively, of the Gaussian component of the total fit in the pass region. These are summarized in Table B.2. As for pruning (Table 4.7), we find that the W jet mass scale is larger in simulation than in data, of roughly 2%. The jet mass resolution, on the other hand, is larger in data, of roughly 8%, whereas for pruning the resolution is larger in simulation (11%). However, both are statistically insignificant and comparable with unity within uncertainties.

Parameter	Data	Simulation	Data/Simulation
PUPPI softdrop $\langle m \rangle$	$81.9 \pm 0.3$ GeV	$82.0 \pm 0.2$ GeV	$0.999 \pm 0.004$ (stat) $\pm 0.0006$ (sys)
PUPPI softdrop $\sigma$	$8.9 \pm 0.4$ GeV	$8.3 \pm 0.3$ GeV	$1.08 \pm 0.07$ (stat) $\pm 0.08$ (sys)

**Table 4.10:** Summary of the fitted W-mass peak fit parameters.

The W-tagging efficiency scale factors, jet mass scale and resolution affects the signal yield and are included as described in Section 4.1.7: as a scale of the total signal yield and an uncertainty on the signal efficiency due to a shift and broadening of the W-jet mass peak.

### 4.2.6 W-tagging mistagging rate measurement

We additionally measure the W-tagging fake rate in data in a QCD dijet enriched region and compare this to the prediction from QCD MC using the three different combination of generators: HERWIG++, PYTHIA and MADGRAPH +PYTHIA. Figure 4.52 shows the mistag rate as a function of  $p_T$  for three different taggers: CHS pruning +  $\tau_{21}$ , PUPPI softdrop + PUPPI  $\tau_{21}$  and PUPPI softdrop +  $\tau_{21}^{DDT}$ . We find a substantial difference in the modeling of substructure variables between the different generators, most likely coming from their very different description of gluon radiation (dominant in QCD multijet events). The best description is obtained with HERWIG++, while all three generators model the tagging  $p_T$  dependence well. We additionally study the difference in the total quark/gluon-content for the two PUPPI softdrop based taggers:  $\tau_{21}$  and  $\tau_{21}^{DDT}$ . Figure 4.53 shows the stacked relative q/g content in a Pythia 8 QCD dijet sample for a cut on PUPPI  $\tau_{21}$  and  $\tau_{21}^{DDT}$ . We see that the quark content increases as a function of jet  $p_T$  when cutting on the DDT, while it decreases when cutting on  $\tau_{21}$ . This can be attributed to the fact that the  $m/p_T$  distribution for quark and gluon jets are very different from one another, and this difference increase as the jet  $p_T$  increases. Figure 4.54 shows the  $m/p_T$  for jets originating from a quark (blue) and a gluon (red) for a jet  $p_T$  of 200 GeV (left) and 1600 GeV. We see that the mass over  $p_T$  for gluon jets is significantly higher for gluon jets than for quark jets. With the

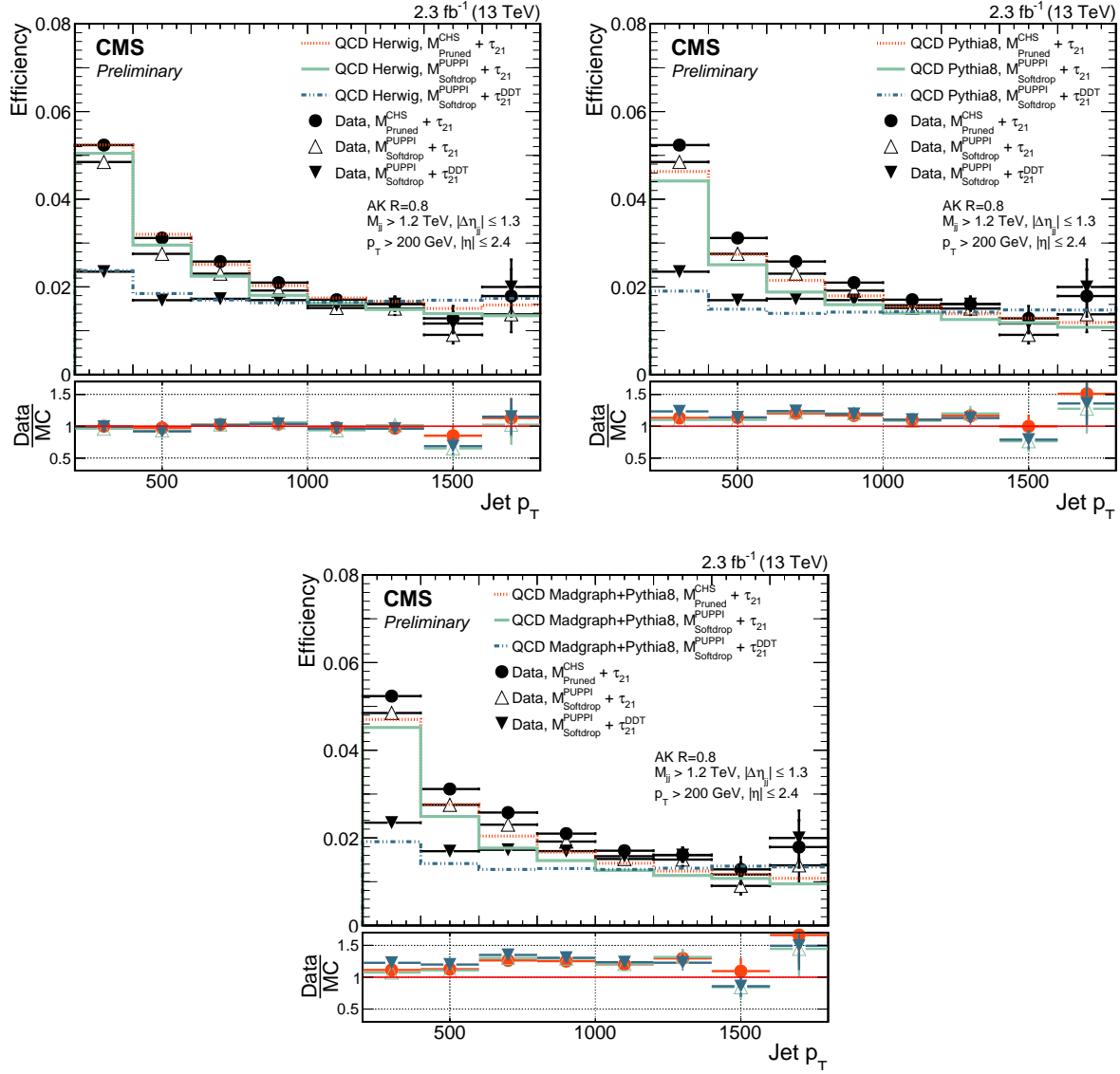


**Figure 4.52:** The fraction of jets that pass the  $m_{\text{jet}} + \tau_2/\tau_1$  selections in a dijet enriched sample for data and for simulation as a function of jet  $p_T$ . Here comparing HERWIG++ (left), PYTHIA8 (right) and PYTHIA8 with MADGRAPH as matrix-element generator (left).

<sup>2148</sup>  $\tau_{21}^{\text{DDT}}$  tagger being defined as in Equation 4.10, the DDT will therefore act more aggressive on jets with a high  $m/p_T$ , effectively removing more gluon jets.

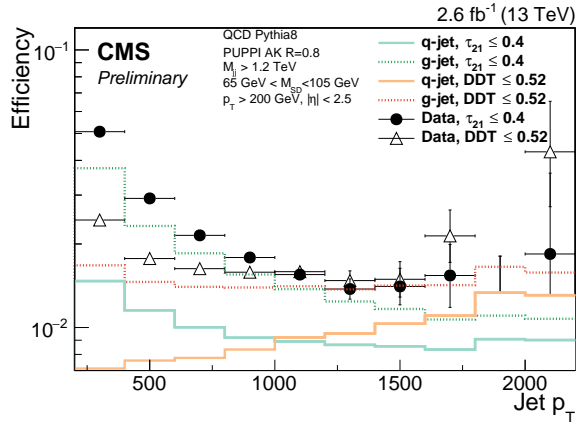


**Figure 4.53:** The fraction of jets that pass the PUPPI softdrop  $m_{\text{jet}}$  with  $\tau_2/\tau_1$  (turquoise) or  $\tau_{21}^{DDT}$  (orange) selections in a dijet enriched sample. The jets from QCD MC are split into two contributions: jets originating from gluons (dotted line) and jets originating from quarks (solid line).

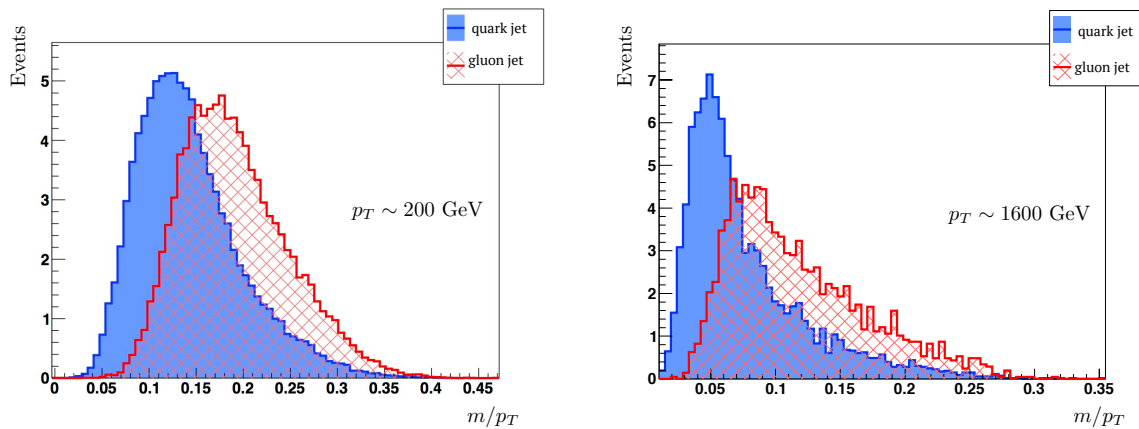


**Figure 4.54:** The jet mass divided by the jet  $p_T$  for quark (blue) and gluon (red) jets for a jet  $p_T$  of 200 (left) and 1600 GeV (right). Created with [76].

### 4.2.7 Mass and purity categorization

The PUPPI softdrop jet mass and PUPPI  $\tau_{21}$  distribution after loose analysis preselections, as outlined in Section 4.2.3, are shown in Figure 4.55. We see some disagreement between data and MC, especially in the high-purity region ( $\text{PUPPI } \tau_{21}^{DDT} < 0.4$ ), confirming what we observed in Section 4.2.6. As this analysis is sensitive to both heavy resonances decaying into two vector

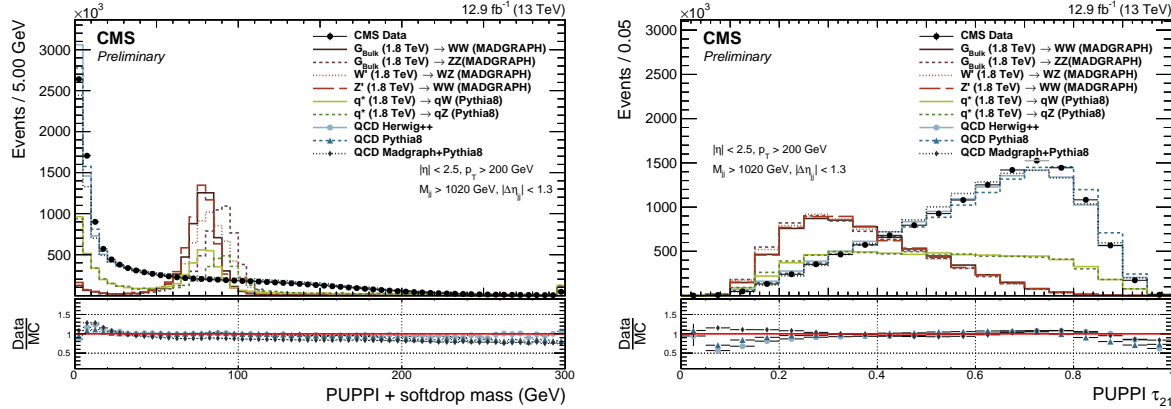


**Figure 4.55:** PUPPI softdrop jet mass distribution (left) and PUPPI n-subjettiness  $\tau_{21}$  (right) distribution for data and simulated samples. Simulated samples are scaled to match the distribution in data.

bosons and excited quark resonances  $q^*$  decaying to qW and qZ, we look for events with both a single W/Z-tag and events with two W/Z-tags. Vector boson candidates are selected with a PUPPI softdrop jet mass of  $65 < m_{\text{jet}} < 105$  GeV. Further, and similar to what was done in Search I, we select “high purity” (HP) W/Z jets by requiring PUPPI  $0 < \tau_{21} \leq 0.40$  and “low purity” (LP) jets with  $0.40 < \tau_{21} \leq 0.75$ . The events with one W/Z-tag are classified in HP and LP events according to the two categories described previously. Events with two W/Z-tagged jets are always required to have one HP tagged jet, and are further divided into LP and HP categories depending on whether the other jet is of high or low purity. We additionally split into two mass categories in order to enhance the analysis sensitivity, with the W window defined as  $65 \text{ GeV} < m_{\text{pruned}} < 85 \text{ GeV}$  and the Z boson window as  $85 \text{ GeV} < m_{\text{pruned}} < 105 \text{ GeV}$ . This results in ten different signal categories. They are as follows:

- High-purity double W/Z-tag, 3 mass categories: WW, ZZ and WZ
- Low-purity double W/Z-tag, 3 mass categories: WW, ZZ and WZ
- High-purity single W/Z-tag, 2 mass categories: qW and qZ

- 2169 • Low-purity single W/Z-tag, 2 mass categories: qW and qZ

2170 **4.2.8 Background modeling: F-test**

2171 With the full analysis selections and categorization defined, we move to the determination of  
 2172 background fit function. Following the same strategy as in Section 4.1.5, we determine the number  
 2173 of necessary parameters in order to describe the background through a Fishers F-test, comparing  
 2174 the same fit functions as in Section 4.1.5. This test is first exercised in QCD MC and then in a  
 2175 data sideband before the final determination in the data signal region. As the F-test method  
 2176 was presented in detail in the context of Search I, only a brief summary and the fits in the new  
 2177 single-tag categories will be presented here, while all fits and F-test results can be found in  
 2178 Appendix B.3.

2179 A two or three parameter fit is sufficient to describe the background for all the double tag  
 2180 categories: a two parameter fit is sufficient for the “high-purity” WZ and ZZ categories. as  
 2181 well as the “low-purity” WW category, while the remaining analysis categories require a three  
 2182 parameter background fit. From the fits to the single tag categories, shown in Figure 4.56, a three  
 2183 parameter fit is sufficient for all categories except the “high-purity” qW category. In this category  
 2184 the improvement in fit quality when increasing the number of parameters is so large adding that  
 2185 adding an additional fit parameter is justified, and we continue by using a 5 parameter fit for  
 2186 this category. A summary of what fit functions are used for each analysis category is listen in  
 Table 4.11.

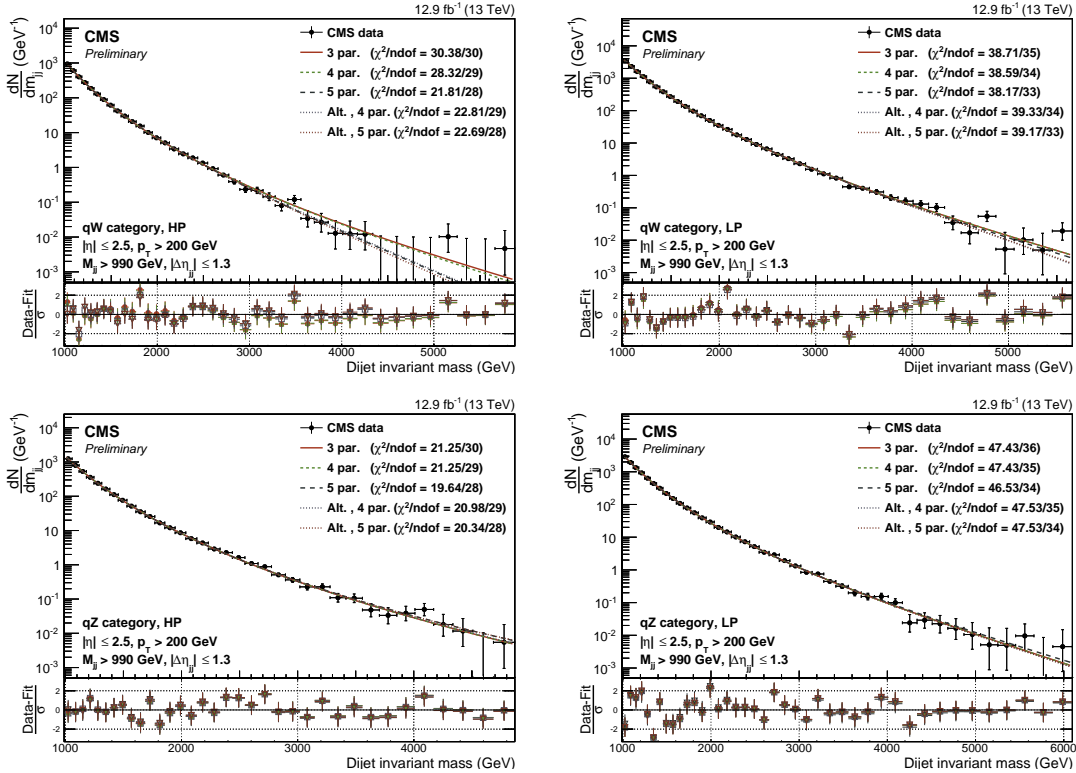
Mass category	N pars.	
	HP	LP
WW	3	2
WZ	2	3
ZZ	2	3
qW	5	3
qZ	3	3

Table 4.11: Fit parameters used in each analysis category

2187

2188 **4.2.9 Signal modeling**

2189 The signal is modeled from signal MC in the same way as was done in Section 4.1.6, assuming a  
 2190 Gaussian core and an exponential tail. The interpolated signal shapes for  $q^* \rightarrow qW$  and  $q^* \rightarrow qZ$



**Figure 4.56:** Background fit for the  $M_{jj}$  distribution in the data signal region for the single-tag analysis. Here for the high- (left) and low-purity (right) single W/Z-tag categories qW (top) and qZ (bottom).

in their most sensitive analysis categories (qW and qZ, respectively) are shown in Figure 4.57.  
The signal shapes for the double-tag category can be compared to those in Figure 4.22.

### 4.2.10 Systematic uncertainties

The largest sources of systematic uncertainty for this analysis is, as for Search I, related to the signal modeling and are due to the uncertainty in the tagging efficiency of the W/Z-tagger, the jet energy/mass scale, the jet energy/mass resolution and integrated luminosity. The W/Z tagging uncertainty is estimated in  $t\bar{t}$  events, as described in Section 4.1.7, and yield uncertainties on the scale factors for the HP and LP tagging categories. The  $p_T$ - and  $\eta$ -dependent jet energy scale and resolution uncertainties on the resonance shape were approximated by a constant 2% and 10% uncertainty in Search I (Section 4.1.7) and are not expected to change for the 2016 analysis. The jet energy response and resolution uncertainty are taken into account as shape uncertainty by shifting and widening the signal resonance model, while all other signal uncertainties only

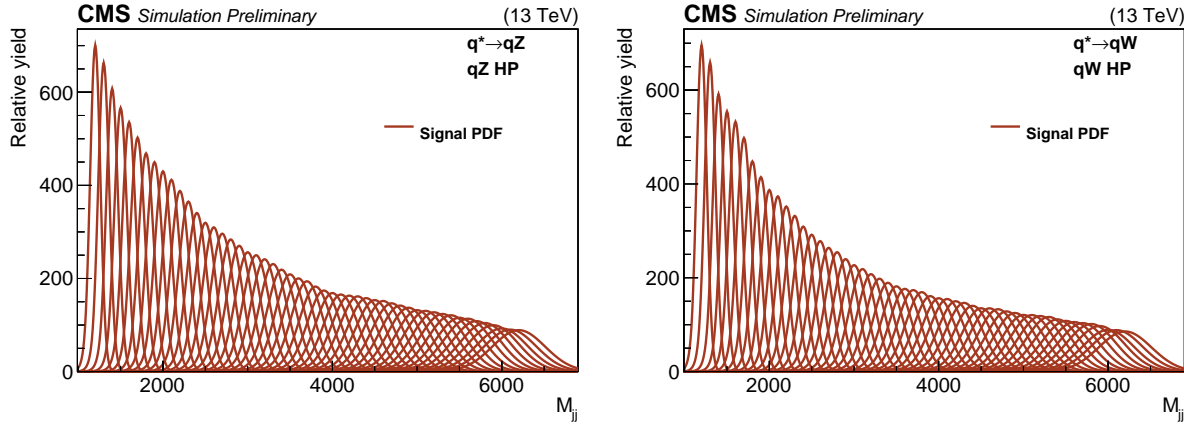


**Figure 4.57:** Interpolated signal shapes for a  $q^* \rightarrow qZ$  (left) and  $q^* \rightarrow qW$  (right) signal.

affect the yield. The list of most relevant systematic uncertainties are listed in Table 4.12.

Source	Relevant quantity	HP+HP unc. (%)	HP+LP unc. (%)
Jet energy scale	Resonance shape	2	2
Jet energy resolution	Resonance shape	10	10
Jet energy scale	Signal yield	<0.1–4.4	
Jet energy resolution	Signal yield	<0.1–1.1	
Jet mass scale	Signal yield	0.02–1.5	
Jet mass resolution	Signal yield	1.3–6.8	
Pileup	Signal yield	2	
Integrated luminosity	Signal yield	6.2	
PDFs ( $W'$ )	Signal yield	4–19	
PDFs ( $Z'$ )	Signal yield	4–13	
PDFs ( $G_{\text{bulk}}$ )	Signal yield	9–77	
Scales ( $W'$ )	Signal yield	1–14	
Scales ( $Z'$ )	Signal yield	1–13	
Scales ( $G_{\text{bulk}}$ )	Signal yield	8–22	
Jet mass scale	Migration	<0.1–16.8	
Jet mass resolution	Migration	<0.1–17.8	
W-tagging $\tau_{21}$	Migration	15.6	21.9
W-tagging $p_T$ -dependence	Migration	7–14	5–11

**Table 4.12:** Summary of the signal systematic uncertainties for the analysis and their impact on the event yield in the signal region and on the reconstructed dijet invariant mass shape (mean and width).

### **4.2.11 Results**

As mentioned in the introduction to this chapter, the analysis of the 2016 dataset was done in two steps: One based on  $12.9 \text{ fb}^{-1}$  of early 2016 data, demonstrating the new PUPPI softdrop based tagger and single-tag analysis categories, and one topping up with the full  $35.9 \text{ fb}^{-1}$  dataset. The results from both will be presented in the following.

#### **Early analysis**

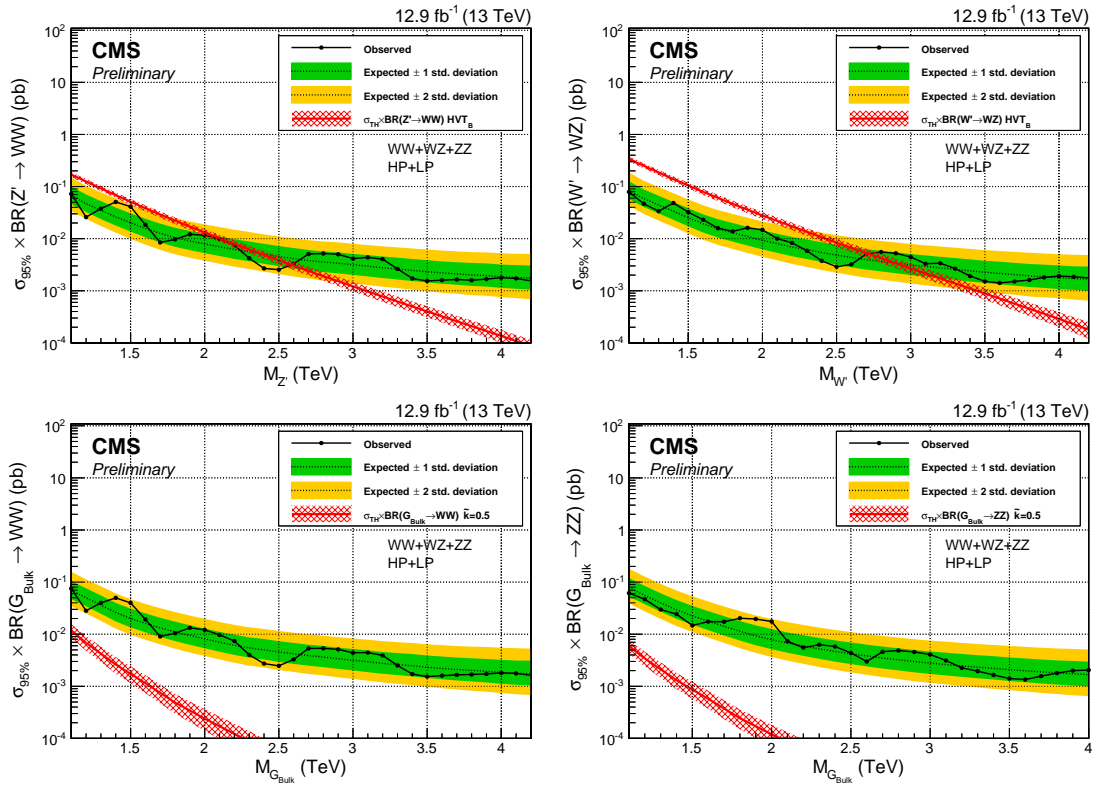
Exclusion limits are set in the context of the bulk graviton model, the HVT model B scenario and excited quark resonances, assuming the resonances to have a natural width negligible with respect to the experimental resolution (as in Search I).

Figure 4.58 shows the 95% confidence level (CL) expected and observed exclusion limits on the signal cross section as a function of the resonance mass for the different signal hypotheses in the double-tag analysis. The limits are compared with the cross section times the branching fraction to WW and ZZ for a bulk graviton with  $\tilde{k} = 0.5$ , and with the cross section times the branching fraction to WZ and WW for spin-1 particles predicted by the HVT model B for both the singlet ( $W'$  or  $Z'$ ) and triplet ( $W'$  and  $Z'$ ) hypothesis. For the HVT model B, we exclude  $W'$  ( $Z'$ ) resonances with masses below 2.7 (2.6) TeV. The signal cross section uncertainties are displayed as a red checked band and result in an additional uncertainty on the resonance mass limits of 0.05 (0.04) TeV. The cross section limits for  $Z' \rightarrow WW$  and  $G_{\text{bulk}} \rightarrow WW$  are not identical due to the different acceptance for those two signal scenarios.

Figure ?? shows the corresponding exclusion limits for excited quarks decaying into qW and qZ. We exclude excited quark resonances decaying into qW and qZ with masses below 5.0 and 3.9 TeV, respectively. The signal cross section uncertainties are displayed as a red checked band and result in an additional uncertainty on the resonance mass limits of 0.1 TeV.

#### **Full 2016 dataset**

The results obtained with the full  $\sim 36 \text{ fb}^{-1}$  of 2016 data are as follows: For a  $G_{\text{bulk}}$  we exclude production cross sections in a range from 36.0 fb, at a resonance mass of 1.3 TeV, to 0.6 fb at resonance masses above 3.6 TeV.  $W'$  ( $Z'$ ) resonances are excluded with masses below 3.2 (2.7) TeV for the HVT model B, in addition to  $W'$  resonances with a mass between 3.3 and 3.6 TeV. For excited quark resonances, we can exclude the production of  $q^*$  decaying to qW or qZ for masses below 5.0 and 4.7 TeV. Figure 4.60 and 4.61 show the resulting 95% confidence level expected and observed exclusion limits on the signal cross section as a function of the resonance mass for



**Figure 4.58:** Observed (black solid) and expected (black dashed) 95% CL upper limits on the production of a narrow-width resonance decaying to a pair of vector bosons for different signal hypotheses. Limits are set in the context of a spin-1 neutral  $Z'$  (left) and charged  $W'$  (right) resonances resonance, and compared with the prediction of the HVT model B. On the bottom, limits are set in the context of a bulk graviton decaying into WW (left) and ZZ (right) with  $\tilde{k} = 0.5$  and compared with the model prediction. Signal cross section uncertainties are displayed as a red checked band.

2235 VV and QV resonances, respectively.

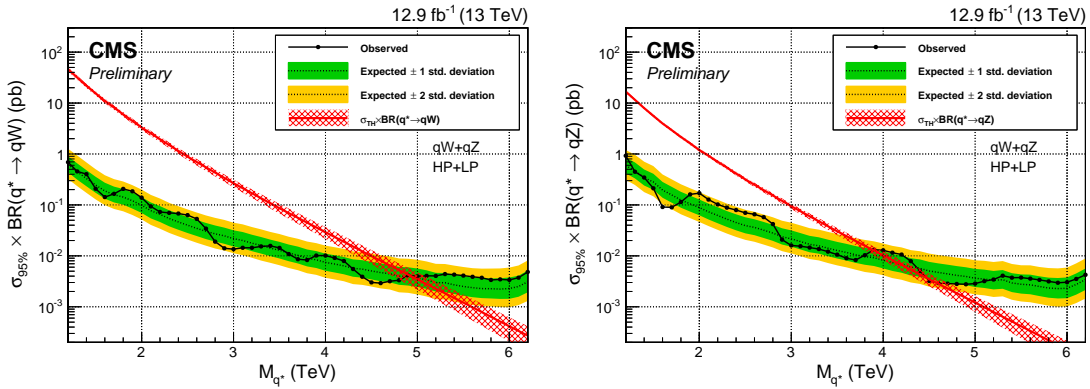


**Figure 4.59:** Observed (black solid) and expected (black dashed) 95% CL upper limits on the production of an excited quark resonance decaying into qW (left) or qZ (right). Signal cross section uncertainties are displayed as a red checked band.

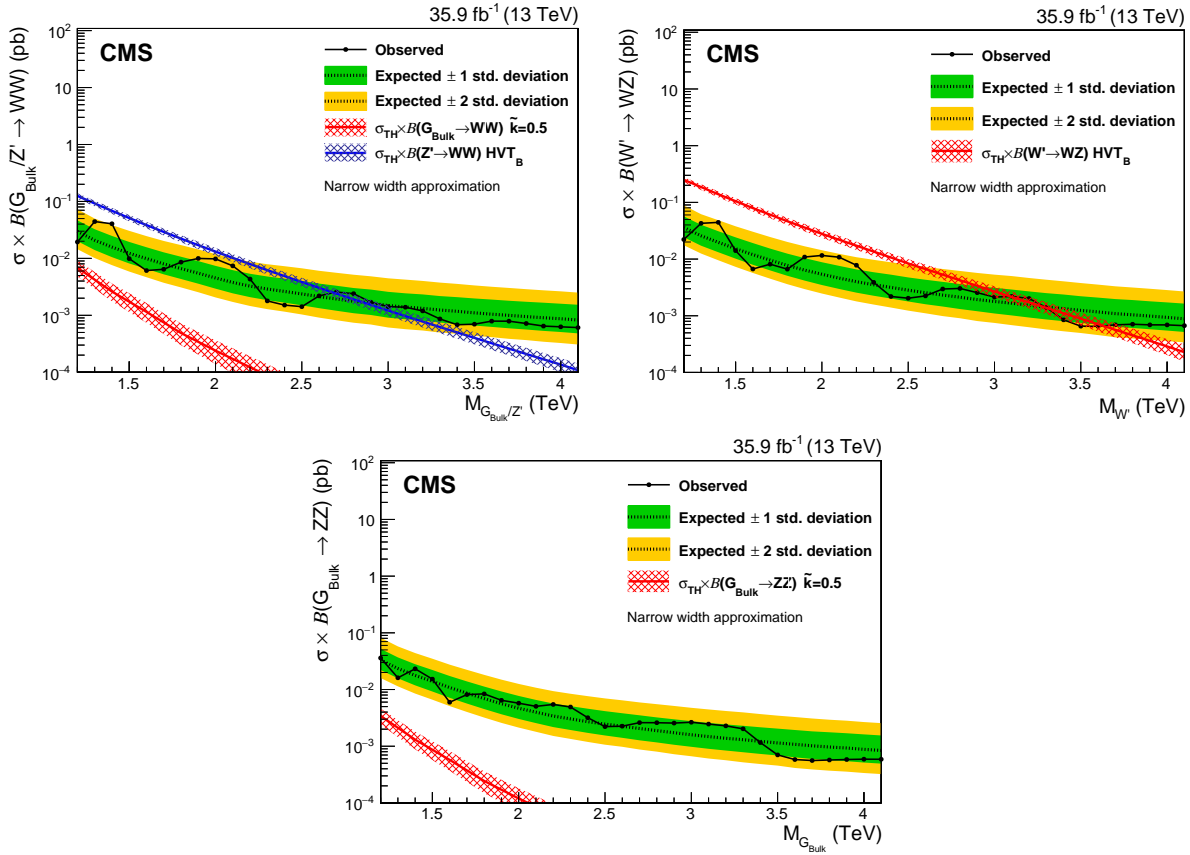


**Figure 4.60:** Observed (solid line) and expected (dashed line) 95% CL upper limits on the production cross section of a narrow resonance decaying into two vector bosons for different signal hypotheses: A  $Z'$  or  $G_{\text{bulk}}$  resonance decaying into  $WW$  (top left), a  $Z'$  decaying into  $WZ$  (top right) and a bulk graviton decaying into  $ZZ$  (bottom).

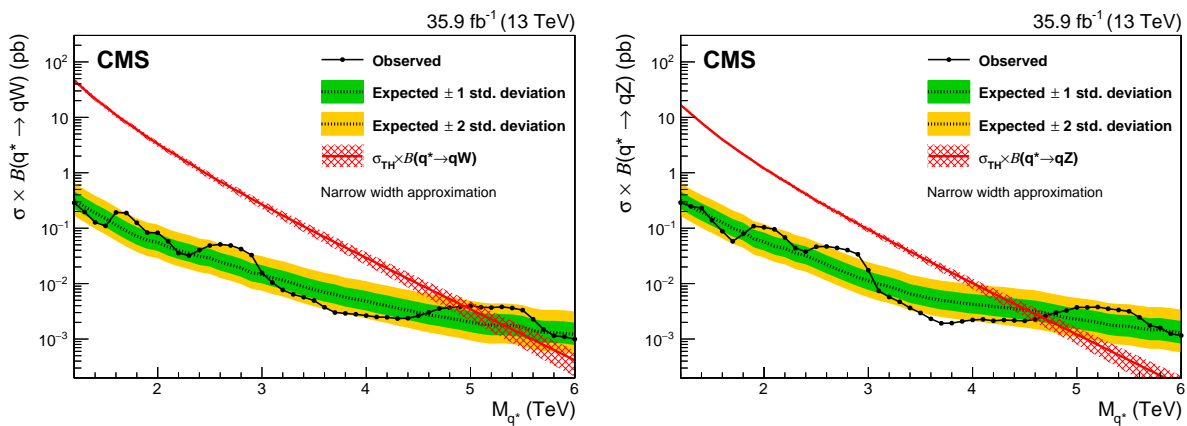
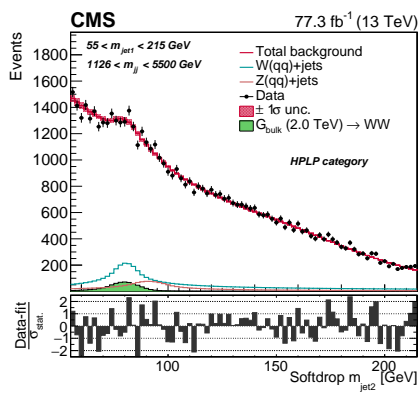


**Figure 4.61:** Observed (solid line) and expected (dashed line) 95% CL upper limits on the production of an excited quark resonance decaying into qW (left) or qZ (right).

### 2236 4.3 Search III: A novel framework for multi-dimensional searches

2237 After two successful analyses of 13 TeV data, no excess had confirmed the 8 TeV bump and the  
 2238 available phase space for New Physics to hide out was shrinking. However, this fact wouldn't  
 2239 disarm everybody. On the BSM theory front, ideas were simmering about whether it was possible  
 2240 that the small bumps we were observing here and there in the dijet invariant mass spectrum were  
 2241 due to us catching the tail of another type of boson with a mass slightly different from that of a  
 2242 W or a Z boson? And that perhaps these jets were not 2-prong objects, but in reality 4-prong?  
 2243 With Run 2 coming to an end, marking the beginning of a two year long shut-down, it was time  
 2244 to think about how we could probe alternative BSM models as effectively as possible. Our idea  
 2245 was therefore the following: We would build a novel framework capable of easily scanning the  
 2246 full softdrop jet mass and N-prong spectrum, and which, in addition, would lead to a gain in  
 2247 sensitivity for the standard VV all-hadronic search. We would do this by taking advantage of  
 2248 the fact that we were looking for bumps in a three-dimensional plane: the softdrop mass of the  
 2249 two jets as well as their invariant mass. As a validation of the method, the method would be  
 2250 demonstrated in the context of the VV all-hadronic search, replacing the dijet fit method. We  
 2251 would then extend this to simultaneously search for resonances decaying to  $W(qq)$ ,  $Z(qq)$  and  
 2252  $H(qq)$  and, finally, take full advantage of the framework and look for generic resonances peaking  
 2253 anywhere in the jet mass and dijet invariant mass spectrum.

2254  
 2255 Search III introduces a novel three-dimensional search method, allowing to simultaneously search  
 2256 for  $W/Z/H$  signals, and eventually non-SM bosons, in the softdrop jet mass spectrum. It is  
 2257 the first analysis to measure the  $V+jets$  cross section and the jet mass scale/resolution from a  
 2258  $W(qq)+jets$  and  $Z(qq)+jets$  mass peak. Published with full 2016+2017 dataset,  $\sim 80 \text{ fb}^{-1}$ .



### 4.3.1 Small bumps and tri-bosons

Ever since the ATLAS observation of a  $3.4\sigma$  excess in the search for VV resonances in the all-hadronic final state [51], several little bumps kept re-appearing near 2 TeV. These were not statistically insignificant, as we've already seen in Search I and Search II, but rather small elusive enhancements, illustrated by the collection of ATLAS/CMS observations in Figure 4.62. Due to

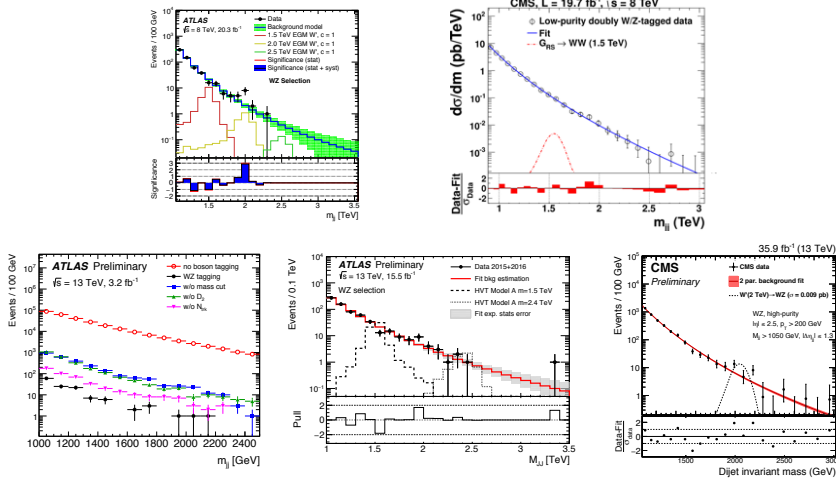


**Figure 4.62:** Several small bumps observed in VV resonance searches in the all-hadronic final state, both in ATLAS and in CMS [77].

their small size and the way the excesses seemed to slightly shift around, these were obviously not diboson resonances. However, could they be caused by us catching the tails of some non-SM boson with a mass slightly different from that of a SM vector boson, as illustrated in Figure 4.63? Further, these could be 4-pronged objects rather than 2-prong, which would cause the excess to

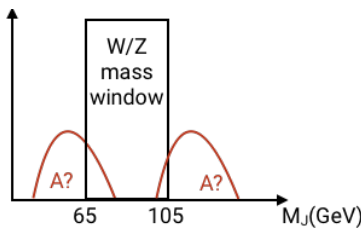


**Figure 4.63:** Slight excesses in diboson analyses could be caused by catching the tail of a non-SM object peaking at slightly higher/lower jet mass than at the W/Z mass.

vary in size depending on the 4-prong efficiency of the analysis specific W-tagger used. An explanation for the observed excesses was proposed in [78]. This paper pointed out that, if

2270 particles like  $W'$  and  $Z'$  exist, an extended scalar sector is needed in order to give mass to the  
 2271 vector bosons. These heavy scalars will decay to lighter bosons, if kinematically allowed, leading  
 2272 to multiboson signals from cascade decays. Some example signatures are illustrated in Figure 4.64.  
 Signatures like these would peak in the groomed jet mass spectrum and, depending on what the

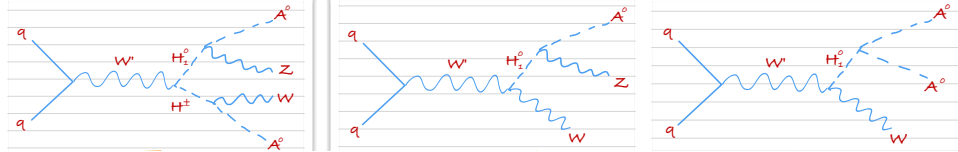


**Figure 4.64:** A  $W'$  decaying to a neutral  $H^0$  and a charged  $H^\pm$  scalar particle leading to a quadriboson final state (left), and a  $W'$  decaying to a neutral scalar particle  $H^0$  and a  $W$  leading to a triboson final state (middle and right) [78].

2273  
 2274 final bosons decay into, have very different substructure profiles (4- and 4-prong, 2- and 4-prong  
 2275 etc.).

2276 In order to effectively search for such types of signals, or any signal peaking in the softdrop  
 2277 jet mass spectrum, we therefore wanted to build a generic new framework allowing to look for  
 2278 peaks anywhere in the groomed mass - dijet invariant mass spectrum. Rather than selecting  
 2279 jets with a groomed mass between 65 and 105 GeV and look for resonances peaking in the dijet  
 2280 invariant mass, we'd look for resonances peaking anywhere in the three dimensional plane formed  
 2281 by the groomed mass of each jet and their invariant mass. The benefits of this procedure, was  
 2282 that it would allow us to scan the full groomed mass spectrum in one analysis. We would first  
 2283 demonstrate the method through the  $VV$  all-hadronic analysis, which is the paper introduced  
 2284 here.

### 2285 4.3.2 Analysis strategy

2286 The background estimation used in Search I and Search II rely on a one dimensional fit of the  
 2287 dijet invariant mass signal region after a tight jet mass cut (65-105 GeV) has been applied. We  
 2288 now take advantage of the fact that the signal peaks in three dimensions; dijet invariant mass  
 2289 ( $M_{VV}$ ) and the jet groomed mass of jet 1 and jet 2 ( $M_{jet1}$  and  $M_{jet2}$ ), and attempt to extract  
 2290 the signal from the three dimensional  $M_{VV}$ - $M_{jet1}$ - $M_{jet2}$  plane. The benefits of doing so is that  
 2291 we now can perform different searches in the  $WW$ ,  $WZ$ ,  $ZZ$ ,  $WH$  or  $XX$  final states encoded in  
 2292 the same analysis. Additionally, tight jet mass cuts are no longer needed as we fit the full jet  
 2293 mass line-shape to extract the signal. This effectively increases our signal statistics as a large  
 2294 fraction of the  $W$  and  $Z$  signal fall outside the above mass window. Fitting the jet groomed mass  
 2295 and resonance mass together also allow us to add nuisance parameters that simultaneously affect

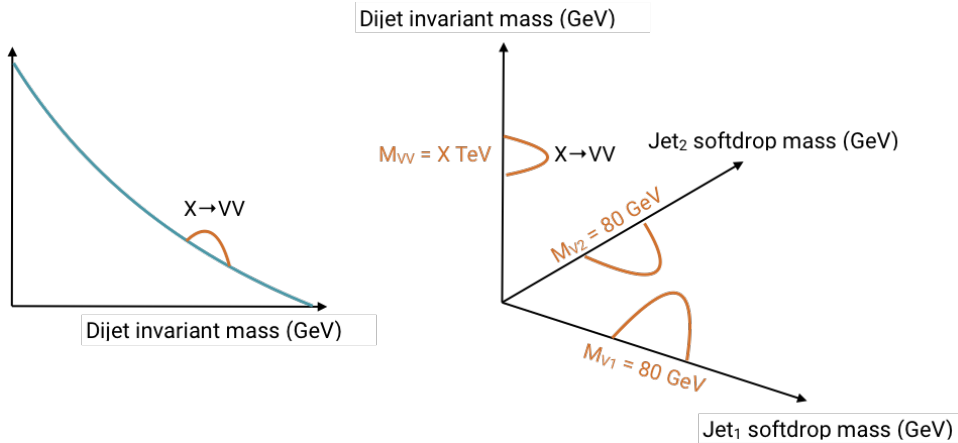


**Figure 4.65:** The one dimensional VV analysis versus the three dimensional fit.

the jet groomed mass and the resonance mass, fully accounting for the correlation between the variables. We would model the background starting from simulation, rather than the dijet fit to data, which would allow us to model peaky distributions like a trigger turn-on. This could allow the search to go even lower in  $M_{VV}$ , something we will discuss further in Section 4.3.5. This chapter, and its corresponding publication, is an analysis of the 2016 and 2017 dataset, corresponding to  $\sim 80 \text{ fb}^{-1}$ , and serves as the first documentation and demonstration of the novel three-dimensional fit method. In Section 4.5, I'll discuss how we plan to take this framework further in searches for VH and HH as well as for generic resonances peaking in jet softdrop mass.

### 4.3.3 Data and simulated samples

The data analyzed in this search consists of  $35.9 \text{ fb}^{-1}$  of data collected in 2016 and  $41.4 \text{ fb}^{-1}$  of data collected in 2017, yielding a total of  $77.3 \text{ fb}^{-1}$ . The simulated samples are the same as those described in Section 4.2.3, with specific detector conditions to match the 2016 and 2017 dataset.

### 4.3.4 Event selection

Events are selected following the same criteria as in Search I and Search II (see Section 4.1.4) and can be summarized as follows:

- PF jet Tight ID applied
- Jet  $\eta < 2.5$

- 2314     • Jet  $p_T > 200$  GeV

- 2315     •  $|\Delta\eta|_{jj} < 1.3$

2316     The two jets with the highest groomed jet mass in the event are selected as potential vector boson  
 2317     candidates. In addition, the dijet invariant mass is required to be  $> 1126$  GeV in order to be on  
 2318     the trigger plateau. As already mentioned in the introduction, the background modeling used  
 2319     in this analysis is capable of modeling turn-ons and is something we explored. However, while  
 2320     the background modeling was reliable, we found it difficult to extract a signal peaking on top of  
 2321     a turn-on and had to abandon the trigger modeling for this first demonstration of the method.  
 2322     More details will be given in Section 4.3.5.

2323

2324     The dijet invariant mass and  $|\Delta\eta|_{jj}$  distribution for the two leading jets in the event after the  
 2325     above preselections have been applied is shown in Figure 4.66. The jet  $p_T$  and  $\eta$  distributions for  
 2326     signal and for background is shown in Figure 4.67.

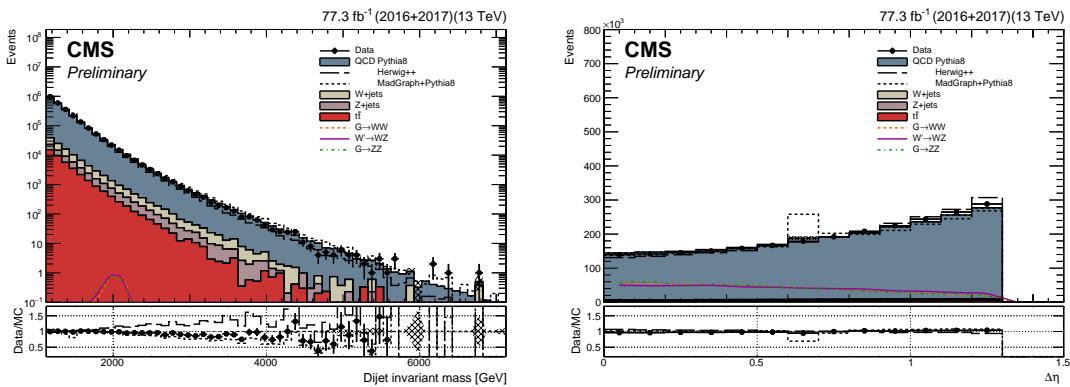


**Figure 4.66:** The dijet invariant mass (left) and  $|\Delta\eta|_{jj}$  (right) for the two leading jets after preselections are applied. The signal is scaled by an arbitrary number.

### 2327   4.3.5 Triggering

2328     The triggers used for 2016 data are the same as in Section 4.1.4, while the thresholds in 2017  
 2329     have increased in order to push the trigger rate to a level acceptable for the increased luminosity.  
 2330     The triggers used for 2017 data are

- 2331     • HLT\_PFHT1050

- 2332     • HLT\_AK8PFJet500

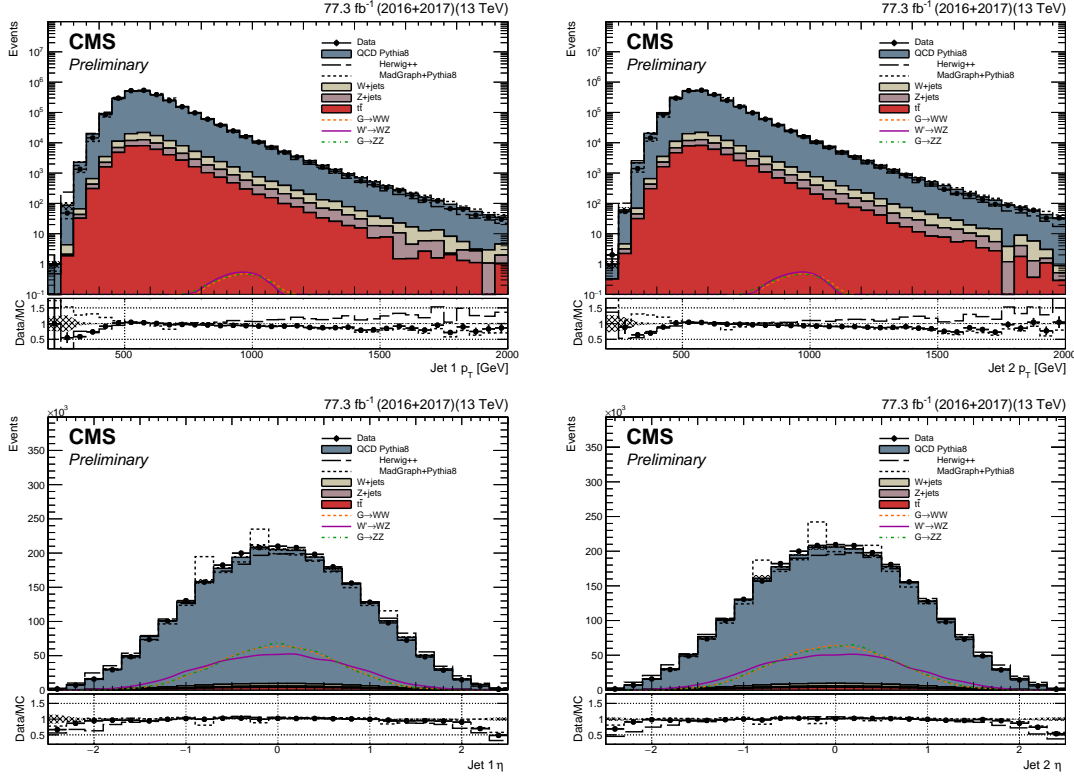


**Figure 4.67:** Jet  $p_T$  (top) and  $\eta$  (bottom) of the leading (left) and second leading (right) jet in the event. The signal is scaled by an arbitrary number.

- 2333     ● HLT\_AK8PFJet360/380/400/420\_TrimMass30
- 2334     ● HLT\_AK8PFHT750/800/850/900\_TrimMass50

2335 . For the results presented here, the analysis threshold is set by the trigger turn-on point (where  
 2336 the combination of all triggers are  $> 99$  percent efficient). The trigger turn-on is evaluated in the  
 2337 Single Muon dataset, using the HLT\_Mu50 and HLT\_IsoMu27 triggers as reference triggers. The  
 2338 trigger turn-on curves as a function of dijet invariant mass and jet soft drop mass are shown in  
 2339 Figure 4.68. The combination of all triggers are  $> 99\%$  efficient above a dijet invariant mass of  
 2340 1126 GeV and this sets the analysis threshold.

### 2341 Trigger turn-on modeling

The analysis threshold for searches depending on the dijet fit is set by the trigger turn-on point as the analysis relies on a background fit of the dijet invariant mass spectrum with a smoothly falling function. As the background modeling for this analysis does not depend on a smoothly

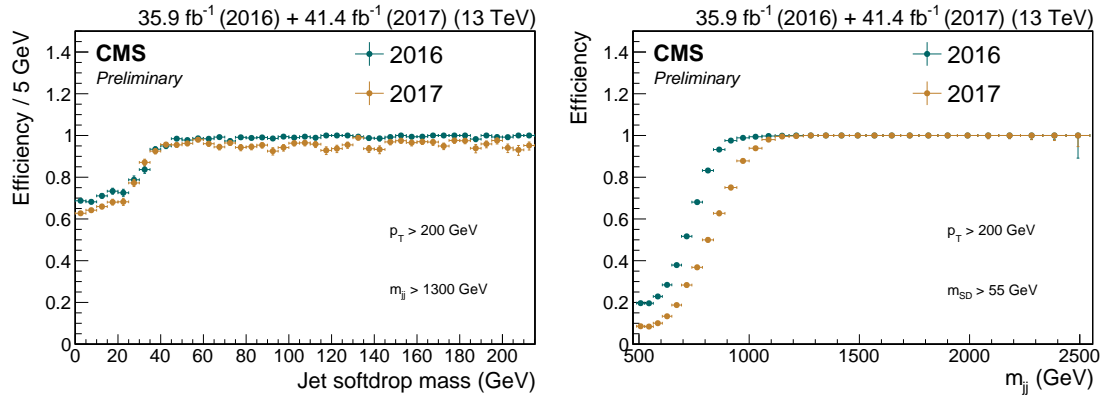


**Figure 4.68:** Trigger turn-on curves in the 2016 and 2017 datasets for the  $H_T$  based (left) and groomed mass based (right) trigger paths.

falling spectrum (as will be described in detail in Section ??), and in order to compensate for a loss in acceptance due to increased trigger thresholds, we attempted to model the trigger turn-on directly from data and apply a trigger weight in simulation. To do so, we first study the one dimensional trigger turn-ons versus dijet invariant mass and softdrop jet mass to understand where in  $M_{VV}$  and  $M_{\text{jet}1}/M_{\text{jet}2}$  the triggers are fully efficient. We then derive a three dimensional histogram of the trigger efficiency versus dijet invariant mass ( $M_{VV}$ ) and the jet groomed mass of jet 1 and jet 2 ( $M_{\text{jet}1}$  and  $M_{\text{jet}2}$ ), where each bin corresponds to the trigger efficiency for a given value of  $M_{VV}-M_{\text{jet}1}-M_{\text{jet}2}$ . The procedure is as follows: From the one dimensional histograms, the points of full efficiency versus  $M_{VV}$ ,  $M_{\text{jet}1}$  and  $M_{\text{jet}2}$  are defined. For every bin above this threshold, the trigger efficiency is fixed to one (100 percent efficiency). For all bins below this trigger threshold, we fit slices of  $M_{VV}$  with a sigmoid function, evaluate the trigger weights from this function, and set the bin content of the three dimensional weight histogram accordingly. For every bin below this point, the trigger weight is extracted by fitting slices of  $M_{VV}$  in each bin of  $M_{\text{jet}1}/M_{\text{jet}2}$ . As the trigger efficiency falls below 50 percent around a dijet invariant mass of 800 GeV (Figure 4.68), searching for resonances with masses below this point is non-feasible. In addition, the full signal shape needs to be contained within the dijet invariant mass spectrum, excluding resonance masses of 0.8 and 0.9 TeV. The lowest mass point signal sample to set limits on for this analysis is therefore at 1 TeV and the analysis threshold is fixed at  $M_{VV}=900$  GeV in order to fully contain the signal shape. Starting from  $M_{VV}=893$  GeV (dijet bin closest to 900 GeV) and  $M_{\text{jet}1}/M_{\text{jet}2}=40$  GeV, a coarsely binned three-dimensional histogram (10 GeV  $M_{\text{jet}1}/M_{\text{jet}2}$  binning and “dijet” binning in  $M_{VV}$ ) is filled with the fraction of events that pass

one of the signal triggers,

$$w_{ijk}^{Bin} = \frac{\text{PASS}(m_{jj}^i - m_{j1}^j - m_{j2}^k)}{\text{ALL}(m_{jj}^i - m_{j1}^j - m_{j2}^k)}.$$

The resulting coarse histogram is then expanded in  $M_{VV}$  to 10 GeV dijet invariant mass bins, interpolating between the points using sigmoid fit for each  $M_{\text{jet}1} - M_{\text{jet}2}$  bin (the fine binning in dijet invariant mass is sufficient enough to yield a smooth reweighted distribution so no expansion is done in  $M_{\text{jet}1}/M_{\text{jet}2}$ ). From this histogram, each slice in  $M_{VV}$  is fitted with a sigmoid function,

$$s(x) = \frac{1}{1 + e^{-p_1(x-p_2)}}$$

- <sup>2342</sup> the trigger weight of each bin  $M_{VV}-M_{\text{jet}1}-M_{\text{jet}2}$  is extracted from the fit and set accordingly. Figure 4.69 shows the total projections on each axis for the full trigger weight histogram. The

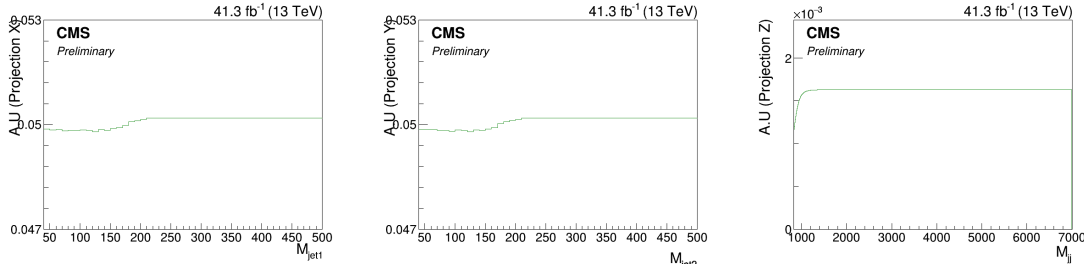


**Figure 4.69:** One-dimensional projections of the trigger weight histogram for  $M_{\text{jet}1}$ ,  $M_{\text{jet}2}$  and  $M_{VV}$  respectively.

- <sup>2343</sup>
- <sup>2344</sup>  $M_{\text{jet}}$  and  $M_{VV}$  spectra for the lowest mass-point signal sample and for the QCD background  
<sup>2345</sup> before and after trigger weights are applied, are shown in Figure 4.70 and are compared to data.  
<sup>2346</sup> > 95% of the signal efficiency is retained, and reweighted QCD simulation agrees well with data.  
<sup>2347</sup> The modeling of the trigger turn-on was successful and implemented in the background fit method  
<sup>2348</sup> in the 3D analysis. We found that the method could model the turn-on well. However, when  
<sup>2349</sup> studying the bias on the extracted signal rate for a possible signal in this turn-on region, we  
<sup>2350</sup> found that this was large due to us attempting to fit a peak on top of a peaky background. As  
<sup>2351</sup> we wanted this analysis describing the 3D fit method to become available as soon as possible, we  
<sup>2352</sup> therefore abandoned modeling of the trigger turn-on for this paper. However, we still wish to  
<sup>2353</sup> pursue this strategy in the future.

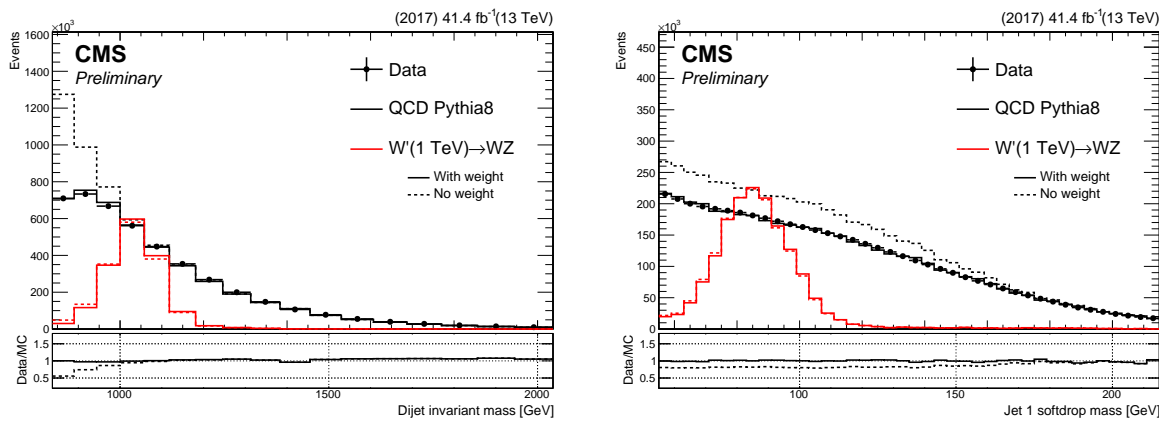


**Figure 4.70:** The  $M_{VV}$  (left) and  $M_{jet}$  (right) spectra for signal and background before and after trigger weights are applied.

### 2354 4.3.6 A mass and $p_T$ decorrelated tagger

2355 In order to identify W and Z jet candidates, two algorithms are run on the AK8 PUPPI jet:  
 2356 softdrop [?] and the N-subjettiness ratio  $\tau_{21}$  [?]. The softdrop jet mass is used to improve the  
 2357 mass resolution of the jet, while N-subjettiness serves as a discriminant by yielding a probability  
 2358 of how compatible the jet is with having N axes. For this search, we require the softdrop-jet mass  
 2359 to be in a window around the W/Z/H/top mass, between 55 and 215 GeV, something which we  
 2360 plan to extend in the future. In order to improve the statistical power of the jet substructure  
 2361 variable  $\tau_{21}$  and ensure a minimal sculpting of the jet mass as a function of jet  $p_T$ , we decorrelate  
 2362 the variable from the jet softdrop mass and the jet  $p_T$ -scale dependence following what was  
 2363 done in Ref. [?]. This decorrelation is performed by flattening the  $\tau_{21}$  profile dependence on  
 2364  $\rho' = \log(m^2/p_T/\mu)$ , where  $\mu = 1$  GeV. Figure 4.71 shows the profile distribution of  $\tau_{21}$  as a  
 2365 function of  $\rho' = \log(m^2/p_T/\mu)$ , applying the preselections as listed above together with a softdrop  
 mass cut of  $55 \text{ GeV} < M_{\text{jet}} < 215 \text{ GeV}$  (right). A linear transformation is then defined as

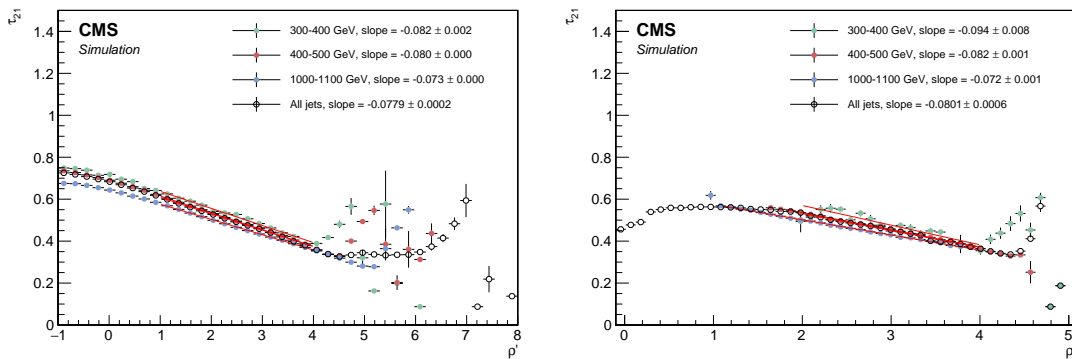


**Figure 4.71:** Profile distributions of  $\tau_{21}$  as a function of  $\rho' = \log(m^2/p_T/\mu)$ , where  $\mu = 1$  GeV (bottom), before applying a softdrop mass cut (left) and after applying a softdrop mass cut of  $55 \text{ GeV} < M_{\text{jet}} < 215 \text{ GeV}$  (right).

2366

$$\tau_{21}^{DDT} = \tau_{21} - M \times \rho', \quad (4.11)$$

2367 where the slope  $M$  is fitted from the linear part of the spectra of the  $\tau_{21}$  profile versus  $\rho'$  with full  
 2368 selections (bottom left plot). For our purposes, the slope is extracted from fitting the inclusive  
 2369  $p_T$ -spectrum (“All jets”) with a mass window applied as it most closely corresponds to our full  
 2370 analysis selections. The resulting slope is  $M = -0.080$ , slightly steeper than than the 2016 value  
 2371 of  $M = -0.063$  [?]. The profile of the retuned  $\tau_{21}^{DDT}$  versus  $\rho'$  is shown in Figure 4.72, exhibiting  
 2372 the desired flattened spectra. Working points for  $\tau_{21}^{DDT}$  are chosen in the following way: First,

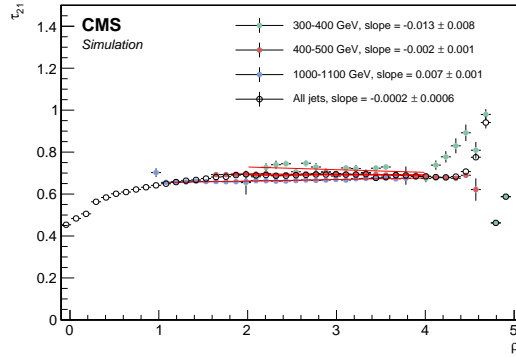


**Figure 4.72:** Profile distributions of  $\tau_{21}^{DDT}$  as a function of  $\rho' = \log(m^2/p_T/\mu)$ , where  $\mu = 1$  GeV.

2373 we check which  $\tau_{21}^{DDT}$  cut corresponds to the highest Punzi significance as a function of the  
 2374 resonance mass for different signal samples, shown in Figure 4.73. All other analysis cuts have been applied. The cut maximizing the Punzi significance at low resonance mass, where

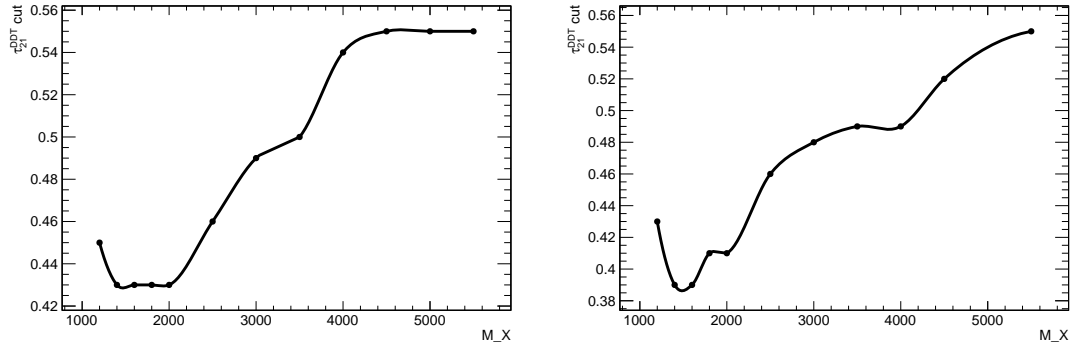


**Figure 4.73:** The  $\tau_{21}^{DDT}$  cut corresponding to the highest Punzi significance for a given signal resonance mass, here for Bulk  $G \rightarrow WW$  (left) and Bulk  $G \rightarrow ZZ$ .

2375  
 2376 the background is highest, is chosen as the “high purity” (HP) working point. This corresponds  
 2377 to  $\tau_{21}^{DDT} \leq 0.43$ . Second, we find the cut which, together with events falling in the HP region,  
 2378 contains at least 95 percent of the signal as well as optimizes the Punzi significance. This is  
 2379 found to be  $0.43 < \tau_{21}^{DDT} \leq 0.79$ , and is classified as the low purity (LP) category. The purpose  
 2380 of this category is to enhance the overall sensitivity, especially where the background is low. We  
 2381 observe a significant gain in signal efficiency at a fixed mistag rate with the retuned DDT tagger.  
 2382 The signal efficiency versus mistagging rate for all three taggers is shown in Figure 4.74, and we  
 2383 see the retuned  $\tau_{21}^{DDT}$  performing better than  $\tau_{21}$  and the version of  $\tau_{21}^{DDT}$  using the old tune. In

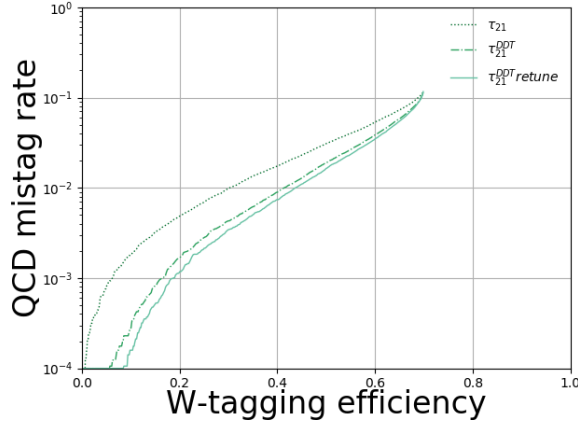


**Figure 4.74:** Performance of  $\tau_{21}$  and  $\tau_{21}^{DDT}$  (2016 and 2017 tune) in the background-signal efficiency plane.

addition to cutting on  $\tau_{21}^{DDT}$  a loose cut of  $\rho = \log(m^2/p_T^2) < -1.8$  is applied. The reason for this is that, while the distribution of  $\rho$  is flat as a function of jet transverse momentum for QCD jets, this only holds in the region where perturbative contributions dominate and breaks down at around  $\rho = \log(m^2/p_T^2) < -2.0$  due to the AK8 cone size being too small to contain the full jet at high masses. This has a negligible effect on the signal, which mainly peaks around 80 GeV and has a relatively high jet transverse momenta. Figure 4.75 shows the signal and background distribution for the PUPPI softdrop jet mass and  $\tau_{21}^{DDT}$ . The signal softdrop mass distribution peaks nicely around the W mass, while the multijets background spectrum is peaked at lower softdrop masses. Also, in addition to having a higher signal efficiency for a given mistag rate,  $\tau_{21}^{DDT}$  has the added benefit of being better modeled in MC than  $\tau_{21}$ .

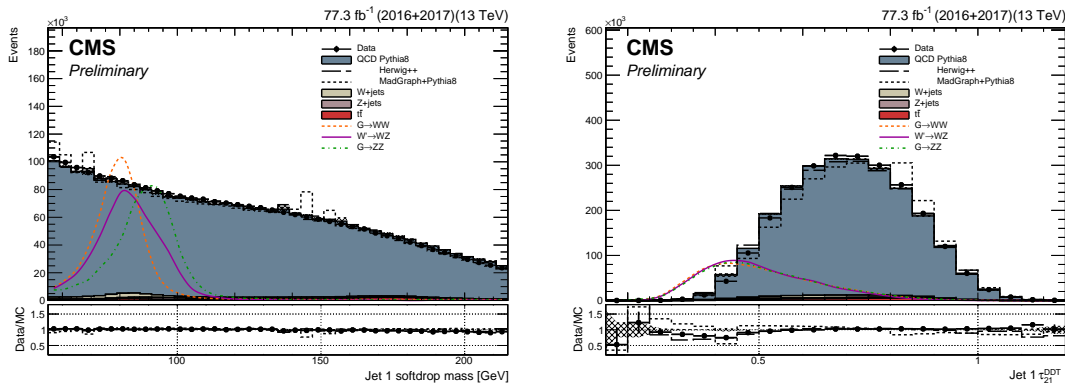


**Figure 4.75:** PUPPI softdrop jet mass distribution (left) and PUPPI N-subjettiness  $\tau_{21}^{DDT}$  (right). Signal is scaled with an arbitrary number.



2393 **Data to simulation scale factors**

2394 Following what was done in Section 4.1.7 and 4.2.5, we derive W-tagging scale factors for the  
2395 efficiency of the selection on  $\tau_{21}^{DDT}$  by estimating the ratio of the selection efficiencies on data and  
2396 simulation. The PUPPI softdrop mass range is extended to 55 to 215 GeV, and the two purity  
2397 categories are

- 2398 • Pass region:  $0 < \tau_{21}^{DDT} \leq 0.43 \sim$  high purity
- 2399 • Fail region:  $0.43 < \tau_{21} \leq 0.79 \sim$  low purity

2400 The obtained scale factors are listed in Tables 4.13 and 4.14 for 2016 and 2017 data, respectively,  
2401 with the corresponding simultaneous fits shown in Fig. 4.76. The jet mass scale and resolution  
2402 together with their are estimated in the same fits and also listed in Table 4.14. Two additional  
2403 uncertainties are added: one due to generator differences and one due to NNLO corrections.  
2404 These are evaluated by comparing the extracted efficiency with and without top  $p_T$  reweighting (a  
2405 weight derived from data in order to better describe the observed  $p_T$  distribution. Calculated for  
2406 each top jet as  $w = \exp^{0.0615 - 0.0005 * p_{T,top}}$ ) and when using  $t\bar{t}$  simulation produced with different  
2407 generators. The scale factors, jet mass scale and jet mass resolution with their total uncertainty  
2408 after adding systematics, are listed in Table 4.15. As before, the scale factor is added as a scale  
2409 of the signal yield and the jet mass scale and resolution are used to smear MC, and are  
2410 additionally inserted as systematic uncertainties in the final fit (scale up/down).

	m [GeV]	$\sigma$ [GeV]	W-tag efficiency
$\tau_{21}^{DDT} < 0.43$			
Data	$81.999 \pm 0.454$ GeV	$7.148 \pm 0.544$ GeV	$0.080 \pm 0.008$
Simulation	$80.890 \pm 0.160$ GeV	$6.579 \pm 0.149$ GeV	$0.085 \pm 0.003$
Data/simulation	$1.014 \pm 0.006$	$1.086 \pm 0.086$	$0.937 \pm 0.094$
$0.43 < \tau_{21}^{DDT} < 0.79$			
Data			$0.920 \pm 0.008$
Simulation			$0.915 \pm 0.003$
Data/simulation			$1.006 \pm 0.009$

**Table 4.13:** Jet mass scale, jet mass resolution and  $\tau_{21}^{DDT}$  scale factors as evaluated in the full 2016 Single Muon dataset.

2410

2411  **$p_T$  dependence**

2412 As the  $\tau_{21}^{DDT}$  working point used for this search is so tight, the statistics when evaluating data to  
2413 simulation scalefactors are very low in the pass category. A  $p_T$ -binned measurement has therefore

$\tau_{21}^{DDT} < 0.43$	m [GeV]	$\sigma$ [GeV]	W-tag efficiency
Data	$80.784 \pm 0.391$ GeV	$7.694 \pm 0.445$ GeV	$0.065 \pm 0.006$
Simulation	$82.208 \pm 0.293$ GeV	$7.127 \pm 0.284$ GeV	$0.068 \pm 0.005$
Data/simulation	$0.983 \pm 0.006$	$1.080 \pm 0.076$	$0.955 \pm 0.113$
$0.43 < \tau_{21}^{DDT} < 0.79$			
Data			$0.935 \pm 0.006$
Simulation			$0.932 \pm 0.005$
Data/simulation			$1.003 \pm 0.008$

**Table 4.14:** Jet mass scale, jet mass resolution and  $\tau_{21}^{DDT}$  scalefactors as evaluated in the full 2017 Single Muon dataset.

	SF $\pm \sqrt{\text{Stat.} + \text{Sys}_{\text{Generator}} + \text{Sys}_{\text{NNLO}}}$	SF $\pm$ Total Unc.
$HPSF_{DDT}^{2017}$	$0.955 \pm \sqrt{0.113^2 \text{ (stat.)} + 0.003^2 \text{ (sys.)} + 0.043^2 \text{ (sys.)}}$	$0.955 \pm 0.121$
$HPSF_{DDT}^{2016}$	$0.937 \pm \sqrt{0.094^2 \text{ (stat.)} + 0.003^2 \text{ (sys.)} + 0.043^2 \text{ (sys.)}}$	$0.937 \pm 0.103$
$LPSF_{DDT}^{2017}$	$1.003 \pm \sqrt{0.008^2 \text{ (stat.)} + 0.003^2 \text{ (sys.)} + 0.02^2 \text{ (sys.)}}$	$1.003 \pm 0.008$
$LPSF_{DDT}^{2016}$	$1.006 \pm \sqrt{0.009^2 \text{ (stat.)} + 0.003^2 \text{ (sys.)} + 0.02^2 \text{ (sys.)}}$	$1.006 \pm 0.009$
$JMS^{2017}$	$0.983 \pm \sqrt{0.006^2 \text{ (stat.)} + 0.002^2 \text{ (sys.)} + 0.001^2 \text{ (sys.)}}$	$0.983 \pm 0.007$
$JMS^{2016}$	$1.014 \pm \sqrt{0.006^2 \text{ (stat.)} + 0.002^2 \text{ (sys.)} + 0.001^2 \text{ (sys.)}}$	$1.014 \pm 0.007$
$JMR^{2017}$	$1.080 \pm \sqrt{0.076^2 \text{ (stat.)} + 0.027^2 \text{ (sys.)} + 0.001^2 \text{ (sys.)}}$	$1.080 \pm 0.081$
$JMR^{2016}$	$1.086 \pm \sqrt{0.086^2 \text{ (stat.)} + 0.027^2 \text{ (sys.)} + 0.001^2 \text{ (sys.)}}$	$1.086 \pm 0.090$

**Table 4.15:** Final jet mass scale, jet mass resolution and  $\tau_{21}^{DDT}$  scalefactors.

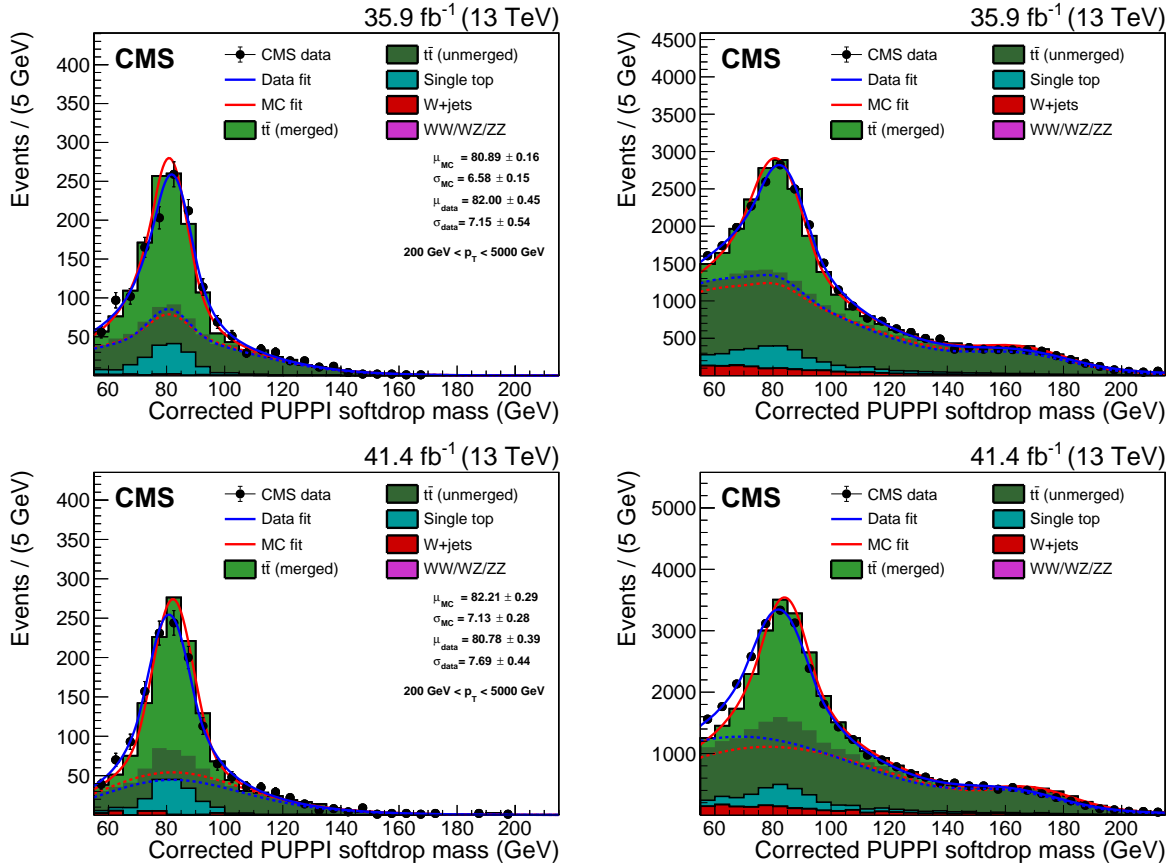


**Figure 4.76:** PUPPI softdrop jet mass distribution that pass (left) and fail (right) the  $\tau_{21}^{DDT} 0.43$  selection in the  $t\bar{t}$  control sample. The result of the fit to data and simulation are shown by the solid blue and solid red line, respectively. The background components of the fit are shown as dashed-dotted lines. The fit to 2016 data is shown in the upper panels and the fit to 2017 data in the lower panels.

not been possible. In order to get a feeling for how W-tagging efficiency, PUPPI softdrop jet mass scale and mass resolution scale factors change with jet transverse momentum, we do a measurement in 4 different  $p_T$  bins using the looser PUPPI softdrop +  $\tau_{21}$  tagger. The systematics are evaluated the same way as above (one due to top  $p_T$  reweighting and one comparing different  $t\bar{t}$  samples). Figure 4.77 shows the extracted W-tagging efficiency for data (black markers) and for simulation (red markers) using a PUPPI softdrop +  $\tau_{21} < 0.4$  based tagger as a function of jet  $p_T$ . The inclusive efficiency measurement is marked with triangles. The lower panel shows the efficiency ratio of data over simulation, corresponding to the W-tagging scale factor. All scale factors are compatible with unity, but the uncertainty on the measurement grows as statistics decrease. The corresponding extracted scale factors are listed in Table 4.16. With the observation

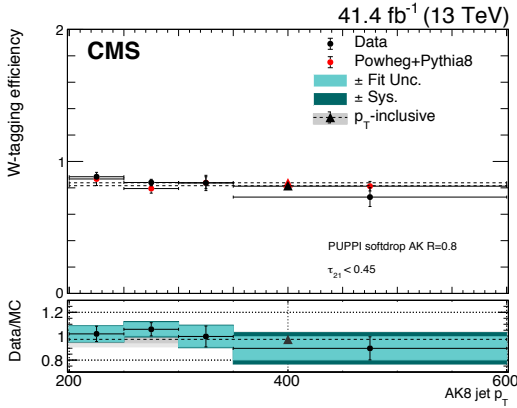


**Figure 4.77:** The W-tagging efficiency in data (black circles) and in simulation (red circles) as a function of jet  $p_T$ . The  $p_T$ -inclusive measurement is marked with triangles. The lower panel shows the efficiency in data divided by the efficiency in simulation, corresponding to the W-tagging uncertainty. The blue bands mark the fit and systematic uncertainties.

Bin	SF $\pm \sqrt{\text{Stat.} + \text{Sys}_{\text{Generator}} + \text{Sys}_{NNLO}}$	SF $\pm$ Total Unc.
200 - 250 GeV	$1.019 \pm \sqrt{0.064^2 + 0.005^2 + 0.022^2}$	$1.02 \pm 0.07$
250 - 300 GeV	$1.058 \pm \sqrt{0.055^2 + 0.033^2 + 0.002^2}$	$1.06 \pm 0.06$
300 - 350 GeV	$0.998 \pm \sqrt{0.087^2 + 0.035^2 + 0.007^2}$	$1.00 \pm 0.09$
350 - 600 GeV	$0.898 \pm \sqrt{0.097^2 + 0.089^2 + 0.007^2}$	$0.90 \pm 0.13$
$\geq 200$ GeV	$0.974 \pm \sqrt{0.029^2 + 0.055^2 + 0.015^2}$	$0.97 \pm 0.06$

**Table 4.16:** The data to simulation scalefactor scale factor for the PUPPI softdrop +  $\tau_{21}$  based tagger in bins of jet  $p_T$ . All scalefactors are compatible with unity.

of this clear trend of an uncertainty increase as a function of  $p_T$ , we evaluate a  $p_T$ -dependent W-tagging scalefactor uncertainty in the following way: Using signal Monte Carlo generated with two different shower generators, PYTHIA8 and HERWIG++, we compute the difference in tagging efficiency between the two at low- $p_T$ , where we have a real measurement in data, and compare that to the difference in tagging efficiency between the two at high- $p_T$ . In other words, we take a double ratio

$$\sigma_{p_T, \text{Bin}=i} = \frac{\left(\frac{\epsilon_{\text{PYTHIA}}}{\epsilon_{\text{HERWIG}}}\right)_{p_T, \text{Bin}=i}}{\left(\frac{\epsilon_{\text{PYTHIA}}}{\epsilon_{\text{HERWIG}}}\right)_{500 \text{ GeV}}} \quad (4.12)$$

This parametrization is then applied as a growing uncertainty on the signal yield as a function of resonance mass, where  $p_{T,\text{Bin}=i} = M_{X,i}/2$ , due to an uncertainty on the W-tagging efficiency. In contrast with what was found for the  $\tau_{21}$  based tagger (Section 4.1.7), where this uncertainty grew logarithmically with  $p_T$ , we find that the corresponding double ratio stabilizes around 1 TeV

<sup>2434</sup> when using  $\tau_{21}^{DDT}$  and is better described by a sigmoid function. The resulting parametrization is shown in Figure 4.78.

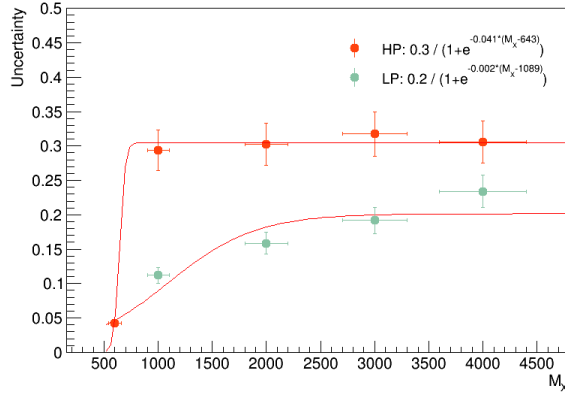


**Figure 4.78:** The parametrized uncertainty on W-tagging efficiency as a function of resonance mass ( $2 \times p_T$ ) extracted using the difference in tagging efficiency between PYTHIA and HERWIG++ Monte Carlo relative to the difference at 500 GeV

<sup>2435</sup> In addition to measuring the tagging  $p_T$  dependence we also extract the change in PUPPI  
<sup>2436</sup> softdrop jet mass scale and resolution as a function of  $p_T$ , as this should be roughly the same  
<sup>2437</sup> independent of whether  $\tau_{21}$  or  $\tau_{21}^{DDT}$  is used. We find that the jet mass scale ranges between 0.5  
<sup>2438</sup> and 2.5%, and the jet mass resolution between 4 and 10%, the latter measurement not being  
<sup>2439</sup> statistically significant as the uncertainties are large, around  $\sim 10\%$ ). We therefore use a fixed  
<sup>2440</sup> uncertainty of 2 and 10% for the PUPPI softdrop jet mass scale and resolution, respectively,  
<sup>2441</sup> which should be sufficient to cover a broadening and a shift at high  $p_T$ .  
<sup>2442</sup>

### 4.3.7 The multidimensional fit

As mentioned in the introduction to this chapter, the three-dimensional fit method takes advantage of the fact that the signal peaks in three dimensions; dijet invariant mass ( $M_{VV}$ ) and the jet groomed mass of jet 1 and jet 2 ( $M_{jet1}$  and  $M_{jet2}$ ) and attempt to extract the signal from the three dimensional  $M_{jet1}(x)$ - $M_{jet2}(y)$ - $M_{VV}(z)$  plane. In order to do so, four different types of PDFs need to be created in order to have a complete model:

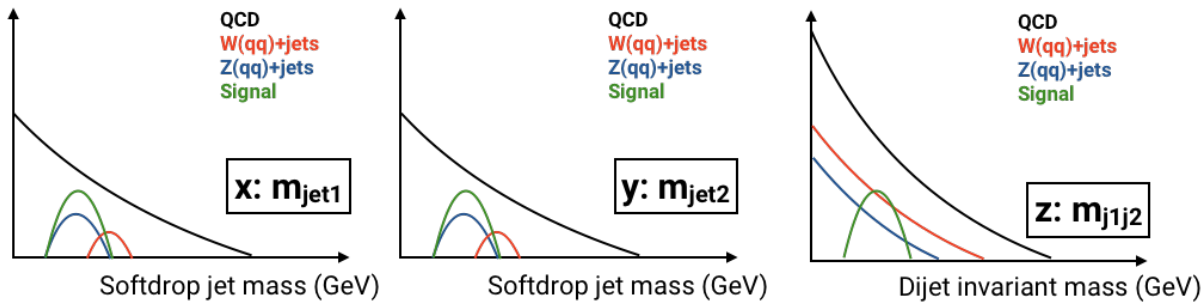


**Figure 4.79:** An illustration of the shape of the signal and the relative background contributions in the three relevant dimensions  $M_{jet1}(x)$ ,  $M_{jet2}(y)$  and  $M_{VV}(z)$ .

2448

- 2449 • **Signal 3D PDF:** Resonant in x, y and z. Parametrized as function of the resonance mass  
2450  $M_X$
- 2451 • **Non-resonant background:** Non-resonant in x, y and z and dominant background.  
2452 Created through a forward folding kernel approach
- 2453 • **Resonant background:** Mainly  $W/Z+jets$  (some  $t\bar{t}$ ). Resonant in x and y, smoothly  
2454 falling in z.
- 2455 • **Alternative shapes:** 5 additional shape uncertainties implemented through vertical  
2456 morphing

2457 These are illustrated in Figure 4.79 and will be described in detail in the following.

### 4.3.8 Modeling of the signal

2459 The signal shape in three dimensions is defined as a product of the shape of the resonance mass  
2460 and the jet masses:

$$P_{sig}(M_{VV}, M_{jet1}, M_{jet2} | \theta(M_X)) = P_{VV}(M_{VV} | \theta_1(M_X)) \times P_{j1}(M_{jet1} | \theta_2(M_X)) \times P_{j2}(M_{jet2} | \theta_2(M_X)). \quad (4.13)$$

The shapes for  $M_{VV}$ ,  $M_{jet1}$  and  $M_{jet2}$  all depend on the hypothesized mass of the new particle ( $M_X$ ) and a set of parameters  $\theta = (\theta_1, \theta_2)$  that in principle depend on  $M_X$ . The signal is parametrized by fitting the resonance mass and jet mass line shapes for each mass point, extracting the fitted parameters and then interpolating these as a function of the resonance mass hypothesis. For the resonance mass  $M_{VV}$ , the sum of a crystal-ball function and a Gaussian shape is used for each mass point, following the shapes used in Search II. Figure 4.80 shows the derived parameters and interpolation as a function of resonance mass. The final  $M_{VV}$  shapes as extracted from the parametrization are shown in Figure 4.81.

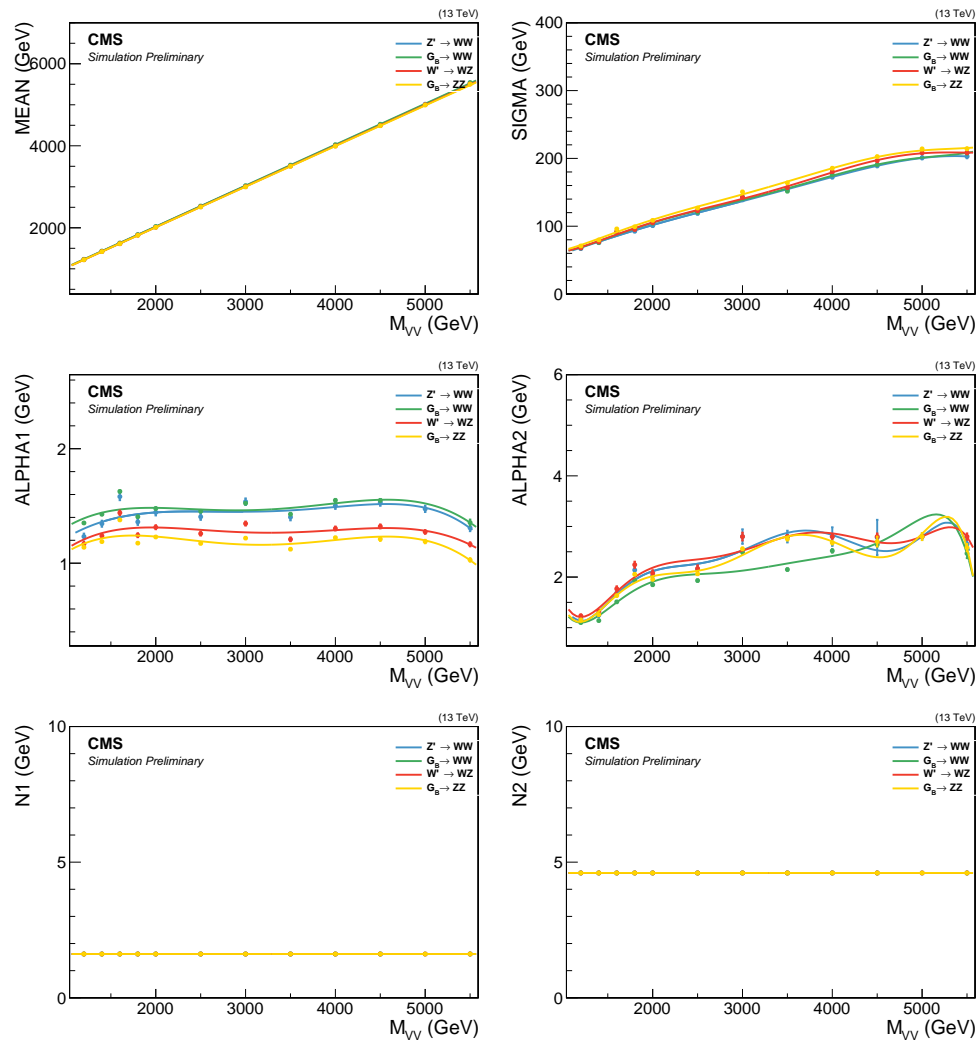


**Figure 4.80:** The interpolated Crystal-ball parameters for the dijet invariant mass as a function of  $M_X$ . The small variations for ALPHA2 have been shown to have no effect on the overall modeling.

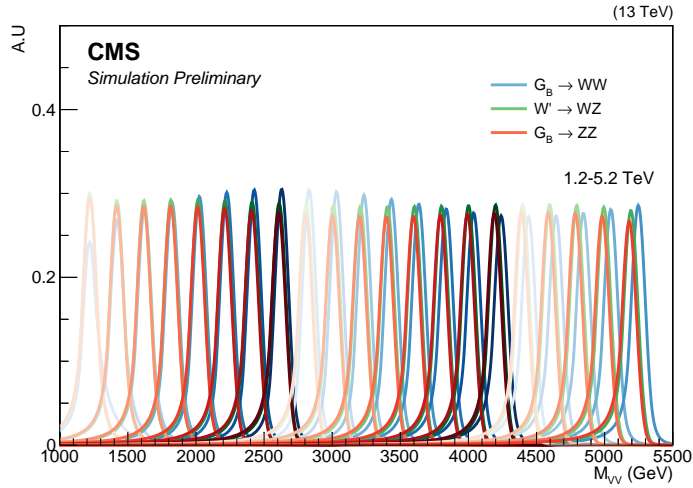


**Figure 4.81:** Final  $M_{VV}$  signal shapes extracted from the parametrization. Here for a  $G_{\text{bulk}}$  decaying to  $WW$  (blue) and  $ZZ$  (red) and for a  $W'$  decaying to  $WZ$  (green).

2469 The same procedure is used to model the jet mass: The  $M_{\text{jet}1}$  spectrum for each resonance  
 2470 mass hypothesis is fitted using a double Crystal-ball function, the fitted parameters are extracted  
 2471 and interpolated as functions of the resonance mass. This is done separately for  $M_{\text{jet}1}$  and  $M_{\text{jet}2}$ .  
 2472 The fitted parameters and interpolations are shown in Figure 4.82 for  $M_{\text{jet}1}$ , the corresponding  
 2473 distributions for  $M_{\text{jet}2}$  are in Appendix C.1. The final  $M_{\text{jet}1}$  shapes as extracted from the  
 2474 parametrization are shown in Figures 4.83. Finally, the signal yield is parametrized as a function  
 2475 of the resonance mass. For each mass point  $M_X$  and each purity category, the signal yield per  
 2476 picobarn of cross section is calculated as the integral of the Monte Carlo histogram. The yields  
 2477 are then interpolated as a function of  $M_X$ . The signal efficiency as a function of resonance mass  
 2478 is shown in Figure 4.84.

### 2479 4.3.9 Modeling of the non-resonant background

2480 In order to model the QCD multijets background in the three-dimensional  $M_{VV}$ - $M_{\text{jet}1}$ - $M_{\text{jet}2}$   
 2481 plane, we use the following conditional product:

$$P(M_{VV}, M_{\text{jet}1}, M_{\text{jet}2}) = P_{VV}(M_{VV}|\theta_1) \times P_{cond,1}(M_{\text{jet}1}|M_{VV}, \theta_2) \times P_{cond,2}(M_{\text{jet}2}|M_{VV}, \theta_2). \quad (4.14)$$

2482 This probability density requires a computation of the conditional two-dimensional shapes of  
 2483  $M_{\text{jet}1}/M_{\text{jet}2}$  given  $M_{VV}$ , as well as a one dimensional shape of the  $M_{VV}$  distribution.

2484 The following fit range and binning is used for the three axes:  $M_{\text{jet}1}/M_{\text{jet}2}$  is fitted from 55  
 2485 to 215 GeV using 2 GeV bins.  $M_{VV}$  is fitted from 1126 to 5500 GeV. The lower bound is chosen

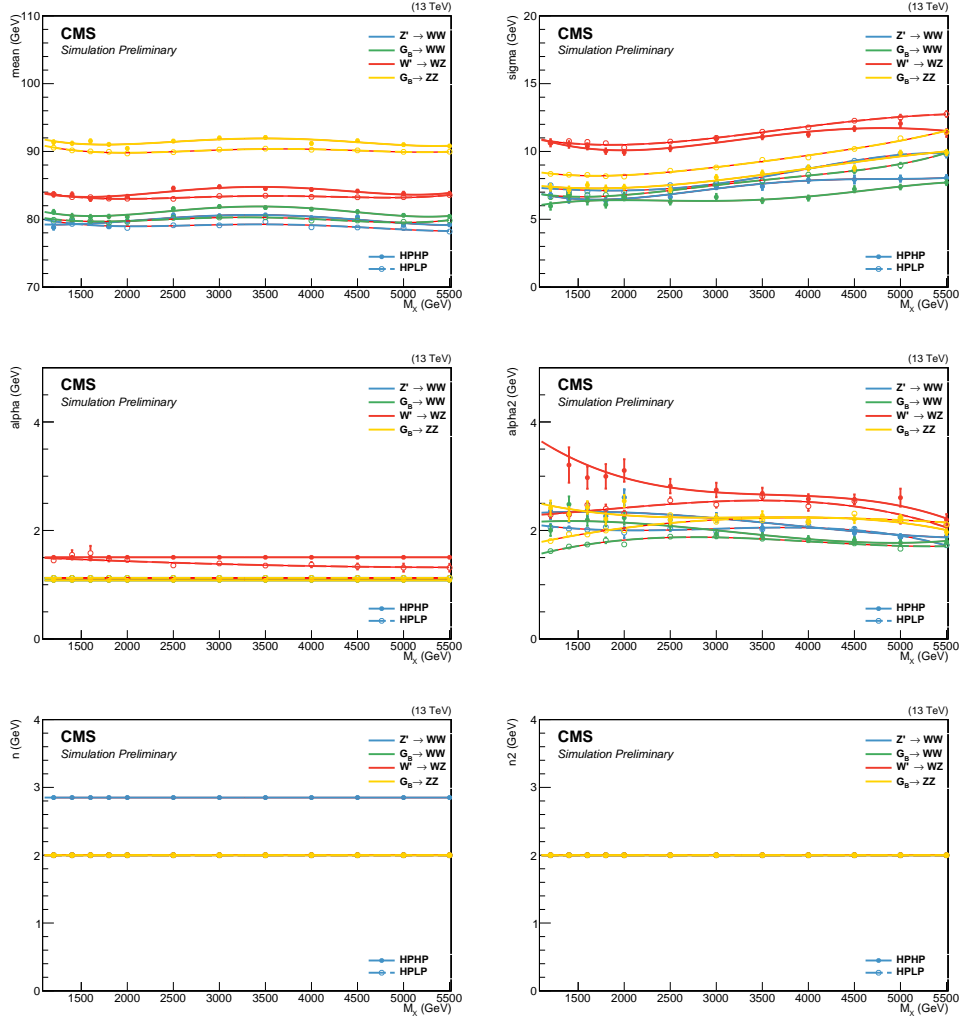


**Figure 4.82:** The interpolated double Crystal-ball parameters for the softdrop jet mass as a function of  $M_X$ . To improve the stability of the fit some parameters are set constant. Here for jet 1.

such that to avoid complications in the fitting procedure due to trigger turn-on effects, while the upper bound is chosen considering the highest dijet invariant mass found in data as well as avoiding mis-reconstruction effects at very large  $m_{jj}$  and low jet masses. For  $M_{VV}$ , the “dijet binning” is used. This binning corresponds to the actual dijet mass resolution and is, in units of GeV:

2490

2491        Dijet binning = 1126, 1181, 1246, 1313, 1383, 1455, 1530, 1607, 1687, 1770, 1856, 1945,  
 2492        2037, 2132, 2231, 2332, 2438, 2546, 2659, 2775, 2895, 3019, 3147, 3279, 3416, 3558, 3704,

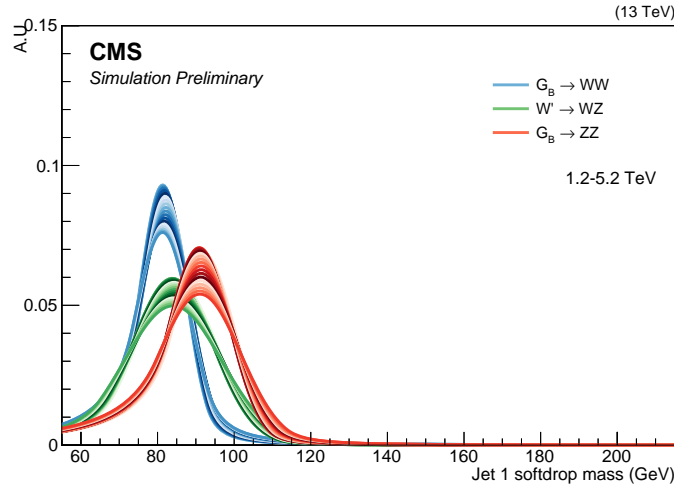


**Figure 4.83:** Final  $M_{\text{jet}}$  signal shapes extracted from the parametrization for a  $G_{\text{bulk}}$  decaying to ZZ, a  $G_{\text{bulk}}$  decaying to WW and for a  $W'$  decaying to WZ.

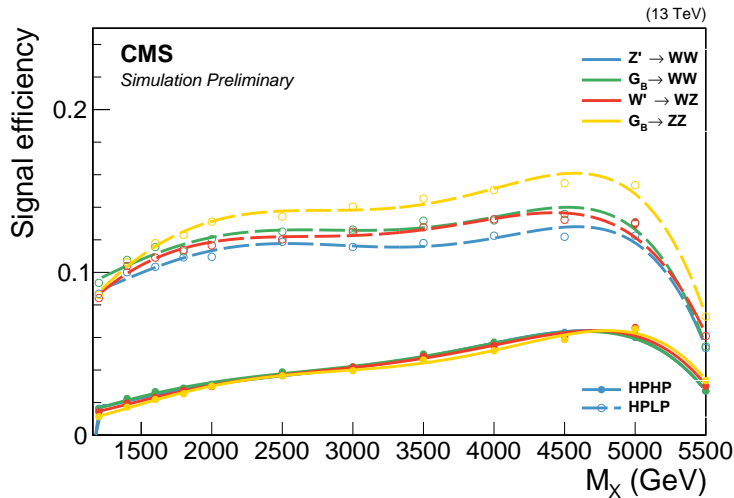


**Figure 4.84:** Signal efficiency as a function of resonance mass.

2493 3854, 4010, 4171, 4337, 4509, 4686, 4869, 5058, 5253, 5500

2494

2495 The background model is built starting from simulation and we encode sufficient nuisance  
 2496 parameters into the fit, allowing the shape to adapt itself to data. For this we use a “forward-  
 2497 folding” approach. For each MC event in the two(one)-dimensional  $M_{\text{vv}}-M_{\text{jet}}$  ( $M_{\text{jet}}$ ) space, a  
 2498 2D(1D) Gaussian kernel is built starting from generator level quantities. Each of these Gaussians

then contribute to the total probability density of the final two(one)-dimensional probability density functions

First, the resonance mass and softdrop jet mass scale and resolution are derived. For this we use the anti- $k_T$  generated jet collection matched to jets identified as V-jets on reconstruction level. We then derived the  $M_{\text{jet}}$  and  $M_{\text{VV}}$  scale and resolution from a Gaussian fit to  $M_i(\text{reco})/M_i(\text{gen})$  ( $i = M_{\text{jet}}$  or  $i = M_{\text{VV}}$ ) in bins of generator jet  $p_T$ . Figure 4.85 shows the fit to  $M_{\text{jet}}(\text{reco})/M_{\text{jet}}(\text{gen})$  (left) and  $M_{jj}(\text{reco})/M_{jj}(\text{gen})$  (right) for an arbitrary bin. The Gaussian mean yields the mass scale and the Gaussian width the mass resolution. The resonance mass and softdrop jet mass

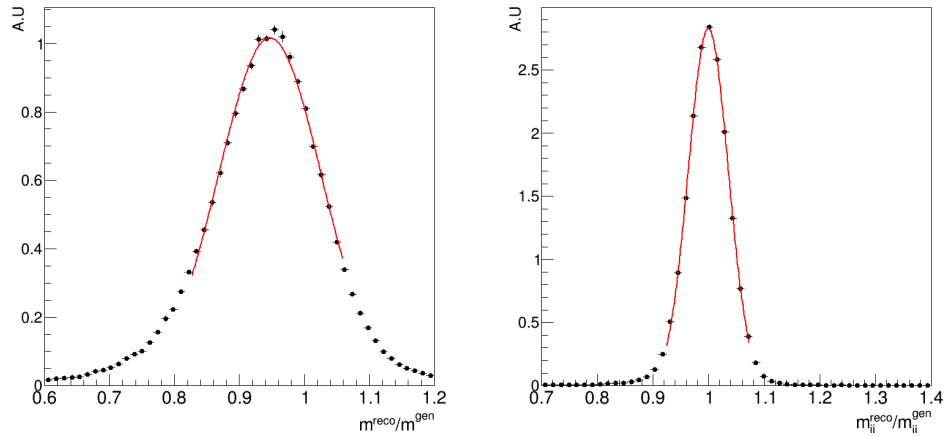


**Figure 4.85:** Fit to  $M_{\text{jet}}(\text{reco})/M_{\text{jet}}(\text{gen})$  (left) and  $M_{jj}(\text{reco})/M_{jj}(\text{gen})$ . The mass resolution is taken as the width of the fitted Gaussian, while the Gaussian mean yields the mass scale.

scale and resolution as a function of generator jet  $p_T$  is shown in Figure 4.86. The projection of these resolution functions are shown in Figure 4.87. The mass scale and resolution are then used to populate the conditional 2D histogram as follows. Each generated event is smeared with a 2D Gaussian kernel

$$k(M_{\text{jet}}, M_{\text{VV}}) = \frac{w_i}{\sqrt{2\pi}r_{M_{\text{VV}},i} \cdot r_{M_{\text{jet}},i}} \exp \left( -\frac{1}{2} \left( \frac{M_{\text{VV}} - s_{M_{\text{VV}},i}}{r_{M_{\text{VV}},i}} \right)^2 - \frac{1}{2} \left( \frac{M_{\text{jet}} - s_{M_{\text{jet}},i}}{r_{M_{\text{jet}},i}} \right)^2 \right), \quad (4.15)$$

where  $s_i, r_i$  are the scale and the resolution derived in the previous step and  $w_i$  is the event weight product (e.g PU, cross sections etc.). The resulting kernel values are filled into a 2D histogram. This procedure is performed separately for  $M_{\text{jet}1}$  and  $M_{\text{jet}2}$ . To build the one-dimensional template for the dijet invariant mass the same procedure as above is used, with the exception that the smearing is done with one-dimensional Gaussian kernel only depending on  $M_{\text{VV}}$ . The templates are then added together to form a three-dimensional PDF. Finally, we fit this 3D PDF to QCD

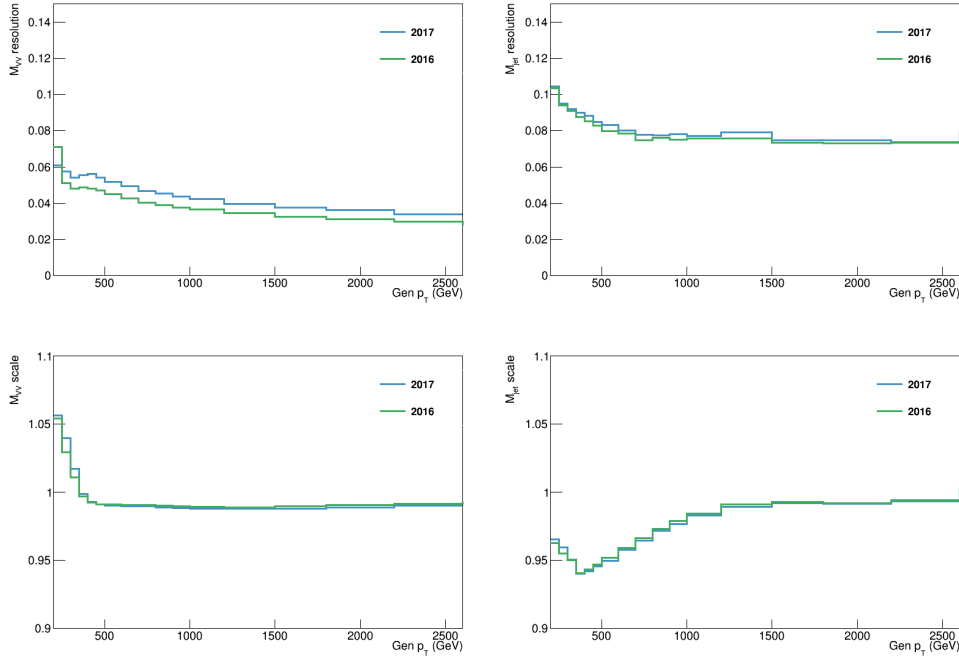


**Figure 4.86:** Resolution (top) and scale (bottom) for  $M_{VV}$  (left) and the  $M_{jet}$  (right) as a function of generator jet  $p_T$ .

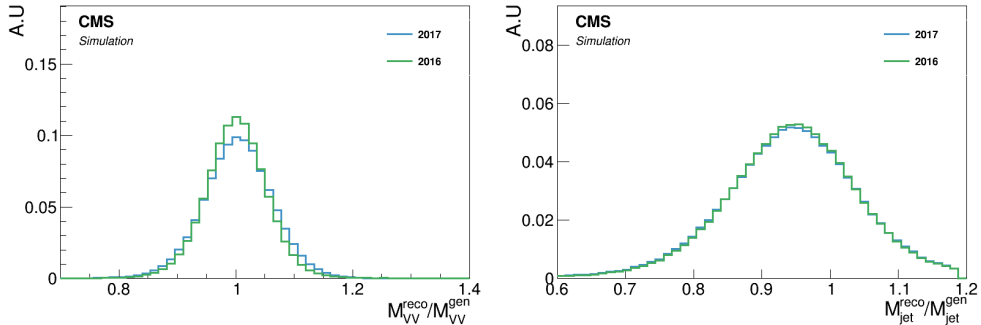


**Figure 4.87:** Projections of the resolution functions for all generator jet  $p_T$  bins for  $M_{VV}$  (left) and  $M_{jet}$  (right).

2517 MC in order to remove any residual bias (mainly at the extreme ends of the spectra). The result  
 2518 is a full, smooth shape replacing the prediction from simulation.

2519 As the high purity category is limited by statistics, we rather build this template starting  
 2520 from the low purity templates. This is done by fitting the low purity 3D template to QCD MC in  
 2521 the high purity category. Figure 4.88 show the final templates (solid lines) together with the QCD

MC (data points) derived from the 2017 MC in the low purity (top) and high purity category (bottom). Good agreement between simulation and templates in all three dimensions is observed, within statistical uncertainties. The corresponding distributions in 2016 MC can be found in Appendix C.2.

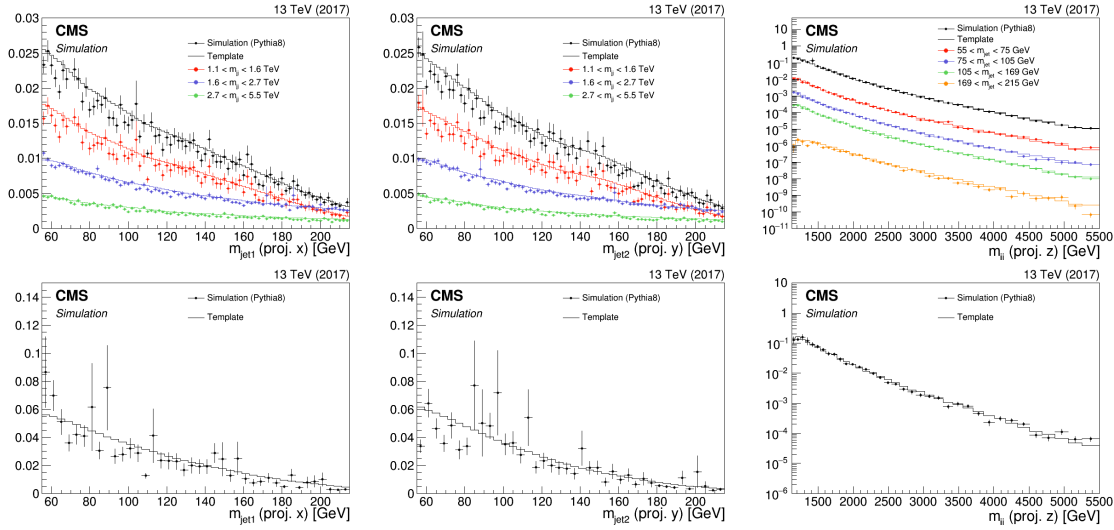


**Figure 4.88:** Comparison between QCD MC simulation (markers) and kernels derived from generator level quantities (lines) for the HPHP (top) and HPLP (bottom) categories using 2017 MC. The kernels are shown for  $M_{\text{jet}1}$  (left),  $M_{\text{jet}2}$  (middle) and  $M_{\text{vv}}$  (right).

In order to validate the kernel transfer method, we check that we can fit a higher-statistics high purity region by loosening the  $\tau_{21}^{\text{DDT}}$  cut to 0.49. This results in 12 times more background events, and should uncover whether any degeneracy is present in the fits themselves and whether the low purity kernel indeed is capable of modeling the high purity region, without being camouflaged by large error bars. The resulting kernel versus MC spectra are shown in Figure 4.89. Good closure is observed in all three dimensions, demonstrating that the HPLP kernels adapt well to the HPHP MC data points even when statistics are sufficient, and we consider the method sound.

2533

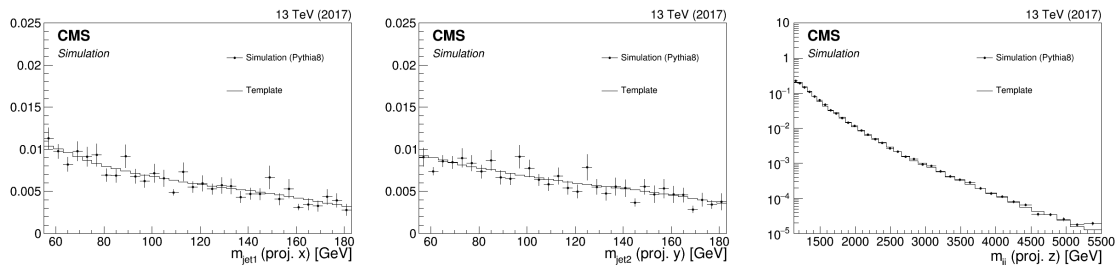


**Figure 4.89:** Comparison between QCD MC simulation (markers) and kernels derived from generator level quantities (lines) in the HPHP category, using a looser cut on  $\tau_{21}^{DDT}$ .

<sup>2534</sup> **4.3.10 Modeling of the resonant background**

In addition to the QCD multijet background, there are a few sub-dominant processes to consider which contain one real vector boson and at least one QCD-jet. These are W+jets, Z+jets and events from  $t\bar{t}$  processes. They are resonant around the W/Z mass in the two softdrop jet mass dimensions and must therefore be treated differently than the non-resonant QCD background. Figure 4.90 shows the projections on  $M_{jet1}$  (left),  $M_{jet2}$  (middle) and  $M_{VV}$  (right). As the jets are

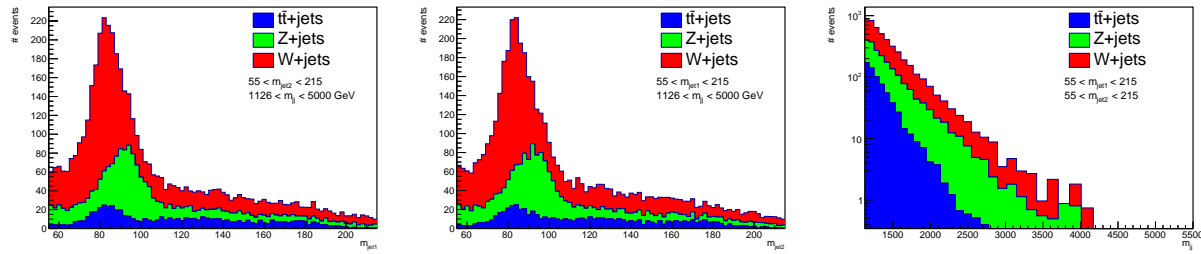


**Figure 4.90:** Projections of the sub-dominant backgrounds on the jet mass axes  $M_{jet1}$  (left) and  $M_{jet2}$  (middle), as well as on the dijet invariant mass  $M_{VV}$  (right). Here in the low purity category.

randomly sorted, each jet mass dimension contains two contributions: A resonant part consisting of real vector boson jets, peaking around the V mass, and a non-resonant part composed of jets originating from a quark or a gluon, similar to the QCD multijets background. These two contributions are modeled separately as we know that the non-resonant part of the jet mass spectrum is correlated with the dijet invariant mass (like QCD), while the resonant part is not. We additionally want to encode the fact that we know these backgrounds in reality only peaks in one jet mass axis (there is only one real vector boson) by requiring the PDFs to consist of a resonant part on one axis, and a non-resonant part on the other axis. A three dimensional PDF for the sub-dominant backgrounds is built as a product of three one dimensional pdf's as follows:

$$P_{res}(M_{jet1}, M_{jet2}, M_{VV}) = P_{VV}(M_{VV}) \times P_{jet1}(M_{jet1}, M_{jet2}) \times P_{jet2}(M_{jet2}, M_{jet1}) \quad (4.16)$$

where

$$P_{jet1}(M_{jet1}, M_{jet2}) = f \times R(M_{jet2}) \times P_{res}(M_{jet1}) + (1 - f)P_{non-res}(M_{jet1}) \quad (4.17)$$

$$P_{jet2}(M_{jet2}, M_{jet1}) = (1 - f) \times R(M_{jet1}) \times P_{res}(M_{jet2}) + fP_{non-res}(M_{jet2}) \quad (4.18)$$

2535 Here,  $R(M_{\text{jet}})$  parametrizes the correlation between  $M_{\text{jet}1}$  and  $M_{\text{jet}2}$  and  $f$  is a fit parameter that  
 2536 is used to adjust the fraction of real vector boson jets in  $M_{\text{jet}1}$  compared to  $M_{\text{jet}2}$ . Its value can  
 2537 vary 10% around  $f = 0.5$ , the expected median when using a random jet sorting.  
 2538 As the contribution of the  $t\bar{t}$  background is much smaller than the one coming from V+jets (less  
 2539 than 2%), it is modeled together with the W+jets contribution. Therefore only two PDFs are  
 2540 built for the resonant background: One for the W+jets and  $t\bar{t}$ , and one for Z+jets.  
 2541 The available MC statistics in the high purity category is very low and therefore the parametrization  
 2542 of the resonant background is done for the low purity category only, and the resulting shapes are  
 2543 then used for both purity categories. The uncertainties for the different purity categories are,  
 2544 however, included as separate nuisance parameters in the fit.

2545 The non-resonant  $M_{\text{VV}}$  PDF is constructed using the same kernel approach as is used to  
 2546 model the QCD multijet background with one minor difference: Due to the low statistics in the  
 2547 high- $M_{\text{VV}}$  tail, an additional smoothing of the jet mass tail using a leveled exponential

$$\frac{dN}{dm_{jj}} = \frac{P_0(1 - m_{jj}/s)^{P_1}}{(m_{jj}/s)^{P_2}} \quad (4.19)$$

2548 is performed. Here,  $s$  is the center of mass energy. The function is fitted to the spectrum starting  
 2549 from a dijet mass of 1.1 (2.1) TeV for high purity (low purity). Two uncertainties on this shape is  
 2550 added in order to accommodate for MC mis-modeling due to higher order QCD and electroweak  
 2551 corrections: One proportional to  $M_{\text{VV}}$  and one proportional to  $1/M_{\text{VV}}$ . The resulting  $M_{\text{VV}}$   
 2552 kernels (solid lines) for the W+jets background are shown in Figure 4.91 and are compared to  
 2553 MC simulation (markers). The blue line corresponds to the nominal shape, while the red and  
 2554 green lines correspond to the uncertainties proportional to  $M_{\text{VV}}$  and  $1/M_{\text{VV}}$ , respectively. The  
 2555 corresponding distributions for the Z+jets background are shown in Appendix C.3.

As mentioned above, the modeling of the  $M_{\text{jet}}$  spectrum is split into two different PDFs: One describing the resonant and one describing the non-resonant part. We distinguish between the two by requiring the resonant contribution to consist of jets matched to a generated boson within a cone of  $\Delta R = 0.8$ . A double-sided crystal-ball function is then fitted to the resonant spectrum for W+jets and Z+jets separately. This allows us to fully correlate uncertainties on the mean and width of the  $M_{\text{jet}}$  distribution for signal with the corresponding values for W/Z+jets, as these uncertainties affect all jets generated from real vector bosons in the same way. This effectively gives us a way of constraining these parameters directly from data. The parametrization of the resonant part of the jet mass spectrum for  $M_{\text{jet}1}$  is shown in Figure 4.92 for W+jets and  $t\bar{t}$  (left) and Z+jets. The small enhancement around 170 GeV is caused by fully merged top jets and is so small (< 2% in the low purity and < 0.5% in the high purity category) that we do not take

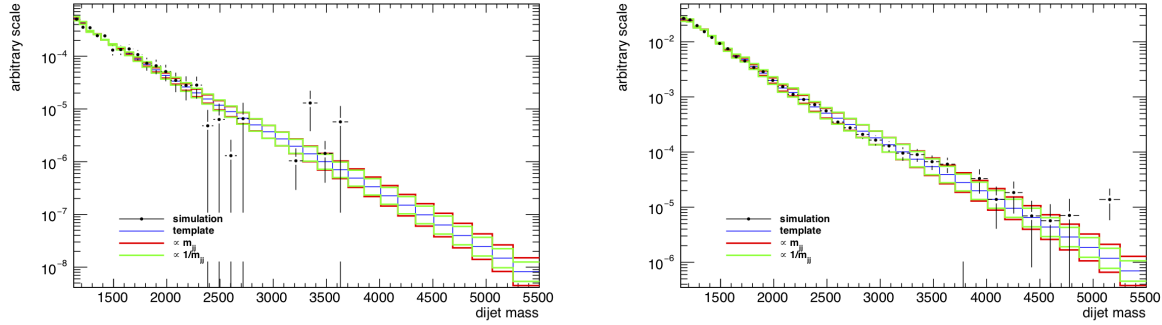


**Figure 4.91:** One dimensional  $M_{VV}$  kernels (solid line) compared to MC (markers) for the  $W+jets$  background in the HPHP (left) and HPLP (right) categories. The blue line corresponds to the nominal shape, while the red and green lines correspond to uncertainties proportional to  $M_{VV}$  and  $1/M_{VV}$ , respectively.

it into account in the final PDF. The non-resonant part of the  $V+jets$  background is modeled

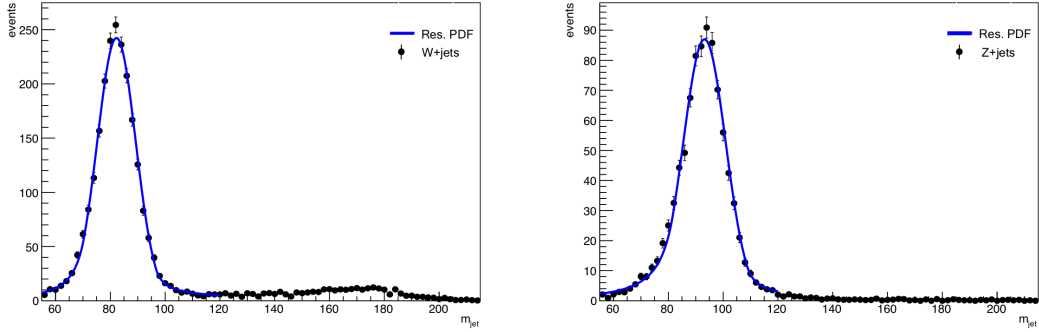


**Figure 4.92:** Fit to the resonant part of the  $V+jets$  and  $t\bar{t}$  spectrum for  $W+jets$  and  $t\bar{t}$  (left) and  $Z+jets$  (right).

using a simple Gaussian fit to the spectrum of jets not matched to a real vector bosons, as shown in Figure 4.93. For the resonant modeling, correlations between the jet mass  $M_{jet}$  and dijet invariant mass  $M_{VV}$  have been found small enough to be neglected (the jet mass spectrum does not, within statistical uncertainties, depend on the jet  $p_T$ ). However, there is a strong correlation between the softdrop jet mass of each jet due to the fact that when one of the two jets originates from a real boson peaking around the  $V$  mass, the other is bound to be a quark jet. Therefore, the fraction of real boson jets contained in  $M_{jet1}$  affects the fraction of real  $V$  jets in  $M_{jet2}$ . To account for this, the fraction of real  $V$  jets versus quark/gluon jets jets, is parametrized as a

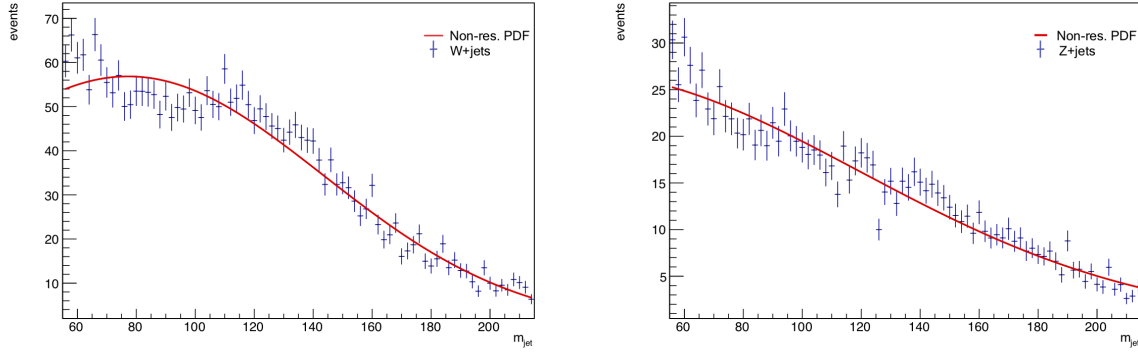


**Figure 4.93:** Fit to the non-resonant part of the  $V+jets$  and  $t\bar{t}$  spectrum for  $W+jets$  and  $t\bar{t}$  (left) and  $Z+jets$  (right).

function of the jet mass. As the jets are randomly sorted, we define the parametrization as

$$R(M_{jet}) = \frac{N_{res,jet1}(M_{jet2}) + N_{res,jet2}(M_{jet1})}{N_{non-res,jet1}(M_{jet2}) + N_{non-res,jet2}(M_{jet1})}. \quad (4.20)$$

2556 Where  $N(M_{jet})$  denotes the number of events within a given  $M_{jet}$  window. The resulting ratio is then fitted with a polynomial function, as shown in Figure 4.94. As a closure test, the

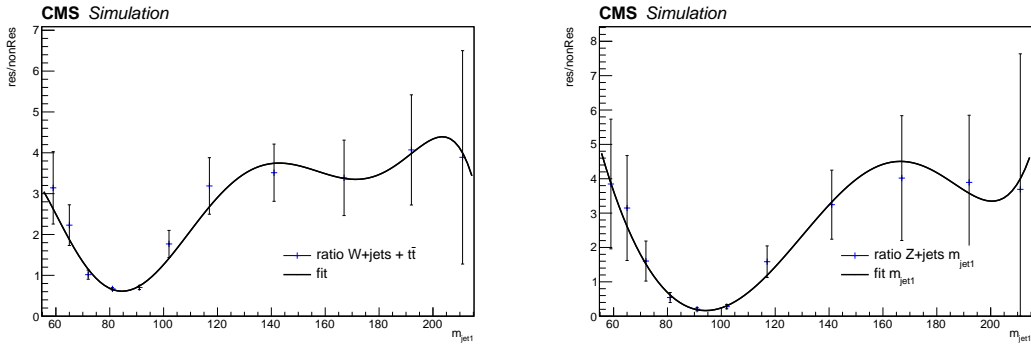


**Figure 4.94:** Ratio of resonant to non-resonant events in  $W+jets$  (left) and  $Z+jets$  (right) as a function of jet mass.

2557  
2558 three dimensional kernel as defined in Equation 4.16 is fitted to the  $V+jets$  and  $t\bar{t}$  simulation.  
2559 Figure 4.95 shows the fitted kernel (red) together with the MC data points (black markers) in  
2560 the low (top) and high (bottom) purity categories. Mostly good agreement is observed along all  
2561 dimensions, with some deviations in the very high  $M_{VV}$  tail in the high purity category. This is,  
2562 however, a region dominated with very little statistics and is completely swallowed up by the

QCD multijets background which has the same shape.

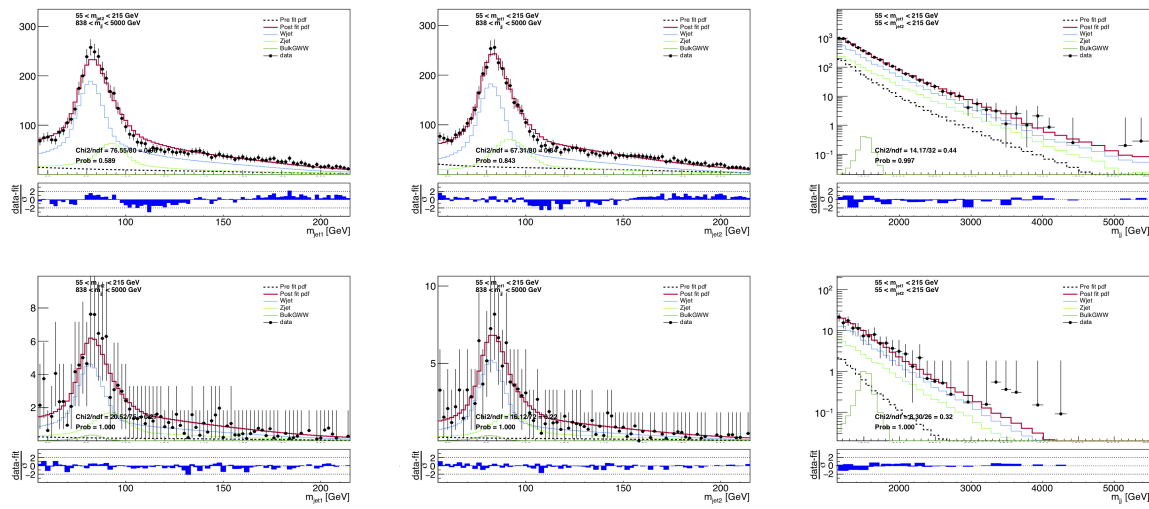


**Figure 4.95:** Final fits of the complete background model (red line) to the MC simulation of the V+jets backgrounds (black markers) for the high purity category.

### 2564 4.3.11 Systematic uncertainties

2565 Systematic uncertainties are inserted as nuisance parameters in the fit and affect the normalization  
 2566 and shape of both signal and background.

#### 2567 Signal normalization uncertainties

2568 As all background contributions are data driven, the largest systematic uncertainties affect only  
 2569 the signal.

- 2570 • **luminosity** 2.6%(2.3%) for the 2016(2017) dataset
- 2571 •  $\tau_{21}^{DDT}$  **efficiency** 1-12% systematic uncertainty on the signal efficiency scale factor for the  
 2572  $\tau_{21}^{DDT}$  selection (listed in Table 4.15). Anti-correlated between the HP and LP categories.
- 2573 •  $\tau_{21}^{DDT}$   **$p_T$  extrapolation** An additional uncertainty arising from the extrapolation of  
 2574 the V-tagging efficiency scale factors towards higher transverse momenta. Treated as  
 2575 correlated between the  $\tau_{21}^{DDT}$  categories and is given as  $3.9\% \times \ln(p_T/200 \text{ GeV})$  and  
 2576  $8.5\% \times \ln(p_T/200 \text{ GeV})$  for the LP and HP regions, respectively.
- 2577 • **PDF and factorization/renormalization scale** 2% uncertainty on the signal accep-  
 2578 tance due to choice of PDFs and factorization/renormalization scale.

#### 2579 Background normalization uncertainties

2580 The QCD multijet background has a poorly known cross section and is therefore allowed to  
 2581 float within 50% of the yield expected by simulation. For the resonant V+jets background, the  
 2582 following uncertainties on the normalization is added: One due to cross section ( $\sim 5\%$ ), one due  
 2583 to NLO QCD corrections ( $\sim 10\%$ ) and one due NLO electroweak corrections ( $\sim 15 - 35\%$ ).

#### 2584 Signal and resonant background shape uncertainties

2585 There are two shape uncertainties correlated between the signal and V+jets background: System-  
 2586 atics due to jet mass scale (JMS) and jet mass resolution (JMR). These are evaluated in a  $t\bar{t}$   
 2587 control region, listed in Table 4.15, and affect the mean and width of the jet mass PDFs. Three  
 2588 additional shape uncertainties are added for the signal: Uncertainties due to jet energy scale  
 2589 (JES), jet energy resolution (JER) and PDF. The uncertainty due to JES/JER is evaluated by  
 2590 reweighting the transverse momentum of each MC event in signal MC, then fitting a Gaussian  
 2591 to the dijet invariant mass spectrum and calculating the change in the mean and variance with

respect to no reweighting. These are then used as uncertainties on the signal  $M_{VV}$  shape (2% for the dijet mass scale, 5% for the resolution).

Uncertainties due to the PDF are evaluated by reweighting each event according to  $\approx 100$  PDF variations. The impact on the signal shapes are again evaluated by fitting a Gaussian to the  $m_{jet}$  and  $m_{jj}$  distributions before and after changing PDF weights. The obtained variation is < 1% for the 2017 signal MC, but slightly higher in 2016. An overall uncertainty on the acceptance of 3% is therefore applied.

### Non-resonant background shape uncertainties

Alternate shapes for the non-resonant background components are added to the fit through vertical template morphing. This creates nuisance parameters for each additional shape shape, allowing the derived nominal 3D PDF to vary within the respective nuisances to match the data. Shape uncertainties that simultaneously affect all three dimensions are used, totaling to 5 to take all possible effects into account. The first effect accounts for variation of the underlying transverse momentum spectrum and is obtained through an alternate shape produced by varying the jet masses  $M_{jet}$  and dijet mass  $M_{VV}$  by a quantity proportional to  $M_{VV}$  and  $M_{jet}$ . The second effect considered is a variation of the scale, where the corresponding alternate shape is obtained by simultaneously varying  $M_{jet}$  and  $M_{VV}$  up and down by a quantity proportional to  $1/M_{VV}$  and  $1/M_{jet}$ . Finally, as we do not know a priori whether Nature behaves more like PYTHIA8, HERWIG++ or MADGRAPH+PYTHIA8, we account for differences due to MC generation and parton shower modeling by adding three additional shapes corresponding to the PDFs obtained using different QCD MC generators.

Those five shape uncertainties are assigned very large pre-fit values (allowed to float within 33%), effectively allowing the simulation to take any value to describe the data. The alternate shapes described above are shown in Figure 4.96, here for the 2017 analysis.

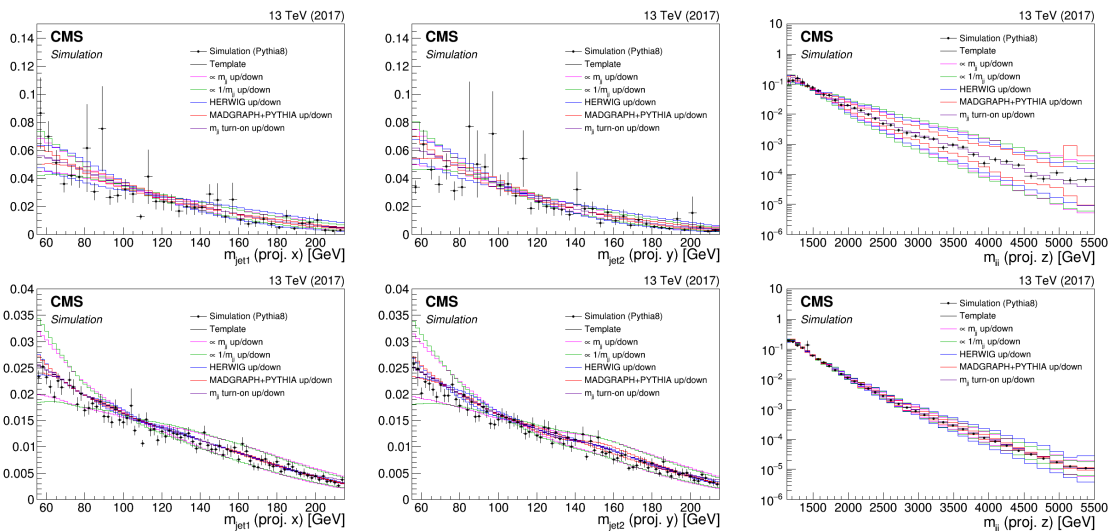


**Figure 4.96:** The nominal MC data (markers) and smooth nominal kernel obtained from PYTHIA8 (black line), together with the five alternate shapes added to the fit as shape nuisance parameters. Here for the high (top) and low (bottom) categories.

## 4.4 Background model validation

In order to convince ourselves that the fit is robust, several checks are performed in simulation and in a data control region before unblinding the data signal region.

### 4.4.1 Variations of QCD multijet predictions

First, we check that the main template (generated starting from QCD PYTHIA8 MC) can fit predictions from alternate QCD multijets samples in order to demonstrate that systematic uncertainties in the modeling of parton showers are covered by the relevant nuisance parameters. Fits to three different QCD samples are compared: PYTHIA8 (nominal), HERWIG++ (alternate shape 1) and MADGRAPH+PYTHIA8 (alternate shape 2). To ensure a smooth data distribution not affected by low statistics present in the MC spectra, we generate a toy dataset under the templates rather than using MC events directly. The postfit distributions after fitting each toy, is shown in Figures 4.97-4.99 for the HPHP (top) and HPLP category (bottom).

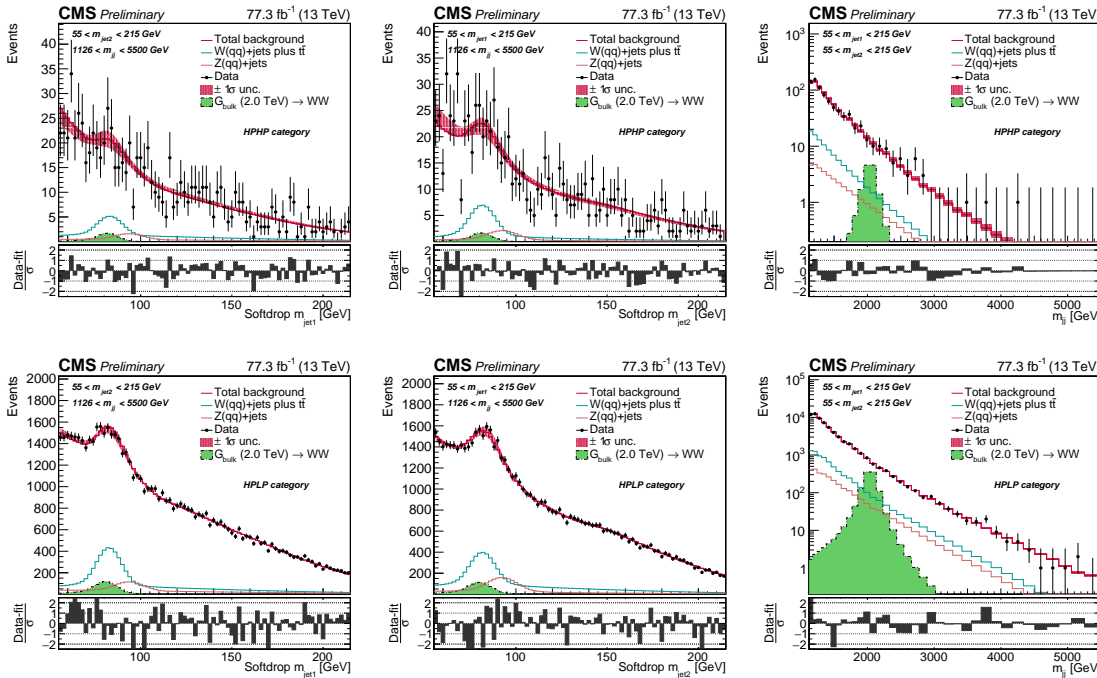


**Figure 4.97:** Postfit distributions after a combined fit to a toy datasets generated under the QCD PYTHIA8 template. The projections of  $M_{\text{jet}1}$  (left),  $M_{\text{jet}2}$  (middle) and  $M_{VV}$  (right) are shown for the HPHP (top) and HPLP (bottom) category.

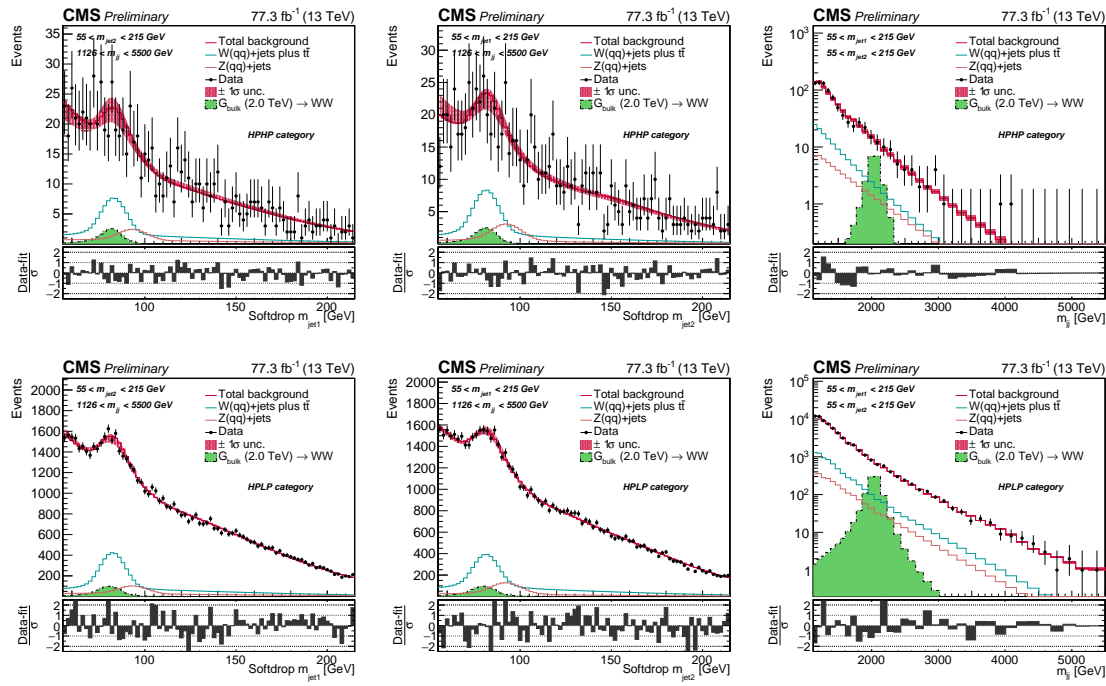


**Figure 4.98:** Postfit distributions after a combined fit to a toy datasets generated under the QCD HERWIG++ template. The projections of  $M_{\text{jet}1}$  (left),  $M_{\text{jet}2}$  (middle) and  $M_{\text{VV}}$  (right) are shown for the HPHP (top) and HPLP (bottom) category.

To quantify the fit quality of these, a goodness-of-fit test is performed using a saturated model (which is valid when data are non-Gaussian), shown in Figure 4.100. The test statistics are Gaussian distributed and the toy dataset is in good agreement with the background only hypothesis, demonstrating the fits ability to account for differences in QCD multijet predictions.

#### 4.4.2 Fit to data control region

TO validate the method in data, the 3D fit procedure is tested in a data control region where both jets are required to have  $0.43 < \tau_{21}^{DDT} \leq 0.79$ , the so-called LPLP category. The templates are built following the procedure described in Section 4.3.9. In this category, the contribution of the resonant background is negligible with respect to the dominant QCD multijet background and is removed from the fit. The post-fit distributions in the data control region are shown in Figures 4.101–4.103 for different jet mass and dijet invariant mass bins. A goodness-of-fit check is performed, shown on the left plot in Figure 4.104, and we again find that the toys are Gaussian distributed and the LPLP data is in good agreement with the background-only hypothesis. The post-fit value and uncertainty of each nuisance parameter involved in the fit is also studied, where

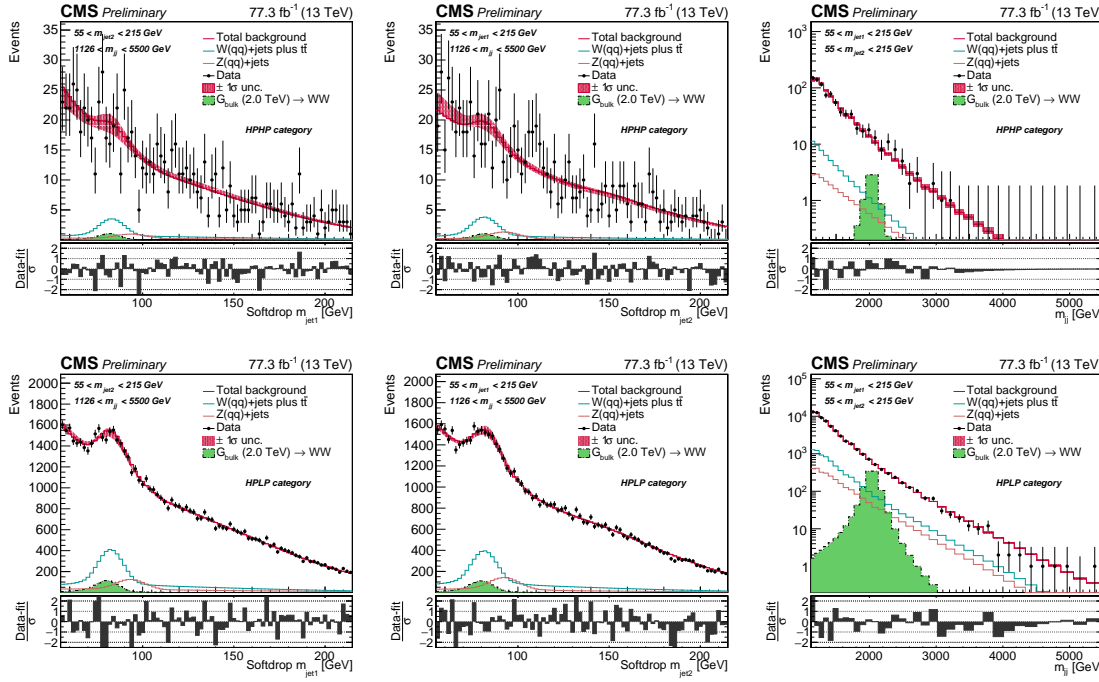


**Figure 4.99:** Postfit distributions after a combined fit to a toy datasets generated under the QCD QCD MADGRAPH+PYTHIA8 template. The projections of  $M_{\text{jet}1}$  (left),  $M_{\text{jet}2}$  (middle) and  $M_{VV}$  (right) are shown for the HPHP (top) and HPLP (bottom) category.

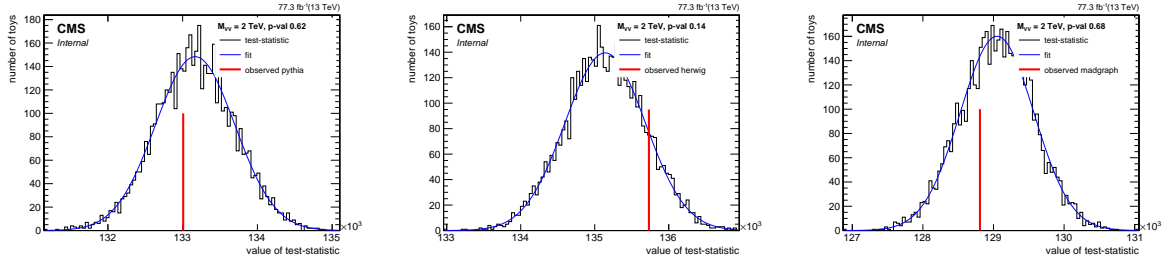


**Figure 4.100:** The likelihood for toys generated around the background-only hypothesis compared to the likelihood value of a toy dataset generated under the PYTHIA (left), HERWIG (middle) and MADGRAPH+PYTHIA8 template (right).

deviations from the pre-fit value is quantified through the “pull”, defined as  $p_\theta = (\theta - \theta_{in})/\sigma_\theta$ , where,  $\theta$  and  $\sigma_\theta$  are the post-fit value of the nuisance parameter and its uncertainty, and  $\theta_{in}$  the pre-fit value. The pulls for all nuisance parameters are shown in the right plot in Figure 4.104, where the uncertainty is defined as the ratio between the post- and pre-fit uncertainties. The post-fit values show a reasonable deviation from the chosen pre-fit values of 0. The uncertainties

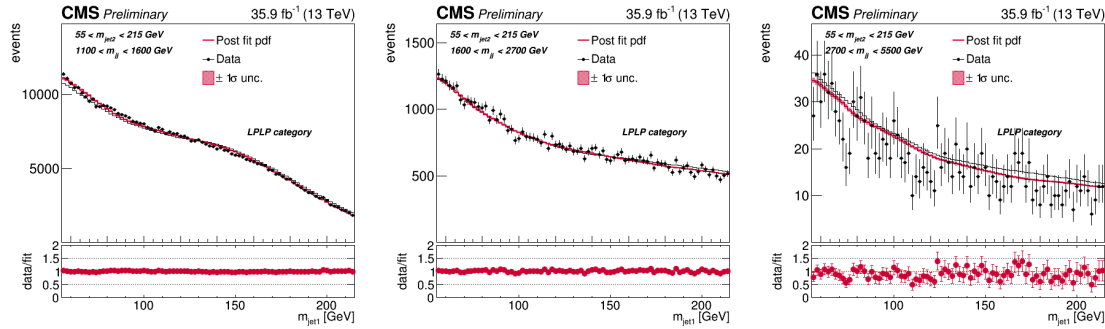


**Figure 4.101:** Distributions obtained from the fit to 2016 LPLP data. Here the projections of  $M_{\text{jet}1}$  are shown for the several ranges of  $M_{\text{VV}}$  and for the full  $M_{\text{jet}2}$  range.

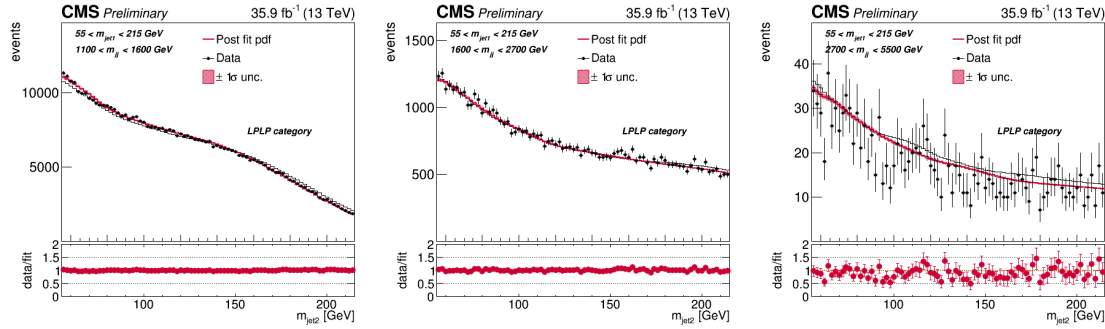


**Figure 4.102:** Distributions obtained from the fit to 2016 LPLP data. Here the projections of  $M_{\text{jet}2}$  are shown for the several ranges of  $M_{\text{VV}}$  and for the full  $M_{\text{jet}1}$  range.

2647 are strongly constrained by data, as expected given the large pre-fit uncertainty assigned to let  
2648 the shapes adjust to the real data.

#### 2649 4.4.3 Bias test in pseudodata

2650 Finally, we study whether there is any bias on the extracted signal rate due to the background  
2651 model. A  $G_{\text{bulk}} \rightarrow WW$  signal, with different mass and signal strength  $\mu_{\text{in}}$ , is injected on top of the  
2652 full background. The signal strength is chosen such that it corresponds to a significance of 4-4.5  
2653 standard deviations for each signal mass, resulting in jet mass and dijet invariant mass spectra as  
2654 shown in Figure 4.105. For each tested signal mass point, a signal plus background fit is performed.  
2655 The signal normalization is free to float in the fit, which determines the signal strength  $\mu$  and its  
2656 uncertainty  $\sigma_\mu$ . For each toy, the pull of the signal strength  $p_\mu = (\mu - \mu_{\text{in}})/\sigma_\mu$  is calculated. The  
2657 procedure is repeated  $\sim 1000$  times for each category, and the cumulative distribution of the pulls

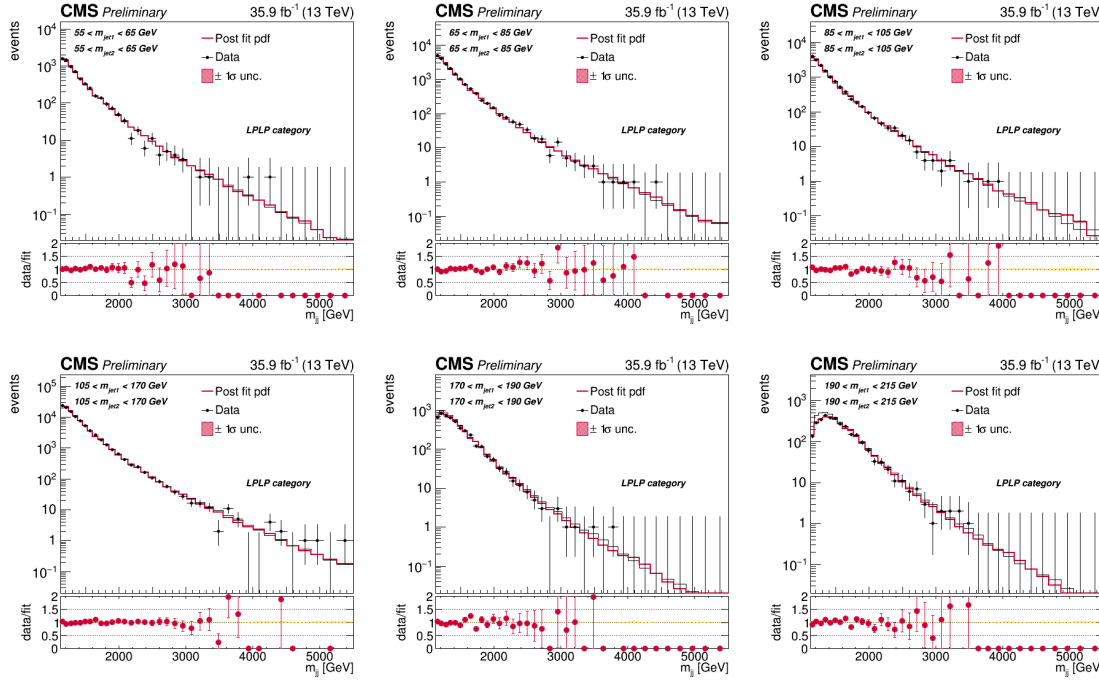


**Figure 4.103:** Distributions obtained from the fit to 2016 LPLP data. Here the projections of  $M_{VV}$  are shown for several equal ranges of  $M_{jet1}$  and  $M_{jet2}$ .

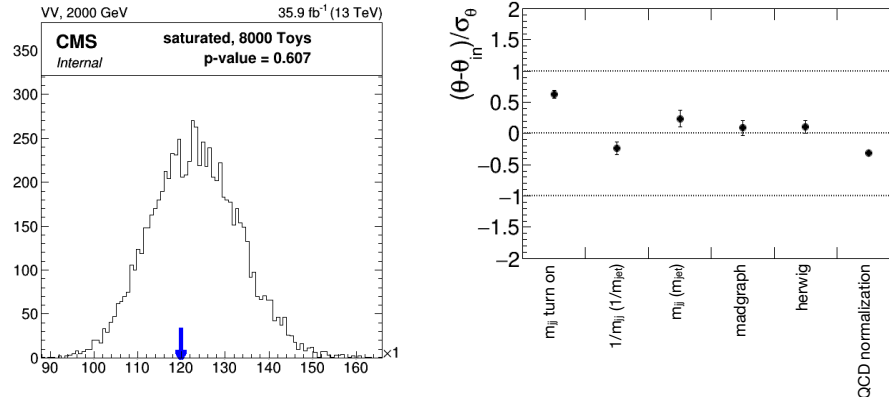


**Figure 4.104:** Left: the likelihood for toys generated around the background-only fit to LPLP data, compared to the likelihood on data. Data is in good agreement with the background-only hypothesis. Right: pulls of the nuisance parameters for a background-only fit.

2658 is fitted with a Gaussian function to determine the mean and its uncertainty, which represent  
 2659 the bias. This is shown in Figure 4.106. Ideally, the distribution should be Gaussian distributed  
 2660 with a mean around 0 and a width of 1. The bias, as shown in Figure 4.107, is consistency below

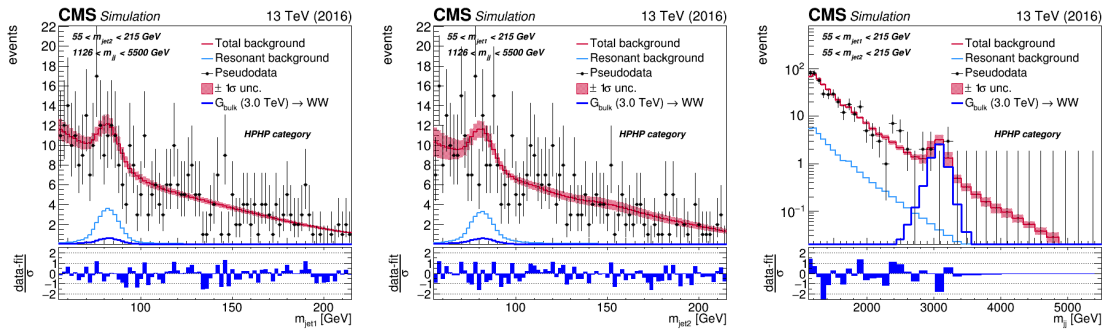


**Figure 4.105:** The post-fit distribution after injecting a signal with a mass of 3 TeV on top of the background in the HPHP (top) and HPLP (bottom) category. are shown separately for the two categories.

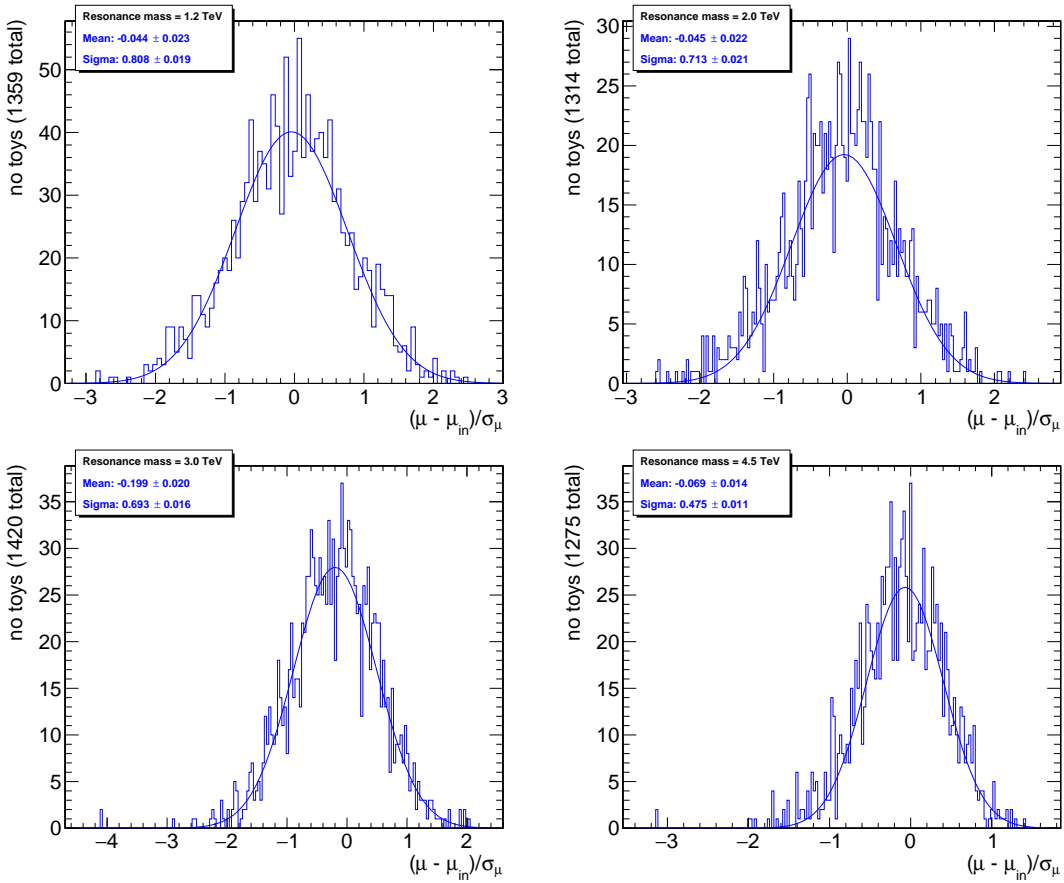


**Figure 4.106:** Cumulative distributions of the pulls for the signal strength for 4 different signal mass-points.

50% and therefore no additional correction/bias term is introduced. In addition, we calculate

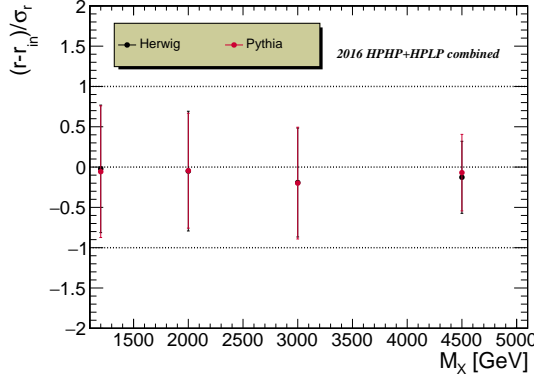


**Figure 4.107:** Estimated bias as a function of the resonance mass.

the pull for each nuisance parameter and fit the cumulative distribution with a Gaussian in order to determine the mean and its uncertainty, representing the shift of the parameters  $\theta$  with respect to the pre-fit values. The results are shown in Figure 4.108. The mean of the cumulative distributions of the pulls is found to be zero for all nuisance parameters, as expected. The width of the distribution can range from very small values to about 1, depending on the assigned pre-fit uncertainty and the power of the data to constrain it.

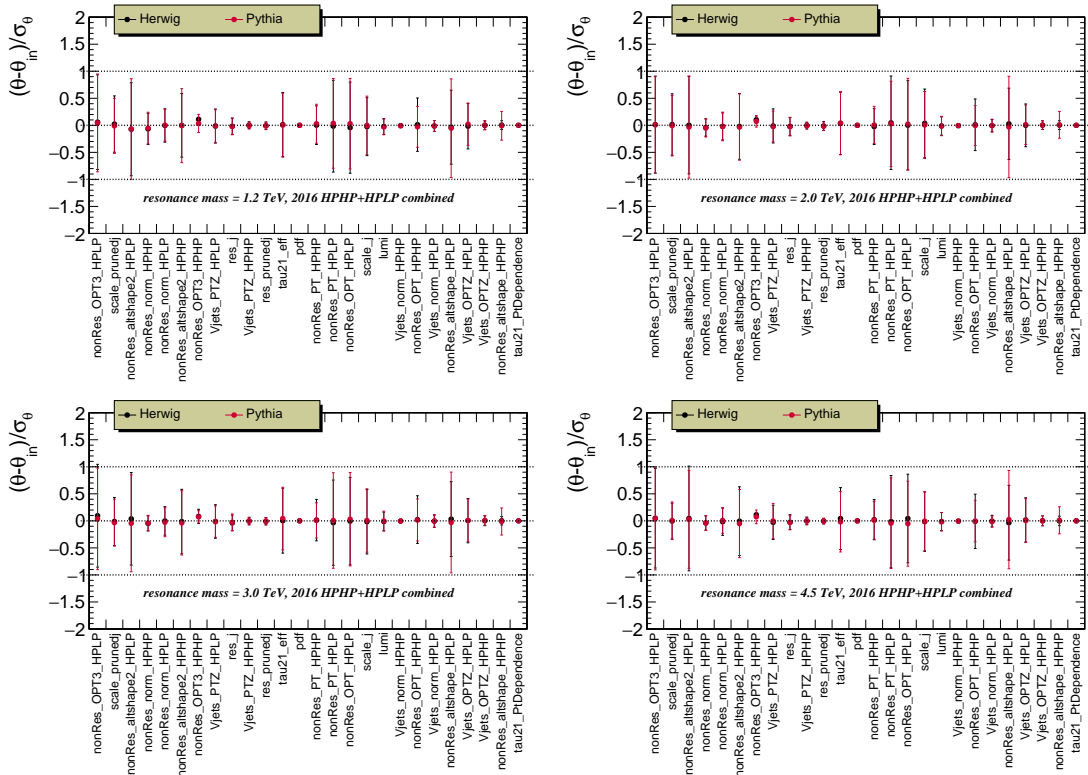


**Figure 4.108:** Pulls of the nuisance parameters estimated for the signal masses and strengths under test. Results are shown of the signal+background combined fits of the two HPHP and HPLP categories to toy datasets generated from the nominal PYTHIA8 templates corresponding to the 2016 integrated luminosity and signal+background pdf.

2668 **4.4.4 Results**

2669 The distributions obtained from a combined fit to the observed data in 2016 and 2017 are shown  
2670 in Figure 4.109 and 4.110, with the corresponding predicted and observed number of background  
2671 events in the signal region summarized in Table 4.17. We observe a beautiful double peak from  
2672 the  $W(q\bar{q})$  and  $Z(q\bar{q})+jets$  background, especially clear in the low purity category. This allows us  
2673 to, for the very first time extract the softdrop jet mass scale and resolution from a  $V(q\bar{q})+jets$   
2674 double peak, which we'll discuss in Section 4.4.4. It also gives us the opportunity to measure the  
 $V(q\bar{q})+jets$  cross section, a measurement we are currently planning on how to best extract.

	HPHP	HPLP
$W+jets$	$113.3 \pm 18.1$ 100.4 (exp.)	$4257.4 \pm 257.0$ 4318.0 (exp.)
$Z+jets$	$46.5 \pm 8.3$ 50.2 (exp.)	$1747.5 \pm 163.7$ 2159.0 (exp.)
QCD	$651.6 \pm 4.0$ 684.4 (exp.)	$51190.5 \pm 313.1$ 53767.5 (exp.)
Observed yield	$778 \pm 28$	$57227 \pm 239$
Post-fit total background	$811.4 \pm 20.3$	$57195.5 \pm 436.8$

**Table 4.17:** Expected and observed yields and their total uncertainty (stat.+sys.) in the two purity categories.

2675

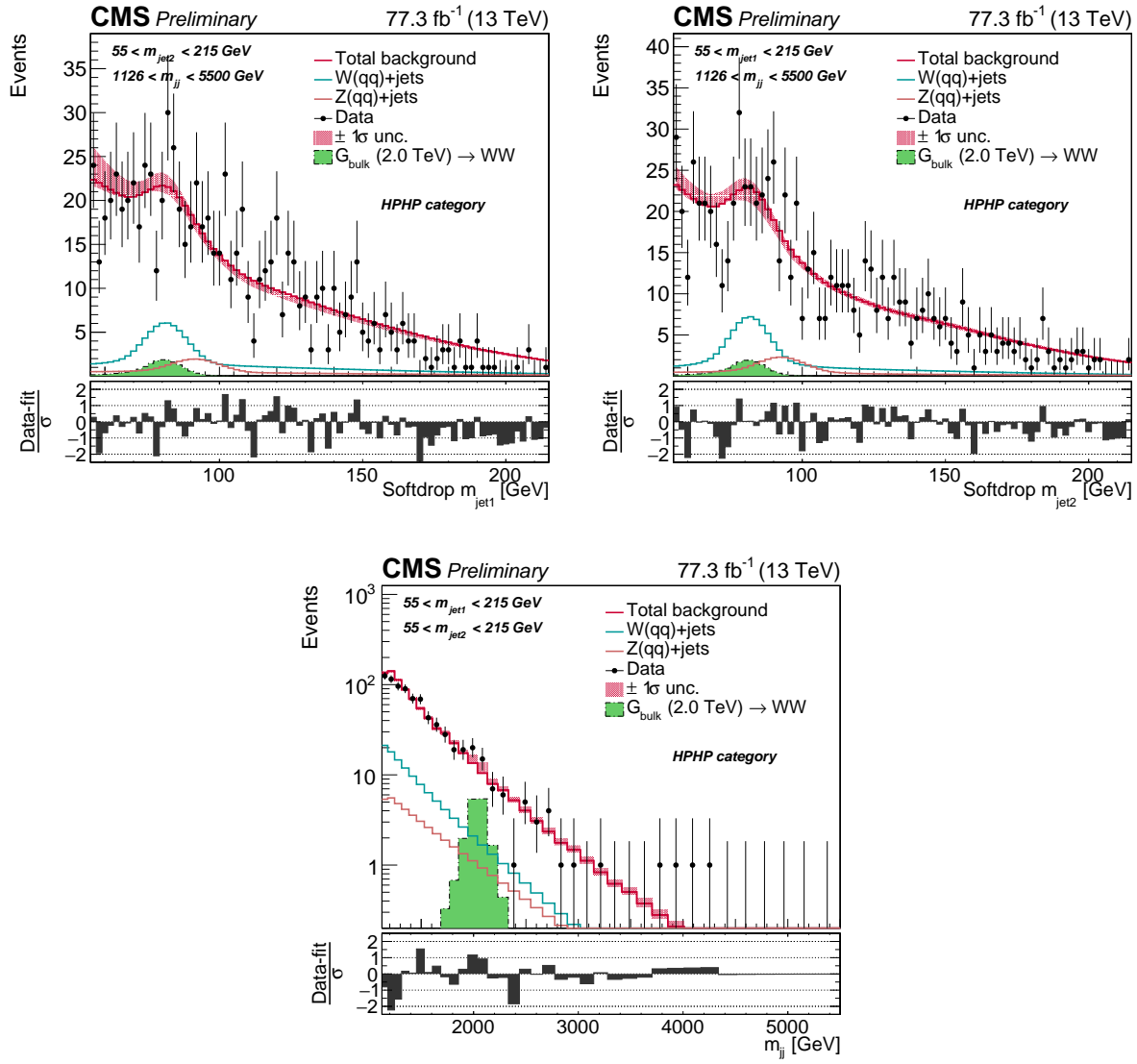


**Figure 4.109:** Postfit distribution after a fit to 2016 and 2017 data projected onto the  $M_{\text{jet}1}$  (left),  $M_{\text{jet}2}$  (middle), and  $M_{\text{ll}}$  (right) axis. Here for the high purity category. The background shape uncertainty is shown as a red shaded band, and the statistical uncertainties of the data are shown as vertical bars. The overlaid signal distribution is arbitrarily normalized.

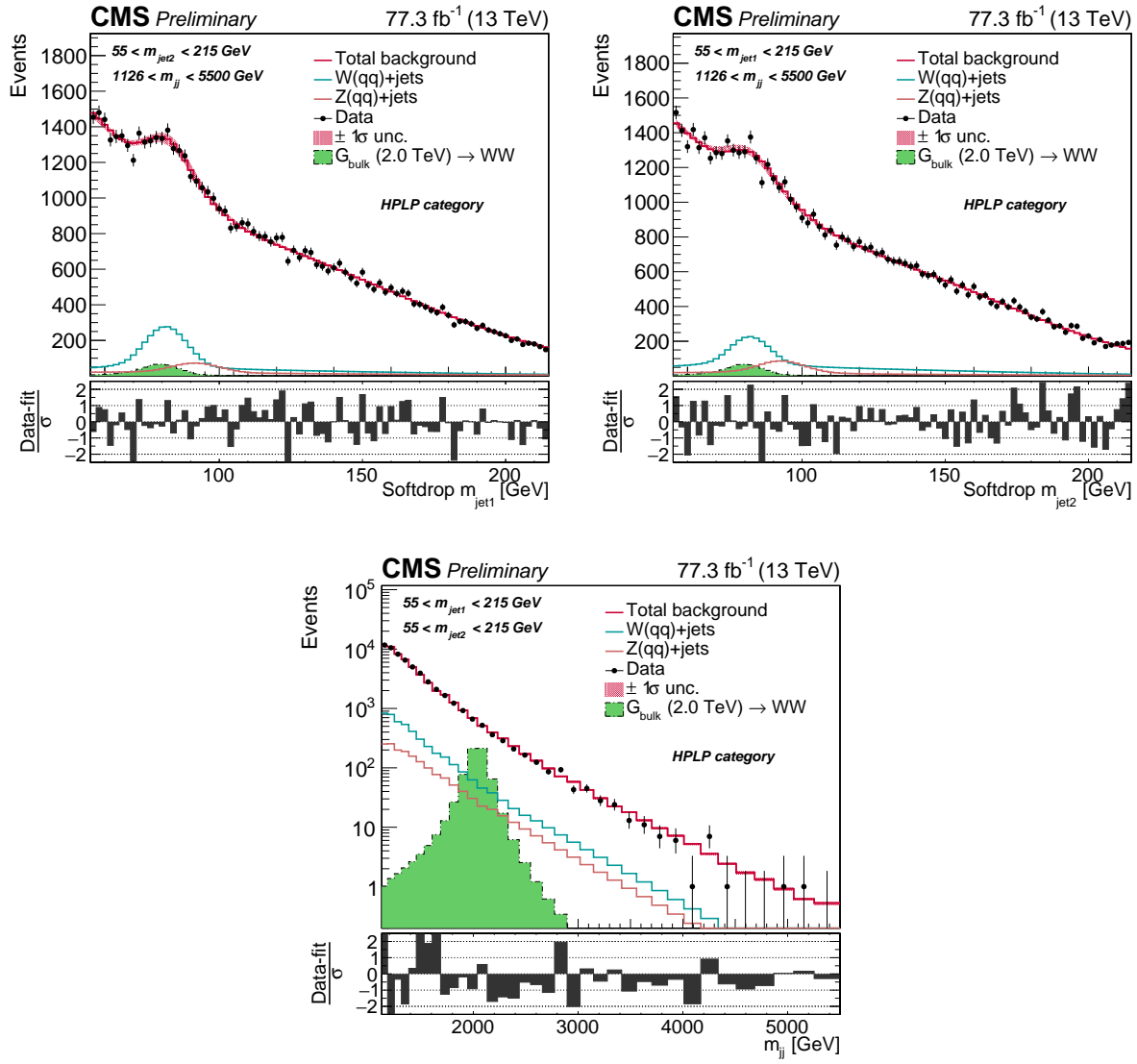


**Figure 4.110:** Postfit distribution after a fit to 2016 and 2017 data projected onto the  $M_{\text{jet}1}$  (left),  $M_{\text{jet}2}$  (middle), and  $M_{jj}$  (right) axis. Here for the HPLP (bottom) category. The background shape uncertainty is shown as a red shaded band, and the statistical uncertainties of the data are shown as vertical bars. The overlaid signal distribution is arbitrarily normalized.

**2676 Limits**

2677 As for Search I and Search II, exclusion limits on the cross section of the process  $X \rightarrow VV$  are  
 2678 set in the context of the Bulk Graviton model and the HVT model B scenario (again obtained  
 2679 using the asymptotic CL<sub>S</sub> method). Figure 4.111 show the resulting expected and observed 95%  
 2680 confidence level exclusion limits on the signal cross section as a function of the resonance mass for  
 2681 all signal models. The obtained limits are compared with the resonance production cross section  
 times the branching fraction to WW, ZZ and WZ. To settle the question of whether the 3D

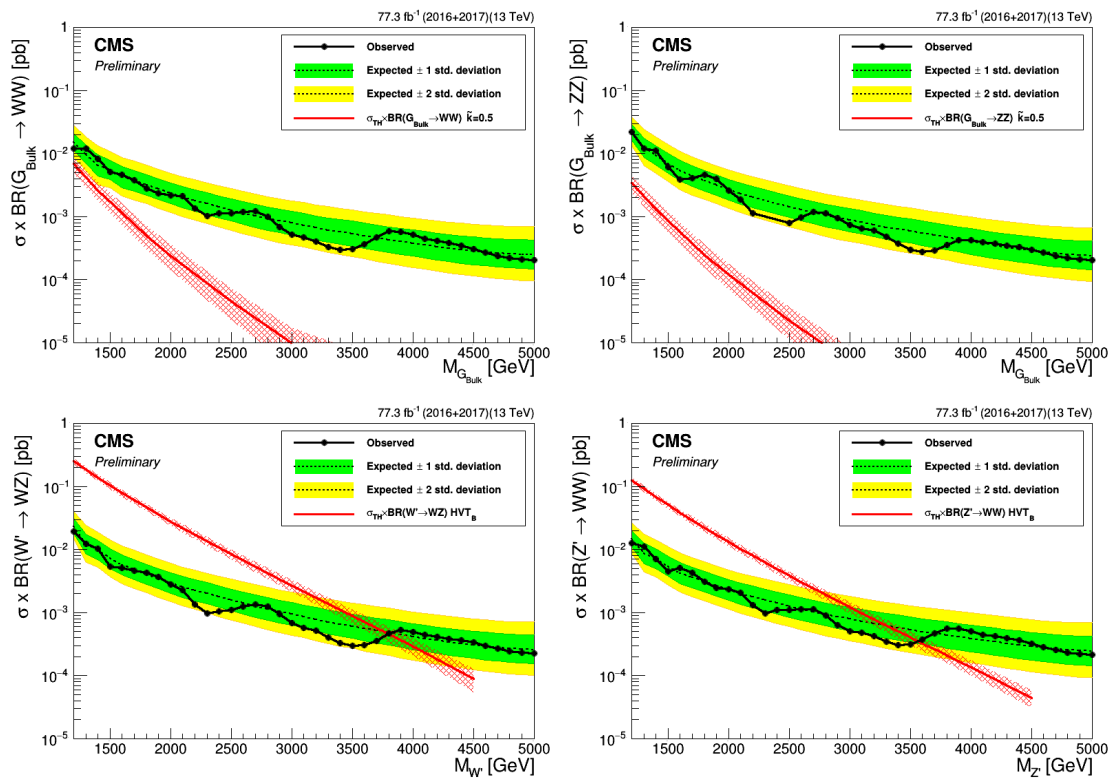


**Figure 4.111:** Expected limits obtained combining  $35.9 \text{ fb}^{-1}$  and  $41.4 \text{ fb}^{-1}$  of data of data after combining all purity categories for Bulk  $G \rightarrow WW$  (top left), Bulk  $G \rightarrow ZZ$  (top right),  $W' \rightarrow WZ$  (bottom left) and  $Z' \rightarrow WW$  (bottom right) signals.

2682 fit method yields an improvement upon the 1D search method, we compare the limits obtained  
 2683 above to those obtained using the 1D fit method (the results from SearchII). In Figure 4.112  
 2684 we see a 20–30% improvement for all signal hypothesis with the new method (comparing the  
 2685 1D and 3D 2016 limits only), and a total gain of about 35–40% when combining the 2016 and  
 2686 2017 datasets. In Figure 4.113, we additionally compare the 3D limits to those obtained by the  
 2687 ATLAS collaboration in a similar search [79] and find this search to be up to 35% more sensitive  
 2688

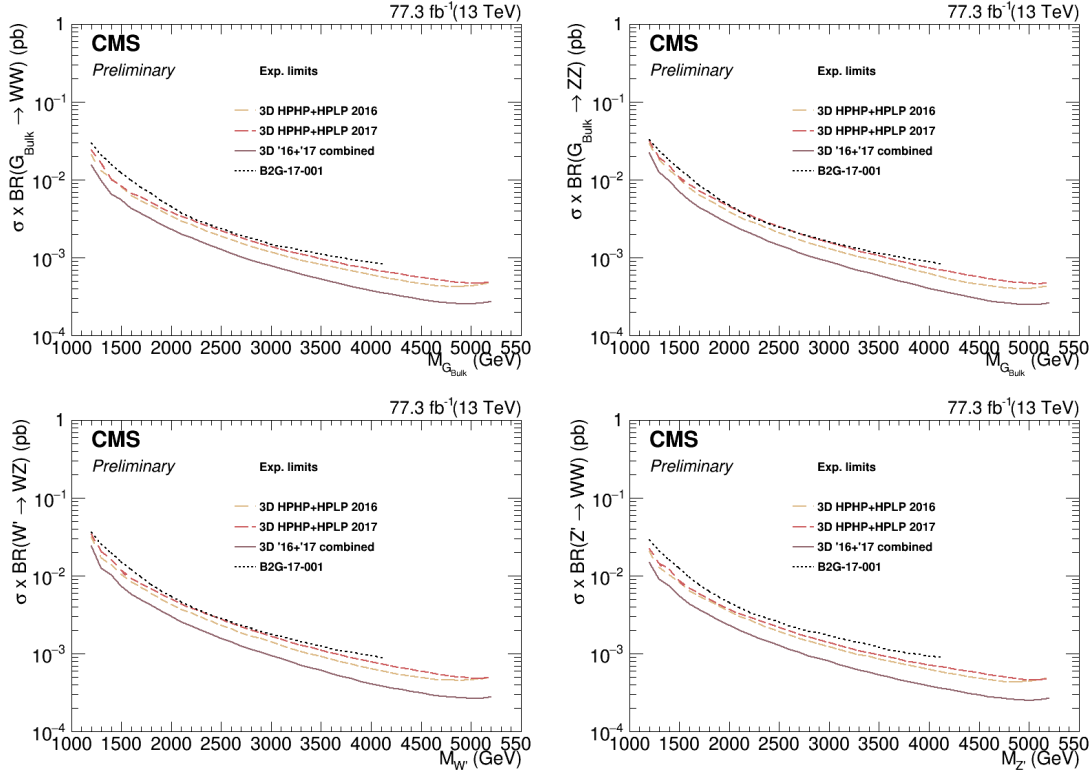


**Figure 4.112:** CA comparison of the 3D expected limits split into dataset (2016 and 2017), to that obtained with the 1D fit using 2016 data. Here for  $G_{\text{bulk}} \rightarrow WW$  (top left),  $G_{\text{bulk}} \rightarrow ZZ$  (top right),  $W' \rightarrow WZ$  (bottom left) and  $Z' \rightarrow WW$  (bottom right) signals.

for the two signal scenarios considered (the  $G_{\text{bulk}}$  limits can not be compared due to different values of  $\tilde{k}$ ). Finally, in Figure 4.114 we show a breakdown of the limits per purity category. As expected, the HPHP category dominates at low mass where background is high and the HPLP category dominates at high mass due to low background and high signal efficiency.

### 2693 Pulses of nuisance parameters

As summarized in Section 4.3.11, we add a list of systematic uncertainties to the fit as nuisance parameters. To quantify how much the nuisances we insert differs from the ones preferred by the fit, we compute the pull

$$p_\theta = (\theta - \theta_{in})/\sigma_\theta \quad (4.21)$$

where  $\theta_{in}$  is the nuisance value pre-fit,  $\theta$  the corresponding parameter post-fit and  $\sigma_\theta$  its error. and its error bar calculated as the ratio between post- and pre-fit uncertainty. Figure 4.115

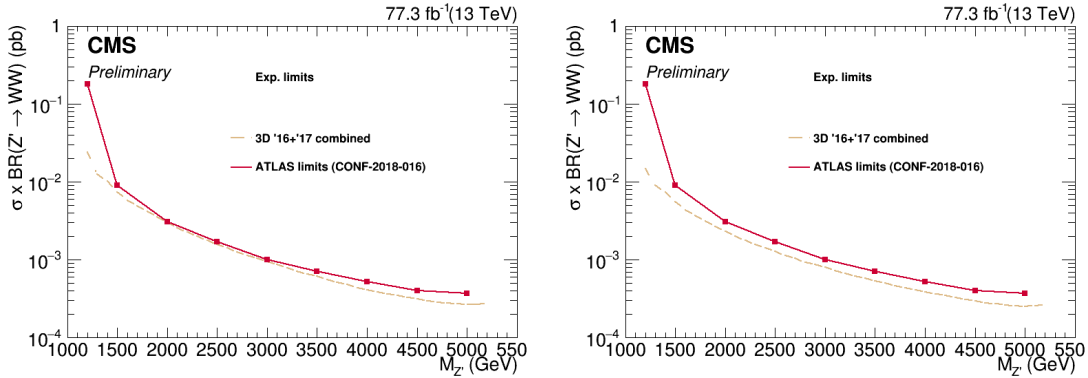


**Figure 4.113:** A comparison of the limits obtained above, to those by the ATLAS collaboration in a similar search [79]. Here for  $W'$  (left) and  $Z'$  (right) signal hypotheses.

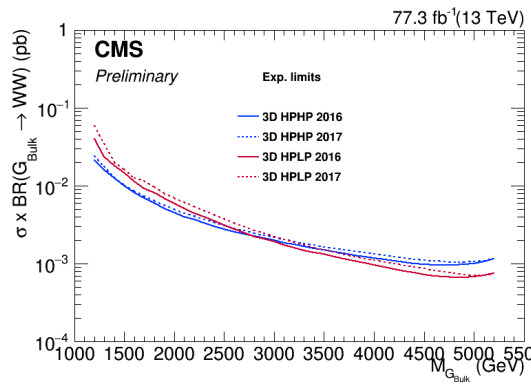


**Figure 4.114:** Limits split into purity categories (HPHP and HPLP) for a Bulk  $G \rightarrow WW$  signal hypothesis.

2699 shows the pulls for a signal+background fit to the combined (2016+2017) dataset (left) and  
 2700 when fitting the two separately (right), here using a signal hypothesis corresponding to a 2  
 2701 TeV  $G_{\text{bulk}}$ . We observe that the  $W$ -tagging efficiency (“`CMS_VV_JJ_tau21_eff`”), the softdrop  
 2702 jet mass scale (“`CMS_scale_prunedj`”) and resolution (“`CMS_res_prunedj`”) gets pulled and  
 2703 constrained by the  $W(\text{qq})$  and  $Z(\text{qq})+\text{jets}$  mass peaks. In addition, the QCD shape parameters  
 2704 (“`CMS_VV_JJ_nonRes_*`”) are significantly pulled and constrained by data because of their large  
 2705 pre-fit uncertainty and unknown a-priori pre-fit value (again, we do not know if Nature is PYTHIA8,  
 2706 HERWIG++ or MADGRAPH+PYTHIA8. Though from this measurement, HERWIG++ seems to  
 2707 take the prize (“`altshape2`”)).

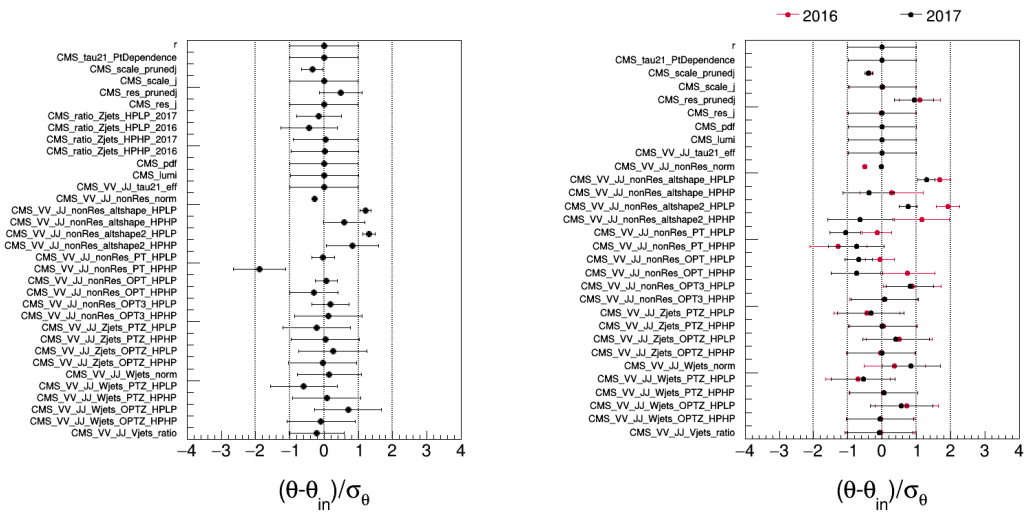


**Figure 4.115:** Pulls of each nuisance parameter for a combined signal+background fit to the combined 2016+2017 dataset (left) and when fitting the two separately.

<sup>2708</sup> **4.5 Summary and outlook**

<sup>2709</sup> In this chapter, we have followed the search for VV resonances in the all-hadronic final state  
<sup>2710</sup> through three stages and corresponding publications: From being one of the first ever analysis in  
<sup>2711</sup> the “boosted” final state at 13 TeV and the very first to take advantage of substructure at trigger  
<sup>2712</sup> level, through leading the development of a new W-tagging algorithm and mass corrections now  
<sup>2713</sup> default in CMS and finally ending with the development of a multi-dimensional fit for generic  
<sup>2714</sup> searches in jet groomed mass and dijet invariant mass.

<sup>2715</sup> Each analysis has built on significant improvements that came with the analysis before it:  
<sup>2716</sup> The substructure triggers and mass corrected softdrop jet mass are both used for the 3D fit, the  
<sup>2717</sup> early discovery of the softdrop signal efficiency dependence on  $p_T$  led us to derive corrections for  
<sup>2718</sup> it. Now the question which remains is: *What comes next?*.

<sup>2719</sup> A few ideas were already mentioned in the introduction to Search III, Section 4.3. The natural  
<sup>2720</sup> next step for this search is an incorporation of the VH(bb) and H(bb)H(bb) final states into the  
<sup>2721</sup> three-dimensional fit. Orthogonality between the three is guaranteed through b-tagging categories,  
as illustrated in Figure 4.116. This process is already underway, aiming for a publication of the

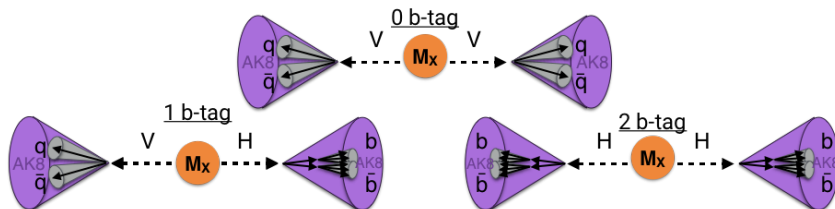


**Figure 4.116:** The VV, VH(bb) and H(bb)H(bb) analyses can all be incorporated into the multidimensional framework. Orthogonality between the analyses is ensured through b-tagging categories.

<sup>2722</sup>  
<sup>2723</sup> full Run 2 dataset (data collected in 2016, 2017 and 2018) in one common framework.

<sup>2724</sup> Secondly, after 14 TeV there will not be another increase in the collision center-of-mass energy  
<sup>2725</sup> at the LHC. That means that we want the best possible sensitivity when analyzing the dataset  
<sup>2726</sup> which is to come. One way of doing so is through changing the search method, as we did with  
<sup>2727</sup> the three dimensional fit, another is to work towards a better W-tagger.

<sup>2728</sup> Beyond that, and perhaps more interestingly, is the search for generic resonances peaking  
<sup>2729</sup> anywhere in the softdrop jet mass and dijet invariant mass spectrum, where the jets themselves  
<sup>2730</sup> could have other compositions than two subjets (for instance a scalar decaying to two vector  
<sup>2731</sup> bosons, who's decay products are merged into one jet; a 4-prong object). One caveat of the  
<sup>2732</sup> current setup is that it constrains the signal to be a 2-pronged object through its n-subjettiness

2733 cut. In order for the multi-dimensional framework to be truly generic, the tagger needs to be  
2734 replaced by a generic anti-QCD tagger. Such a tagger works as an anomaly detector by encoding  
2735 the probability density function for quark/gluon jets as a function of certain variables, variables  
2736 for which signal jets are assumed to have a different probability density. In our case, good  
2737 variables would for instance be groomed mass or substructure, as any generic signal is assumed  
2738 to be peaking in softdrop mass and have some (unknown) substructure. The tagger itself is given  
2739 no information about what a potential signal looks like and will only return the probability of  
2740 any jet being a QCD jet. Such taggers are usually deep neural network (DNN) based where the  
2741 quark/gluon jet PDF is obtained through training of the network, as demonstrated in [80, 81].  
2742 In order for such an encoding to work, the deep neural network needs access to the features  
2743 distinguishing q/g jets from signal jets without these features being biased towards any signal in  
2744 particular. The network must learn how to encode “non-substructure”.  
2745 As a side project in parallel to working on the multi-dimensional fit, I spent the last half year of  
2746 my PhD working on a deep neural network capable of discriminating q/g jets from W jets in  
2747 order to improve W-tagging performance and improve the search sensitivity of VV analyses to  
2748 come. Based solely on jet constituent four-vectors, the idea is to let the neural network itself  
2749 compute grooming and substructure like variables, without feeding it any high-level features  
2750 (like softdrop mass and  $\tau_{21}$ ). This type of architecture is, in addition to improving W-tagging  
2751 performance, ideal for the purpose described above: Encoding QCD in terms of substructure like  
2752 features. The final chapter of this thesis is therefore dedicated to the two last points: How to  
2753 improve W-tagging in CMS for future analyses and how to design a neural network capable of  
2754 learning jet substructure in an unbiased manner.



2755

---

## CHAPTER 5

---

2756

### Encoding jet substructure in a deep neural network

2757

2758 **5.1 Infusing deep neural networks with physics**

2759 *The previous chapter ended by mentioning two ingredients that will become important for future  
 2760 searches with the multi-dimensional fit: A better vector boson tagger, and a generic anti-QCD  
 2761 tagger for signal independent searches. As a side project during my final PhD semester, I worked  
 2762 on a solution for the first, which has the added benefit of being a stepping stone towards the latter.  
 2763 This is what I will cover in the final chapter of this thesis.*

2764

2765 *When applying machine learning to particle physics problems, the input has historically con-  
 2766 sisted of pre-computed high-level features (quantities based on lower-level variables and certain  
 2767 theoretical assumptions). With the rise of deep learning however, computational graphs have  
 2768 achieved an increased capability to find even the smallest correlations in datasets, allowing them  
 2769 to construct complex features on their own. The deep neural network (DNN) I will present in  
 2770 the following is based on the assumption that, given sufficient instructions about the laws of  
 2771 Nature, a neural network should be capable of reconstructing its own high-level features based on  
 2772 lower-level variables only. In addition, if smartly designed, the network should be capable of finding  
 2773 novel correlations and physical features, *a-priori* unknown, by allocating a physical meaning to  
 2774 the training weights deep within the network. The deep neural network I will present here, is  
 2775 trained to discriminate quark/gluon jets from  $W$ -jets. However, as I will discuss in the final  
 2776 section of this chapter, it is also the perfect starting point for developing a generic anti-QCD tagger.*

2777

2778 *The work presented in the following has not been published and still qualifies as work in progress.  
 2779 However, I believe developing taggers such as these is of great importance for future versions of  
 2780 the searches presented here, and is something I hope to continue working on in the future..*

COLA:

$$k_{\mu\nu} = \begin{bmatrix} E_1 & E_2 \\ P_1^x & P_1^y \\ P_2^x & P_2^y \end{bmatrix}_{(4,2)}$$

$$\tilde{k}_{\mu\nu} = k_{\mu\nu} \cdot \begin{bmatrix} L_{11} \\ L_{12} \\ L_{13} \\ L_{14} \end{bmatrix}_{(4,1)}$$

$$(4,2)$$

$$\tilde{k}_{\mu\nu} = \begin{bmatrix} L_{11} & L_{12} \\ L_{12} & L_{13} \\ L_{13} & L_{14} \\ L_{14} & L_{11} \end{bmatrix}_{(4,4)}$$

$$(4,4)$$

$$L_{ij} = \sum_{m=1}^M w_{im} P_m^j$$

$$w_{11} = \frac{1}{2}, w_{12} = \frac{1}{2}, w_{13} = 0, w_{14} = 0$$

$$w_{21} = 0, w_{22} = \frac{1}{2}, w_{23} = \frac{1}{2}, w_{24} = 0$$

$$w_{31} = 0, w_{32} = 0, w_{33} = \frac{1}{2}, w_{34} = \frac{1}{2}$$

$$w_{41} = 0, w_{42} = 0, w_{43} = 0, w_{44} = \frac{1}{2}$$

$$E_1 = \sum_{m=1}^M w_{1m} E_m$$

$$E_2 = \sum_{m=1}^M w_{2m} E_m$$

$$P_1^x = \sum_{m=1}^M w_{3m} P_m^x$$

$$P_1^y = \sum_{m=1}^M w_{4m} P_m^y$$

$$P_2^x = \sum_{m=1}^M w_{1m} P_m^x + w_{2m} P_m^y$$

$$P_2^y = \sum_{m=1}^M w_{3m} P_m^x + w_{4m} P_m^y$$

$$\sum E = \sum_{m=1}^M w_{1m} E_m + \sum_{m=1}^M w_{2m} E_m$$

$$\sum P_x = \sum_{m=1}^M w_{3m} P_m^x + \sum_{m=1}^M w_{4m} P_m^y$$

$$\sum P_y = \sum_{m=1}^M w_{4m} P_m^y - \sum_{m=1}^M w_{3m} P_m^x$$

$$\sum P_z = \sum_{m=1}^M w_{1m} P_m^z + \sum_{m=1}^M w_{2m} P_m^z$$

linear combinations  
of momenta

“What can we teach the machine?” → “What can we learn from the machine?”.

Work in progress

2781 **5.2 LoLa**

2782 LoLa is a deep neural network architecture which was first introduced for top tagging [82]. It is  
2783 based on the idea that, given enough information about the laws of Nature, a neural network  
2784 should be capable of calculating jet substructure observables on its own given only low-level  
2785 information. The network is designed to discriminate between AK R=0.8 jets originating from  
2786 W bosons from those originating from quarks or gluons, solely based on the jet constituent  
2787 four-vectors (variables with little discriminating power on their own) as illustrated in Figure 5.1.  
 Rather than being fed high-level features, the neural network is given tools to perform calculations

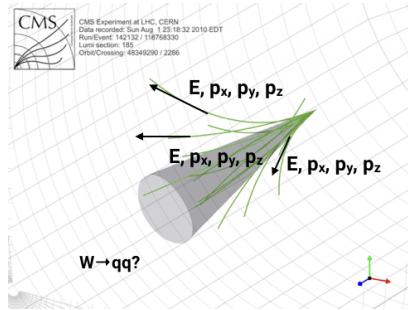


**Figure 5.1:** LoLa uses only jet constituent four-vectors as input to discriminate W from q/g jets.

2788  
2789 on Lorentz vectors using the Minkowski metric. Through two novel layers, linear combinations  
2790 similar to jet clustering and jet substructure algorithms are performed, allowing the algorithm  
2791 to create its own substructure variables. Additionally, training weights deep within the network  
2792 correspond to physical quantities reconstructed by the algorithm; distance between particles,  
2793 masses and energies, linear combinations of particle four-vectors etc. Besides the end goal of  
2794 discriminating Ws from quarks and gluons, one could therefore hope to learn of new correlations  
2795 separating QCD from vector boson jets.

2796 **5.2.1 Architecture**

2797 The LoLa architecture is designed as a four layer deep, feed-forward sequential network doing  
2798 supervised learning on fixed size input vectors. Two novel layers are introduced, the Combination  
2799 Layer (CoLa) and the Lorentz Layer (LoLa), which perform basic jet clustering and substructure  
2800 calculations as well as implements the Minkowski metric. These two layers are then followed by  
2801 two fully connected layers, consisting of 100 and 50 nodes respectively, before the final output  
2802 is computed using a Softmax activation function, yielding two output probabilities between 0

and 1. The loss function to be minimized is “categorical crossentropy” (or log loss) where the two categories in use are W versus non-W probabilities. Only the W jet probability is stored. The optimizer used in the training is the, now standard, ADAM optimizer [83], which adapts the learning rate of the model parameters during training. The code itself is written using the Keras [84] interface with a TensorFlow [85] backend. The full architecture with input and output dimension per layer is shown in Figure 5.2. The three first boxes are matrices, while the final four boxes correspond to vectors of different length. In the following, each layer will be explained in detail.

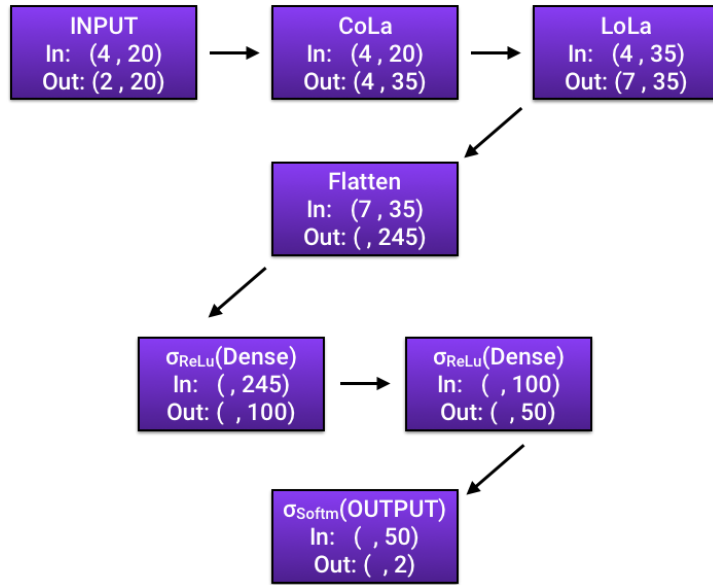


**Figure 5.2:** The full LoLa architecture. “In” denotes the dimension of the input tensor to the given layer, “Out” is the output tensors dimensions.

2810

### 2811 5.2.2 Input

This algorithm is trained to discriminate between fully merged hadronic W-jets coming from the process  $G_{\text{bulk}} \rightarrow WW \rightarrow q\bar{q}q\bar{q}$  (where  $M_{G_{\text{bulk}}} = 0.6 - 4.5 \text{ TeV}$ ), and quark/gluon jets from a QCD sample generated with PYTHIA8Pythia 8. All jets are clustered with the anti- $k_T$  algorithm with a distance parameter of  $R=0.8$ , with the PUPPI pileup removal algorithm applied. In addition, they are required to have  $p_T > 200 \text{ GeV}$  and  $|\eta| < 2.5$ . Jets are defined as W-jets if they are matched to a generator level hadronically decaying W bosons, with the following matching criteria: The generated vector boson needs to be within  $\Delta R < 0.6$  of the jet axis, and the quark decay products need to be within  $\Delta R < 0.8$  of the jet axis. The  $p_T$  and  $\eta$  distribution of signal and background

jets, is shown in Figure 5.3. From these signal and background jets, only the jet constituent four

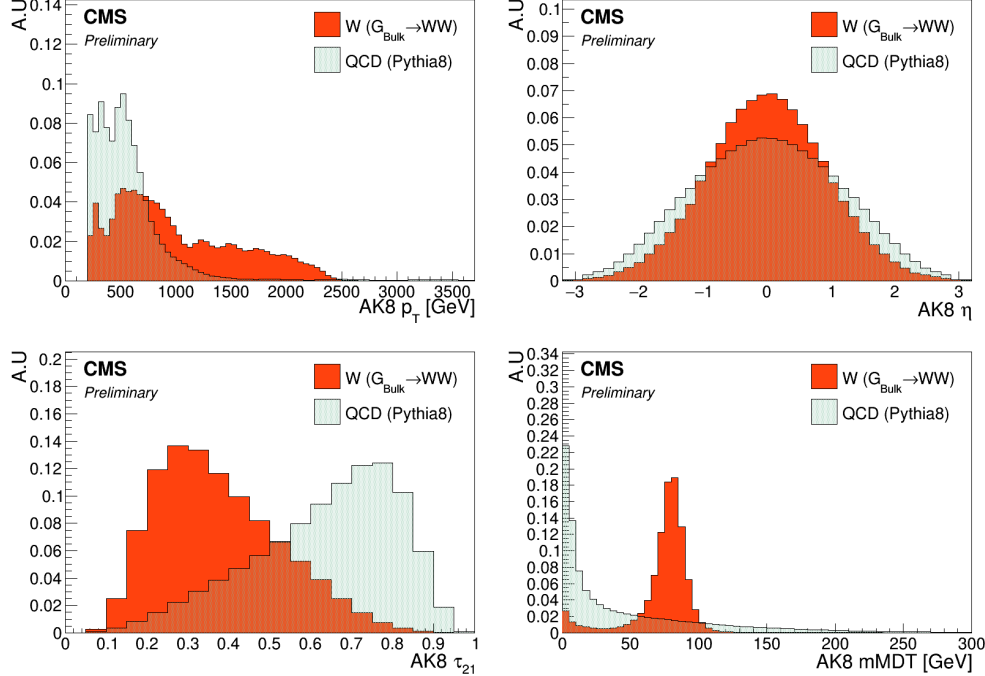


**Figure 5.3:** Jet  $p_T$  (top left),  $\eta$  (top right),  $\tau_{21}$  (bottom left) and softdrop jet mass (bottom right) for signal and background jets.

2820

vectors of the 20 highest- $p_T$  particles are used as input to the deep neural network:  $E$ ,  $p_x$ ,  $p_y$  and  
2821  $p_z$ . I use 20 constituents as any larger number has a negligible affect on the performance, while  
2822 performance tends to drop once going below 15. The input is therefore a  $4 \times N = 20$  matrix for  
2823 each signal and background jet, one four-vector for each of the 20 jet constituents:  
2824

$$x_{\mu,i} = \begin{pmatrix} E^1 & E^2 & \dots & E^N \\ p_x^1 & p_x^2 & \dots & p_x^N \\ p_y^1 & p_y^2 & \dots & p_y^N \\ p_z^1 & p_z^2 & \dots & p_z^N \end{pmatrix} \quad (5.1)$$

2825 The total number of jet constituents is shown in Figure 5.4, and the input variables (here for all  
2826 constituents) is shown in Figure 5.5.

2827 It is clear that the input variables provide little discriminating power on their own. Therefore,  
2828 the network must learn how to derive other physical quantities where the signal and background  
2829 PDFs differ to a larger extent. This is achieved through the two custom layers described in the

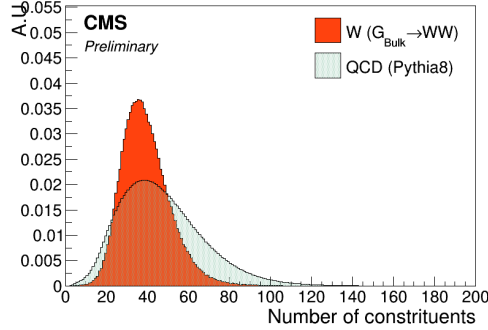


**Figure 5.4:** The number of jet constituents for signal (red) and background (blue). Only the 20 highest- $p_T$  constituents are used during training.

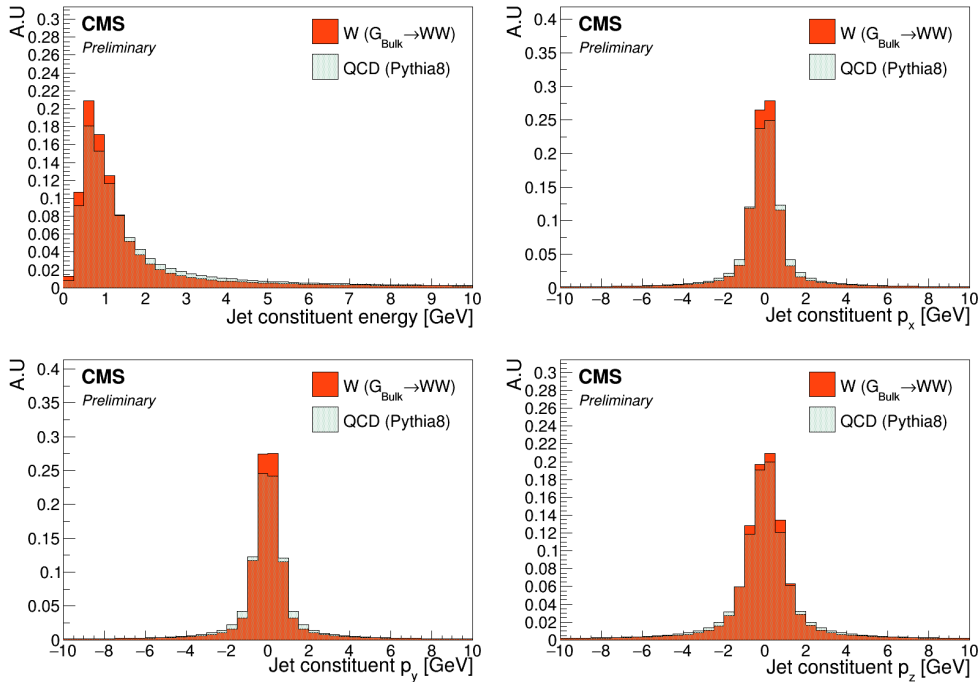


**Figure 5.5:** Energy (top left),  $p_x$  (top right),  $p_y$  (bottom left) and  $p_z$  (bottom right) for all jet constituents. These values are used as input to the neural network training.

2830 following.

### 2831 5.2.3 The Combination Layer

2832 The Combination Layer (CoLa) consists of a matrix which, when taking the scalar product with  
2833 the input matrix, computes linear combinations of the jet constituents, similar to what is done in

2834 recombination jet algorithms. The main goal here is to create additional four-vectors as input for  
2835 the next layer. The CoLa matrix is a concatenation of the following: A vector of 1's of length  $N$ ,  
2836 the  $N \times N$  identity matrix ( $N = 20$ ) and a matrix of  $N \times M$  trainable weights.

$$C_{i,j} = \begin{pmatrix} 1 & 1 & 0 & \dots & 0 & w_{1,N+2} & w_{1,N+3} & \dots & w_{1,(N+2)+M} \\ 1 & 0 & 1 & \dots & 0 & w_{2,N+2} & w_{2,N+3} & \dots & w_{2,(N+2)+M} \\ \vdots & \vdots & \vdots & \ddots & \vdots & \vdots & \vdots & \vdots & \vdots \\ 1 & 0 & 0 & 0 & 1 & w_{N,N+2} & w_{N,N+3} & \dots & w_{N,(N+2)+M} \end{pmatrix} \quad (5.2)$$

2837 When performing the following multiplication

$$x_{\mu,i}^C = x_{\mu,i} C_{i,j} \quad (5.3)$$

the resulting output matrix will have dimensions  $4 \times (1 + N + M)$  and consists of the following: A first column containing the sum of all constituent momenta, the four-momenta of each individual constituent, and  $M=14$  different linear combinations of particles with trainable weights. The first corresponds to the neural network computing the four-vector of the “full” jet, at least the full jet in terms of its 20 highest- $p_T$  constituents. The second, simply passes each original constituent four-momentum to the next layer. The final, and most interesting part, lets the network construct alternative subjet four-vectors by letting it weigh constituents up and down as it sees fit in order to reach optimal discrimination power. As an example, lets look at the effect of CoLa in the simple case of only two input jet constituents and two trainable linear combinations:

$$\begin{pmatrix} E^1 & E^2 \\ p_x^1 & p_x^2 \\ p_y^1 & p_y^1 \\ p_z^1 & p_z^2 \end{pmatrix} \begin{pmatrix} 1 & 1 & 0 & w_{1,4} & w_{1,5} \\ 1 & 0 & 1 & w_{2,4} & w_{2,5} \end{pmatrix} = \begin{pmatrix} E^1 + E^2 & E^1 & E^2 & w_{1,4}E^1 + w_{2,4}E^2 & w_{1,5}E^1 + w_{2,5}E^2 \\ p_x^1 + p_x^2 & p_x^1 & p_x^2 & w_{1,4}p_x^1 + w_{2,4}p_x^2 & w_{1,5}p_x^1 + w_{2,5}p_x^2 \\ p_y^1 + p_y^1 & p_y^1 & p_y^1 & w_{1,4}p_y^1 + w_{2,4}p_y^1 & w_{1,5}p_y^1 + w_{2,5}p_y^1 \\ p_z^1 + p_z^2 & p_z^1 & p_z^2 & w_{1,4}p_z^1 + w_{2,4}p_z^2 & w_{1,5}p_z^1 + w_{2,5}p_z^2 \end{pmatrix}$$

2838 In the two last columns, the neural network makes two “subjet” four-vectors by weighting the  
2839 relative contribution of each particle as it sees fit. This is similar to jet grooming (Section 3.5.1)  
2840 or PUPPI pileup subtraction (Section 3.3.2), and should allow the network to learn which  
2841 constituents are part of the hard scatter and which are not. The  $x_{\mu,i}^C$  matrix is finally passed on  
2842 to the next layer, the Lorentz Layer.

#### 5.2.4 The Lorentz Layer

2844 The Lorentz Layer (LoLa) is responsible for encoding how particles move in space-time through  
2845 a simple set of rules. Each column (four-vector) of  $x_{\mu,i}^C$ , is used to compute, and afterwards is

2846 replaced by, the following  $k = 7$  features:

$$x_{k,i}^L = \begin{pmatrix} m^2(x_{\mu,i}^C) \\ p_T(x_{\mu,i}^C) \\ w_{ij}^E E(x_{\mu,j}^C) \\ w_{ij}^{s1} \sum d^2(x_{\mu,i}^C, x_{\mu,j}^C) \\ w_{ij}^{s2} \sum d^2(x_{\mu,i}^C, x_{\mu,j}^C) \\ w_{ij}^{m1} \min d^2(x_{\mu,i}^C, x_{\mu,j}^C) \\ w_{ij}^{m2} \min d^2(x_{\mu,i}^C, x_{\mu,j}^C) \end{pmatrix} \quad (5.4)$$

2847 Going through from top to bottom, these are:

- 2848 • The invariant mass and  $p_T$  of each four-vector
- 2849 • A linear combination of all four-vector energies where each is scaled by a trainable weight
- 2850 • The sum of distances between the four-vector under consideration and every other column
- 2851 reweighted with a trainable weight
- 2852 • The minimum distance between the four-vector under consideration and every other column
- 2853 where each distance again is reweighted by a trainable weight.

2854 The Minkowski metric enters explicitly in the first and in the last four calculations, where the  
2855 neural network is told to abide by the rules

$$m^2(x_{\mu,i}^C) = g^{\mu\nu} x_{\mu,i}^C x_{\nu,i}^C \quad (5.5)$$

2856 and

$$d^2(x_{\mu,i}^C, x_{\mu,j}^C) = (x_{\mu,i}^C - x_{\mu,j}^C)_\mu g^{\mu\nu} (x_{\mu,i}^C - x_{\mu,j}^C)_\nu \quad (5.6)$$

2857 with  $g^{\mu,\nu} = [-1, 1, 1, 1]$ , when calculating the invariant mass and distance between particles/subjets.  
2858 This tells the neural network to use a space-time geometry in all its calculations to respect Lorentz  
2859 Invariance. The four final rows of LoLa are the most interesting: Here the network computes  
2860 quantities similar to n-subjettiness by summing up the distances between all constituents, the  
2861 jet axis and the subjets produced by CoLa. If, for instance, the network has been capable of  
2862 reconstructing two hard subjets in the final columns of CoLa, which do linear combinations of  
2863 particles, it can create its own “ $\tau_2$ ” variable by taking the distance between those subjets and  
2864 all the jet constituents (and weighing down the column corresponding to the full jet four-vector,

column one). Then it can do the same by calculating the distance between the full jet four-vector and all constituents (now weighing down the linear combinations) and compute “ $\tau_2$ ”.

The two custom layers, CoLa and LoLa, therefore come together in order to encode jet clustering and substructure in a novel way. They provide the network with the necessary tools in order to create its own physical quantities, through linear combinations with trainable weights, which then again are used to produce other physical quantities with new trainable weights. This allows the network full freedom to explore all interesting particle correlations, where the resulting output features have a physical meaning that can be probed.

LoLa turns the question “What can we teach the machine?” around to “What can we learn from the machine?”.

### 5.3 Performance

The deep neural network is trained on 320k signal and background jets for up to 100 epochs, but allow for an early stopping after ten epochs if the loss is stable. The test sample consists of 60k W jets and 60k quark/gluon jets. To quantify the performance we look at the signal efficiency versus mistagging rate comparing the performance of LoLa to that of the taggers used previously in this thesis: PUPPI softdrop with  $\tau_{21}$  and PUPPI softdrop with  $\tau_{21}^{DDT}$ . The performance of these three different taggers, is shown in Figure 5.6. The point where the blue curves end, represent the signal efficiency for a mass cut of  $65 \text{ GeV} < \text{Softdrop jet mass} < 105 \text{ GeV}$ , here roughly 70%. We clearly see that LoLa performs significantly better than the current baseline W-taggers

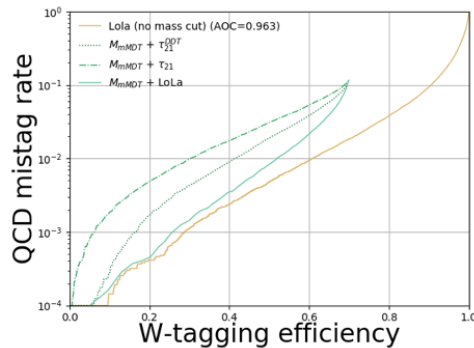


**Figure 5.6:** Performance of LoLa compared to other W-tagging discriminants in the background-signal efficiency plane: PUPPI softdrop +  $\tau_{21}$  (dashed blue), PUPPI softdrop +  $\tau_{21}^{DDT}$  (dotted blue), LoLa with a softdrop mass window applied (solid blue) and the nominal LoLa tagger with no mass cut applied.

2883

2884 based on  $\tau_{21}$  and  $\tau_{21}^{DDT}$ , with a roughly 20% higher signal efficiency at a given mistagging rate.

2885 LoLa also has a higher signal acceptance, as it can be used without a mass window applied. If  
 2886 LoLa were to replace the tagger used in Search II (a better comparison than Search III as the  
 2887 latter uses a rather unconventional mass window), which has a signal efficiency of  $\sim 42\%$  at a 2%  
 2888 mistagging rate for a single jet, the signal efficiency for the same mistagging rate would be 65%,  
 2889 a 55% increase. For an analysis requiring two tagged jets, that would imply going from an 18 to  
 2890 a 43% total signal efficiency, a significant gain.

## 2891 5.4 $p_T$ and mass dependence

2892 Despite being a key feature, absolute performance is not all that quantifies how good one tagger  
 2893 is compared to another. One a tagger is planned to be used in physics analysis, there are three  
 2894 key questions one needs to consider:

- 2895 • Is the absolute performance better (compared to common methods)?
- 2896 • Is the tagger  $p_T$ -dependent?
- 2897 • Does the tagger sculpt the mass spectrum?

2898 These three measures are equally important in quantifying performance and, in the following,  
 2899 I will attempt to explain why this is the case and which approaches are used here in order to  
 2900 tackle them.

2901 Any deep neural network trained to distinguish W jets from q/g jets, will naturally learn that  
 2902  $p_T$  and mass are discriminating features unless it is penalized for it. Figure 5.7 shows the LoLa  
 discriminant as a function of jet  $p_T$  and softdrop jet mass. A strong correlation is observed both

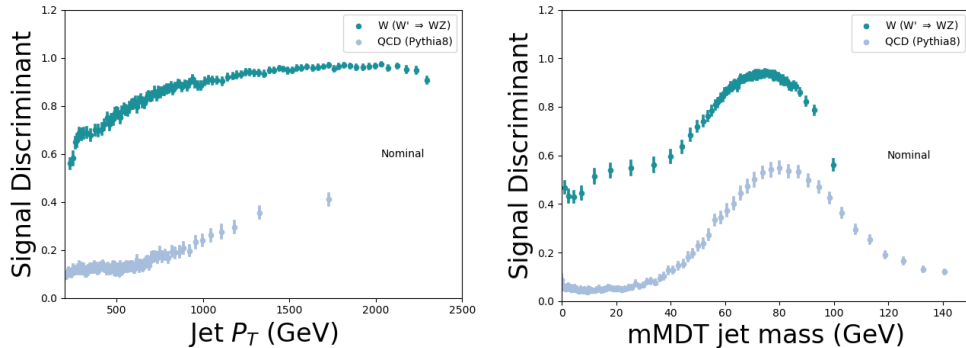


**Figure 5.7:** The LoLa discriminant as a function of jet  $p_T$  (left) and softdrop jet mass (right). A strong correlations with both variables is observed

2903  
 2904 for signal and for background jets (closer to 1 means more signal like), with a rising slope as a

function of  $p_T$  (meaning the network interprets a higher jet  $p_T$  as more signal like) and a bump around the W mass for both signal and for background.

### 5.4.1 $p_T$ decorrelation

A tagger which is  $p_T$  dependent is a problem for the following reasons: Firstly, the signal efficiency is variable, which requires a working point that scales with  $p_T$ . That in itself is not problematic and can easily be computed. However, it implies that when computing efficiency scale factors from data, a range of different scale factors for different working points is required. In addition, the performance is measured at low  $p_T$ , a region where the tagging efficiency can be substantially different from the analysis signal region due to the strong  $p_T$  correlation present. Finally, the dijet invariant mass is intrinsically linked to the  $p_T$  spectrum, meaning that any  $p_T$  dependence in addition can introduce sculpting of the dijet invariant mass spectrum.

From the top left plot in Figure 5.3, one clearly sees that the jet  $p_T$  distribution is very different for signal and for background. In order to avoid that the network learns jet  $p_T$  to be a discriminating feature, I therefore compute a jet-by-jet weight intended to flatten the jet  $p_T$  spectrum. This weight is passed as a sample weight to the training set, reweighting each jets contribution to the total loss (making high mass QCD jets and low mass signal jets count more). Figure 5.8 shows the jet  $p_T$  distribution without any  $p_T$ -reweighting applied (solid lines) and after applying a  $p_T$ -weight (dashed lines). The training is then repeated, this time passing a sample weight

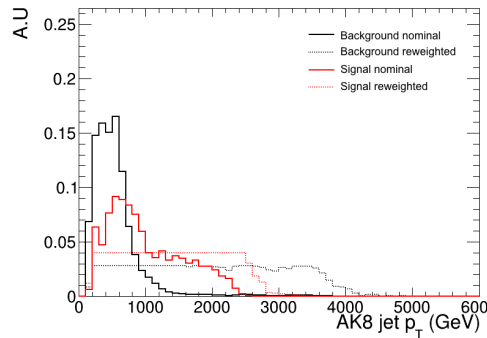


**Figure 5.8:** Jet  $p_T$  distribution before (solid lines) and after (dashed line) applying a weight intended to flatten the jet  $p_T$  spectrum.

with each jet, and the final discriminant compared to the nominal training. Figure 5.9 shows the performance of the same taggers as above but with one additional line, LoLa  $p_T$ -reweighted. A clear drop in performance is observed, as expected when removing information from the training. However, when we again look at the discriminant output as a function of jet  $p_T$  in Figure 5.10,

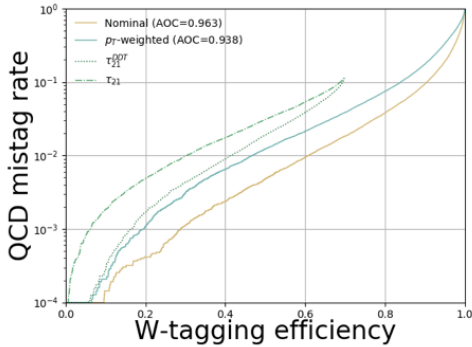


**Figure 5.9:** Performance of the  $p_T$ -reweighted LoLa tagger (solid blue) and the nominal LoLa tagger (solid yellow).

2927 the correlation we observed before has vanished and we are left with a tagger not depending  
on the jet  $p_T$ . For completeness, Figure 5.11 shows the  $\tau_{21}$  and  $\tau_{21}^{DDT}$  discriminants versus jet

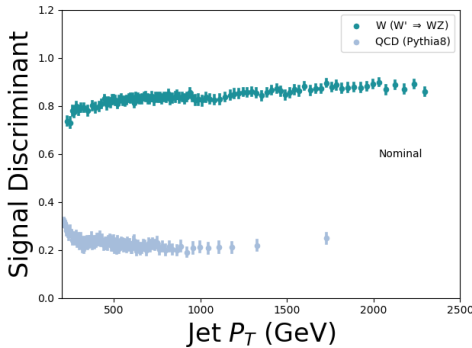


**Figure 5.10:** The LoLa discriminant as a function of jet  $p_T$  after training with a weight intended to flatten the sample  $p_T$  spectrum.

2928  
2929  $p_T$ . Whereas the nominal LoLa discriminant had a much larger correlation with jet  $p_T$  than  
2930 the  $\tau_{21}$ -based taggers, the  $p_T$ -reweighted version is as decorrelated from  $p_T$  as the  $\tau_{21}$  variables  
2931 while still exhibiting a better absolute performance than the baseline taggers. In summary,  
2932 reweighting strategies as the one described above yield a loss in overall performance, as expected  
2933 when removing information from the training. However, the  $p_T$  dependence of the tagger is  
2934 strongly reduced, meaning that it might perform better overall in physics analysis when systematic  
2935 uncertainties are taken into account. There is therefore no clear answer as to which method is  
2936 better before running a full analysis including systematics for  $p_T$ -dependent tagging.

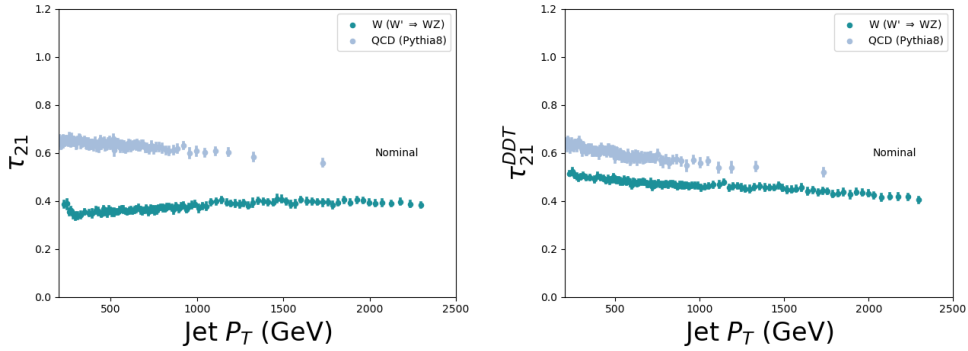


**Figure 5.11:** The  $\tau_{21}$  (left) and  $\tau_{21}^{DDT}$ (right) discriminant as a function of jet  $p_T$ .

### 5.4.2 Mass sculpting

Any smart deep neural network intended to separate Ws from quarks and gluons, will inevitably learn the W mass as it clearly is very different from the q/g mass. Unfortunately, as these taggers are meant to be used in physics analysis where we often estimate the background in mass sidebands, this has some undesired side effects. If a deep neural network has learned the mass then, after applying a cut on the discriminant, the background jet mass distribution becomes severely sculpted and difficult to constrain.

After applying a cut on the LoLa discriminant corresponding to a 1% mistagging rate, we see in the left plot in Figure 5.12 that the W jet signal shape is nicely retained. In addition, there are no QCD jets left at low mass so no jet mass window is needed when using this tagger, leading to a significantly higher signal acceptance. However, when looking more closely at the QCD background on the right plot of Figure 5.12, where all histograms are normalized to unit area, we see that the bulk of the remaining 1% QCD jets is right below the W mass peak and has been sculpted to look exactly like the signal. This mass sculpting is in and on its own not a problem, the tagger still manages to get rid of most of the background. However, in many physics analysis, in order to evaluate the background rate in the data signal region, mass sidebands are used. If the background distribution is peaky rather than smoothly falling, the shape and consequently the expected yield is very difficult to constrain. That leads to large uncertainties on the background rate and might eventually make an analysis less sensitive than when using a tagger with a worse absolute performance, but reduced mass correlation. In addition, if one were to search for peaks in the softdrop jet mass, as is the case for the multidimensional fit, this becomes increasingly difficult when attempting to fit a potential signal peak on top of a peaking background.

It should again be mentioned, that also for the baseline taggers based on  $\tau_{21}$ , mass sculpting is a known feature. Figure 5.13 shown the same softdrop jet mass spectrum before and after a cut

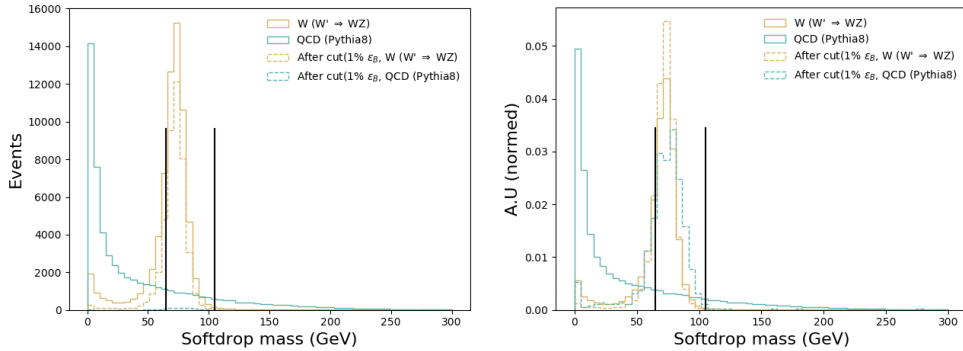


**Figure 5.12:** The softdrop jet mass distribution before (solid lines) and after (dotted lines) a cut on the LoLa discriminant corresponding to a 1% mistagging rate has been applied. The left plot shows the real number of events left after the cut, the right is normalized to area.

2961 corresponding to a 1% mistagging rate on  $\tau_{21}$  (left) and  $\tau_{21}^{DDT}$  (right). Here  $\tau_{21}$  clearly exhibits  
 2962 mass sculpting, but not as peaky as was the case for LoLa.  $\tau_{21}^{DDT}$  exhibits the least amount of  
 2963 sculpting, but is also the tagger with the worst absolute performance.

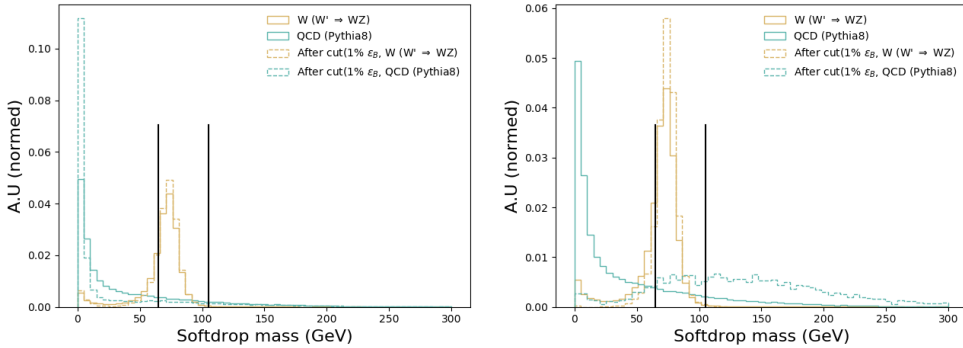


**Figure 5.13:** The softdrop jet mass distribution before (solid lines) and after (dotted lines) a cut on  $\tau_{21}$  (left) and  $\tau_{21}^{DDT}$  (right). All spectra are normalized to unit area.

2964 I have not yet had the chance to implement a mass decorrelation strategy for LoLa, but I  
 2965 see two ways going forward: The first is, following the example of what was done to decorrelate  
 2966 LoLa from jet  $p_T$ , to pass a mass dependent sample weight to the training. LoLa would then be  
 2967 trained with a weight derived to flatten the two dimensional jet mass - jet  $p_T$  plane. Another  
 2968 option would be to train LoLa together with an adversarial, a dedicated deep neural network  
 2969 running in parallel to LoLa and attempting to learn the jet mass from the LoLa output. The  
 2970 total loss function would then be a sum of the two, where the better the adversarial is in learning  
 2971 the mass, the worse the total loss function gets. Both these options are something I'd like to

2972 explore in the future.

2973 In summary, mass- and  $p_T$ -dependence are in their own right not a problem for a tagger.  
2974 The problem occurs when using these taggers in actual physics analyses where background rate  
2975 uncertainties and tagging  $p_T$  dependence uncertainties has a large impact on the final sensitivity.  
2976 There is a trade-off between signal efficiency and (analysis-dependent) systematics. For LoLa,  
2977 rather than choosing, I'd like to provide two different taggers: A nominal tagger, where no mass/ $p_T$ -  
2978 decorrelation is attempted, and a decorrelated version. Then both can be tested in a full analysis  
2979 chain before deciding on which tagger to use when looking at data.

## 2980 5.5 Validation on an independent sample

2981 LoLa is additionally validated on independent samples as an unbiased measure of performance  
2982 allowing to compare different CMS W-tagging algorithms to one another: A  $Z' \rightarrow WW$  sample  
2983 with  $M_{Z'} = 3\text{ TeV}$  produced with MadGraph and a QCD PYTHIA 8 sample in a  $p_T$  bin of 1000  
2984 to 1400 GeV. Here, only jets with  $1000\text{ GeV} < p_T < 1400\text{ GeV}$  and  $|\eta| < 1.5$  are used. The  
2985 signal efficiency versus mistagging rate for LoLa compared to the baseline PUPPI Softdrop +  
2986  $\tau_{21}$  tagger, is shown in Figure ???. As was pointed out in Section ???, a mass cut is not necessary  
2987 when using LoLa, but has been added to this plot for completeness. A significant improvement in  
2988 tagging efficiency is observed for LoLa compared to the default tagger, also when being validated  
2989 on a sample completely independent from the training sample. The cut corresponding to a 30  
2990 % signal efficiency working point are used as reference working points when we will look at  
2991 the tagging performance as a function of jet  $p_T$  and pileup in the following, and is marked by  
2992 triangles in the plot. The signal efficiency and mistagging rate as a function of jet  $p_T$ , is shown in  
2993 Figure 5.15. Again we observe the strong correlation between LoLa tagging efficiency and jet  
2994 transverse momenta. There is, however, no point in the spectra where the  $\tau_{21}$  tagger has a higher  
2995 signal over background ratio than LoLa. LoLa performs its worst at very high jet  $p_T$ , but in this  
2996 region the background is very small (dijet invariant masses around 2.5-3 TeV) so the absolute  
2997 performance here matters less than at lower  $p_T$ . Figure 5.16 shows the tagging efficiency and  
2998 mistagging rate as a function of pileup. Both taggers under study are more or less decorrelated  
2999 from pileup, with a flat efficiency up to 50 reconstructed primary vertices. In Run 3, this number  
3000 is of course expected to be significantly higher, around 140-200, and the study should be redone  
3001 up to a higher number of reconstructed primary vertices.

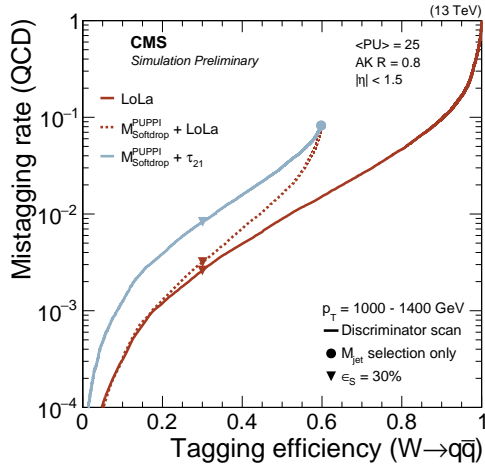


**Figure 5.14:** Performance of LoLa and PUPPI Softdrop +  $\tau_{21}$  in the background-signal efficiency plane. The PUPPI softdrop jet mass selection of  $65 < M_{SD} < 105 \text{ GeV}$ , and the 30 percent efficiency points are indicated with symbols.

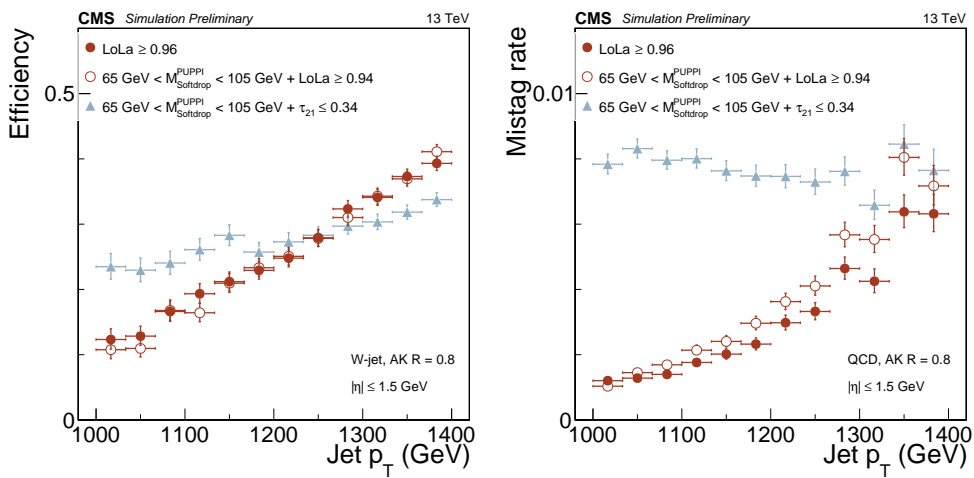


**Figure 5.15:** Efficiency (left) and mistag rate (right) of the LoLa selection corresponding to a 30 percent signal efficiency as a function of jet  $p_T$ .

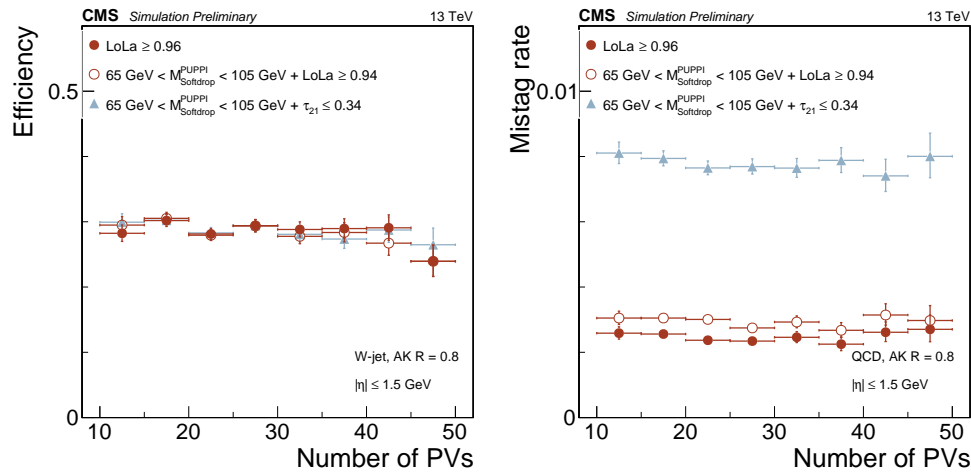


**Figure 5.16:** Efficiency (left) and mistagging rate (right) of the LoLa selection corresponding to a 30 percent signal efficiency as a function of the number of reconstructed vertices.

## 3002 5.6 Summary and outlook

3003 In this chapter, we have seen a promising new W-tagging algorithm for future VV searches. Its  
3004 absolute performance is better than that of the baseline PUPPI softdrop +  $\tau_{21}$  tagger up to a jet  
3005  $p_T$  of at least 1400 GeV, roughly corresponding to a dijet invariant mass of 2.5-3 TeV, and could  
3006 lead to an increase in total signal efficiency from 18 to 43 % for the searches presented here. With  
3007 a  $p_T$  decorrelation method already in place, it could already now be used for the one dimensional  
3008 VV search presented in Search I and Search II. However, if to be used in the multidimensional  
3009 search framework, a mass decorrelation method needs to be established. I have already outlined  
3010 two possibilities of how to achieve this in Section 5.4.2, where one of these has already been  
3011 shown to work in the context of  $p_T$  decorrelation. This is, as of this writing, left to future studies.

3012  
3013 When discussing the future of the multidimensional search, I mentioned how a deep neural  
3014 network such as the one presented here could be used to encode jet substructure in a way useful in  
3015 order to develop a generic anti-QCD tagger. This has already been achieved by a parallel analysis  
3016 team through the use of auto-encoders, published ten days before this writing and documented  
3017 in [80], and has shown very promising results. However, this strategy is, to my knowledge after  
3018 discussing with the authors, no longer pursued after observing that the auto-encoder version of  
3019 LoLa was very difficult to decorrelate from the jet mass. It is my belief that this can be overcome  
3020 by changing some of the features calculated in the Lorentz Layer (in [80], only the invariant  
3021 mass is calculated and the other features listed in Equation 5.4 are stripped away) and this is  
3022 something I would also like to pursue in future studies in order to achieve the truly generic search  
3023 for boosted dijet resonances in the  $M_{\text{jet}1}$ - $M_{\text{jet}2}$ - $M_{\text{VV}}$  plane.

---

3024

## CHAPTER 6

---

3025

## Conclusion and outlook

3026 In this doctoral thesis I have presented three searches for new heavy ( $> 1\text{TeV}$ ) resonances decaying  
3027 to two vector bosons in the all-hadronic final state, using datasets collected by the CMS experiment  
3028 corresponding to an integrated luminosity of 2.7(2015), 35.9(2016) and 77.3(2016+2017)  $\text{fb}^{-1}$ .  
3029 Due to the high energy (“boost”) of the vector bosons, their decay products are so collimated  
3030 that they get merged into one single jet, leading to a dijet final state topology. Dedicated jet  
3031 grooming and jet substructure techniques are therefore explored in order to discriminate vector  
3032 bosons from the overwhelming QCD multijet background.

3033

3034 Each of the analyses presented has provided original contributions to the field: The first search  
3035 was the first of its kind to ever be performed at  $\sqrt{s} = 13\text{ TeV}$ , following an observed excess of  
3036  $3.4\ (1.3)\ \sigma$  by ATLAS (CMS) in the 8 TeV dataset, and the first time CMS demonstrated the  
3037 efficiency of using jet grooming techniques at trigger level. It, at the time, set the most stringent  
3038 limits to date for the signal scenarios under consideration.

3039 The second search introduces a novel pileup resistant and perturbative safe vector boson tagging  
3040 algorithm based on PUPPI softdrop jet mass, ensuring a high and stable signal efficiency up to  
3041 pileup of at least 50 interactions per event. The optimization, validation and full commissioning  
3042 of the tagger was performed in the context of this search. Dedicated jet mass corrections in order  
3043 to account for an observed  $p_T$  and  $\eta$  dependence in PUPPI softdrop jet mass, due to the nature  
3044 of the softdrop algorithm, were also developed. The PUPPI softdrop based tagger, together with  
3045 the jet mass corrections, became, and still is, the recommended algorithm for W-tagging in CMS.  
3046 The final analysis introduces a band new way of doing diboson resonance searches through a tree  
3047 dimensional fit of the dijet invariant mass and the softdrop mass of the two jets. By optimization  
3048 of the W-tagging algorithm used in this search and the nature of the search method, we have,  
3049 for the first time, been able to extract the jet mass scale and resolution for a merged  $W(\bar{q}q)$   
3050 and  $Z(\bar{q}q)$  peak from the V+jets Standard Model process. The method itself leads to a 20-30 %  
3051 higher sensitivity than the default search method.

3052

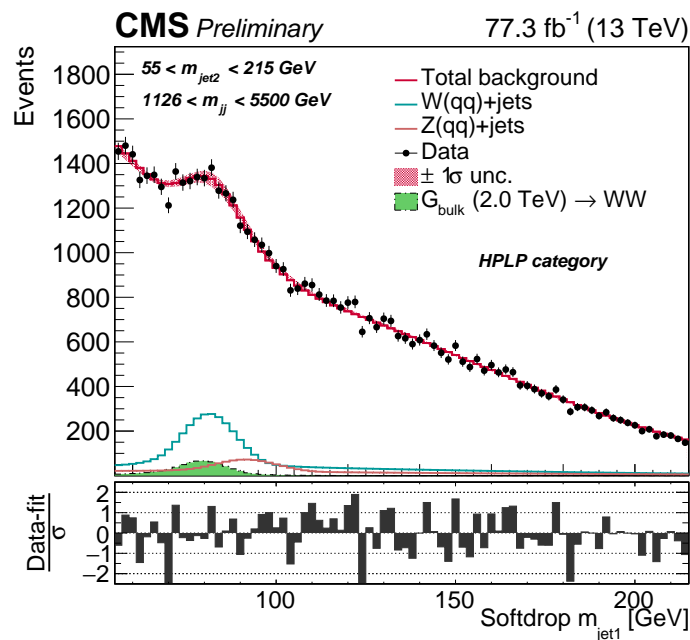
3053 The benefit of using a three-dimensional fit based on dijet invariant mass and the softdrop  
3054 jet masses of the two jets, is that one can look for resonances peaking anywhere in the jet  
3055 mass and dijet invariant mass spectrum. The natural next step for this search is therefore the  
3056 incorporation of  $VH(bb)$  and  $H(bb)H(bb)$  final states into the three-dimensional fit framework,  
3057 where orthogonality is guaranteed through b-tagging categories. This process is ongoing and  
3058 planned for the full Run 2 dataset (including the data collected in 2018).

3059 Going further, one can incorporate searches for generic resonances peaking anywhere in the  
3060 softdrop jet mass and dijet invariant mass spectrum in the multi-dimensional fit, where the

3061 jets themselves can have other substructure compositions than two subjets. This type of model  
 3062 independent search requires a generic anti-QCD tagger in order to be truly model independent.  
 3063 In the final chapter of this thesis I presented ongoing work on a deep neural network based  
 3064 W-tagging algorithm for future searches, capable of more than doubling the analysis signal  
 3065 efficiency by incorporating jet substructure algorithms within the deep layers. As there will be no  
 3066 center-of-mass energy increase after the LHC reaches 14 TeV, achieving the best possible analysis  
 3067 sensitivity for the dataset to come will be of key importance. I also showed how such a deep  
 3068 neural network model is the ideal starting point for building a signal independent anti-QCD tagger.

3069

3070 With  $\sim 80 \text{ fb}^{-1}$  of 13 TeV data analyzed and no excess observed, the future of this search  
 3071 therefore lies in: Increasing the analysis sensitivity through novel taggers, as the one I have  
 3072 presented here, and, making the search strategy as generic as possible through multi-dimensional  
 3073 scans and generic anti-QCD taggers, both of which have been built a foundation for in this  
 3074 doctoral work..





## APPENDIX A

### Search I: Limits per mass category

#### A.1 Limits per mass category

The asymptotic limits obtained with  $2.6 \text{ fb}^{-1}$  of 13 TeV CMS data per mass and purity category.

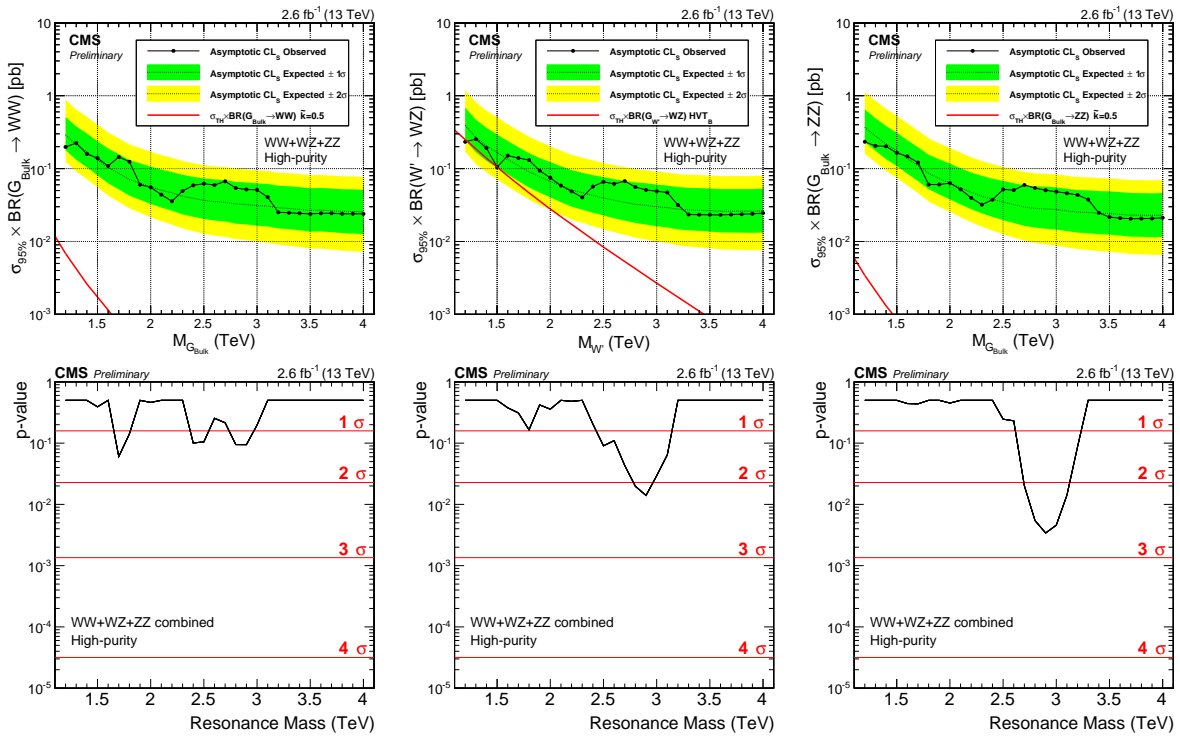


**Figure A.1:** Expected/observed limits and corresponding p-values obtained in the high purity category using  $2.6 \text{ fb}^{-1}$  of CMS data. Here for a Bulk  $G \rightarrow WW$  (left),  $W' \rightarrow WZ$  (middle) and  $G \rightarrow ZZ$  (right) signal.

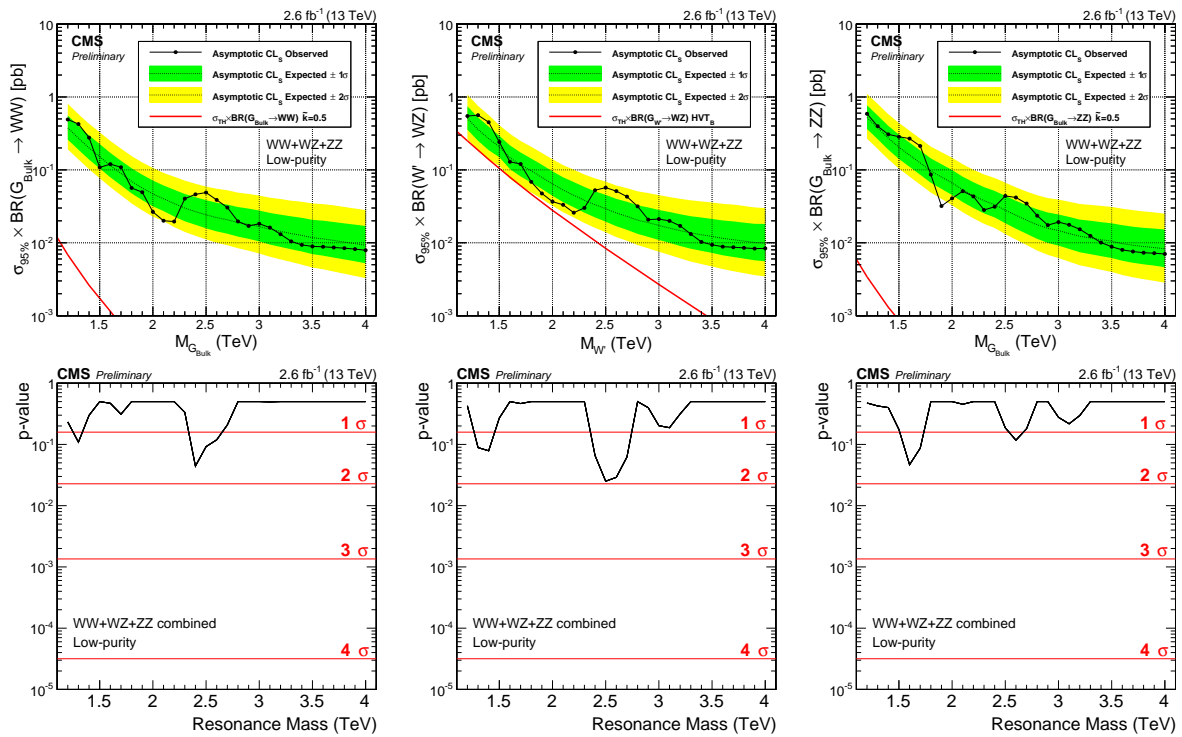


**Figure A.2:** Expected/observed limits and corresponding p-values obtained in the low purity category using  $2.6 \text{ fb}^{-1}$  of CMS data. Here for a Bulk  $G \rightarrow WW$  (left),  $W' \rightarrow WZ$  (middle) and  $G \rightarrow ZZ$  (right) signal.

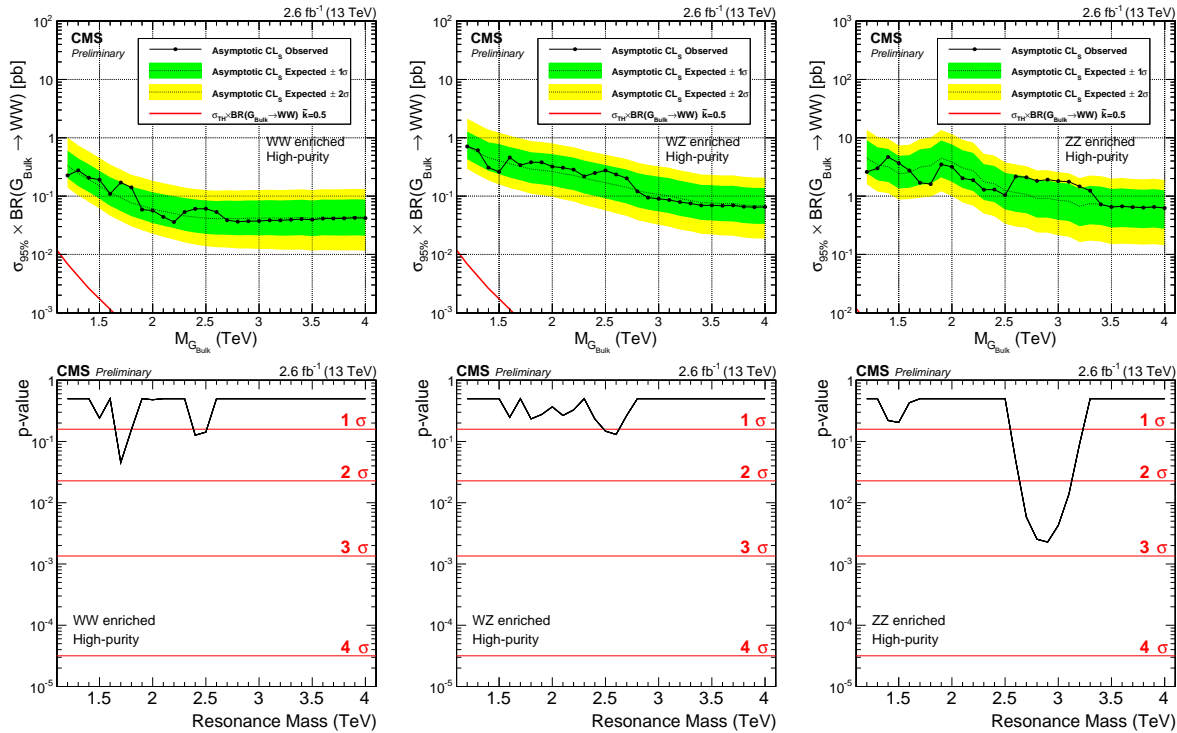


**Figure A.3:** Expected/observed limits and corresponding p-values obtained for the different mass categories using  $2.6 \text{ fb}^{-1}$  of CMS data. Here for a Bulk  $G \rightarrow WW$  signal in the HP category

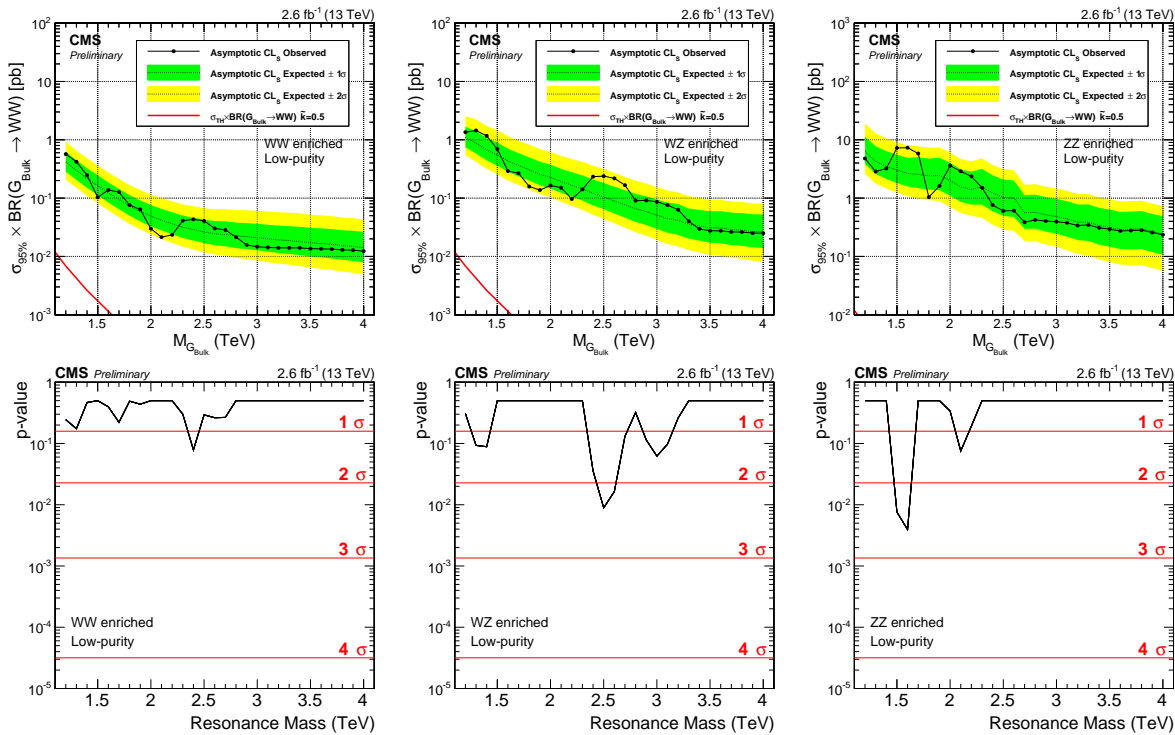


**Figure A.4:** Expected/observed limits and corresponding p-values obtained in the different mass categories using 2.6 fb<sup>-1</sup> of CMS data. Here for a Bulk  $G \rightarrow WW$  signal in the LP category.

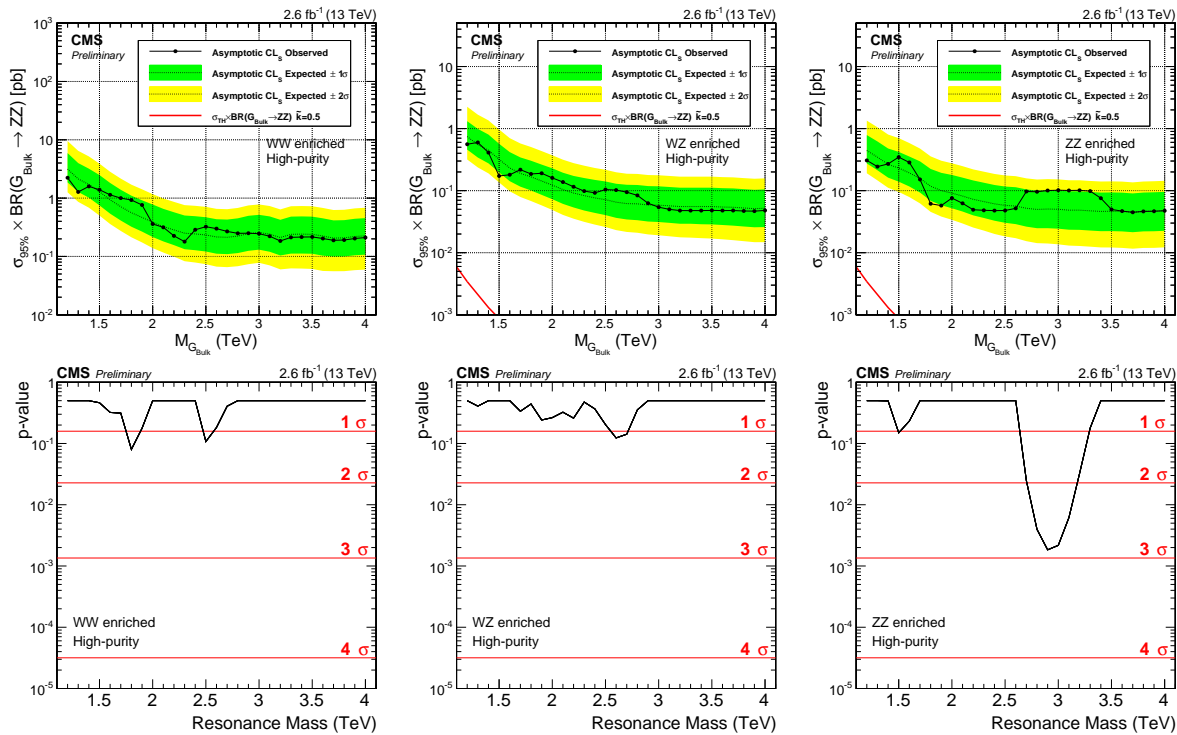


**Figure A.5:** Expected/observed limits and corresponding p-values obtained in the different mass categories. Here for a  $G \rightarrow ZZ$  signal in the HP category.

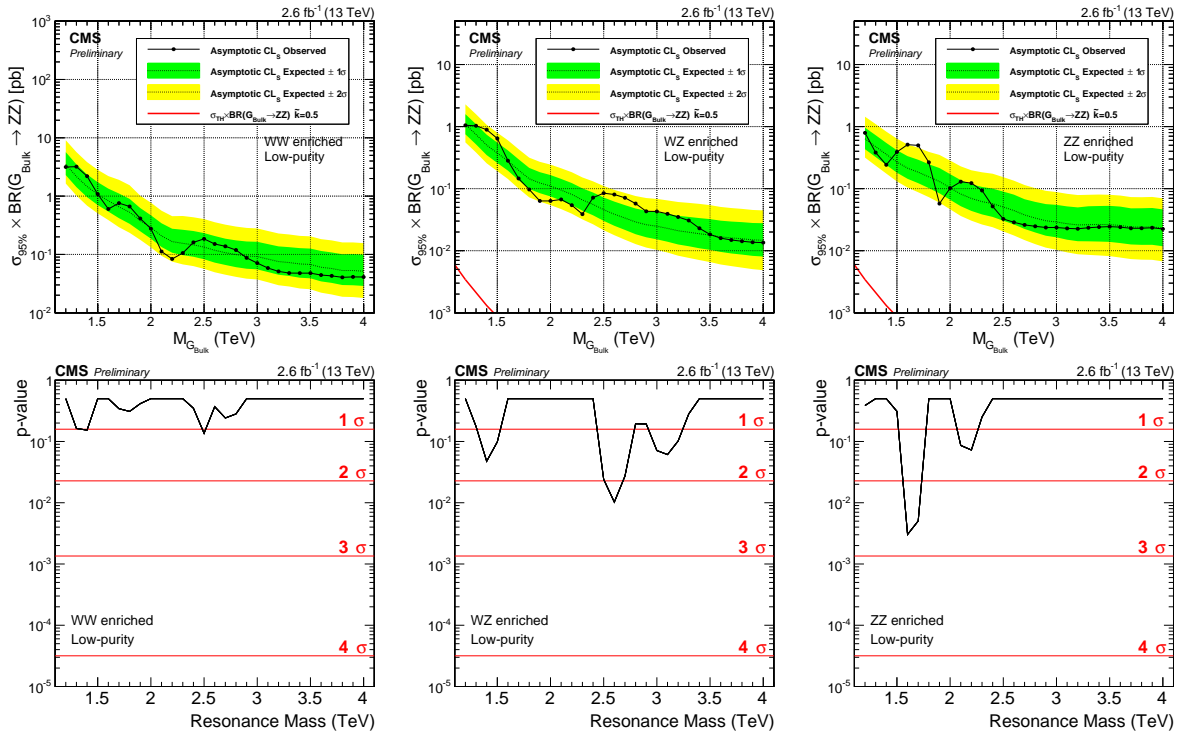


**Figure A.6:** Expected/observed limits and corresponding p-values obtained in the different mass categories. Here for a  $G \rightarrow ZZ$  signal in the LP category.

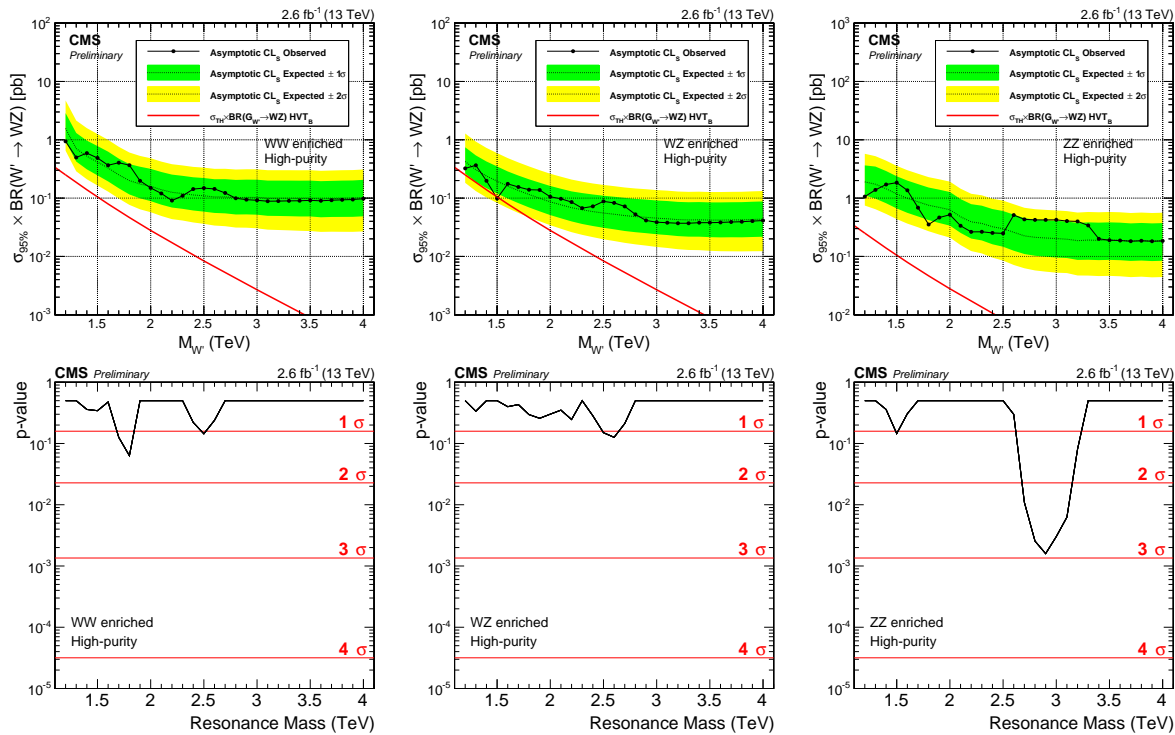


**Figure A.7:** Expected/observed limits and corresponding p-values obtained in the different mass categories. Here for a  $W' \rightarrow WZ$  signal in the high-purity category.

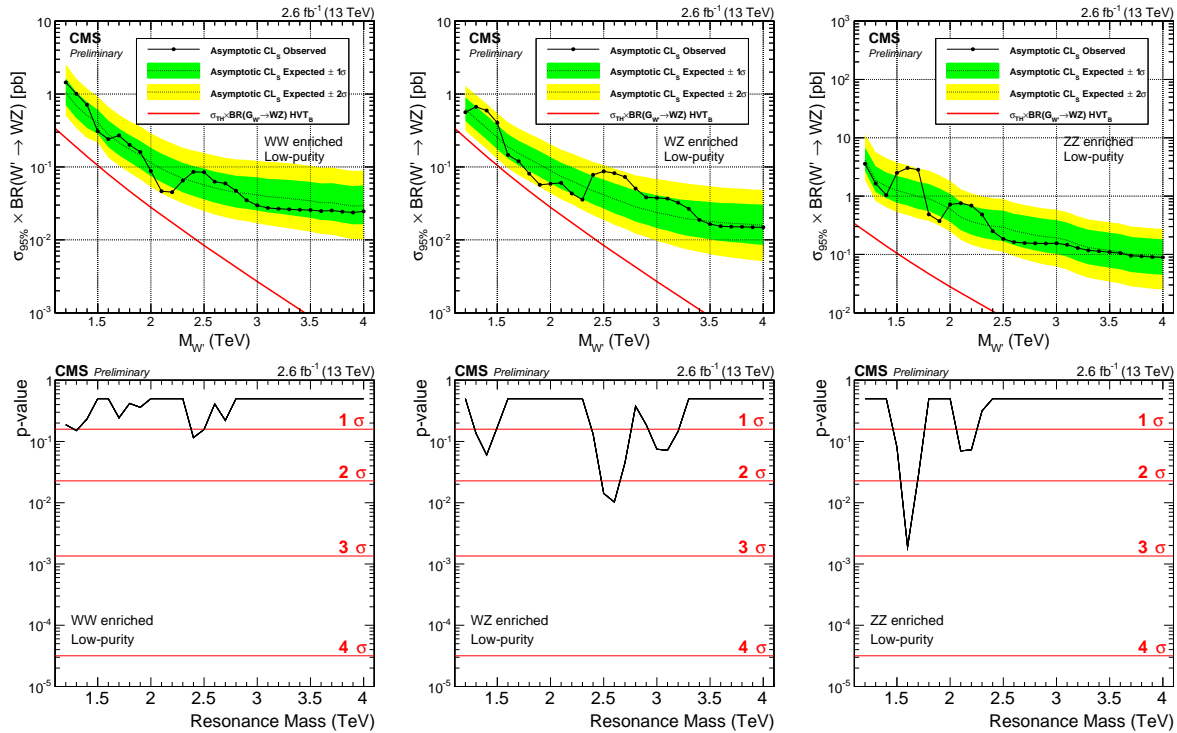


**Figure A.8:** Expected/observed limits and corresponding p-values obtained in the different mass categories. Here for a  $W' \rightarrow WZ$  signal in the low purity category.

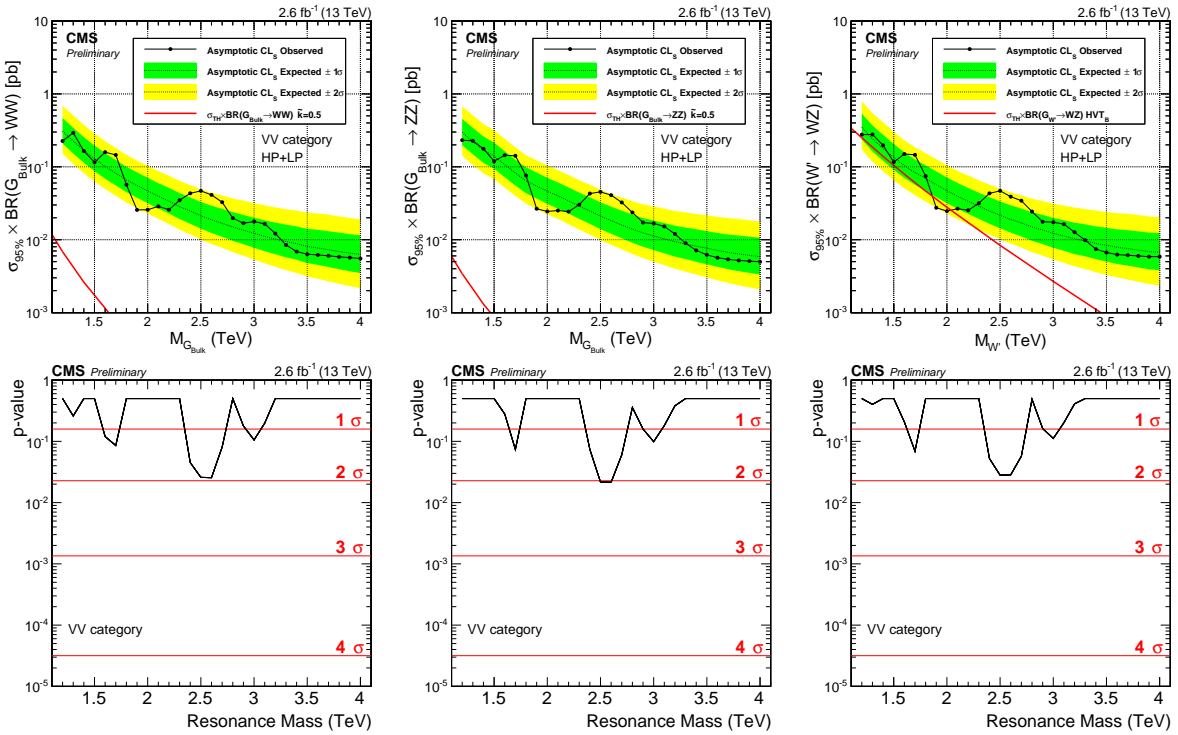


**Figure A.9:** Expected/observed limits and corresponding p-values obtained without splitting into mass categories. This analysis is performed as a cross check analysis and directly compares with the method used in the corresponding Run 1 analysis [?]. Here for a Bulk  $G \rightarrow WW$  (left),  $G \rightarrow ZZ$  (middle) and  $W' \rightarrow WZ$  signal (right).



3080

---

## APPENDIX B

---

3081

## Search II

### 3082 B.1 W-tagging scale factor measurement: Additional plots

3083 Figures B.1 show the  $t\bar{t}$  real W (top) and non-W (bottom) PUPPI softdrop jet mass distributions  
 3084 for jets that passed (left) and failed (right column) the N-subjettiness selections  $\text{PUPPI } \tau_{21} < 0.40$ .  
 Figures B.2 shows the fitted PUPPI softdrop jet mass distributions for the non-dominant

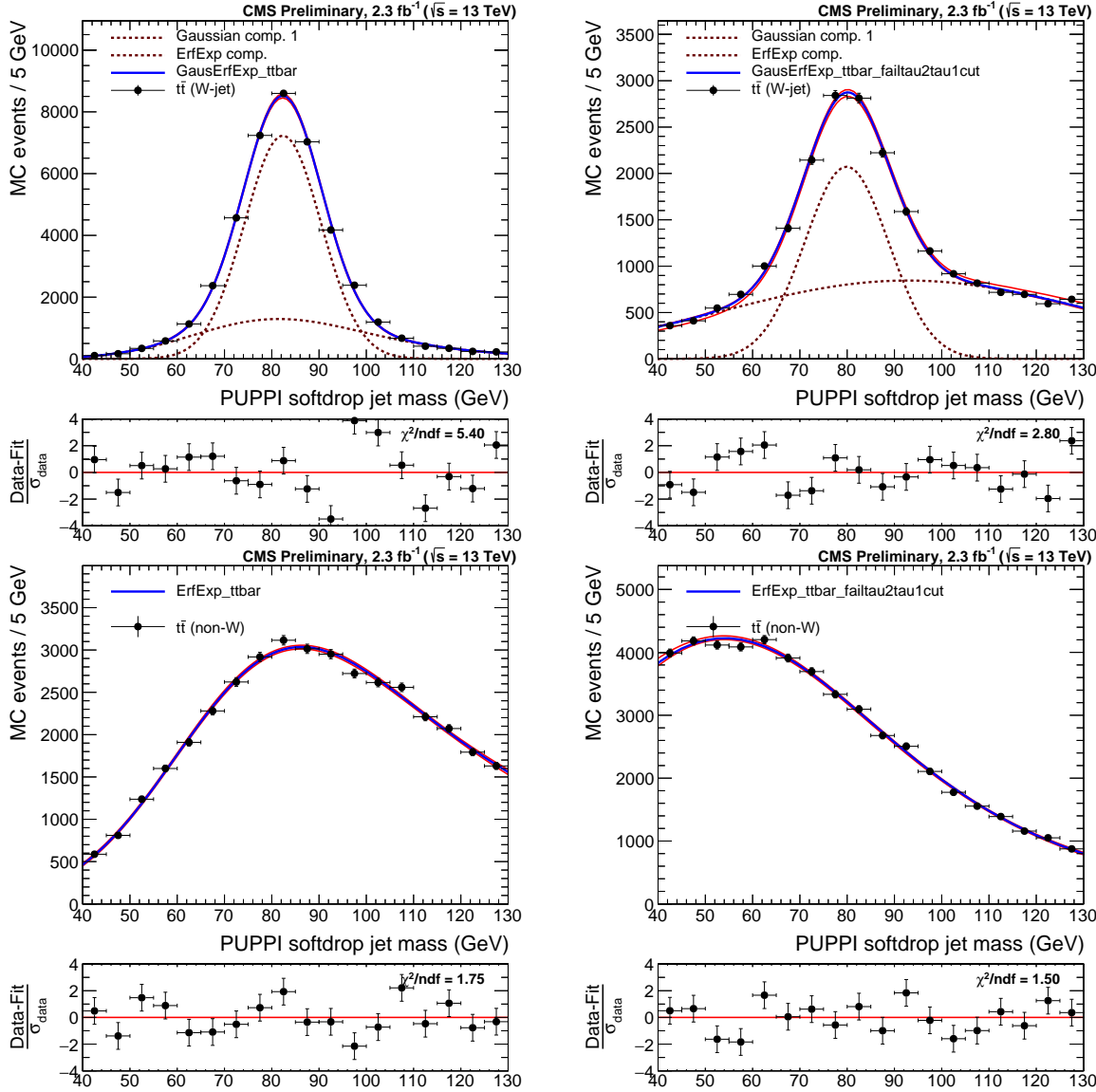


**Figure B.1:** Fit to the real W (top) and non-W (bottom) softdrop jet mass distribution for jets that pass (left) and fail (right) the cut on  $\text{PUPPI } \tau_{21} < 0.4$ .

3085

3086 backgrounds in the evaluation of the W-tagging scale factors. Here for jets that pass (top) and

failed (bottom) the N-subjettiness selections PUPPI  $\tau_{21} < 0.40$ .

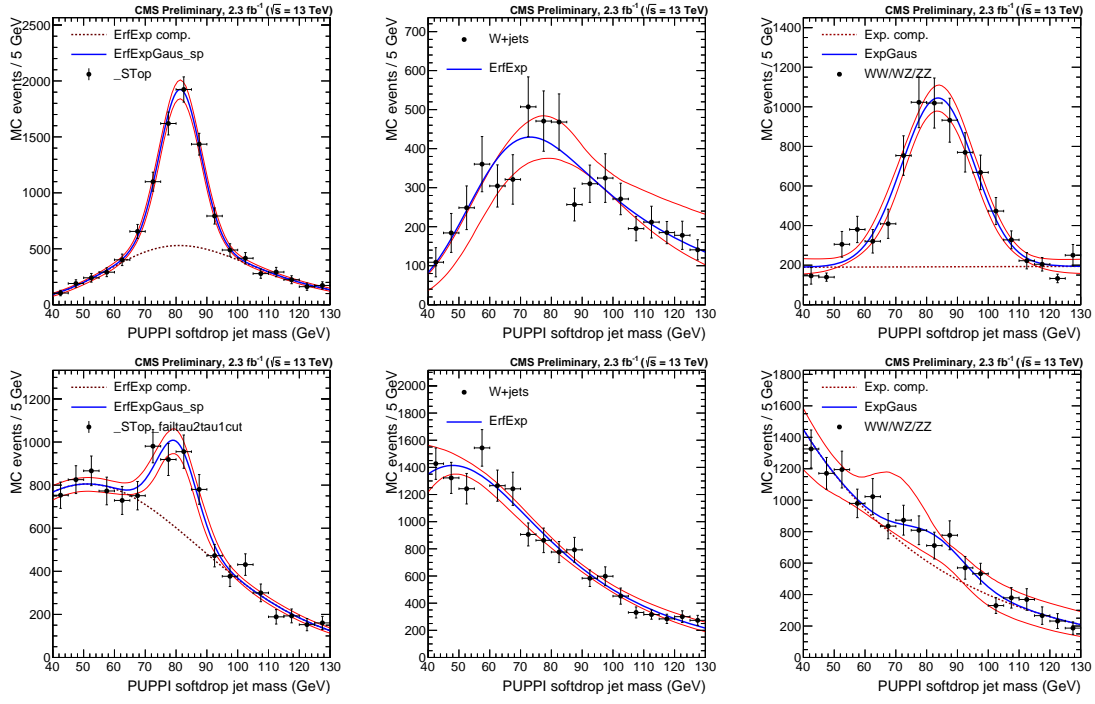


**Figure B.2:** Fits to the PUPPI softdrop jet mass spectrum for the non-dominant backgrounds (Single top, W+jets and VV respectively) in the pass (top) and fail (bottom) regions.

3087

## 3088 B.2 Efficiency scale factors for $2.5 \text{ fb}^{-1}$

Category	Working point	Eff. data	Eff. simulation	Scale factor
HP	$\tau_2/\tau_1 < 0.4$	$0.785 \pm 0.045$	$0.81 \pm 0.01$	$0.97 \pm 0.06 \text{ (stat)} \pm 0.04 \text{ (sys)} \pm 0.06 \text{ (sys)}$
LP	$0.45 < \tau_2/\tau_1 < 0.75$	$0.215 \pm 0.057$	$0.204 \pm 0.041$	$1.13 \pm 0.24 \text{ (stat)} \pm 0.17 \text{ (sys)} \pm 0.12 \text{ (sys)}$

**Table B.1:** W-tagging scale factors for both categories the high purity and low purity categories for two taggers: Pruned jet mass +  $\tau_{21}$  and PUPPI softdrop jet mass + PUPPI  $\tau_{21}$ .

3089

## B.3 Background fit checks

The background from QCD multijet events is modelled by a smoothly falling distribution in each analysis category. The method consists of a smoothness test of the observed data where the

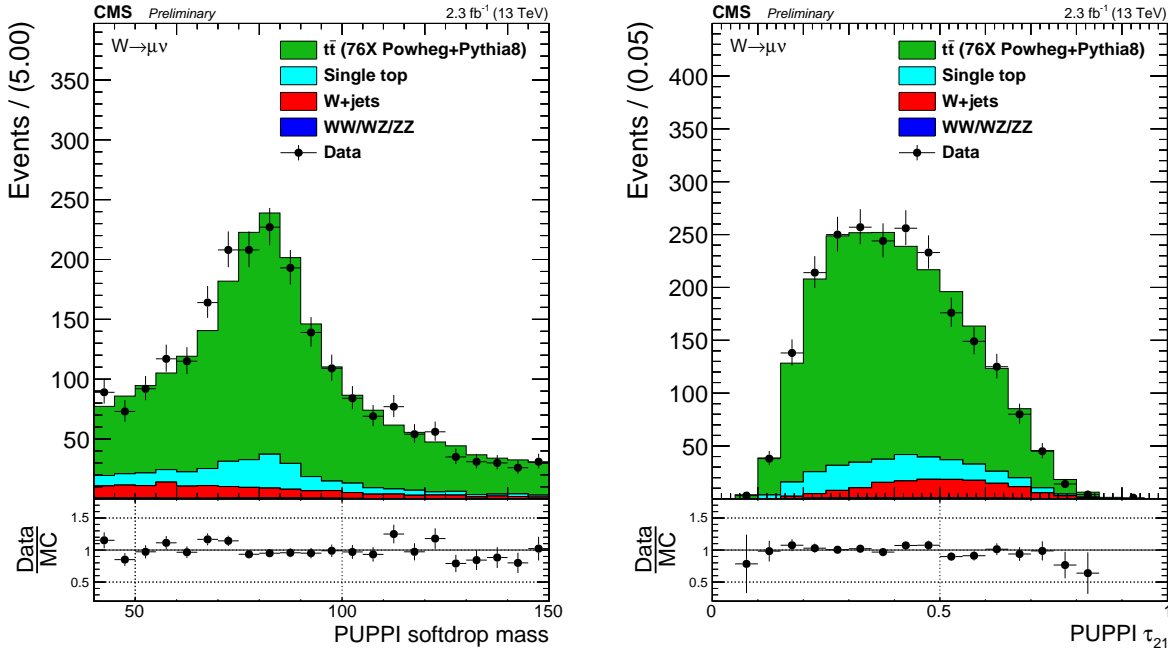


**Figure B.3:** Distribution of the PUPPI softdrop mass (left) and PUPPI n-subjettiness (right) distribution in the  $t\bar{t}$  control sample.

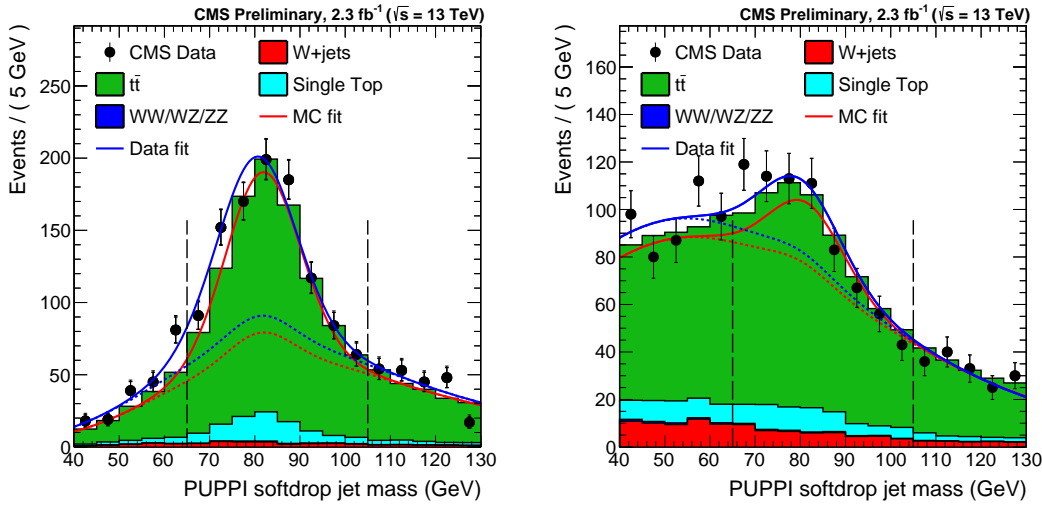


**Figure B.4:** PUPPI softdrop jet mass distribution that pass (left) and fail (right) the PUPPI  $\tau_2/\tau_1 < 0.40$  selection. Results of both the fit to data (blue) and simulation (red) are shown and the background components of the fit are shown as short-dashed lines.

Parameter	Data	Simulation	Data/Simulation
PUPPI softdrop $\langle m \rangle$	$80.3 \pm 0.8$ GeV	$81.9 \pm 0.01$ GeV	$0.98 \pm 0.01$
PUPPI softdrop $\sigma$	$9.0 \pm 0.9$ GeV	$8.5 \pm 0.4$ GeV	$1.07 \pm 0.12$

**Table B.2:** Summary of the fitted W-mass peak fit parameters.

background is assumed to be described by the following empirical probability density function:

$$\frac{dN}{dm} = \frac{P_0(1 - m/\sqrt{s})^{P_1}}{(m/\sqrt{s})^{P_2}} \quad (\text{B.1})$$

where  $m$  is the dijet invariant mass,  $\sqrt{s}$  the centre of mass energy,  $P_0$  is a normalisation parameter for the probability density function and  $P_1$  and  $P_2$  describe the shape. To ensure that this function is sufficient to describe the data in all the different analysis categories, we first perform a test to check that no additional parameters are needed and to check the systematics due to choice of fit function. For these studies we use a data sideband, where one of the two jets is required to have a mass between  $20 \text{ GeV} < M_{\text{Softdrop}} < 65 \text{ GeV}$ . In order to quantify how many parameters are necessary, a Fishers F-test [65] is performed for the fits to data in the data sideband. The critical value that the test statistic must exceed is chosen to be  $\alpha > 10\%$ . If the returned Confidence Level is larger than  $\alpha$ , the simpler fit is preferred. The three parameter fit is compared with the following 2, 4 and 5 parameter functions:

$$\frac{dN}{dm} = \frac{P_0}{(m/\sqrt{s})^{P_2}} \quad (\text{B.2})$$

$$\frac{dN}{dm} = \frac{P_0(1 - m/\sqrt{s})^{P_1}}{(m/\sqrt{s})^{P_2 + P_3 \times \log(m/\sqrt{s})}} \quad (\text{B.3})$$

$$\frac{dN}{dm} = \frac{P_0(1 - m/\sqrt{s})^{P_1}}{(m/\sqrt{s})^{P_2 + P_3 \times \log(m/\sqrt{s}) + P_4 \times \log(m/\sqrt{s})^2}} \quad (\text{B.4})$$

Additionally, fits with an alternative fit function has also been performed (for the single-tag categories we try both 4 and 5 parameter versions):

$$\frac{dN}{dm} = \frac{P_0(1 - m/\sqrt{s} + P_3(m/\sqrt{s})^2)^{P_1}}{(m/\sqrt{s})^{P_2}} \quad (\text{B.5})$$

$$\frac{dN}{dm} = \frac{P_0(1 - m/\sqrt{s} + P_3(m/\sqrt{s})^2)^{P_1}}{(m/\sqrt{s})^{P_2 + P_4 \times \log(m/\sqrt{s})}} \quad (\text{B.6})$$

### **3105 B.3.1 Background fit checks in data sideband**

3106 We perform a test in a data sideband to make sure the fit functions work on real data and  
 3107 to exercise the estimation of number of necessary fit parameters via an F-test. The sideband  
 3108 is constructed by requiring one of the two jets two have a mass in the low softdrop jet mass  
 3109 sideband, between  $20 \text{ GeV} < M_{\text{Softdrop}} < 65 \text{ GeV}$ , while the full W/Z-tag selections are applied to  
 3110 the other jet. The low-mass jet is also required to pass the  $\tau_{21}$  cut corresponding to the given  
 3111 category. For the single-tag category, the sideband is constructed by requiring one of the two jets  
 3112 to have a mass in the low softdrop jet mass sideband, between  $20 \text{ GeV} < M_{\text{Softdrop}} < 65 \text{ GeV}$  and  
 3113 the other in a high-mass sideband, between  $105 \text{ GeV} < M_{\text{Softdrop}} < 200 \text{ GeV}$ . One of the jets is  
 3114 also required to pass the  $\tau_{21}$  cut corresponding to the given category. We first check whether  
 3115 the sideband can be used to exercise the F test by checking whether or not there are features  
 3116 introduced in the dijet mass spectrum that may be hard to cover with the fit using QCD MC. To  
 3117 do so we look at the dijet invariant mass spectrum in the signal region divided by the distribution  
 3118 in the sideband. The obtained distributions are shown in Figure B.5 for three different generators,  
 3119 where the pure Pythia8 QCD samples (top left) has the highest statistics. The distributions are  
 3120 mostly smooth, but we do see features introduced in the “WW HP” and “ZZ HP” categories  
 3121 which might prove difficult to fit, as well as in the tail of the single-tag categories. These kinks  
 3122 shift around depending on what MC generator is used and do not seem to be a systematic feature  
 3123 caused by the cuts that have been applied, but rather due to limited statistics. We proceed with  
 3124 exercising the F-test in a data sideband, with the caveat that there might be features introduced  
 3125 in the spectrum where statistics are low.

3126 Figure B.6 shows the fit to data in the data sideband for the WW and ZZ mass categories,  
 3127 both in the HP and in the LP n-subjettiness categories. The corresponding residuals,  $\chi^2$  and  
 3128 F-test results are shown i Table B.7 through B.10. For the double-tag categories, a two or three  
 3129 parameter function is sufficient to describe the data and we conclude that the function as defined  
 3130 in B.1 is sufficient for all mass categories. For the single-tag category a five parameter fit seems  
 3131 to be required in order to describe the data and the fit quality is not optimal. To ensure that the  
 3132 fit functions with sufficient number of parameters is able to describe the shape in the single-tag  
 3133 categories, we have additionally looked at the fit quality in QCD MC (see below). Here, the  
 3134 default dijet function seems sufficient to describe the distributions. The sideband in the single-tag  
 3135 categories in QCD MC do not show the same features as the data sideband as shown in Figure  
 3136 B.7.

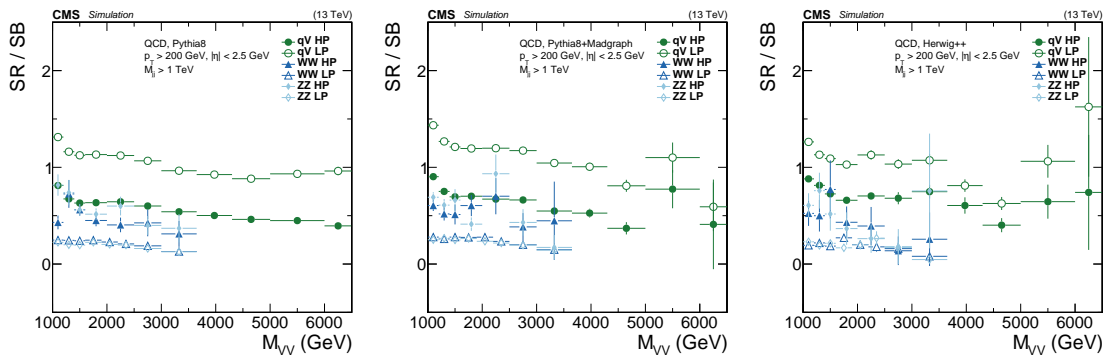


**Figure B.5:** Dijet mass spectrum in the signal region divided by the dijet mass spectrum in the sidebands using QCD Pythia8 (left), QCD Pythia8+Madgraph (middle) and QCD Herwig++ (right) simulated samples. Here for the double W/Z-tag and the single V-tagged HP and LP categories. Some jumps are observed in the high-mass tail of the dijet invariant mass distribution in the high-purity WW/ZZ categories, but otherwise no strange features seem to be induced by using the sideband.

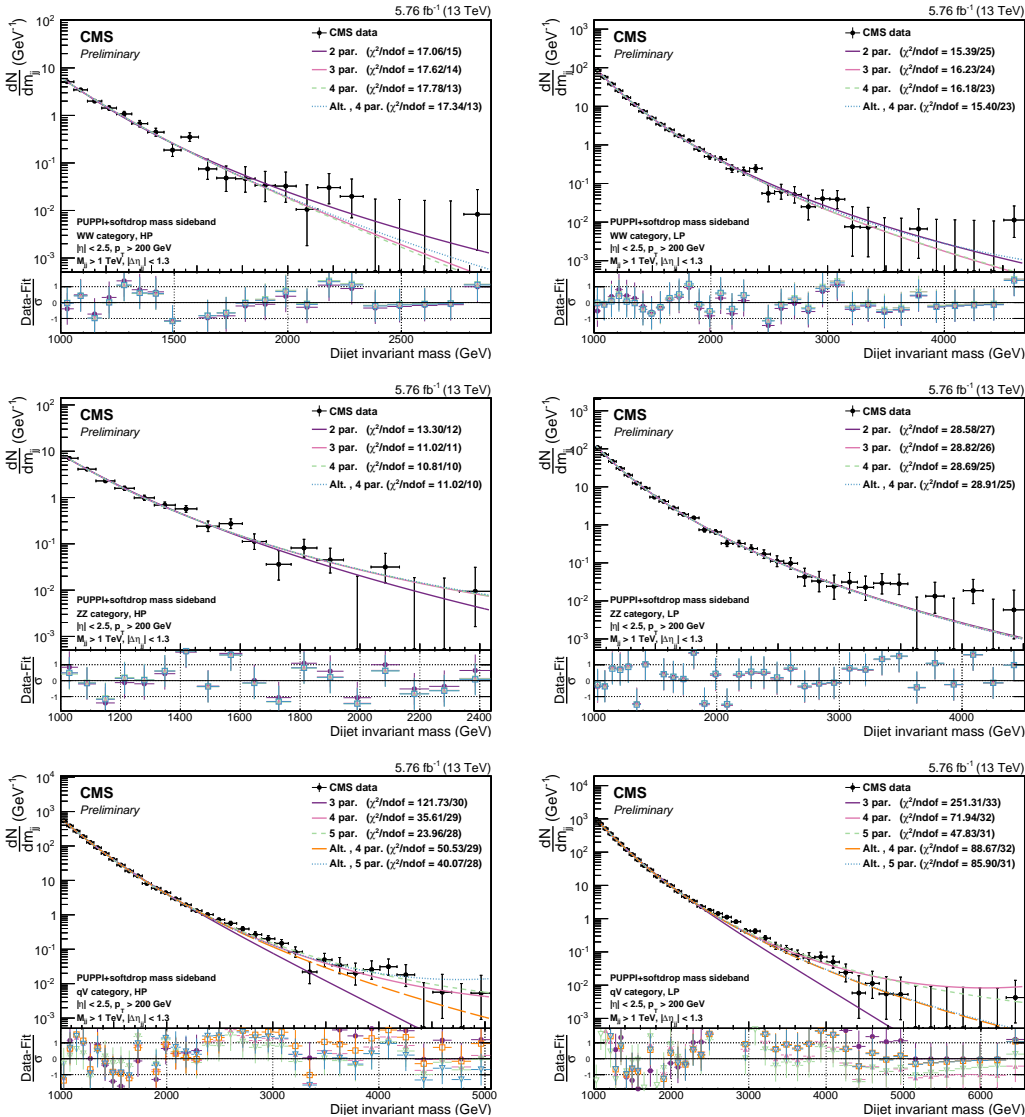


**Figure B.6:** Fitted dijet mass spectrum in the different mass and purity categories in a data sideband: WW high-purity (top left) and low-purity (top right), ZZ high-purity (middle left) and low-purity (middle right), qV high-purity (bottom left) and low-purity (bottom right).

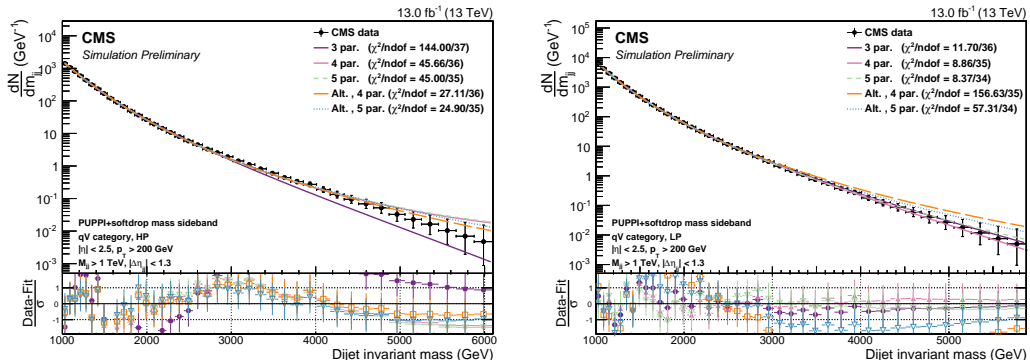


**Figure B.7:** Fitted dijet mass spectrum in the QCD MC sideband: qV high-purity (left) and low-purity (right).

WW category, HP			
Function	Residuals	$\chi^2$	ndof
2 par	0.129	17.060	15
3 par	0.111	17.623	14
4 par	0.111	17.783	13
Fishers23	2.430	CL	0.140
Fishers34	0.012	CL	0.914

**Table B.3:** Residuals,  $\chi^2$ , and degrees of freedom for the WW category, HP category. A 2 parameter fit is needed to describe these data.

WW category, LP			
Function	Residuals	$\chi^2$	ndof
2 par	0.908	15.388	25
3 par	0.279	16.225	24
4 par	0.263	16.178	23
Fishers23	56.395	CL	0.000
Fishers34	1.406	CL	0.247

**Table B.4:** Residuals,  $\chi^2$ , and degrees of freedom for the WW category, LP category. A 3 parameter fit is needed to describe these data.

### **3137 B.3.2 Background fit checks in QCD MC**

3138 As an additional check, we look at the fit functions in the different signal categories using QCD  
 3139 MC. This is shown in Figure B.8 for the double and Figure B.9 for the single tag categories. Here  
 3140 all fit functions and their pull distributions are plotted. The fits are performed in a mass range  
 3141 corresponding to the expected distribution in the different categories for  $13 \text{ fb}^{-1}$  of data. We  
 3142 have adapted the error bars to correspond to the maximum of the expected Poisson error for  $13$   
 3143  $\text{fb}^{-1}$  of data and the pure simulation error (accounting for the different weights assigned to the  
 3144  $p_T$ -binned QCD MC sample). The reason for this choice is to get an estimate of whether the  
 3145 set of fit functions we plan to use to fit the background distribution in data, and plan to use in  
 3146 order to understand the systematic uncertainty due to our choice of fit function, are appropriate  
 3147 and do not produce fake bumps/kinks. As this distribution is the pure MC simulation curve,  
 3148 whose variation at high masses is much smaller than the expected poisson error for  $13 \text{ fb}^{-1}$  of  
 3149 data, we expect the  $\chi^2/\text{ndof}$  to be lower than one. In order to protect against the fact that the  
 3150 MC simulation at lower dijet masses does not have more statistics than the expected data for

ZZ category, HP			
Function	Residuals	$\chi^2$	ndof
2 par	0.215	13.296	12
3 par	0.133	11.022	11
4 par	0.119	10.810	10
Fishers23	7.465	CL	0.018
Fishers34	1.304	CL	0.278

**Table B.5:** Residuals,  $\chi^2$ , and degrees of freedom for the ZZ category, HP category. A 3 parameter fit is needed to describe these data.

ZZ category, LP			
Function	Residuals	$\chi^2$	ndof
2 par	2.459	28.583	27
3 par	2.363	28.817	26
4 par	2.175	28.694	25
Fishers23	1.107	CL	0.302
Fishers34	2.244	CL	0.146

**Table B.6:** Residuals,  $\chi^2$ , and degrees of freedom for the ZZ category, LP category. A 2 parameter fit is needed to describe these data.

3151 13  $\text{fb}^{-1}$  of data, we use the largest of the Poisson and the MC error. The resulting errors are  
 3152 therefore a mixture of Poisson and the MC error and the  $\chi^2/\text{ndof}$  for the QCD MC fits should  
 3153 not be considered. Fit quality in the form of  $\chi^2/\text{ndof}$  should only be estimated from the fits to  
 3154 data sideband where pure Poisson errors are used Overall the fits to QCD MC in the different  
 3155 categories describe the data well, with a two or three parameter function sufficient to describe the  
 3156 distributions. However, due to an under fluctuation of the first bin in the “ZZHP” category, the  
 3157 higher parameter fits are steered by the first bin leading to discrepancies in the tail. This is the  
 3158 lowest statistics category and the danger for underfluctuations does exist. We have investigated  
 3159 the dijet invariant mass distribution down to a dijet invariant mass threshold of 800 GeV to  
 3160 make sure we are not seeing a turn-on effect. This is shown in Figure B.10. The fits in the data  
 3161 sideband for the same category (Figure B.6, middle left) do not show the same trend.

## 3162 B.4 F-test in signal region

3163 The final F-test performed in order to define the number of fit parameters to be used to fit the  
 3164 background in each analysis category, is performed in the signal region. The resulting fits and

qV category, HP			
Function	Residuals	$\chi^2$	ndof
3 par	128.276	121.731	30
4 par	29.113	35.606	29
5 par	7.036	23.962	28
Alt. 4 par	37.232	50.528	29
Alt. 5 par	30.948	40.068	28
Fishers34	102.185	CL	0.000
Fishers45	90.988	CL	0.000
FishersAlt4Alt5	5.888	CL	0.022

**Table B.7:** Residuals,  $\chi^2$ , and degrees of freedom for the qV category, HP category. A 5 parameter fit is needed to describe these data.

qV category, LP			
Function	Residuals	$\chi^2$	ndof
3 par	671.341	251.311	33
4 par	171.593	71.942	32
5 par	80.801	47.830	31
Alt. 4 par	215.431	88.666	32
Alt. 5 par	214.766	85.896	31
Fishers34	96.109	CL	0.000
Fishers45	35.957	CL	0.000
FishersAlt4Alt5	0.099	CL	0.755

**Table B.8:** Residuals,  $\chi^2$ , and degrees of freedom for the qV category, LP category. A 5 parameter fit is needed to describe these data.

3165 F-test values for the double tag categories are shown in Figure B.11 and Tables B.9 to B.14.

3166 The F-test results for the single-tag category are listed in Tables B.15 to B.18. Here, a three  
 3167 parameter fit is sufficient for all categories except the “high-purity” qW category where a 5  
 3168 parameter fit is preferred.

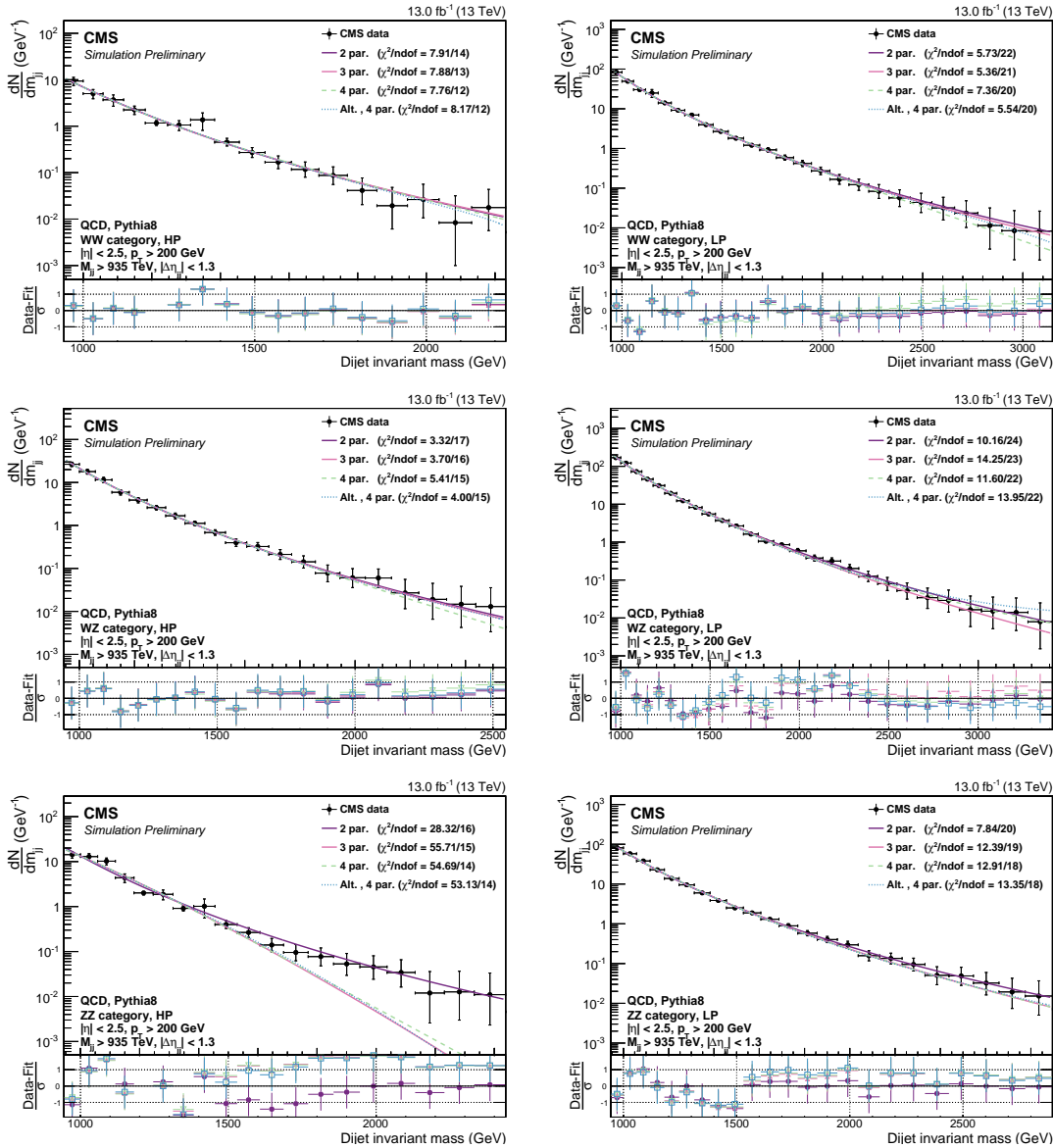


**Figure B.8:** Background fit for the  $M_{jj}$  distribution in QCD MC corresponding to  $13 \text{ fb}^{-1}$ . Here for the high- and low-purity double W/Z-tag category for the three different mass categories: WW category (top), WZ category (middle) and ZZ category (bottom).

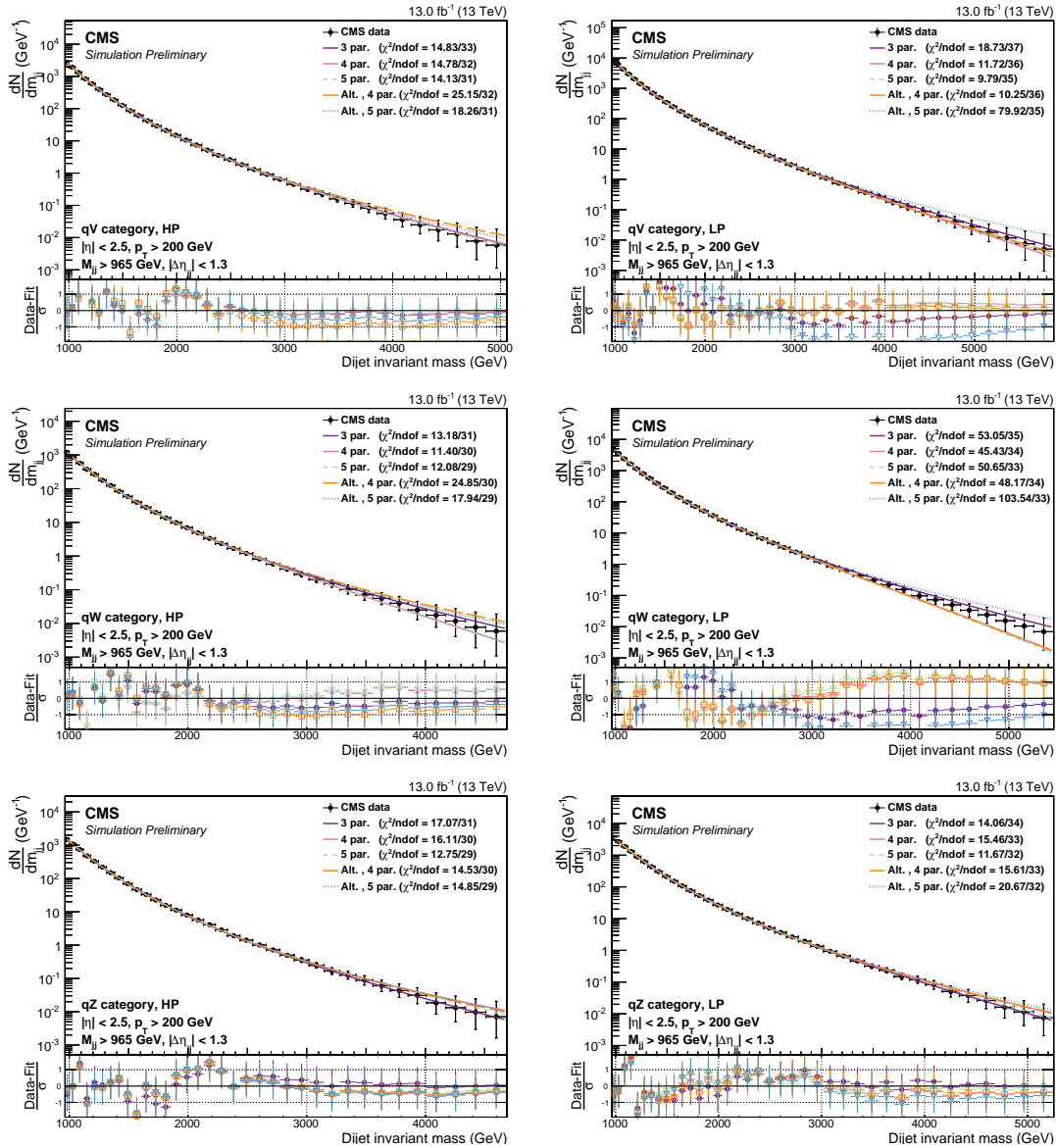


**Figure B.9:** Background fit for the  $M_{jj}$  distribution in QCD MC corresponding to  $13 \text{ fb}^{-1}$ . Here for the high- and low-purity single W/Z-tag category for the two different mass categories: wW category (top) and qZ category (bottom).

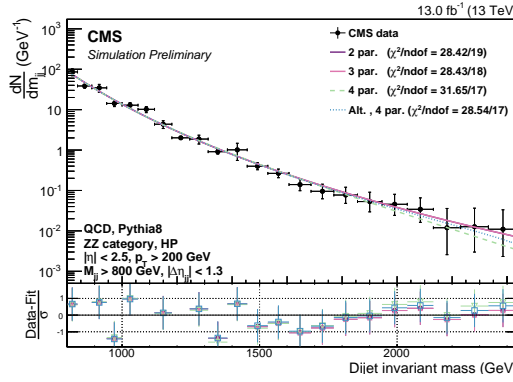


**Figure B.10:** Background fit for the  $M_{jj}$  distribution in QCD MC corresponding to  $13 \text{ fb}^{-1}$ . Here for the high-purity double Z-tag category using a dijet invariant mass threshold of 800 GeV. No turn-on effect at low invariant masses is observed.

WW category, HP			
Function	Residuals	$\chi^2$	ndof
2 par	0.251	17.673	16
3 par	0.187	14.863	15
4 par	0.183	14.618	14
Fishers23	5.454	CL	0.033
Fishers34	0.391	CL	0.541

**Table B.9:** Residuals,  $\chi^2$ , and degrees of freedom for the WW category, HP category. A 3 parameter fit is needed to describe these data.

WW category, LP			
Function	Residuals	$\chi^2$	ndof
2 par	2.974	13.997	23
3 par	3.082	14.775	22
4 par	3.080	14.768	21
Fishers23	-0.805	CL	1.000
Fishers34	0.015	CL	0.905

**Table B.10:** Residuals,  $\chi^2$ , and degrees of freedom for the WW category, LP category. A 2 parameter fit is needed to describe these data.

WZ category, HP			
Function	Residuals	$\chi^2$	ndof
2 par	2.333	17.562	17
3 par	2.158	16.952	16
4 par	2.114	16.842	15
Fishers23	1.372	CL	0.258
Fishers34	0.338	CL	0.569

**Table B.11:** Residuals,  $\chi^2$ , and degrees of freedom for the WZ category, HP category. A 2 parameter fit is needed to describe these data.

WZ category, LP			
Function	Residuals	$\chi^2$	ndof
2 par	12.301	21.368	25
3 par	6.827	20.715	24
4 par	6.521	20.419	23
Fishers23	20.046	CL	0.000
Fishers34	1.126	CL	0.299

**Table B.12:** Residuals,  $\chi^2$ , and degrees of freedom for the WZ category, LP category. A 3 parameter fit is needed to describe these data.

ZZ category, HP			
Function	Residuals	$\chi^2$	ndof
2 par	0.634	17.919	17
3 par	0.662	17.400	16
4 par	0.716	17.096	15
Fishers23	-0.720	CL	1.000
Fishers34	-1.197	CL	1.000

**Table B.13:** Residuals,  $\chi^2$ , and degrees of freedom for the ZZ category, HP category. A 2 parameter fit is needed to describe these data.

ZZ category, LP			
Function	Residuals	$\chi^2$	ndof
2 par	9.293	19.452	22
3 par	6.884	20.118	21
4 par	6.598	20.076	20
Fishers23	7.701	CL	0.011
Fishers34	0.909	CL	0.351

**Table B.14:** Residuals,  $\chi^2$ , and degrees of freedom for the ZZ category, LP category. A 3 parameter fit is needed to describe these data.

qW category, HP			
Function	Residuals	$\chi^2$	ndof
3 par	69.757	30.375	30
4 par	59.677	28.318	29
5 par	25.298	21.815	28
Alt. 4 par	35.610	22.810	29
Alt. 5 par	25.634	22.687	28
Fishers34	5.067	CL	0.032
Fishers45	39.409	CL	0.000
FishersAlt4Alt5	11.285	CL	0.002

**Table B.15:** Residuals,  $\chi^2$ , and degrees of freedom for the qW category, HP category. A 5 parameter fit is needed to describe these data.

qW category, LP			
Function	Residuals	$\chi^2$	ndof
3 par	153.869	38.713	35
4 par	156.715	38.586	34
5 par	201.767	38.167	33
Alt. 4 par	189.434	39.327	34
Alt. 5 par	192.782	39.170	33
Fishers34	-0.636	CL	1.000
Fishers45	-7.592	CL	1.000
FishersAlt4Alt5	-0.590	CL	1.000

**Table B.16:** Residuals,  $\chi^2$ , and degrees of freedom for the qW category, LP category. A 3 parameter fit is needed to describe these data.

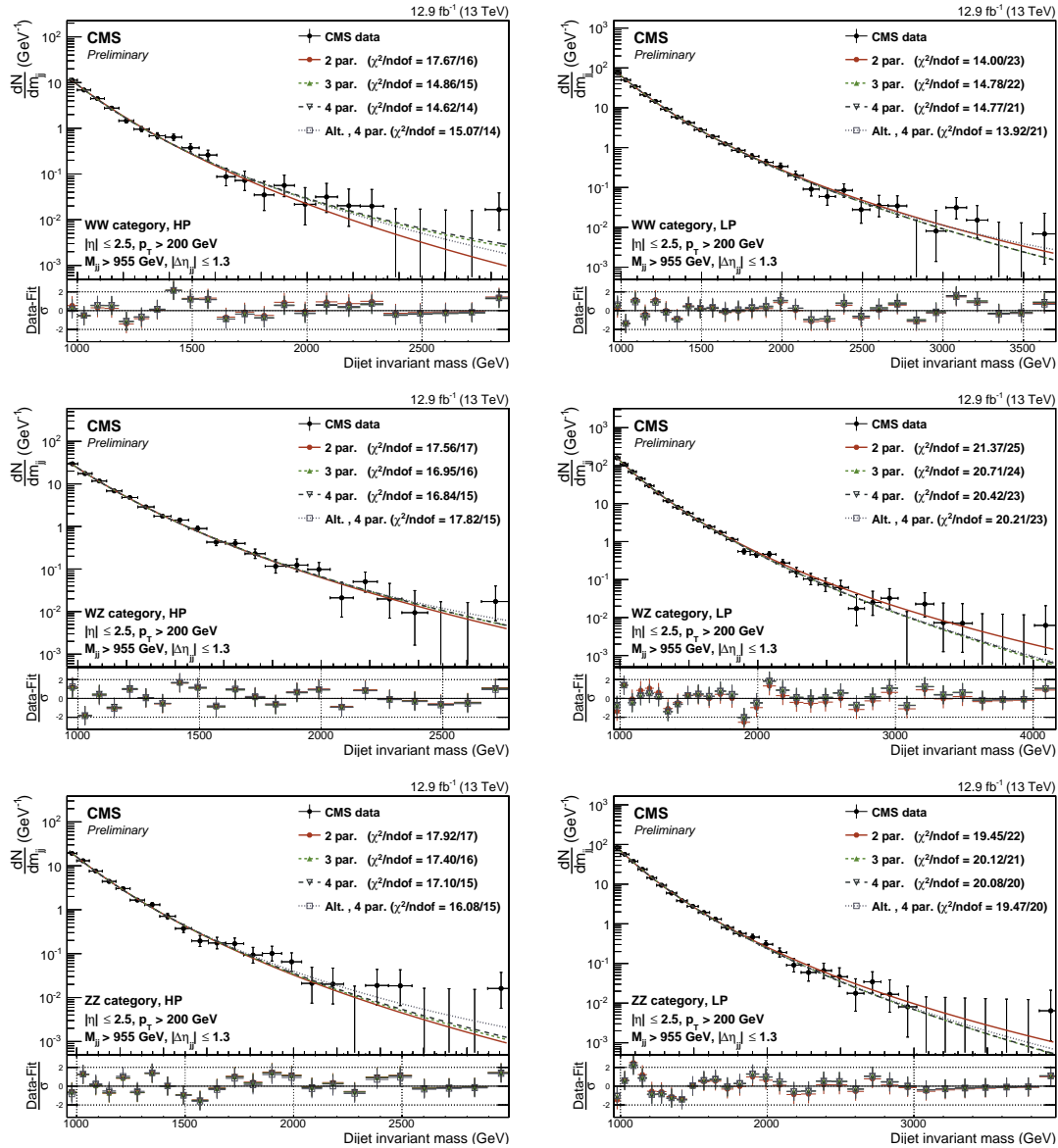


**Figure B.11:** Background fit for the  $M_{jj}$  distribution in the data signal region. Here for the high- (left) and low-purity (right) double W/Z-tag categories WW (top), WZ (middle) and ZZ (bottom).

qZ category, HP			
Function	Residuals	$\chi^2$	ndof
3 par	12.963	21.252	30
4 par	12.961	21.252	29
5 par	9.256	19.644	28
Alt. 4 par	13.931	20.977	29
Alt. 5 par	9.739	20.344	28
Fishers34	0.004	CL	0.948
Fishers45	11.609	CL	0.002
FishersAlt4Alt5	12.484	CL	0.001

**Table B.17:** Residuals,  $\chi^2$ , and degrees of freedom for the qZ category, HP category. A 3 parameter fit is needed to describe these data.

qZ category, LP			
Function	Residuals	$\chi^2$	ndof
3 par	369.554	47.426	36
4 par	369.554	47.426	35
5 par	298.358	46.525	34
Alt. 4 par	379.111	47.531	35
Alt. 5 par	379.120	47.531	34
Fishers34	0.000	CL	0.994
Fishers45	8.352	CL	0.007
FishersAlt4Alt5	-0.001	CL	0.000

**Table B.18:** Residuals,  $\chi^2$ , and degrees of freedom for the qZ category, LP category. A 3 parameter fit is needed to describe these data.



3169

---

## APPENDIX C

---

3170

## Search III

3171 **C.1 Signal fits**

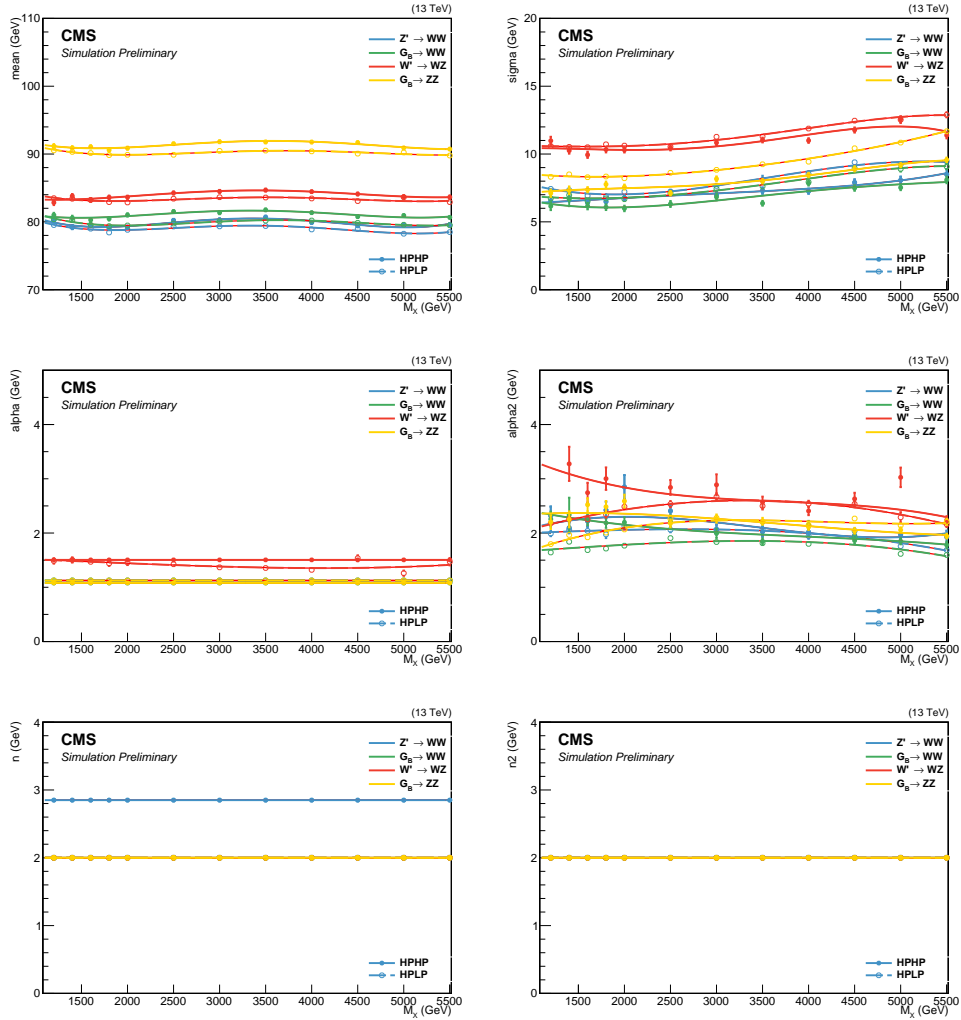


**Figure C.1:** The interpolated double Crystal-ball parameters for the softdrop jet mass as a function of  $M_X$ . To improve the stability of the fit some parameters are set constant. Here for jet 2.

3172 **C.2 2016 kernels**

3173 **C.3 Resonant background**

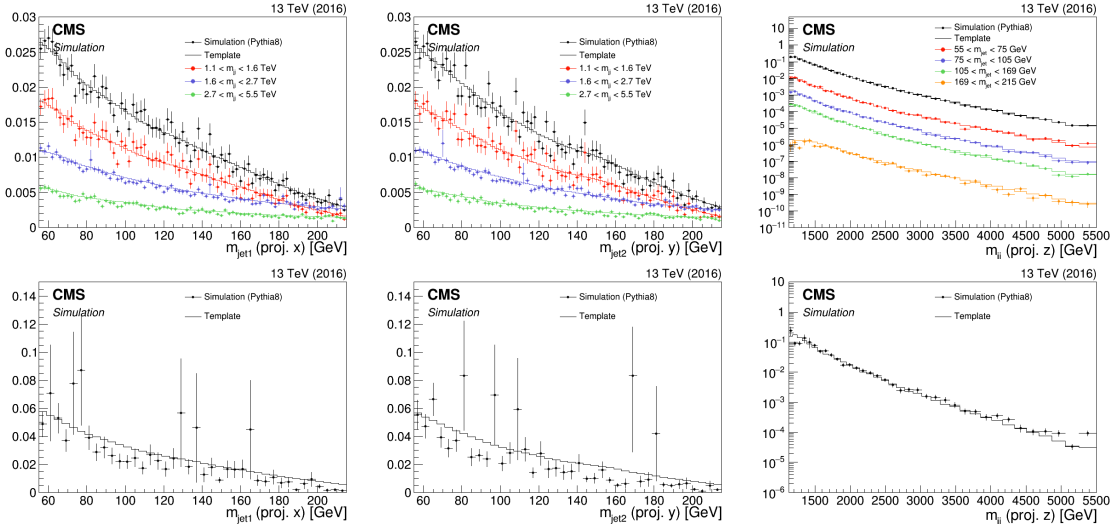


**Figure C.2:** Comparison between QCD MC simulation (markers) and kernels derived from generator level quantities (lines) for the HPHP category (top) and the HPLP category (bottom). The kernels are shown for  $M_{\text{jet}1}$  (left),  $M_{\text{jet}2}$  (middle) and  $M_{\text{VV}}$  (right).

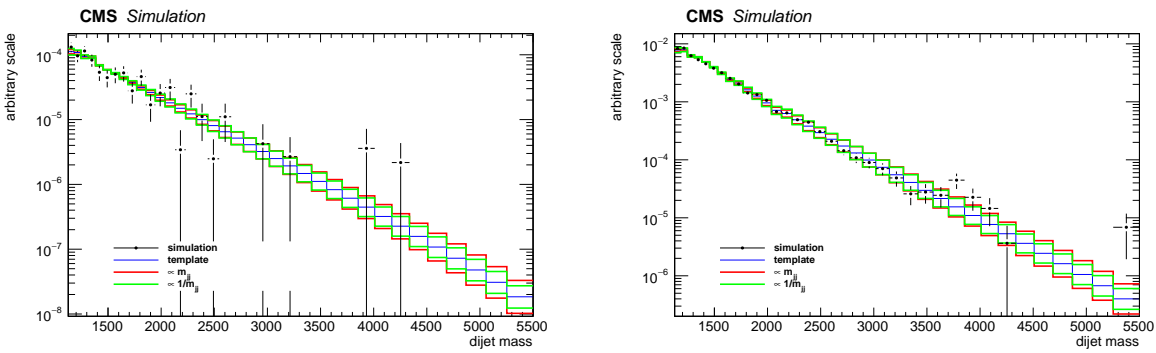


**Figure C.3:** One dimensional  $M_{\text{VV}}$  kernels (solid line) compared to MC (markers) for the  $Z + \text{jets}$  background in the HPHP (left) and HPLP (right) categories. The nominal shape derived from the smoothing procedure can be seen as blue line, alternative shapes derived from varying the slope of the  $M_{\text{VV}}$  spectrum are shown in green and red.



3174

## Bibliography

- 3175 [1] Particle Data Group Collaboration, “Review of Particle Physics”, *Chin. Phys.* **C40** (2016),  
3176 no. 10, 100001, doi:10.1088/1674-1137/40/10/100001.
- 3177 [2] M. Gell-Mann, “Symmetries of Baryons and Mesons”, *Phys. Rev.* **125** (Feb, 1962)  
3178 1067–1084, doi:10.1103/PhysRev.125.1067.
- 3179 [3] W. Pauli, “Mathematical contributions to the theory of Dirac’s matrices”, *Ann. Inst. H.  
3180 Poincaré Phys. Theor.* **6** (1936) 109–136.
- 3181 [4] R. Tumulka, “Pauli Spin Matrices”, pp. 470–472. 07, 2009.  
3182 doi:10.1007/978-3-540-70626-7\_142.
- 3183 [5] S. Duplij and F. Klinkhamer, “Levi-Civita Symbol”, pp. 227–227. Springer Netherlands,  
3184 Dordrecht, 2004. doi:10.1007/1-4020-4522-0\_298.
- 3185 [6] S. Weinberg, “Conceptual Foundations of the Unified Theory of Weak and Electromagnetic  
3186 Interactions”, *Rev. Mod. Phys.* **52** (1980) 515–523, doi:10.1103/RevModPhys.52.515.  
3187 [,543(1979)].
- 3188 [7] F. Englert and R. Brout, “Broken Symmetry and the Mass of Gauge Vector Mesons”, *Phys.  
3189 Rev. Lett.* **13** (Aug, 1964) 321–323, doi:10.1103/PhysRevLett.13.321.
- 3190 [8] P. W. Higgs, “Broken Symmetries and the Masses of Gauge Bosons”, *Phys. Rev. Lett.* **13**  
3191 (Oct, 1964) 508–509, doi:10.1103/PhysRevLett.13.508.
- 3192 [9] G. S. Guralnik, C. R. Hagen, and T. W. B. Kibble, “Global Conservation Laws and Massless  
3193 Particles”, *Phys. Rev. Lett.* **13** (Nov, 1964) 585–587, doi:10.1103/PhysRevLett.13.585.
- 3194 [10] P. W. Anderson, “Coherent Excited States in the Theory of Superconductivity: Gauge  
3195 Invariance and the Meissner Effect”, *Phys. Rev.* **110** (May, 1958) 827–835,  
3196 doi:10.1103/PhysRev.110.827.

- 3197 [11] J. Goldstone, “Field Theories with Superconductor Solutions”, *Nuovo Cim.* **19** (1961)  
 3198 154–164, doi:10.1007/BF02812722.
- 3199 [12] J. Ellis, “Higgs Physics”, 52 pages, 45 figures, Lectures presented at the ESHEP 2013 School  
 3200 of High-Energy Physics, to appear as part of the proceedings in a CERN Yellow Report.
- 3201 [13] B. Bellazzini, C. Csáki, and J. Serra, “Composite Higgses”, *Eur. Phys. J.* **C74** (2014),  
 3202 no. 5, 2766, doi:10.1140/epjc/s10052-014-2766-x, arXiv:1401.2457.
- 3203 [14] R. Contino, D. Marzocca, D. Pappadopulo, and R. Rattazzi, “On the effect of resonances in  
 3204 composite Higgs phenomenology”, *JHEP* **10** (2011) 081, doi:10.1007/JHEP10(2011)081,  
 3205 arXiv:1109.1570.
- 3206 [15] D. Pappadopulo, A. Thamm, R. Torre, and A. Wulzer, “Heavy Vector Triplets: Bridging  
 3207 Theory and Data”, *JHEP* **09** (2014) 060, doi:10.1007/JHEP09(2014)060,  
 3208 arXiv:1402.4431.
- 3209 [16] L. Randall and R. Sundrum, “Large Mass Hierarchy from a Small Extra Dimension”, *Phys.*  
 3210 *Rev. Lett.* **83** (Oct, 1999) 3370–3373, doi:10.1103/PhysRevLett.83.3370.
- 3211 [17] K. Agashe, H. Davoudiasl, G. Perez, and A. Soni, “Warped gravitons at the CERN LHC  
 3212 and beyond”, *Phys. Rev. D* **76** (Aug, 2007) 036006, doi:10.1103/PhysRevD.76.036006.
- 3213 [18] A. L. Fitzpatrick, J. Kaplan, L. Randall, and L.-T. Wang, “Searching for the Kaluza-Klein  
 3214 Graviton in Bulk RS Models”, *JHEP* **09** (2007) 013,  
 3215 doi:10.1088/1126-6708/2007/09/013, arXiv:hep-ph/0701150.
- 3216 [19] CERN, “Accelerators and Schedules”, 2018 (accessed November 12, 2018),  
 3217 <https://beams.web.cern.ch/content/accelerators-schedules>.
- 3218 [20] CMS, “CMS Detector Design”, 2018 (accessed November 21, 2018),  
 3219 <https://cms.cern/news/cms-detector-design>.
- 3220 [21] T. Lenzi, “Development and Study of Different Muon Track Reconstruction Algorithms for  
 3221 the Level-1 Trigger for the CMS Muon Upgrade with GEM Detectors”, Master’s thesis, U.  
 3222 Brussels (main), 2013.
- 3223 [22] A. Dominguez et al., “CMS Technical Design Report for the Pixel Detector Upgrade”,  
 3224 Technical Report CERN-LHCC-2012-016. CMS-TDR-11, CERN, Sep, 2012.
- 3225 [23] CMS Collaboration, “The CMS Experiment at the CERN LHC”, *JINST* **3** (2008) S08004,  
 3226 doi:10.1088/1748-0221/3/08/S08004.

- [24] P. Adzic et al., “Energy resolution of the barrel of the CMS electromagnetic calorimeter”, *JINST* **2** (2007) P04004, doi:10.1088/1748-0221/2/04/P04004.
- [25] C. Biino, “The CMS Electromagnetic Calorimeter: overview, lessons learned during Run 1 and future projections”, *Journal of Physics: Conference Series* **587** (2015), no. 1, 012001.
- [26] L. V. . EP, “Assembly of the 7th wedge. Assemblage du 7eme module”, (Aug, 2000). CMS Collection.
- [27] S. Sharma, “Understanding the performance of CMS calorimeter”, *Pramana* **69** (Dec, 2007) 1069–1074, doi:10.1007/s12043-007-0229-8.
- [28] on behalf of the CMS Collaboration Collaboration, “CMS reconstruction improvement for the muon tracking by the RPC chambers”, *PoS RPC2012* (Sep, 2012) 045. 9 p.  
Presented by Minsuk Kim at the XI workshop on Resistive Plate Chambers and Related Detectors - RPC2012, INFN Laboratori Nazionali di Frascati Italy, February 5-10, 2012.
- [29] CMS, “CMS Luminosity - public results”, 2018 (accessed December 11, 2018),  
<https://twiki.cern.ch/twiki/bin/view/CMSPublic/LumiPublicResults>.
- [30] P. Billoir, “Progressive track recognition with a Kalman-like fitting procedure”, *Computer Physics Communications* **57** (1989), no. 1, 390 – 394,  
doi:[https://doi.org/10.1016/0010-4655\(89\)90249-X](https://doi.org/10.1016/0010-4655(89)90249-X).
- [31] A. S. et. Al., “Particle-flow reconstruction and global event description with the CMS detector”, *Journal of Instrumentation* **12** (2017), no. 10, P10003.
- [32] W. Adam, R. Frühwirth, A. Strandlie, and T. Todorov, “Reconstruction of electrons with the Gaussian-sum filter in the CMS tracker at the LHC”, *Journal of Physics G: Nuclear and Particle Physics* **31** (2005), no. 9, N9.
- [33] T. C. collaboration, “Performance of CMS muon reconstruction in pp collision events at s = 7 TeV”, *Journal of Instrumentation* **7** (2012), no. 10, P10002.
- [34] D. Bertolini, P. Harris, M. Low, and N. Tran, “Pileup per particle identification”, *Journal of High Energy Physics* **2014** (2014), no. 10, doi:10.1007/JHEP10(2014)059.
- [35] Y. L. Dokshitzer, G. D. Leder, S. Moretti, and B. R. Webber, “Better jet clustering algorithms”, *JHEP* **08** (1997) 001, doi:10.1088/1126-6708/1997/08/001,  
[arXiv:hep-ph/9707323](https://arxiv.org/abs/hep-ph/9707323).

- 3256 [36] S. D. Ellis and D. E. Soper, “Successive combination jet algorithm for hadron collisions”,  
 3257 *Phys. Rev.* **D48** (1993) 3160–3166, doi:10.1103/PhysRevD.48.3160,  
 3258 arXiv:hep-ph/9305266.
- 3259 [37] M. Cacciari, G. P. Salam, and G. Soyez, “The anti- $k_t$  jet clustering algorithm”, *JHEP* **04**  
 3260 (2008) 063, doi:10.1088/1126-6708/2008/04/063, arXiv:0802.1189.
- 3261 [38] J. POG, “Jet Identification: Recommendations for 13TeV data analysis”, 2018 (accessed  
 3262 December 18, 2018), <https://twiki.cern.ch/twiki/bin/viewauth/CMS/JetID>.
- 3263 [39] CMS Collaboration, “Determination of Jet Energy Calibration and Transverse Momentum  
 3264 Resolution in CMS”, *JINST* **6** (2011) P11002, doi:10.1088/1748-0221/6/11/P11002,  
 3265 arXiv:1107.4277.
- 3266 [40] D. Krohn, J. Thaler, and L.-T. Wang, “Jet Trimming”, *JHEP* **02** (2010) 084,  
 3267 doi:10.1007/JHEP02(2010)084, arXiv:0912.1342.
- 3268 [41] CMS Collaboration Collaboration, “Pileup Removal Algorithms”, Technical Report  
 3269 CMS-PAS-JME-14-001, CERN, Geneva, 2014.
- 3270 [42] M. Dasgupta, A. Fregoso, S. Marzani, and G. P. Salam, “Towards an understanding of jet  
 3271 substructure”, *JHEP* **09** (2013) 029, doi:10.1007/JHEP09(2013)029, arXiv:1307.0007.
- 3272 [43] J. M. Butterworth, A. R. Davison, M. Rubin, and G. P. Salam, “Jet substructure as a new  
 3273 Higgs search channel at the LHC”, *Phys. Rev. Lett.* **100** (2008) 242001,  
 3274 doi:10.1103/PhysRevLett.100.242001, arXiv:0802.2470.
- 3275 [44] A. J. Larkoski, S. Marzani, G. Soyez, and J. Thaler, “Soft Drop”, *JHEP* **05** (2014) 146,  
 3276 doi:10.1007/JHEP05(2014)146, arXiv:1402.2657.
- 3277 [45] J. Thaler and K. Van Tilburg, “Identifying Boosted Objects with N-subjettiness”, *JHEP*  
 3278 **03** (2011) 015, doi:10.1007/JHEP03(2011)015, arXiv:1011.2268.
- 3279 [46] J. Thaler and K. Van Tilburg, “Maximizing boosted top identification by minimizing  
 3280 N-subjettiness”, *Journal of High Energy Physics* **2012** (Feb, 2012) 93,  
 3281 doi:10.1007/JHEP02(2012)093.
- 3282 [47] S. Bolognesi et al., “Spin and parity of a single-produced resonance at the LHC”, *Phys.  
 3283 Rev. D* **86** (Nov, 2012) 095031, doi:10.1103/PhysRevD.86.095031.
- 3284 [48] CMS Collaboration, “Identification techniques for highly boosted W bosons that decay into  
 3285 hadrons”, *JHEP* **12** (2014) 017, doi:10.1007/JHEP12(2014)017, arXiv:1410.4227.

- 3286 [49] M. Bahr et al., “Herwig++ Physics and Manual”, *Eur. Phys. J.* **C58** (2008) 639–707,  
3287 doi:10.1140/epjc/s10052-008-0798-9, arXiv:0803.0883.
- 3288 [50] T. Sjöstrand et al., “An Introduction to PYTHIA 8.2”, *Comput. Phys. Commun.* **191**  
3289 (2015) 159–177, doi:10.1016/j.cpc.2015.01.024, arXiv:1410.3012.
- 3290 [51] The ATLAS collaboration, “Search for high-mass diboson resonances with boson-tagged jets  
3291 in proton-proton collisions at  $s=8$  TeV with the ATLAS detector”, *Journal of High Energy*  
3292 *Physics* **2015** (Dec, 2015) 1–39, doi:10.1007/JHEP12(2015)055.
- 3293 [52] S. Frixione and B. R. Webber, “Matching NLO QCD computations and parton shower  
3294 simulations”, *JHEP* **06** (2002) 029, doi:10.1088/1126-6708/2002/06/029,  
3295 arXiv:hep-ph/0204244.
- 3296 [53] S. Frixione, P. Nason, and B. R. Webber, “Matching NLO QCD and parton showers in  
3297 heavy flavor production”, *JHEP* **08** (2003) 007, doi:10.1088/1126-6708/2003/08/007,  
3298 arXiv:hep-ph/0305252.
- 3299 [54] S. Frixione, P. Nason, and C. Oleari, “Matching NLO QCD computations with Parton  
3300 Shower simulations: the POWHEG method”, *JHEP* **11** (2007) 070,  
3301 doi:10.1088/1126-6708/2007/11/070, arXiv:0709.2092.
- 3302 [55] S. A. et. al., “Geant4—a simulation toolkit”, *Nuclear Instruments and Methods in Physics*  
3303 *Research Section A: Accelerators, Spectrometers, Detectors and Associated Equipment* **506**  
3304 (2003), no. 3, 250 – 303, doi:[https://doi.org/10.1016/S0168-9002\(03\)01368-8](https://doi.org/10.1016/S0168-9002(03)01368-8).
- 3305 [56] CMS Collaboration, “Event generator tunes obtained from underlying event and  
3306 multiparton scattering measurements”, *Eur. Phys. J. C* **76** (2016) 155,  
3307 doi:10.1140/epjc/s10052-016-3988-x, arXiv:1512.00815.
- 3308 [57] CMS Collaboration Collaboration, “Search for massive resonances in dijet systems  
3309 containing jets tagged as W or Z boson decays in pp collisions at  $\sqrt{s}=8$  TeV”, *JHEP* **08**  
3310 (May, 2014) 173. 37 p. Comments: Replaced with published version. Added journal reference  
3311 and DOI.
- 3312 [58] F. Dias et al., “Combination of Run-1 Exotic Searches in Diboson Final States at the LHC”,  
3313 *JHEP* **04** (2016) 155, doi:10.1007/JHEP04(2016)155, arXiv:1512.03371.
- 3314 [59] CERN, “Collider Reach”, 2019 (accessed January 12, 2019),  
3315 <http://collider-reach.web.cern.ch/>.

- 3316 [60] J. Alwall et al., “The automated computation of tree-level and next-to-leading order  
 3317 differential cross sections, and their matching to parton shower simulations”, *JHEP* **07**  
 3318 (2014) 079, doi:10.1007/JHEP07(2014)079, arXiv:1405.0301.
- 3319 [61] T. Sjöstrand, S. Mrenna, and P. Z. Skands, “A brief introduction to PYTHIA 8.1”, *Comput.  
 3320 Phys. Commun.* **178** (2008) 852, doi:10.1016/j.cpc.2008.01.036, arXiv:0710.3820.
- 3321 [62] G. Punzi, “Sensitivity of searches for new signals and its optimization”, *eConf* **C030908**  
 3322 (2003) MODT002, arXiv:physics/0308063. [,79(2003)].
- 3323 [63] CMS Collaboration, “Search for heavy resonances in the W/Z-tagged dijet mass spectrum  
 3324 in pp collisions at 7 TeV”, *Phys. Lett.* **B723** (2013) 280–301,  
 3325 doi:10.1016/j.physletb.2013.05.040, arXiv:1212.1910.
- 3326 [64] CMS Collaboration Collaboration, “Search for Narrow Resonances using the Dijet Mass  
 3327 Spectrum with 19.6fb-1 of pp Collisions at sqrt(s)=8 TeV”, Technical Report  
 3328 CMS-PAS-EXO-12-059, CERN, Geneva, 2013.
- 3329 [65] D. J. Hand, “Statistical Concepts: A Second Course, Fourth Edition by Richard G. Lomax,  
 3330 Debbie L. Hahs-Vaughn”, *International Statistical Review* **80** (2012), no. 3, 491–491.
- 3331 [66] T. C. collaboration, “Identification of b-quark jets with the CMS experiment”, *Journal of  
 3332 Instrumentation* **8** (2013), no. 04, P04013.
- 3333 [67] T. C. collaboration, “Identification of heavy-flavour jets with the CMS detector in pp  
 3334 collisions at 13 TeV”, *Journal of Instrumentation* **13** (2018), no. 05, P05011.
- 3335 [68] CMS Collaboration Collaboration, “Search for massive resonances decaying into WW, WZ,  
 3336 ZZ, qW and qZ in the dijet final state at  $\sqrt{s} = 13$  TeV using 2016 data”, Technical Report  
 3337 CMS-PAS-B2G-16-021, CERN, Geneva, 2016.
- 3338 [69] M. Dasgupta, A. Powling, and A. Siódmiak, “On jet substructure methods for signal jets”,  
 3339 *JHEP* **08** (2015) 079, doi:10.1007/JHEP08(2015)079, arXiv:1503.01088.
- 3340 [70] U. Baur, I. Hinchliffe, and D. Zeppenfeld, “Excited quark production at hadron colliders”,  
 3341 *Int. J. Mod. Phys. A* **2** (1987) 1285, doi:10.1142/S0217751X87000661.
- 3342 [71] U. Baur, M. Spira, and P. M. Zerwas, “Excited-quark and -lepton production at hadron  
 3343 colliders”, *Phys. Rev. D* **42** (1990) 815, doi:10.1103/PhysRevD.42.815.

- [72] CMS Collaboration Collaboration, “Search for massive resonances decaying into  $WW$ ,  $WZ$ ,  $ZZ$ ,  $qW$ , and  $qZ$  with dijet final states at  $\sqrt{s} = 13$  TeV”, *Phys. Rev. D* **97** (Apr, 2018) 072006, doi:10.1103/PhysRevD.97.072006.
- [73] CMS Collaboration Collaboration, “Jet algorithms performance in 13 TeV data”, Technical Report CMS-PAS-JME-16-003, CERN, Geneva, 2017.
- [74] J. Alwall et al., “Comparative study of various algorithms for the merging of parton showers and matrix elements in hadronic collisions”, *Eur. Phys. J.* **C53** (2008) 473–500, doi:10.1140/epjc/s10052-007-0490-5, arXiv:0706.2569.
- [75] J. Dolen et al., “Thinking outside the ROCs: Designing Decorrelated Taggers (DDT) for jet substructure”, arXiv:1603.00027.
- [76] J. Gallicchio and M. D. Schwartz, “Quark and Gluon Tagging at the LHC”, *Phys. Rev. Lett.* **107** (2011) 172001, doi:10.1103/PhysRevLett.107.172001, arXiv:1106.3076.
- [77] J. A. Aguilar-Saavedra, “Stealth bosons and where to find them”, 2018, <https://indico.cern.ch/event/649482/contributions/2993323/attachments/1688557/2716149/SBAWTFD.pdf>.
- [78] J. A. Aguilar-Saavedra, “Running bumps from stealth bosons”, *Eur. Phys. J.* **C78** (2018), no. 3, 206, doi:10.1140/epjc/s10052-018-5717-0, arXiv:1801.08129.
- [79] ATLAS Collaboration Collaboration, “Search for diboson resonances in hadronic final states in  $79.8 \text{ fb}^{-1}$  of  $pp$  collisions at  $\sqrt{s} = 13$  TeV with the ATLAS detector”, Technical Report ATLAS-CONF-2018-016, CERN, Geneva, Jun, 2018.
- [80] T. Heimel, G. Kasieczka, T. Plehn, and J. M. Thompson, “QCD or What?”, arXiv:1808.08979.
- [81] J. A. Aguilar-Saavedra, J. H. Collins, and R. K. Mishra, “A generic anti-QCD jet tagger”, *JHEP* **11** (2017) 163, doi:10.1007/JHEP11(2017)163, arXiv:1709.01087.
- [82] A. Butter, G. Kasieczka, T. Plehn, and M. Russell, “Deep-learned Top Tagging with a Lorentz Layer”, *SciPost Phys.* **5** (2018), no. 3, 028, doi:10.21468/SciPostPhys.5.3.028, arXiv:1707.08966.
- [83] D. P. Kingma and J. Ba, “Adam: A Method for Stochastic Optimization”, *CoRR* **abs/1412.6980** (2014) arXiv:1412.6980.

- 3373 [84] F. Chollet et al., “Keras”. <https://keras.io>, 2015.
- 3374 [85] M. A. et al, “TensorFlow: Large-Scale Machine Learning on Heterogeneous Systems”, 2015.  
3375 Software available from tensorflow.org.